

ACOUSTIC AND MECHANICAL METAMATERIALS FOR VARIOUS APPLICATIONS

EDITED BY: Fuyin Ma, Siyuan Dai, Han Jia, Yan-Feng Wang and Yong Xiao
PUBLISHED IN: Frontiers in Materials



frontiers

Frontiers eBook Copyright Statement

The copyright in the text of individual articles in this eBook is the property of their respective authors or their respective institutions or funders. The copyright in graphics and images within each article may be subject to copyright of other parties. In both cases this is subject to a license granted to Frontiers.

The compilation of articles constituting this eBook is the property of Frontiers.

Each article within this eBook, and the eBook itself, are published under the most recent version of the Creative Commons CC-BY licence.

The version current at the date of publication of this eBook is CC-BY 4.0. If the CC-BY licence is updated, the licence granted by Frontiers is automatically updated to the new version.

When exercising any right under the CC-BY licence, Frontiers must be attributed as the original publisher of the article or eBook, as applicable.

Authors have the responsibility of ensuring that any graphics or other materials which are the property of others may be included in the CC-BY licence, but this should be checked before relying on the CC-BY licence to reproduce those materials. Any copyright notices relating to those materials must be complied with.

Copyright and source acknowledgement notices may not be removed and must be displayed in any copy, derivative work or partial copy which includes the elements in question.

All copyright, and all rights therein, are protected by national and international copyright laws. The above represents a summary only. For further information please read Frontiers' Conditions for Website Use and Copyright Statement, and the applicable CC-BY licence.

ISSN 1664-8714

ISBN 978-2-83250-055-2

DOI 10.3389/978-2-83250-055-2

About Frontiers

Frontiers is more than just an open-access publisher of scholarly articles: it is a pioneering approach to the world of academia, radically improving the way scholarly research is managed. The grand vision of Frontiers is a world where all people have an equal opportunity to seek, share and generate knowledge. Frontiers provides immediate and permanent online open access to all its publications, but this alone is not enough to realize our grand goals.

Frontiers Journal Series

The Frontiers Journal Series is a multi-tier and interdisciplinary set of open-access, online journals, promising a paradigm shift from the current review, selection and dissemination processes in academic publishing. All Frontiers journals are driven by researchers for researchers; therefore, they constitute a service to the scholarly community. At the same time, the Frontiers Journal Series operates on a revolutionary invention, the tiered publishing system, initially addressing specific communities of scholars, and gradually climbing up to broader public understanding, thus serving the interests of the lay society, too.

Dedication to Quality

Each Frontiers article is a landmark of the highest quality, thanks to genuinely collaborative interactions between authors and review editors, who include some of the world's best academicians. Research must be certified by peers before entering a stream of knowledge that may eventually reach the public - and shape society; therefore, Frontiers only applies the most rigorous and unbiased reviews. Frontiers revolutionizes research publishing by freely delivering the most outstanding research, evaluated with no bias from both the academic and social point of view. By applying the most advanced information technologies, Frontiers is catapulting scholarly publishing into a new generation.

What are Frontiers Research Topics?

Frontiers Research Topics are very popular trademarks of the Frontiers Journals Series: they are collections of at least ten articles, all centered on a particular subject. With their unique mix of varied contributions from Original Research to Review Articles, Frontiers Research Topics unify the most influential researchers, the latest key findings and historical advances in a hot research area! Find out more on how to host your own Frontiers Research Topic or contribute to one as an author by contacting the Frontiers Editorial Office: frontiersin.org/about/contact

ACOUSTIC AND MECHANICAL METAMATERIALS FOR VARIOUS APPLICATIONS

Topic Editors:

Fuyin Ma, Xi'an Jiaotong University, China

Siyuan Dai, Auburn University, United States

Han Jia, Chinese Academy of Sciences (CAS), China

Yan-Feng Wang, Tianjin University, China

Yong Xiao, National University of Defense Technology, China

Citation: Ma, F., Dai, S., Jia, H., Wang, Y.-F., Xiao, Y., eds. (2022). Acoustic and Mechanical Metamaterials for Various Applications. Lausanne: Frontiers Media SA.
doi: 10.3389/978-2-83250-055-2

Table of Contents

04	<i>Numerical and Experimental Research on Single-Valve and Multi-Valve Resonant Systems</i>
	Changan Bai, Tianning Chen and Wuzhou Yu
18	<i>Ultra-Thin Metasurface-Based Absorber of Low-Frequency Sound With Bandwidth Optimization</i>
	Yi-jun Guan, Yong Ge, Hong-xiang Sun, Shou-qi Yuan, Yun Lai and Xiao-jun Liu
26	<i>Enhanced Energy Harvesting of Flexural Waves in Elastic Beams by Bending Mode of Graded Resonators</i>
	Jacopo Maria De Ponti, Luca Iorio, Emanuele Riva, Francesco Braghin, Alberto Corigliano and Raffaele Ardito
33	<i>Hybrid Bandgaps in Mass-coupled Bragg Atomic Chains: Generation and Switching</i>
	Shao-Feng Xu, Zhu-Long Xu and Kuo-Chih Chuang
47	<i>Acoustic Slow-Wave Effect Metamaterial Muffler for Noise Control of HVDC Converter Station</i>
	Dingge Yang, Quanyuan Jiang, Jingfeng Wu, Yanhua Han, Bin Ding, Bo Niu and Guolin Xie
54	<i>Broadband Sound Absorption of Subwavelength Porous Meta-Liner</i>
	Heye Xiao, Tianyue Yuan, Xiang Song, Junli Chen, Jie Zhou, Dan Sui and Jintao Gu
62	<i>Broadband Transformation Acoustic Waveguide With Anisotropic Density Based on Pentamode Metamaterials</i>
	Xing Chen, Li Cai and Jihong Wen
69	<i>Band Structure Analysis of SH Wave Propagating in Nanoscale Layered Metamaterial Structures</i>
	Zhizhong Yan and Xiaotong Yang
82	<i>Impact of the Scatterer Type on Ultrasound Wave Propagation in Microstructure Composites: Calculation and Application</i>
	Yuming Yang, Huilong Duan and Yinfei Zheng
91	<i>Band Gaps and Vibration Attenuation Characteristics Analysis in Homogeneous Beam Coupled With Periodic Oscillators Based on the Method of Reverberation-Ray Matrix</i>
	Li Tang, Xiongliang Yao, Guoxun Wu and Chuanlong Wang
105	<i>Radial Seismic Metamaterials Based on Layering Theory: Broadband Shielding of Ultra-Low Frequency Seismic Surface Waves</i>
	Haixia Liu, Lixia Li, Qi Jia, Sanhe Jiang, Pengguo Li and Xicheng Zhang
120	<i>Acoustic Hologram Reconstruction With Unsupervised Neural Network</i>
	Boyi Li, Mengyang Lu, Chengcheng Liu, Xin Liu and Dean Ta
129	<i>Ultra-Broadband Sound Absorbing Materials Based on Periodic Gradient Impedance Matching</i>
	Fei Wu, Xiao Zhang, Zegang Ju, Jiang Zhao, Man Hu, Mingyuan Gao, Jun Luo and Huayan Pu



Numerical and Experimental Research on Single-Valve and Multi-Valve Resonant Systems

Changan Bai¹, Tianning Chen^{1*} and Wuzhou Yu^{2*}

¹School of Mechanical Engineering, Xi'an Jiaotong University, Xi'an, China, ²Institute of Acoustics, School of Physical Science and Engineering, Tongji University, Shanghai, China

OPEN ACCESS

Edited by:

Fuyin Ma,
Xi'an Jiaotong University, China

Reviewed by:

Jian-Cheng Cai,
Zhejiang Normal University, China
Kai Zhang,
Ocean University of China, China

*Correspondence:

Tianning Chen
tnchen@mail.xjtu.edu.cn
Wuzhou Yu
ywzh@tongji.edu.cn

Specialty section:

This article was submitted to
Metamaterials,
a section of the journal
Frontiers in Materials

Received: 10 August 2021

Accepted: 06 September 2021

Published: 27 September 2021

Citation:

Bai C, Chen T and Yu W (2021)
Numerical and Experimental Research
on Single-Valve and Multi-Valve
Resonant Systems.
Front. Mater. 8:756158.
doi: 10.3389/fmats.2021.756158

Multiple valves in the pipeline system belong to obvious periodic structure distribution types. When a high-speed airstream flows through the pipeline valve, it produces obvious aero-acoustic and acoustic resonance. Acoustic resonant systems with single and six-pipe valves were investigated to understand the flow and acoustic characteristics using a numerical simulation method and testing method. The strongest acoustic resonance occurred at a specific flow velocity with a corresponding Strouhal number of 0.47 corresponding to the geometric parameters in the paper. Moreover, acoustic resonance occurred in a certain velocity range, rather than increasing with the increase of the velocity of the pipeline. This regular increase provided an important theoretical basis for the prediction of the acoustic resonant and ultimate acoustic load of a single-valve system. When the pipeline was attached with multiple valves and the physical dimension was large, the conventional aero-acoustics calculation results were seriously attenuated at high frequency; the calculation method involving a cut-off frequency in this paper was presented and could be used to explain the excellent agreement of the sound pressure level (SPL) below the cut-off frequency and the poor agreement above the cut-off frequency. A new method involving steady flow and stochastic noise generation and radiation (SNGR) was proposed to obtain better results for the SPL at the middle and high frequencies. The comparison results indicated that the traditional method of Lighthill analogy and unsteady flow could accurately acquire aerodynamic noise below the cut-off frequency, while the new method involving steady flow and SNGR could quickly acquire aerodynamic noise above the cut-off frequency.

Keywords: resonance system, pipe valve, steady and unsteady flow, lighthill analogy, stochastic noise generation and radiation

1 INTRODUCTION

Periodic structures are usually used in the design of acoustic metamaterials, and have a large number of applications in low-frequency sound absorption and sound insulation (Ma et al., 2021a). Low-frequency sound absorption and sound insulation performance are often improved by changing the layout of periodic structures and the structural characteristics of single cells (Zhu et al., 2014; Pelat et al., 2020; Ma et al., 2021b).

When high-velocity air flows through variable cross-section pipes, strong resonant noise is generated if the frequency of vortex shedding coincides with the resonant frequency of the bypass pipe. A substantial flow rate causes strong acoustic energy to occur at the junction of the main steam

line valve. The amplified sound pressure wave propagates in the main steam line at the speed of sound and acts on the structure surface. When the acoustic resonant frequency of the pipeline valve is close to the frequency of the structure, the structural vibration increases significantly, leading to severe damage (Shiro et al., 2008).

Mechanical noise, aerodynamic noise (usually called aero-acoustic noise), and cavitation noise represent the primary sound sources effecting a pipeline valve and are investigated using a method that combines theoretical and experimental aspects. In 2005, (Ryu et al. (2005) studied the relationship between the valve spool opening and the noise level in the engine intake and exhaust pipelines via tests, revealing the influence of different valve spool openings on the noise level of pipelines. Alber et al. investigated the characteristics of valve noise sources propagating through structures and air (Alber et al., 2009; Alber et al., 2011). An equivalent analytical model for structural sound propagation analysis was established that could effectively and quickly predict the propagation of valve noise in the structure. The flow velocity, cavity shape, and Strouhal number all had a significant influence on the magnitude of aerodynamic noise. In 2010, (Du and Ouyang (2010) used experimental methods to study the mechanism of howling in the compressor pipeline, and found that the howling was most pronounced at a Strouhal number of 0.51. (Ziada and Shine (1999) summarized the acoustic resonance laws of various valve types and multiple valve combinations, and obtained the relationship between the acoustic resonance frequency and the acoustic resonance order, the corresponding flow velocity, and the diameter of the pipe valve. Oldham et al. adopted a theoretical method (Oldham and Waddington, 2001) to study influencing factors, such as pipeline cut-off frequency and flow velocity on the sound propagation in the pipeline, and calculated the aerodynamic noise in the pipeline system, while Sanjose *et al.* (Alice et al., 2014; Charlebois-Menard et al., 2015; Marsan et al., 2016) built airflow generation devices and test benches. Noise testing of the constructed butterfly valve for aviation was performed using the wall pulsation pressure test method, and the relationship between the Strouhal number and the aerodynamic noise of the valve was studied. Ref(Durgin and Graf, 1992; Uchiyama and Morita, 2015). summarized the mechanism of acoustic resonance of single-valve and multi-valve systems and the acoustic resonance relationship with Strouhal number; the conclusion can be used to summarize the typical acoustic resonance with different valve numbers.

Most previous studies regarding pipeline valve noise are based on experimental tests, and it is apparent from what rare simulation studies do exist that there is a big difference between simulation and testing. The resonance frequency does not match well, and the high-precision resonant sound pressure cannot be directly obtained via the simulation. With the development of computer and numerical methods, numerical simulation has been used to examine the pipeline resonance cavity in recent years. The Lighthill acoustic analogy method (Lighthill, 1952; Lighthill, 1954), in which aerodynamic sound generation makes it possible for tailored algorithms to be used for both tasks, is used nowadays by computational aero-acoustics

tools. This is a straightforward way of arbitrarily combining a sound generation method with another sound transport technique. Its accuracy is limited by the cut-off frequency of computational fluid dynamics (CFD) results. When the characteristic frequency is high, a small grid must be satisfied, which often requires substantial computing resources.

The cavity resonance frequency of the pipe valve can be obtained according to the quarter-wavelength tube formula, and it is inversely proportional to the height of the pipe valve. When the primary pipe size is relatively large, and the flow velocity is high, the characteristic frequency is high. It is difficult to predict the acoustic resonance with limited computing resources and low cut-off frequency. To overcome the expensive computation of an unsteady flow field, a model that synthesizes the flow fluctuations can present an interesting alternative. The SNGR method (Bechara et al., 1994; Bailly and Juve, 2012) has established itself as a complementary module, generating a turbulent velocity field that respects the experimental and theoretical characteristics of the turbulence. Although this method compensates for the expensive cost of unsteady computation, it requires a profound knowledge of turbulence statistics. The source generation process of SNGR is based on two steps. One involves turbulent velocity synthesis, while the other is concerned with source computation based on synthetic velocity, using the Lighthill or the Möhring analogy. The SNGR method is applied for the rapid prediction of external aerodynamic noise, pipeline jet noise, landing gear noise, and vehicle wind noise (Bailly et al., 2012; Paolo et al., 2013; Paolo et al., 2015), and is characterized by the ability to quickly obtain broadband noise magnitudes based on steady-state CFD results. However, since the SNGR method is based on steady-state CFD results, it is difficult to accurately predict low and mid-frequency noise.

In this paper, the aerodynamic noise of a resonance cavity system with a single pipe valve, as well as multi-pipe valves is studied at high flow velocity. Furthermore, the influence of the geometrical size of the pipe valve, the airflow velocity, and the Strouhal number on the frequency of aerodynamic noise is investigated. The SNGR method based on a steady flow field is combined with the acoustic analogy method based on a transient flow field to obtain the full frequency band aerodynamic noise. The accuracy of the simulation method is compared to the experimental data, deriving the method for defining the cut-off frequency. The remainder of the paper is structured as follows: In **Section 2**, the methodology of the resonant pipeline-cavity system is introduced. In the next section, the aerodynamic noise of a single pipe valve, as well as six-pipe valves are then illustrated and discussed. Finally, the conclusions are presented.

2.THE METHODOLOGY OF THE RESONANT PIPELINE-CAVITY SYSTEM

2.1 Unsteady CFD Simulation

An aerodynamic noise test and a simulation of the resonant pipeline-cavity system with a single pipe valve, as well as six-pipe valves, were performed at different flow velocities. Both steady

and unsteady flow fields were simulated using realizable k -epsilon and large eddy simulation (LES). The aerodynamic noise was predicted using the Lighthill analogy methods.

The realizable k -epsilon two-layer model was chosen to predict the steady flow field of the resonant cavity. It has been used effectively for a wide variety of flow simulations, with excellent applicability in free flows with jet and mixed flows or flows with large separations (Shih et al., 1995). The governing equation is expressed as follows:

$$\rho \frac{\partial(ku_j)}{\partial x_i} = \frac{\partial}{\partial x_i} \left(\mu + \frac{\mu_t}{\sigma_k} \right) \frac{\partial k}{\partial x_j} + G_k + G_b - \rho \varepsilon - Y_M + S_k \quad (1)$$

$$\rho \frac{\partial(\varepsilon u_j)}{\partial x_j} = \frac{\partial}{\partial x_j} \left(\mu + \frac{\mu_t}{\sigma_\varepsilon} \right) \frac{\partial \varepsilon}{\partial x_j} + \rho C_{\varepsilon 1} S \varepsilon - \rho C_{\varepsilon 2} \frac{\varepsilon^2}{k + \sqrt{\nu \varepsilon}} + C_{\varepsilon 1} \frac{\varepsilon}{k} C_{\varepsilon 3} G_b \quad (2)$$

$$C_{\varepsilon 1} = \max \left[0.43, \frac{\eta}{\eta + 5} \right], \quad \eta = S \frac{k}{\varepsilon}, \quad S = \sqrt{2S_{ij}S_{ij}}, \quad S_{ij} = \frac{1}{2} \left(\frac{u_i}{x_j} + \frac{u_j}{x_i} \right) \quad (3)$$

Here, G_k is the generating term of the turbulent kinetic k caused by the average velocity gradient; G_b is the generating term of the kinetic k caused by buoyancy; Y_M represents the contribution of the pulsation expansion within the compressible turbulence. $C_{\varepsilon 1}$, $C_{\varepsilon 2}$, and $C_{\varepsilon 3}$ are empirical constants; σ_k and σ_ε are Prandtl numbers corresponding to kinetic energy k and dissipation rate ε ; S_k is the original term.

LES (Lesieur and Metais, 1996) was performed to gain better insight into the noise analysis. During LES, the energy-containing eddies were resolved, while the small-scale structures in the dissipation range were modeled via the subgrid-scale stress term. The governing equations employed for LES were filtered Navier-Stokes and continuity equations:

$$\frac{\partial \bar{u}_i}{\partial t} + \frac{\partial \bar{u}_i \bar{u}_j}{\partial x_j} = -\frac{1}{\rho} \frac{\partial \bar{p}}{\partial x_i} + \nu \frac{\partial^2 \bar{u}_i}{\partial x_j \partial x_j} - \frac{\partial \tau_{ij}}{\partial x_j} \quad (4)$$

$$\frac{\partial \bar{u}_i}{\partial x_i} = 0 \quad (5)$$

Here, \bar{u}_i and \bar{u}_j are the filtering velocity, $i, j = 0, 1, 2$, t is time, ρ is density, \bar{p} is the filtering pressure, ν is kinematic viscosity coefficient, and τ_{ij} is the subgrid stress.

The Smagorinsky-Lilly model represents an eddy viscosity subgrid model, which was proposed by Lilly (Lilly, 1962), and is used to model the subgrid stress. Therefore, to overcome the Smagorinsky-Lilly model constant, which is significantly larger in some turbulent flow problems, Germano proposed the dynamic Smagorinsky model used in the current study, which is based on the idea of eddy viscosity coefficients in Kraichnan spectral space (Germano et al., 1991).

2.2 Lighthill Analogy for Aero-Acoustic Simulation

Lighthill first proposed a hybrid method during the study of nozzle aerodynamic noise in 1952 and 1954, triggering the change

from the N-S equation to the classic Lighthill equation, and marking the generation of modern aeroacoustics. To achieve compatibility with the formulation used in the paper, the alternative equation used for the Lighthill's analogy in the frequency domain was Eq. 6. The spatial derivatives were partially integrated using Green's theorem to obtain the weak variational form, as shown in Eq. 7. This approach to treating the aerodynamic noise problem was intended to be used in low Mach configurations (below 0.3), neglecting the convection and refraction effects in the propagation. This method needed to convert the velocity and density of the sound source area obtained by CFD into a sound source and then use Lighthill's analogy to obtain sound propagation characteristics. The accuracy of the Lighthill analogy was dependent on the fluid and acoustic grids. For broadband noise, a coarse grid led to low accuracy in the middle and high frequencies, but too fine a grid would not be satisfactory if the computing resources or time were limited. Consequently, SNGR could be an option to solve this problem.

$$\frac{\omega^2}{c^2} \varphi + \frac{\partial^2 \varphi}{\partial x_i \partial x_i} = \frac{1}{i\omega} \frac{\partial^2 T_{ij}}{\partial x_i \partial x_j} \quad (6)$$

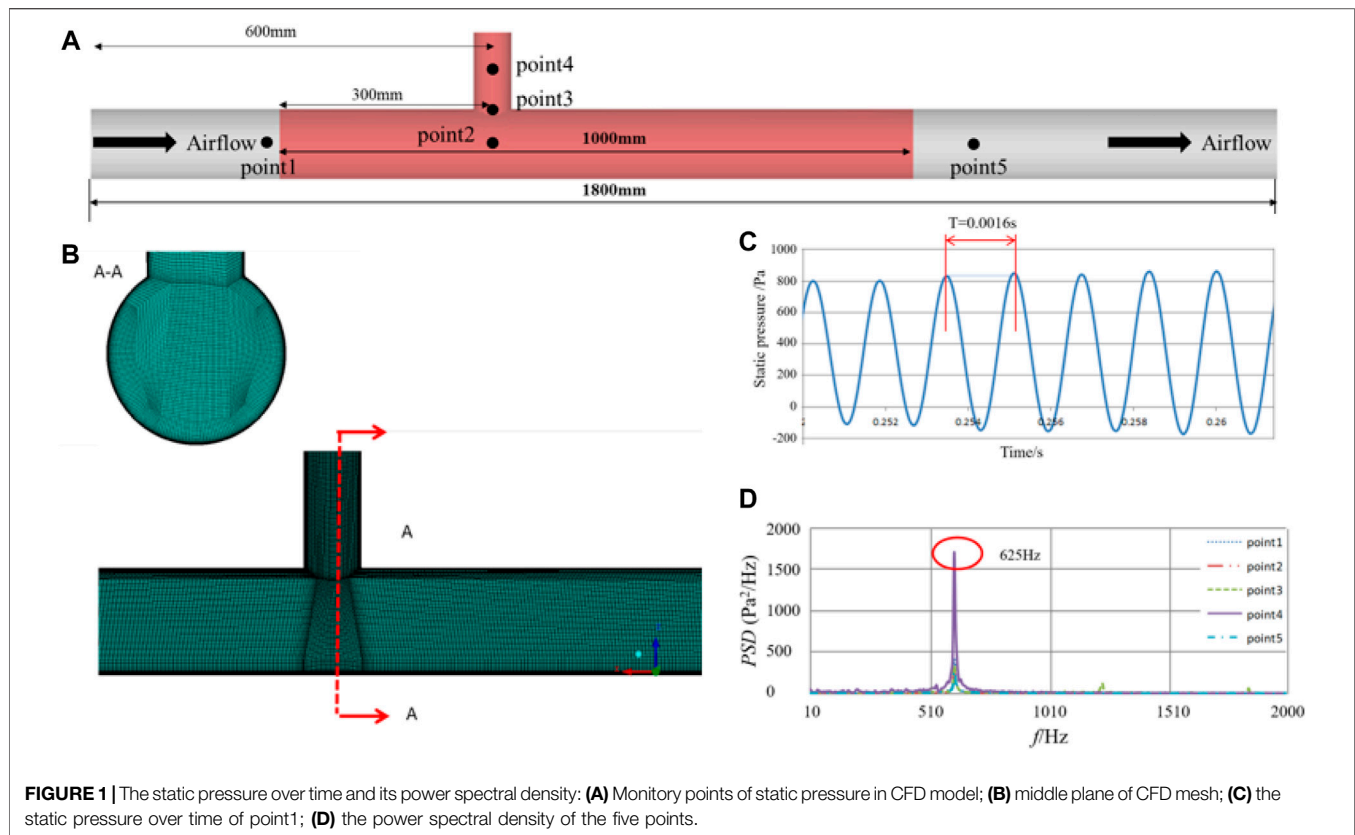
$$\int_{\Omega} \frac{\omega^2}{c^2} \varphi \delta \varphi d\Omega - \int_{\Omega} \frac{\partial \varphi}{\partial x_i} \frac{\partial \delta \varphi}{\partial x_i} d\Omega = \int_{\Omega} \frac{i}{\omega} \frac{\partial \delta \varphi}{\partial x_i} \frac{\partial T_{ij}}{\partial x_j} d\Omega - \int_{\Gamma} \frac{\delta \varphi}{i\omega} \frac{\partial}{\partial x_i} (c^2 \rho \delta_{ij} + T_{ij}) n_i d\Gamma \quad (7)$$

3. AERO-ACOUSTIC ANALYSIS OF THE SINGLE PIPE VALVE

Testing on the resonant pipeline-cavity systems with a single pipe valve was performed at different flow velocities, as shown in Figure 3. For the single-valve system, the effective length and the inner diameter of the straight pipe were 4,000 mm and 110 mm, respectively, while the pipe valve had an inner diameter of 60 mm and a length of 120 mm.

3.1 CFD Simulation Analysis

The numerical model of the straight pipe with a single pipe valve was created, which was consistent with the test. Considering that the current study primarily focuses on the aerodynamic noise characteristics of the pipe valve, the length of the computational domain was 1800 mm, about 30 D (D represents the diameter of the pipe valve), as shown in Figure 1A. There was a 600 mm distance from the upstream of the pipe valve and a 1,200 mm downstream distance. Except for the same seven acoustic measuring points on the wall as in the test, five static pressure measuring points were located in the flow. The position of point1 corresponded with V1. Point2 was located where the center lines of the pipe valve and straight pipe intersected, while point3 and point4 were located at the starting point and midpoint of the centerline of the pipe valve. Point5 was located downstream and 600 mm away from the pipe valve.



The surface and volume meshes of the computational domain were created using ICEM meshing tools. The size of the straight pipe and pipe valve was 4 mm. Furthermore, the height of the first boundary layer mesh was 0.05 mm to ensure that $y^+ \approx 4.0$ at an inlet velocity of 80 m/s. The growth rate and the number of layers were 1.2 and 15, respectively. The boundary layer mesh was applied to all the surfaces, while its quality was acceptable. The total number of grids totaled about 3.9 million, and the middle plane of the grid is depicted in **Figure 1B**.

The incoming velocity of the computational domain inlet was 80 m/s, while the pressure of the computational domain outlet was 0 Pa. The wall boundary conditions were used on the surfaces of the straight pipe and pipe valve. A compressible model and a pressure-based solver were used to carry out the aerodynamic calculations. The discretization of pressure, momentum, and energy were second-order upwind for steady calculations, but the momentum discretization changed into bounded central differencing for unsteady calculations. First, the realizable k -epsilon was run to initialize the flow field in 5,000 iterations, helping to obtain a quick and robust convergence of unsteady simulation. Then, the computation transformed into an unsteady state. LES started to run in a time-step of 0.0001 s with 25 iterations in each time-step. The duration of 0.3 s was roughly 13 times the flow-through time from inlet to outlet. The data sampling began after the flow field reached instability. Data sampling was conducted for 1,000 time-steps, while no universal criterion was available for judging the convergence. Consequently, during this investigation, the calculation was

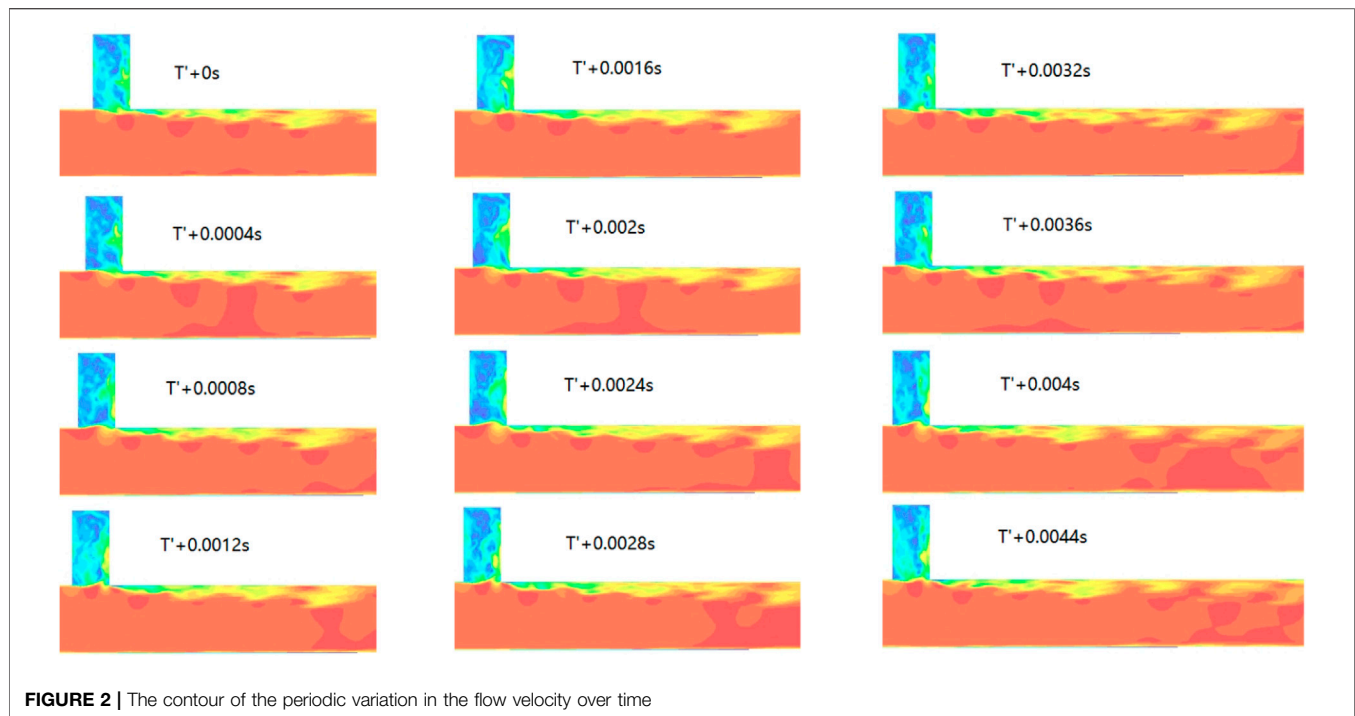
considered convergent when each variable met the convergence criteria, which was about 10^{-4} . Furthermore, the pressure and velocity were monitored to confirm that the flow field variable did not change after multiple iterations.

Over time, the static pressures of the five measuring points in the flow field showed that it displayed a typical periodicity. **Figure 1C** showed the change curve of the static pressure with time for measuring point1, whose duration was 0.0016 s. The power spectral density analysis of each measuring point revealed a significant peak near 625 Hz in **Figure 1D**, which was significantly higher than the other frequencies. Point4 was located in the pipe valve, and exhibited the largest peak value, while point1 was upstream of the pipe valve pipe and displayed the smallest peak value. For the current straight pipe with a pipe valve, an acoustic resonance phenomenon occurred, while the resonance frequency was calculated using **Eq. 8**. The theoretical calculation frequency was consistent with the current unsteady flow field simulation calculation frequency, indicating the accuracy of the unsteady flow-field simulation method.

$$f = \frac{(2n-1)c}{4\left(L - \frac{8r}{3\pi}\right)} \quad (8)$$

Wherein, n is the resonance order; L is the length of the pipe valve; r is the radius of the cavity.

Furthermore, to clearly reflect the changes in the flow field during a specific period, the velocity contour of three periods in the middle plane was chosen. **Figure 2** shows that the area



displaying large velocity fluctuations was concentrated inside and downstream of the pipe valve. The current structure belonged to an open cavity, and the diameter was smaller than the length. For the open cavity, the shear layer formed at the front end of the pipe valve, and the developed shedding vortex propagated downstream, directly hitting the rear end of the pipe valve. Due to the vortex impact, a feedback compression wave propagating upstream was generated in the trailing edge of the cavity. The feedback compression wave propagated upstream and finally reached the leading edge of the cavity. Consequently, noise disturbance was induced, the shear layer of the leading edge was excited again, and the resonance period was closed. The periodic intermittent changes in velocity were indicative of such a flow mechanism.

3.2 Aero-Acoustic Simulation and Experiment

Part of the fluid model was changed into an acoustic model to analyze the resonant cavity system containing a single pipe valve. The grid size of the acoustic model was 10 mm, ensuring that the point per wavelength exceeded 8 at a calculation frequency of 4,000 Hz. This meets the point per wavelength requirements of about 6~8. The velocity and density of the fluid model were converted into the sound source of the acoustic model by interpolation. Furthermore, sound propagation was performed using the Lighthill analogy in the frequency domain. The wall surface of the pipeline was reflected completely, while the end surfaces at both ends of the pipeline were defined as the modal boundary of the pipeline. When the simulated sound wave was transmitted to the end surface of the pipeline, it

propagated down the pipeline without reflection, simulating the true acoustic impedance of the cross-section of the pipeline. Since both the sound source area and the sound propagation area solved the sound wave equation, the acoustic measuring points could be arranged in these locations. The noise test of the resonant pipeline systems with a single pipe valve was performed at different flow velocities, as shown in **Figure 3**

The test facility included an airflow generation system, test piping, and the test system. The airflow system was composed of an air storage tank, flow control valve, straight pipe, front-stage reducer, rear exhaust port, and muffler room, which could produce an airflow up to 100 m/s. As shown in **Figure 3B**, for exploring the influence of different shapes and sizes of the valves on the acoustic results, multiple types of valve resonators with different sizes were selected in the experiment, including but not limited to an L11 model (with valve size $\varnothing 6 \times 12$ cm), L12 model (with valve size $\varnothing 6 \times 24$ cm), and L13 model (with valve size $\varnothing 4 \times 12$ cm). Finally, the L11 model was selected for research and is described in this paper.

The test pipeline system consisted of the main pipeline and the resonant cavity. Due to the high airflow velocity of the resonant cavity, the front end of the microphone was placed as close to the inner wall of the straight pipe and pipe valve as possible to reduce the impact of the airflow on the microphone and to truly reflect the airflow noise in both locations. Moreover, a small amount of porous sound-absorbing material was placed in front of the microphone, which acted as a windproof ball. For the single valve system, seven measuring points were arranged on the straight pipe and the pipe valve, and are shown in **Figure 3C**. P1 and P2 were arranged upstream of the straight pipe, while P5~P7 were located downstream of the straight pipe. The

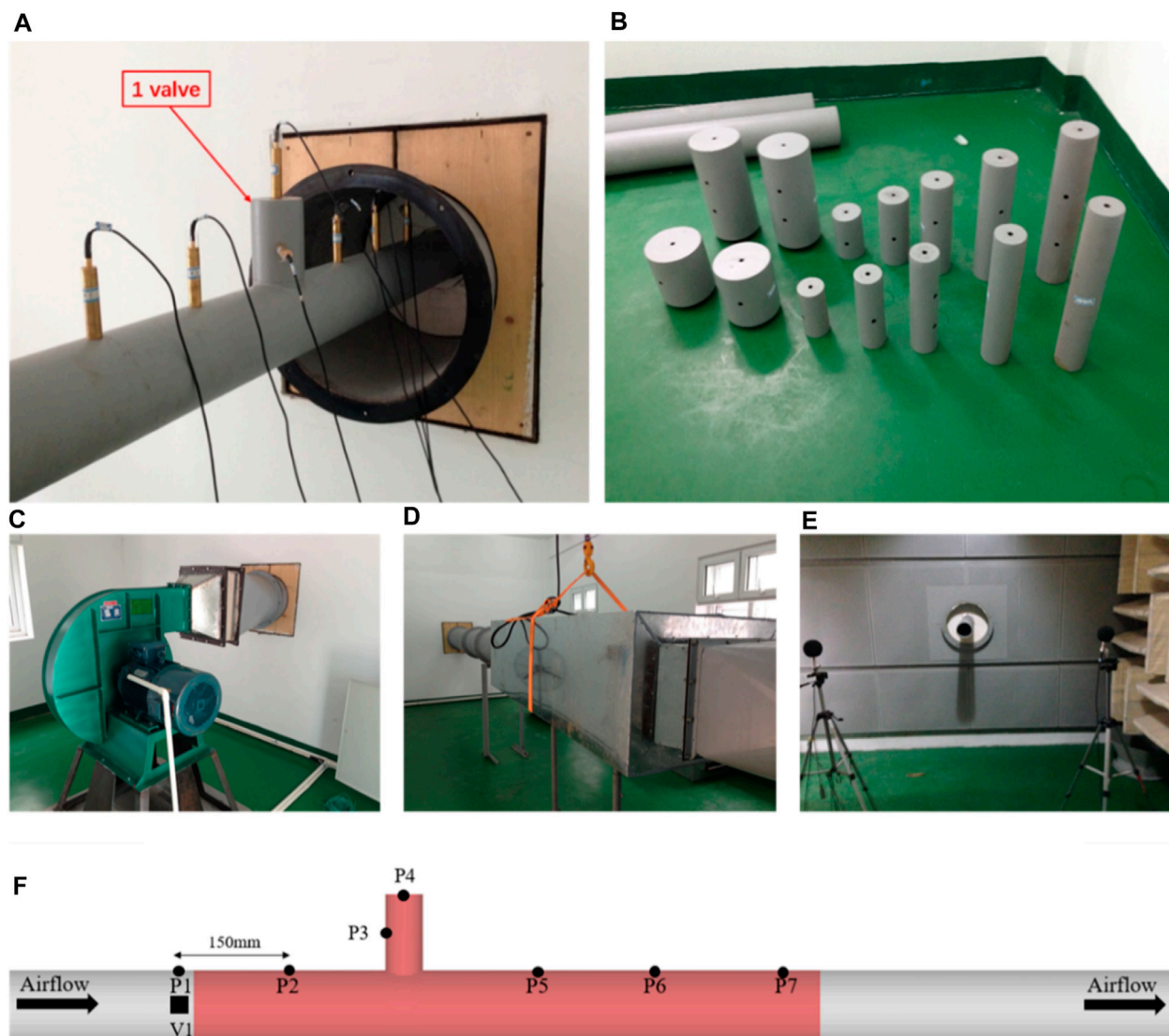


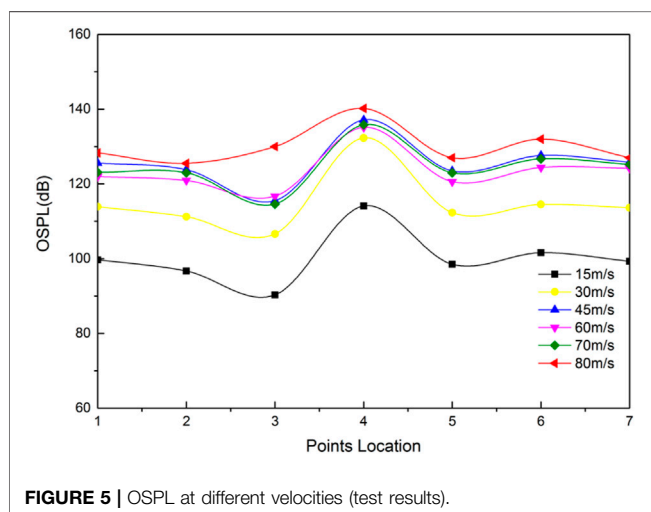
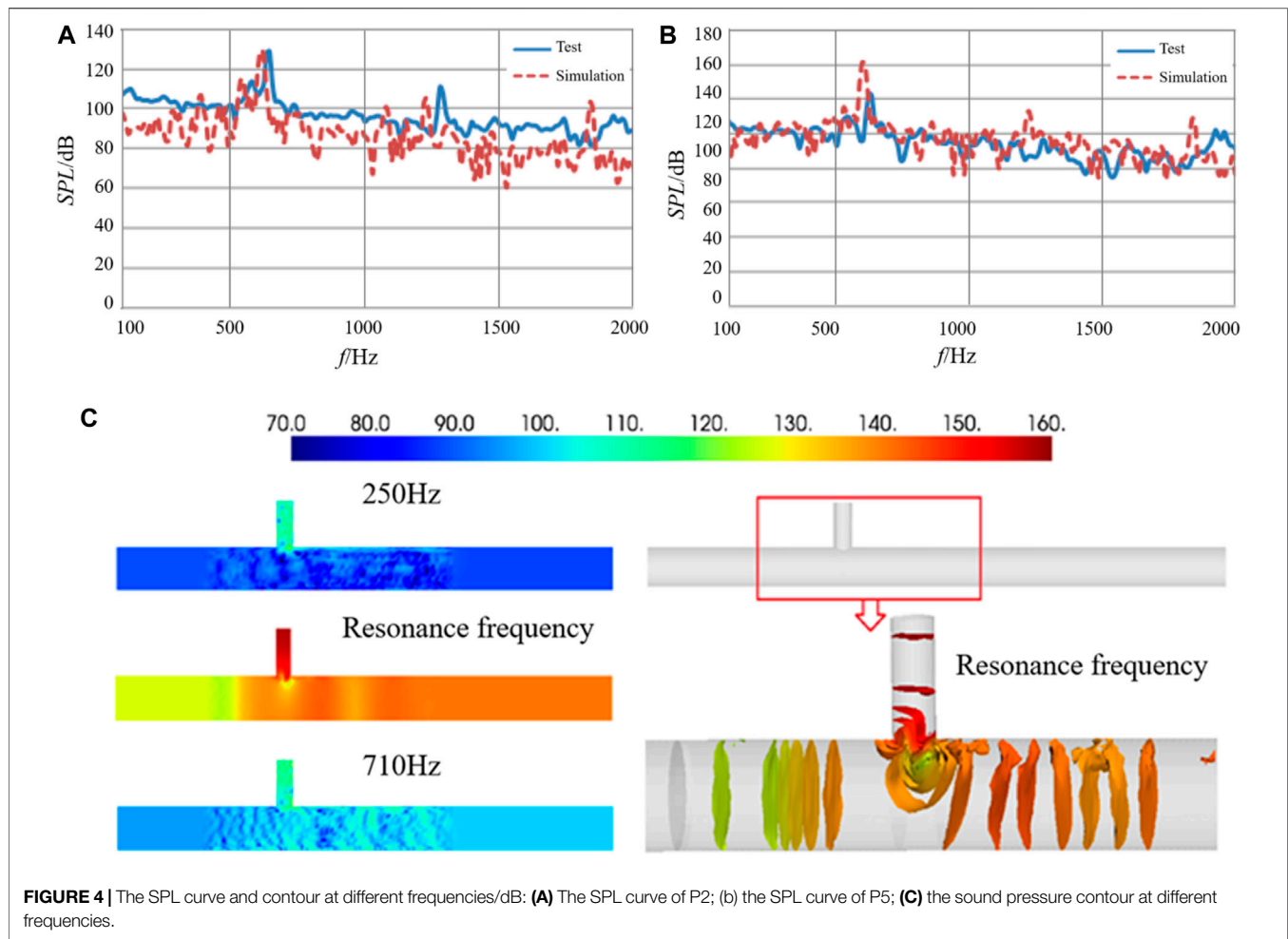
FIGURE 3 | The noise test of the resonant pipeline-cavity system: **(A)** Single pipe valve acoustic testing system; **(B)** multiple types of valve resonators; **(C)** the airflow generation system; **(D)** the muffler in front of the testing system; **(E)** semi-anechoic room in the end; **(F)** Pressure fluidization and velocity monitors in CFD model.

distance between the two measuring points was 150 mm. P3 was located in the center of the side of the pipe valve, and P4 was arranged on top of the pipe valve.

A 1/4 inch MP401 pressure field microphone was used to collect the sound pressure at different airflow velocities, while the velocity in the straight pipe was measured using a Testo 512 differential pressure measuring instrument. An SClab multi-channel, real-time analyzer was used to collect and assess the sound pressure. It should be noted that no interference was evident from other strong sound sources in the test environment. All the test data can be used to create a relationship between the pipe resonance cavity and the sound field, verifying the hybrid simulation method.

The simulation and test results of the upstream and downstream acoustic measuring points of the pipe valve were

selected and compared, as shown in **Figure 4A**. For the upstream measuring point P2, the simulated value of the first-order resonance frequency and magnitude was smaller than the test value 130 dB at about 625 Hz. However, the difference in the second-order resonance frequency and magnitude exhibited an increase, while the values of the third-order resonance were even more significant. Overall, the simulation of the sound pressure level (SPL) in a frequency band below 1800 Hz corresponded well with the experiment, but the agreement at higher frequencies was poor. For the downstream measuring point P5 in **Figure 4B**, the first-order resonance frequency did not differ much, but the magnitude displayed substantial differences. Except for the frequency exceeding 1800 Hz, the simulated value of the SPL of other frequencies differed little from the experimental value, while the overall agreement was good.



The resonant frequency and the SPL contour of the other two frequencies are shown in **Figure 4C**, indicating that when acoustic resonance occurred, the sound pressure in the pipe

was much more substantial than that of other frequencies, and the sound pressure in the pipe valve exceeded that of the straight pipe. Furthermore, the downstream sound pressure of the pipe was higher than the upstream. The frequency characteristics and acoustic resonance intensity could be improved by changing the form and position of the pipe valve, such as the rounding of the connection.

The following section analyzes the resonance characteristics of different speeds based on the test results. **Figure 5** shows that the overall sound pressure level (OSPL) of the test point inside the pipe valve at the same airflow velocity was significantly higher than that of other test points in the straight pipe.

The OSPL increased rapidly in conjunction with an increase in the velocity from 15 m/s to 45 m/s, showing a gradual rise as the velocity increased from 60 m/s to 80 m/s. Due to the acoustic cavity resonance, OSPL depended on the resonance peak. The OSPL of the same test point at a velocity of 45 m/s was higher than at 70 m/s. The small difference between the resonance peaks of 60 m/s to 70 m/s resulted in a small OSPL difference. The Strouhal number defined by **Eq. 9** was 0.83 at a velocity of 45 m/s and decreased to 0.47 at a velocity of 80 m/s, so found that the corresponding Strouhal number range was [0.47, 0.83].

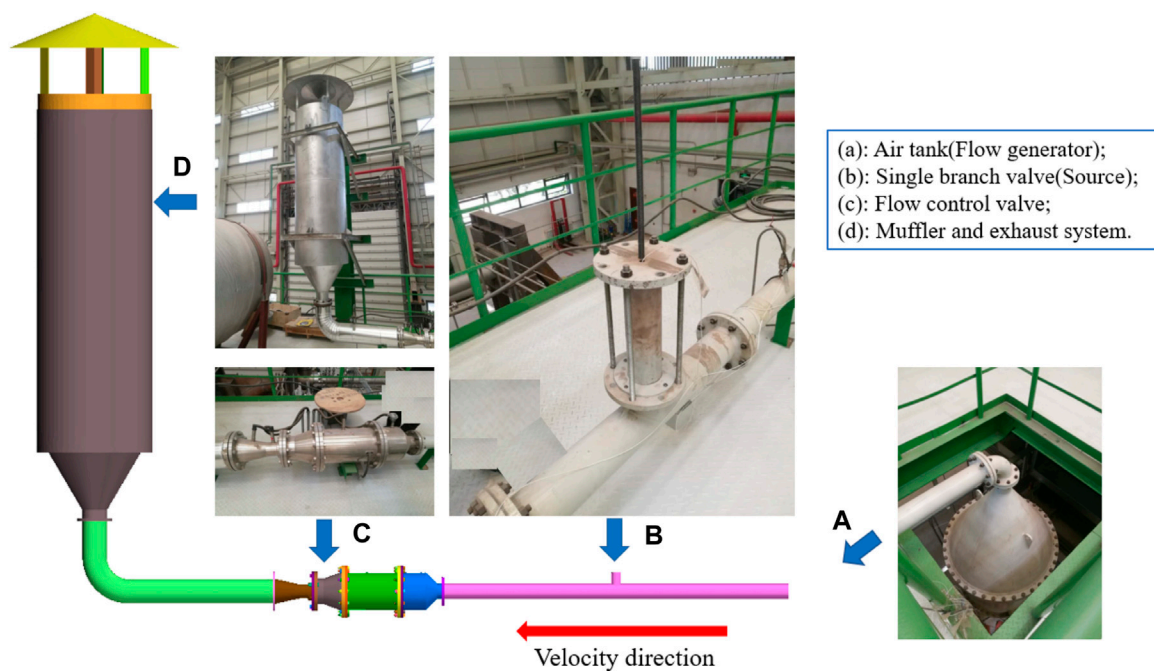


FIGURE 6 | Aero-Acoustics source generation system.

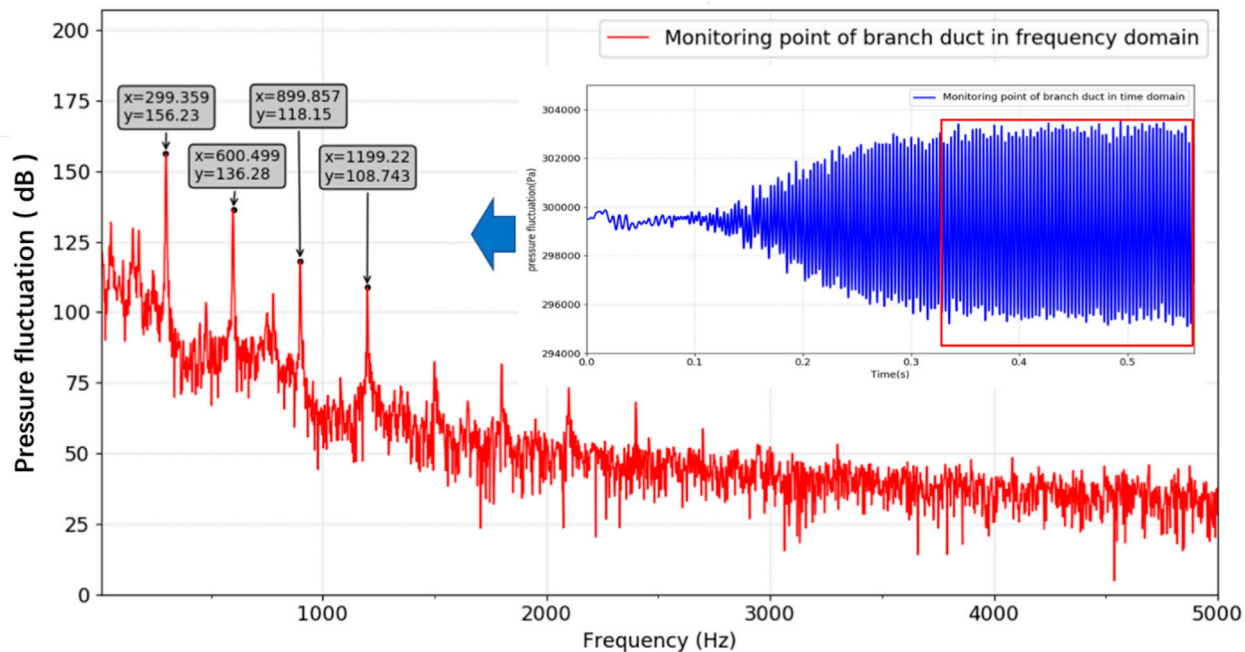
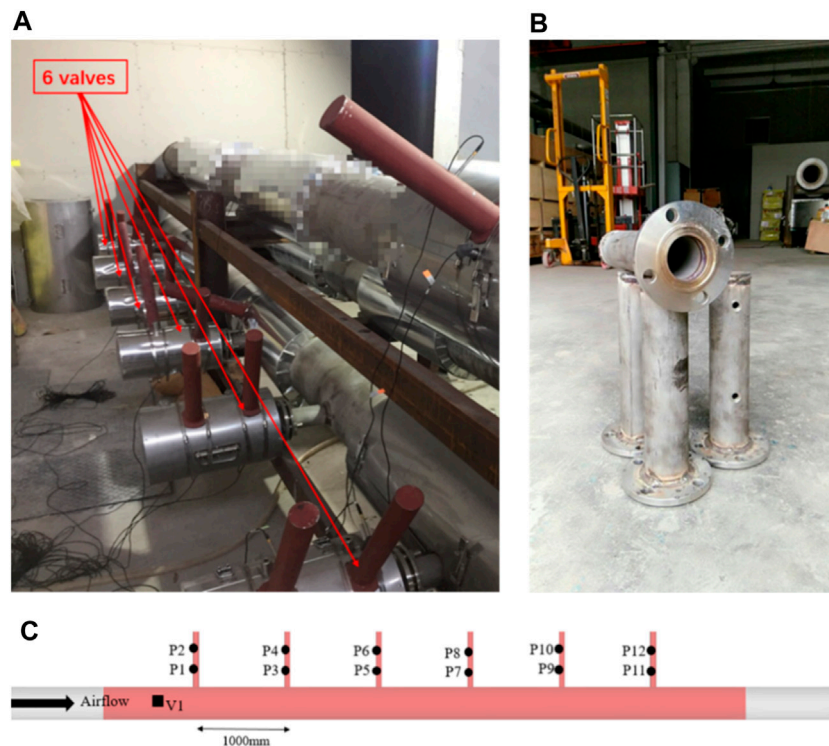


FIGURE 7 | Pressure fluctuation across time (blue) and frequency (red).

TABLE 1 | The frequencies and dB value of pressure fluctuation in main duct and branch duct from CFD.

Loadcases	Named rules	Monitors point in main duct		Monitors in branch duct	
		Frequency (Hz)	Pressure Fluctuation (dB)	Frequency (Hz)	Pressure Fluctuation (dB)
1	Without-C-25m/s	None	None	220	123
2	Without-C-50 m/s	308/620/928	140/129/107	308/620/928	160/138/110
3	Without-C-75 m/s	382/766	141/106	306/766	127/126
4	With-C-25 m/s	None	None	219.2	124
5	With-C-50 m/s	300/600/900	154/127/111	300/600/900	156/136/118
6	With-C-75 m/s	306/864	120/117	306/864	126/126

**FIGURE 8** | The noise test of the resonant pipeline-cavity system: (A) Six pipe valves; (B) microphone location in the test; (C) sound pressure monitors in acoustic model.

$$S_t = \frac{fd}{v} \quad (9)$$

Here, f is the acoustic resonance frequency, d is the diameter of the pipe valve, and v is the velocity.

4 APPLICATION 1: SINGLE-VALVE SYSTEM USED FOR GENERATED SOUND SOURCE

4.1 Model Introduction

In this application, airflow through a single valve or branch duct system produced a big aerodynamic noise, which was used as a sound source in subsequent experiments. The inner diameter of the main pipe was 110 mm, and the diameters of the different

branch ducts were 60 and 90 mm (with chamfering). As showed in **Figure 6**, the airflow was generated by an air tank, and the pressure in the main pipe was adjusted by the pressure control valve. When the airflow flowed through the valve/side branch within a certain velocity range, obvious acoustic resonance was generated in the pipe. The flow rate of the airflow in the main pipeline was controlled by the flow control valve, and finally went to the external free field through the exhaust muffler exhaust. The adjustment range of the pressure control valve was 0.3 ~ 0.7 mpa; the adjustable valve can control the flow rate in the main pipe from 20 m/s to 80 m/s.

4.2 Simulation and Regular Models

The straight pipeline and valve department shown in the experiment were taken as the analysis object in the CFD

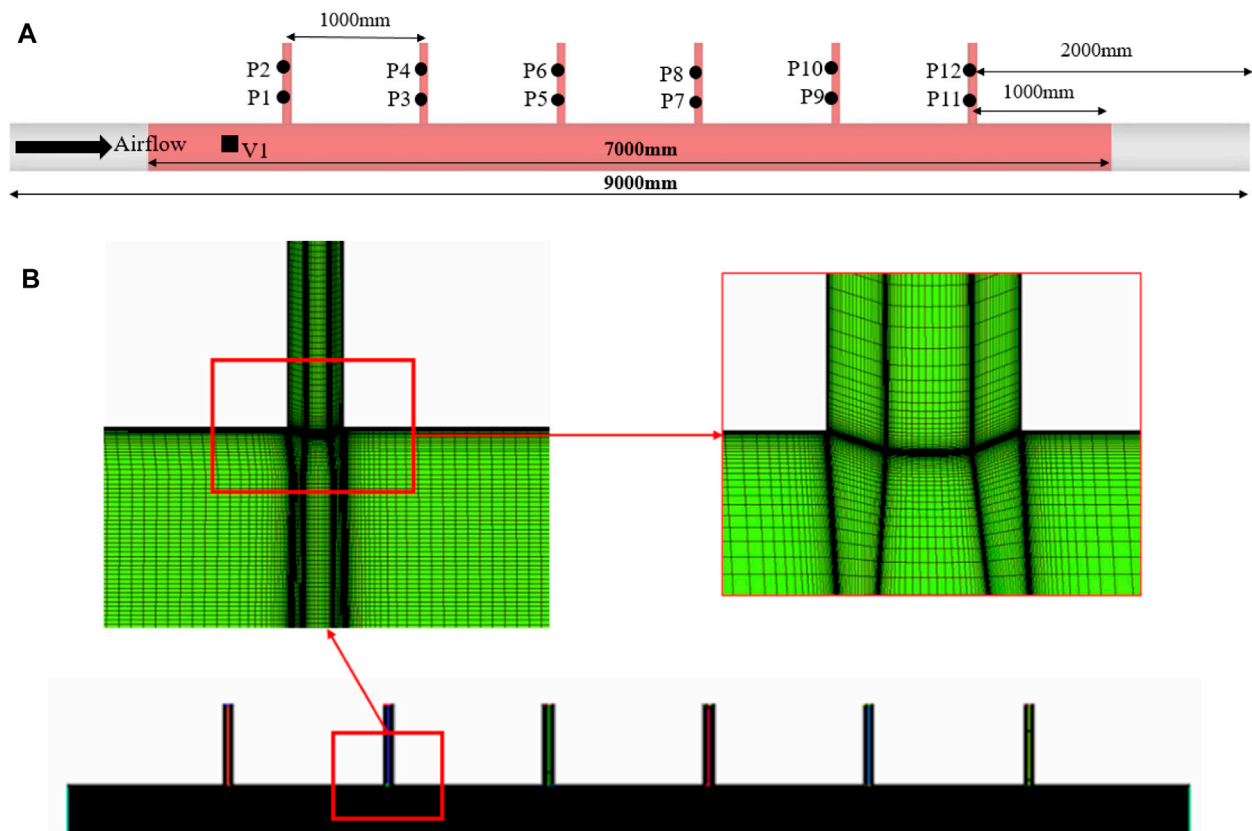


FIGURE 9 | Computational domain and the middle plane of the grid: **(A)** Computational domain; **(B)** middle plane of the grid.

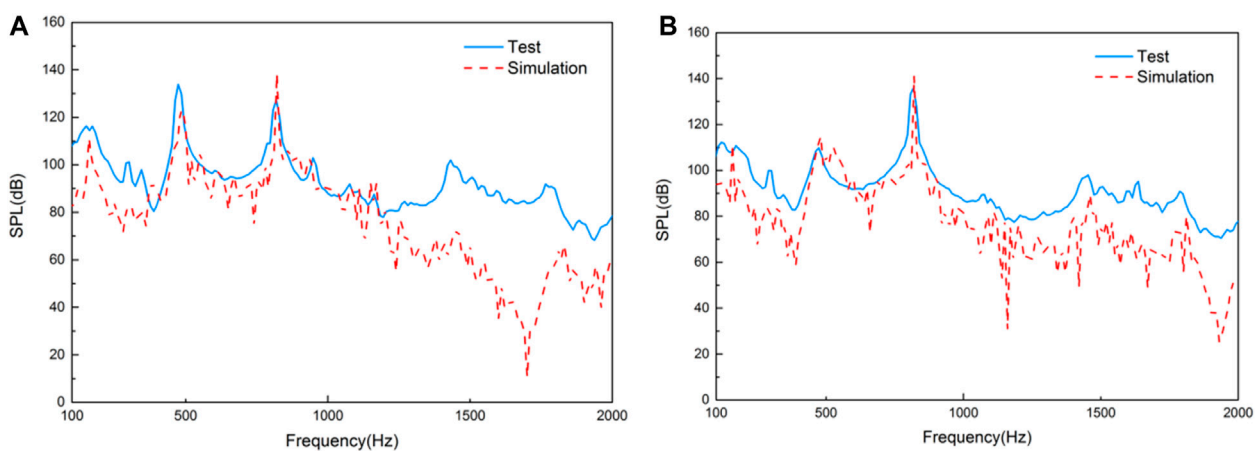


FIGURE 10 | The SPL spectrum comparative curves of different points: **(A)** P3 SPL curves; **(B)** P5 SPL curves.

calculation, and all the settings of the boundary condition and turbulence model are consistent with the model setting methods in Section 3. The side branch pipe model with a diameter of 90 mm with chamfering was selected; the inlet velocity in the main pipeline was 50 m/s, and the outlet pressure in the pipeline

was set to 0.4 MPa. Taking the pressure fluctuation values of the monitor within the valve during the transient CFD calculation, the corresponding curve is shown by the blue line in the figure below. The Pressure Fluctuation gradually presents periodicity after 0.32 s.

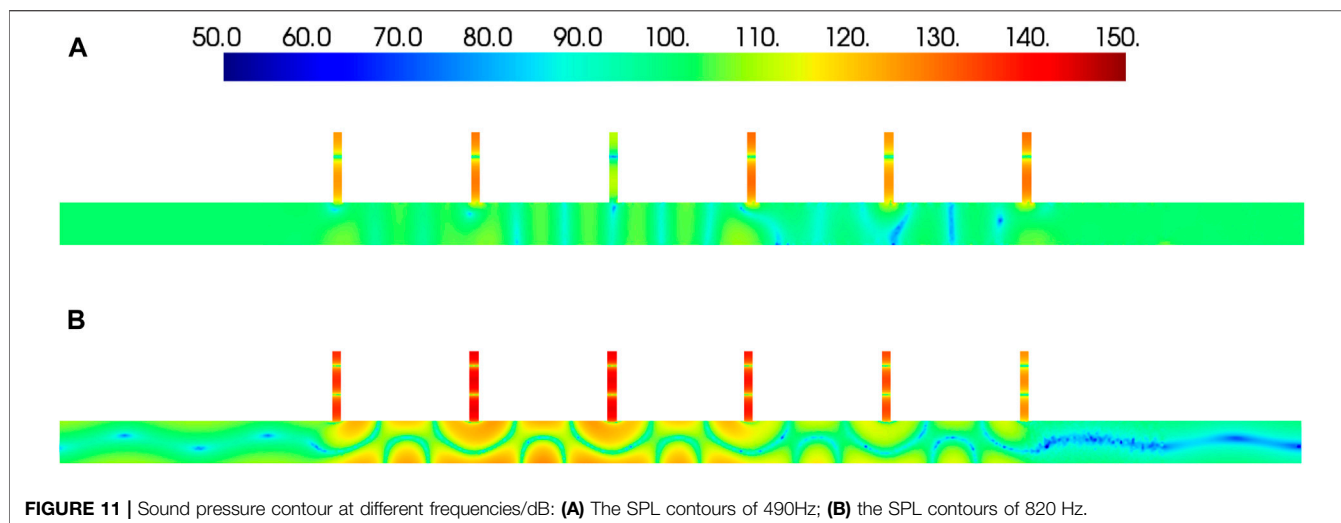


TABLE 2 | Frequencies and SPL of acoustic resonance comparison between simulation and experiment when the diameter (without chamfer) and height of the branch pipe were 60 and 250 mm, respectively.

Loadcases	Simulation	Experiment	Simulation	Experiment	Simulation	Experiment
	Velocity = 25 m/s		Velocity = 50 m/s		Velocity = 75 m/s	
Frequency 1 (Hz)	304	237	304	309	308	345
Error (%)	10.8		1.6		12.0	
SPL 1 (dB)	151	152	179	176	142	141
Error (%)	0.7		-1.7		-0.7	
Frequency 2 (Hz)	474	470	625	619	938	991
Error (%)	-0.8		-1.0		5.7	
SPL 2 (dB)	114	113	138	135	131	132
Error (%)	-0.9		-2.2		0.8	
Frequency 3 (Hz)	861	934	934	928	1,491	1,536
Error (%)	8.5		-0.6		3.0	
SPL 3 (dB)	108	107	153	147	132	114
Error (%)	-0.9		-3.9		-13.6	

As shown in **Figure 7**, the time-domain curve in the above figure was processed by discrete Fourier transform (DFT) to obtain the pressure fluctuation in the frequency domain, as shown by the red line. There were several obvious characteristic peaks in the red line, corresponding to 300 Hz and its harmonic frequencies. These frequencies and peaks corresponded to the frequency (Hz) and pressure fluidizations (dB) of loadcase_5 in the monitors in branch duct column in the following **Table 1**.

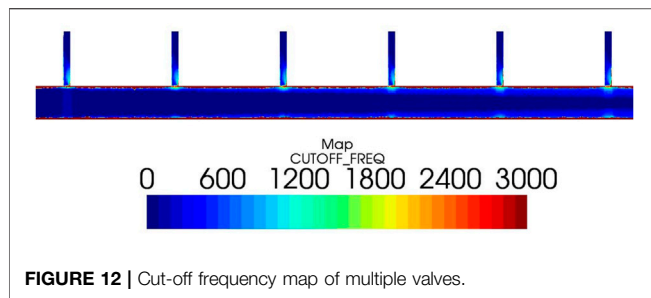
As shown in **Table 1**, there was no acoustic resonance in loadcase_1 and loadcase_4 and there was no obvious characteristic frequency. In loadcase_2 and loadcase_5 there occurred obvious acoustic resonance with three obvious characteristic frequencies and characteristic peaks, respectively. The resonance frequency was concentrated at 300 Hz and its harmonic frequencies and the pressure fluctuation amplitude was much higher than in other working conditions. Obviously, loadcase_5 was the working condition with the strongest SPL in the main pipe, and loadcase_2 was the working condition with the strongest SPL in the resonant cavity\branch pipe.

We imported the CFD data into the CAA program for aero-acoustic calculation, and the simulation results were compared against and verified with the experimental results. The branch duct model without a chamfer and with an inner diameter of 60 mm and height of 250 mm was selected for description. As shown in **Table 2**, there were 3 obvious characteristic peaks in the experimental and simulation results of acoustic resonance phenomena with different flow velocity conditions, and the results of numerical simulation were in good agreement with the experimental data. When the flow velocity was 50 m/s, the maximum SPL of acoustic resonance reached 179dB, which was much larger than the SPL of velocity at 25 m/s and 75 m/s.

5 APPLICATION 2: THE AERO-ACOUSTICS ANALYSIS OF THE MULTI-VALVES

5.1 Numerical Model and Sound Field Prediction

The acoustic test of the resonant pipeline-cavity system with six-pipe valves was performed at different flow velocities, as shown in **Figure 8**. For the multiple-valve system, the effective length and inner diameter



of the straight pipe were 9,000 mm and 305 mm, respectively, while the pipe valve had an inner diameter of 64 mm and a length of 500 mm. The pipe valve spacing was about 1,000 mm. For the multiple-valve system, twelve measuring points were arranged on the six-pipe valves, and are shown in **Figure 8A**. Two measuring points were arranged on each pipe valve at space intervals of 80 mm. A flow velocity measuring point was established in the pipeline system, while there was 300 mm in front of the resonant cavity.

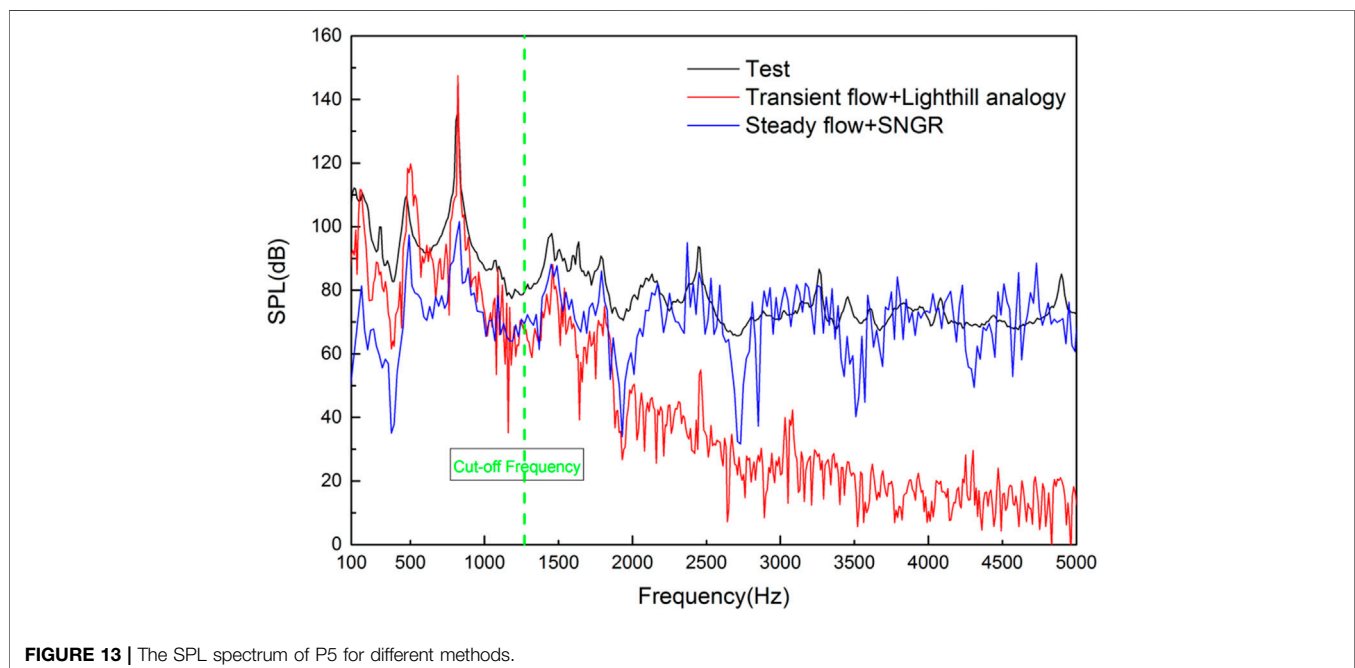
The numerical model of the straight pipe containing six-pipe valves was created, which was consistent with the test. The length of the computational domain was 9,000 mm, about 30 D (D is the diameter of the pipe valve). There was a distance of 2000 mm from upstream of the pipe valve and a 2000 mm downstream distance. All the acoustic measuring point positions of the six-pipe valves were the same as in the test. The surface and volume meshes of the computational domain were created via ICEM. The average sizes of the straight pipe and pipe valves were 8 mm. Furthermore, the height of the first boundary layer mesh was 0.03 mm to ensure $y^+ \approx 2.0$ when the inlet velocity was 65 m/s. The growth rate and the number of layers were 1.2 and 15, respectively. The boundary layer mesh was applied to all the surfaces, and the mesh

quality was acceptable. The total number of grids was about 26.6 million, and the middle plane of the grid is depicted in **Figure 9**. The velocity entering the inlet of the computational domain was 65 m/s, while it displayed the strongest acoustic resonance. The boundary conditions and calculation process were consistent with that of the single pipe valve, and will not be repeated here.

Part of the fluid model was changed into an acoustic model to analyze the resonance cavity system with six-pipe valves. The grid size of the acoustic model was 20 mm, ensuring that the point per wavelength exceeded 8 if the calculation frequency was 2000 Hz. The sound field was predicted using the transient flow and Lighthill analogy, while the boundary conditions and calculation process were also consistent with that of the single-pipe valve system, which will not be repeated here.

P3 and P5 were chosen to compare the differences between the sound pressure levels of the simulation and test results, as shown in **Figure 10**. The first-order resonance frequency of 480 Hz and the second-order resonance frequency of 820 Hz were found at the SPL spectrums of the simulation and test. However, their magnitudes were distinctly different. As for P3, the simulated values of the first-order resonance peak and the second-order resonance peak were about 10 and 9 dB different from the test value. Smaller differences were evident for P5, where only a 3 dB difference was apparent. Overall, the simulation of the SPL in the frequency band below 1,250 Hz corresponded well with the test, matching the cut-off frequency.

The SPL contours of the first-order and second-order resonance frequencies are shown in **Figure 11**, indicating that when acoustic resonance occurred, the sound pressure in the pipe valve exceeded that of the straight pipe. The SPL of the second-order resonance frequency was higher than that of the first-order resonance frequency, for which the SPL of the third pipe valve was the lowest, but changed to the sixth pipe valve for the second-order resonance frequency.



5.2 The Sound Field Prediction via SNGR and Steady Flow

The stochastic noise generation and radiation (SNGR) method re-synthesized the flow field data containing the time term based on the time-averaged velocity and turbulent kinetic energy obtained from the Reynolds Averaged Navier-Stokes calculation results by adding random perturbations. The turbulent pulsation velocity in Eq. 10 and Eq. 11 was synthesized using a stochastic model approach, which could be derived from the N Fourier modes. SNGR produced sound sources equivalent to volume Lighthill analogy sources in the frequency domain, as shown in Eq. 12. SNGR is based on stochastic isotropic turbulence theory, which is suitable for noise generated by small-scale eddies. It was challenging for SNGR to predict noise generated by middle- and large-scale eddies, however, this is exactly what traditional CFD and the Lighthill analogy can do. Therefore, a hybrid simulation method combining LES, the Lighthill analogy, and SNGR was used to predict the aerodynamic noise generated by the resonant cavities of pipeline valves.

$$u_i^t(x_j, t) = 2 \cdot \sum_n^N \tilde{u}^n \cos(\kappa^n k_j^n x_j + \varphi^n + \omega^n \cdot t) \cdot \sigma_j^n \quad (10)$$

$$\tilde{u}^n = \sqrt{E(\kappa^n) \Delta \kappa^n} \quad (11)$$

$$\int_{\Omega} N_a \frac{\partial^2 T_{ij}}{\partial x_i \partial x_j} d\Omega = \int \frac{J}{\rho_0 \omega} \rho \frac{\partial N}{\partial x_i} \frac{\partial}{\partial x_j} (u_i^t \otimes u_j^t)(f) dV \quad (12)$$

Here, $E(k^n)$ is the turbulent energy density spectrum and $S_t = \frac{f d}{v}$ is the wavenumber step; $S_t = \frac{f d}{v}$ is the angular turbulent frequency associated with the n^{th} velocity mode; $S_t = \frac{f d}{v}$ is the random phase associated with the n^{th} velocity mode; k^n is the turbulent wavenumber associated with the n^{th} velocity mode; $S_t = \frac{f d}{v}$ is the random orientation of turbulent wave vector associated with the n^{th} velocity mode; $S_t = \frac{f d}{v}$ corresponds to the direction of the n^{th} velocity mode and is restricted in a plane perpendicular to k_j^n to ensure mass conservation; \otimes denotes the convolution product; and f is the maximum frequency deduced from the Kolmogorov wavenumber.

A requirement for aero-acoustic simulations based on unsteady CFD data demands that the CFD mesh supports the maximum frequency targeted by the user, which is called the mesh cut-off frequency and depends on the turbulent quantities and the cell size presented in the CFD mesh. The cut-off frequency was defined according to Eq. 13 and Eq. 14. Due to the significant turbulence dissipation rate and large grid size, the cut-off frequency in the main stream of the pipe was about 1800 Hz, which was consistent with the distortion frequency shown in Figure 12. One challenge pertained to what could be done in cases where higher frequency noises might be important.

$$F_{cut} - of f = A \times k^\alpha \times \varepsilon^\beta \times \Delta x^\gamma \quad (13)$$

By following the Buckingham π theorem (Buckingham, 1914),

$$\begin{aligned} F_{cut} - of f &= A \times k^\alpha \times \varepsilon^\beta \times \Delta x^\gamma \\ &= k^\alpha \times \varepsilon^{\frac{1}{3}(1-2\alpha)} \times \Delta x^{-\frac{2}{3}(1+\alpha)} \approx \varepsilon^{\frac{1}{3}} \times \Delta x^{-\frac{2}{3}} (\alpha = 0) \quad (14) \end{aligned}$$

Here, k is the turbulent kinetic energy, ε is the turbulent dissipation rate, and Δx is the element size.

SNGR could be used as a method for rapidly predicting the turbulent noise of middle and high frequencies. It generated several realizations of the turbulent velocity field, respecting experimental and theoretical characteristics of the turbulence. Only the velocity, turbulent kinetic energy, and turbulent dissipation rate of the steady-state calculation were exported into the Aero-Acoustics computation procedure as sound sources. The sound propagation was performed using the Lighthill analogy and the same boundary conditions to obtain the sound pressures of both the near-field and far-field. Furthermore, the SNGR and steady flow method was adopted to obtain the sound pressure at a higher frequency, and their comparison results are shown in Figure 13.

The results of the transient flow and the Lighthill analogy corresponded well with the test results below the 1,250 Hz frequency, while their differences gradually increased as the frequency became higher. The blue curve shows that the result of steady flow and SNGR from 1,250 Hz to 5,000 Hz corresponded well with the test. Considering the calculation time and grid complexity of the two calculation methods, it was recommended again that the method involving transient flow and the Lighthill analogy be used for low frequencies while applying the technique involving steady flow and SNGR to middle and high frequencies for similar problems.

6 CONCLUSION

The resonance cavity system with either a single pipe valve or six-pipe valves was investigated via numerical simulation and testing. The traditional method involving unsteady flow and the Lighthill analogy was used to understand the fluid and acoustic characteristics of the resonant cavity system. The acoustic resonance phenomenon occurred within a specific velocity range with 45 m/s and 80 m/s, and the strongest acoustic resonance appeared at a velocity of 80 m/s; the corresponding Strouhal number range was [0.47, 0.83]. The energy of the acoustic resonance was primarily concentrated in the pipe valve.

The traditional method allows for the acquisition of an SPL below the cut-off frequency that displays excellent consistency between the simulation and the test. However, more substantial differences are evident as the frequency increases. A new method involving steady flow and SNGR is proposed to solve the differences encountered at middle and high frequencies. The consistency of the entire frequency band shows that combining the traditional method with this new technique is the ideal choice when confronted with limited time and computer resources. Therefore, it is recommended that the traditional method involving transient flow and the Lighthill analogy be used for low frequencies while applying this new technique involving steady flow and SNGR to middle and high frequencies for similar problems.

DATA AVAILABILITY STATEMENT

The original contributions presented in the study are included in the article/supplementary material, further inquiries can be directed to the corresponding authors.

AUTHOR CONTRIBUTIONS

CB: Mainly creator of the manuscripts; Derivation of the theoretical formula; Experimental data collector; Simulation soft-ware operator. TC: Idea of the innovative in the paper;

REFERENCES

- Alber, T. H., Gibbs, B. M., and Fischer, H. M. (2011). Characterisation of Valves as Sound Sources: Fluid-Borne Sound. *Appl. Acoust.* 72 (7), 428–436. doi:10.1016/j.apacoust.2011.01.007
- Alber, T. H., Gibbs, B. M., and Fischer, H. M. (2009). Characterisation of Valves as Sound Sources: Structure-Borne Sound. *Appl. Acoust.* 70 (5), 661–673. doi:10.1016/j.apacoust.2008.08.002
- Alice, S. C., Marlene, S., Guillaume, L., Stephane, M., and Martin, B. (2014). “Experimental and Numerical Investigation on Noise Induced by a Butterfly Valve,” in 20th AIAA/CEAS Aeroacoustics Conference, Atlanta, GA, 16–20 June 2014 (AIAA 2014-3292). doi:10.2514/6.2014-3292
- Bailly, C., and Juve, D. (2012). “A Stochastic Approach to Compute Subsonic Noise Using Linearized Euler’s Equations,” in 5th AIAA/CEAS Aeroacoustics Conference and Exhibit, Bellevue, WA, U.S.A., 10 May 1999 - 12 May 1999 (AIAA). doi:10.2514/6.1999-1872
- Bailly, C., Lafon, P., and Candel, S. (2012). “Computation of Noise Generation and Propagation for Free and Confined Turbulent Flows,” in 2th AIAA/CEAS Aeroacoustics Conference, State College, PA, U.S.A., 06 May 1996 - 08 May 1996 (AIAA 1996-1732). doi:10.2514/6.1996-1732
- Bechara, W., Bailly, C., Lafon, P., and Candel, S. M. (1994). Stochastic Approach to Noise Modeling for Free Turbulent Flows. *AIAA J.* 32 (3), 455–463. doi:10.2514/3.12008
- Buckingham, E. (1914). On Physically Similar Systems; Illustrations of the Use of Dimensional Equations. *Phys. Rev.* 4 (4), 345–376. doi:10.1103/physrev.4.345
- Charlebois-Menard, M., Sanjose, M., Aurelien, M., Chauvin, A., Pasco, Y., Moreau, S., and Brouillette, M. (2015). “Experimental and Numerical Study of the Noise Generation in an Outflow Butterfly Valve,” in 21th AIAA/CEAS Aeroacoustics Conference, Dallas, TX, USA, June 22–26, 2015 (AIAA 2015-3123). doi:10.2514/6.2015-3123
- Du, J., and Ouyang, H. (2010). Experimental Study of Whistle Noise Generated by Insert Edge and Oil Separator Model of Refrigeration Cycle. *Appl. Acoust.* 71 (7), 597–606. doi:10.1016/j.apacoust.2010.01.011
- Durgin, W. W., and Graf, H. R. (1992). “Flow Excited Acoustic Resonance in a Deep Cavity,” in Symposium on Flow-Induced Vibration and Noise. AMD-Vol. 151/PVP-Vol. 247, Volume 7 (ASME).
- Germano, M., Piomelli, U., and Moin, P. (1991). A Dynamic Subgrid-Scale Eddy Viscosity Model. *Phys. Fluids* 3, 1760–1765. doi:10.1063/1.857955
- Lesieur, M., and Metais, O. (1996). New Trends in Large-Eddy Simulations of Turbulence. *Annu. Rev. Fluid Mech.* 28 (1), 45–82. doi:10.1146/annurev.fl.28.010196.000401
- Lighthill, M. J. (1952). On Sound Generated Aerodynamically I. General Theory. *Proc. R. Soc. Lond. A.* 211 (1107), 564–587. doi:10.1098/rspa.1952.0060
- Lighthill, M. J. (1954). On Sound Generated Aerodynamically II. Turbulence as a Source of Sound. *Proc. R. Soc. Lond. A.* 222 (1148), 1–32. doi:10.1098/rspa.1954.0049
- Lilly, D. K. (1962). On the Numerical Simulation of Buoyant Convection. *Tellus* 14, 148–172. doi:10.3402/tellusa.v14i2.9537
- Ma, F., Wang, C., Liu, C., and Wu, J. H. (2021). Structural Designs, Principles, and Applications of Thin-Walled Membrane and Plate-type Acoustic/elastic Metamaterials. *J. Appl. Phys.* 129, 231103. doi:10.1063/5.0042132
- Ma, T., Chen, Y., Chen, H., Zheng, Y., Huang, G., Wang, J., et al. (2021). Tuning Characteristics of a Metamaterial Beam with Lateral-Electric-Field Piezoelectric Shuntings. *J. Sound Vibration* 491, 115738. doi:10.1016/j.jsv.2020.115738
- Marsan, A., Sanjose, M., Yann, P., Stephane, M., and Martin, B. (2016). “Unsteady wall Pressure Measurements in an Outflow Butterfly Valve Using Remote Microphone Probes,” in 22th AIAA/CEAS Aeroacoustics Conference, Lyon, France, 30 May - 1 June, 2016 (AIAA 2016-2888). doi:10.2514/6.2016-2888
- Oldham, D. J., and Waddington, D. C. (2001). The Prediction of Airflow-Generated Noise in Ducts from Considerations of Similarity. *J. Sound Vibration* 248 (4), 780–787. doi:10.1006/jsvi.2001.3721
- Paolo, D. F., Charles, H., Piergiorgio, F., and Katsutomo, I. (2015). “Side Mirror Noise with Adaptive Spectral Reconstruction,” SAE Technical Papers (SAE 2015-01-2329).
- Paolo, D. F., Piergiorgio, F., Thomas, D., and Charles, H. (2013). “Assessment of SNGR Method for Robust and Efficient Simulations of Flow Generated Noise,” in 19th AIAA/CEAS Aeroacoustics Conference, Berlin, Germany, May 27–29, 2013 (AIAA 2013-2264). doi:10.2514/6.2013-2264
- Pelat, A., Gautier, F., Conlon, S. C., and Semperlotti, F. (2020). The Acoustic Black Hole: A Review of Theory and Applications. *J. Sound Vibration* 476, 115316. doi:10.1016/j.jsv.2020.115316
- Ryu, J., Cheong, C., Kim, S., and Lee, S. (2005). Computation of Internal Aerodynamic Noise from a Quick-Opening Throttle Valve Using Frequency-Domain Acoustic Analogy. *Appl. Acoust.* 66 (11), 1278–1308. doi:10.1016/j.apacoust.2005.04.002
- Shih, T.-H., Liou, W. W., Shabbir, A., Yang, Z., and Zhu, J. (1995). A New K- ϵ Eddy Viscosity Model for High Reynolds Number Turbulent Flows. *Comput. Fluids* 24 (3), 227–238. doi:10.1016/0045-7930(94)00032-t
- Shiro, T., Masaya, O., Keita, O., Takashi, I., and Kazuhiro, Y. (2008). Experiment Study of Acoustic and Flow-Induced Vibrations in BWR Main Steam Lines and Steam Dryers. *ASME 2008 Press. Vessels Piping Conf.* 7, 27–31.
- Uchiyama, Yuta., and Morita, Ryo. (2015). “Experimental Investigation for Acoustic Resonance in Tandem Branches under Each Dry and Wet Steam Flow,” in Pressure Vessels and Piping Conference, November 19, 2015 (Boston, MA: PVP2015-45456, ASME).
- Zhu, R., Liu, X. N., Hu, G. K., Sun, C. T., and Huang, G. L. (2014). A Chiral Elastic Metamaterial Beam for Broadband Vibration Suppression. *J. Sound Vibration* 333, 2759–2773. doi:10.1016/j.jsv.2014.01.009
- Ziada, S., and Shine, S. (1999). Strouhal Numbers of Flow-Excited Acoustic Resonance of Closed Side Branches. *J. Fluids Structures* 13 (1), 127–142. doi:10.1006/jfls.1998.0189

Conflict of Interest: The authors declare that the research was conducted in the absence of any commercial or financial relationships that could be construed as a potential conflict of interest.

The handling editor declared a shared affiliation with several of the authors CB and TC at the time of review.

Publisher’s Note: All claims expressed in this article are solely those of the authors and do not necessarily represent those of their affiliated organizations, or those of the publisher, the editors and the reviewers. Any product that may be evaluated in this article, or claim that may be made by its manufacturer, is not guaranteed or endorsed by the publisher.

Copyright © 2021 Bai, Chen and Yu. This is an open-access article distributed under the terms of the Creative Commons Attribution License (CC BY). The use, distribution or reproduction in other forums is permitted, provided the original author(s) and the copyright owner(s) are credited and that the original publication in this journal is cited, in accordance with accepted academic practice. No use, distribution or reproduction is permitted which does not comply with these terms.



Ultra-Thin Metasurface-Based Absorber of Low-Frequency Sound With Bandwidth Optimization

Yi-jun Guan^{1,2,3}, Yong Ge¹, Hong-xiang Sun^{1,3*}, Shou-qi Yuan^{1*}, Yun Lai^{2*} and Xiao-jun Liu^{2,3*}

¹Research Center of Fluid Machinery Engineering and Technology, School of Physics and Electronic Engineering, Jiangsu University, Zhenjiang, China, ²Key Laboratory of Modern Acoustics, National Laboratory of Solid State Microstructures, Department of Physics and Collaborative Innovation Center of Advanced Microstructures, Nanjing University, Nanjing, China, ³State Key Laboratory of Acoustics, Institute of Acoustics, Chinese Academy of Sciences, Beijing, China

OPEN ACCESS

Edited by:

Fuyin Ma,
Xi'an Jiaotong University, China

Reviewed by:

Nansha Gao,
Northwestern Polytechnical
University, China
Hui Zhang,
Southeast University, China

*Correspondence:

Hong-xiang Sun
jsdxshx@ujs.edu.cn
Shou-qi Yuan
shouqiy@ujs.edu.cn
Yun Lai
laiyun@nju.edu.cn
Xiao-jun Liu
liuxiaojun@nju.edu.cn

Specialty section:

This article was submitted to
Metamaterials,
a section of the journal
Frontiers in Materials

Received: 25 August 2021

Accepted: 20 September 2021

Published: 30 September 2021

Citation:

Guan Y-j, Ge Y, Sun H-x, Yuan S-q,
Lai Y and Liu X-j (2021) Ultra-Thin
Metasurface-Based Absorber of Low-
Frequency Sound With
Bandwidth Optimization.
Front. Mater. 8:764338.
doi: 10.3389/fmats.2021.764338

We report, both theoretically and experimentally, a type of ultra-thin metasurface-based low-frequency sound absorber with bandwidth optimization. Such a metasurface unit consists of an ultrathin resonator (thickness~1/90 wavelength) with a circular hole on the upper panel and four narrow slits inside a multiple-cavity structure. Eigenmode simulations of the unit show rich artificial Mie resonances, in which a type of monopolar Mie resonance mode can be obtained at 238.4 Hz. Based on the excitation of the monopolar mode, we can realize the near-perfect low-frequency sound absorption with the maximum absorption coefficient and fractional bandwidth of 0.97 and 12.9%, respectively, which mainly arises from the high thermal-viscous loss around the circular hole and four narrow slits of the unit. More interestingly, by combining 4 units with different diameters of the circular hole, we further enhance the fractional bandwidth of the compound unit to 18.7%. Our work provides a route to design ultra-thin broadband sound absorbers by artificial Mie resonances, showing great potential in practical applications of low-frequency noise control and architectural acoustics.

Keywords: acoustics, absorber, low-frequency sound, metasurface, bandwidth optimization

INTRODUCTION

Studies on low-frequency sound absorption have attracted great scientific and engineering fascination due to its extensive practical applications in noise control, architectural acoustics, and environmental protection. Traditionally, the realization of sound absorption is mainly based on porous and fibrous materials (Biot, 1956; Zarek, 1978) and micro-perforated plate structures with cavities at the back (Maa, 1998; Arenas and Crocker, 2010). However, these absorbing structures usually have imperfect impedance matching with free space and relatively large sizes comparable to working wavelengths.

In the past few years, rapid development of metamaterials (Liu et al., 2000; Fang et al., 2006; Li et al., 2009; Toyoda et al., 2011; Christensen and de Abajo, 2012; Liang and Li, 2012; Quan et al., 2014; Cummer et al., 2016; Cheng et al., 2019; Gao et al., 2021) and metasurfaces (Li et al., 2013; Tang et al., 2014; Xie et al., 2014; Xie et al., 2017; Assouar et al., 2018; Holloway et al., 2019; Quan et al., 2019; Zhu and Assouar, 2019; Gao et al., 2020; Nikkhah et al., 2020) provides an unprecedented way to overcome the limits of conventional absorption materials and realize high absorption performance. These absorbing structures usually contain subwavelength resonant units to enhance energy density and dissipate sound energy

inside. The previously demonstrated resonant units mainly include Helmholtz resonators (Jimenez et al., 2016; Li et al., 2016; Romero-Garcia et al., 2016; Jimenez et al., 2017; Long et al., 2017), sound membranes (Mei et al., 2012; Ma et al., 2014; Yang et al., 2015; Yang et al., 2015), coiled Fabry-Perot resonators (Zhang and Hu, 2016; Jimenez et al., 2017; Yang et al., 2017), split-ring-resonators (Wu et al., 2016), acoustic metasurfaces (Cai et al., 2014; Li and Assouar, 2016; Tang et al., 2017; Donda et al., 2019; Ge et al., 2019; Long et al., 2019; Gao et al., 2021), etc. The above designs exhibit high efficiency for low-frequency sound absorption. However, due to their resonant nature, the design of sound absorption structures with both broad bandwidth and deep subwavelength thickness remains a challenging task. Theoretical analysis shows that broadband absorption can be achieved by dispersive dissipative meta-films (Duan et al., 2015). Meanwhile, sound absorption can also be theoretically obtained by coherent perfect absorbers based on interference cancellation (Song et al., 2014; Wei et al., 2014).

Recently, a type of maze-like unit consisting of eight zigzag channels has become a hot topic due to its rich artificial Mie resonances and subwavelength size (Cheng et al., 2015; Landi et al., 2018). Based on different types of Mie resonance modes created by the maze-like units, a variety of application designs of low-frequency sound have been realized, including rainbow trapping (Zhou et al., 2016), extraordinary transmission (Xia et al., 2015; Zhang et al., 2017), sound filtering (Sun et al., 2019), energy harvesting (Gao et al., 2019) and directional propagation (Lu et al., 2017). Additionally, a multi-band near-perfect sound absorber based on the multi-orders monopolar and dipolar Mie resonances has been designed (Long et al., 2018). However, this system is composed of a Mie resonator array backed by a rigid wall, and broadband sound absorbers designed by a single layer of Mie resonator array with deep subwavelength thickness still pose a challenge.

In this work, we propose a metasurface unit which consists of an upper surface panel with a central circular hole and a multiple-cavity structure. By applying eigenmode simulations to the unit, a series of artificial Mie resonance modes can be observed, such as a monopolar Mie resonance (MMR) mode at 238.4 Hz and a second MMR mode at 1,145.4 Hz. Based on the thermal-viscous loss created by the circular hole and four narrow slits of the unit under the excitation of the MMR mode, the near-perfect low-frequency sound absorption is observed at 239 Hz, and the maximum absorption coefficient and fractional bandwidth can reach about 0.97 and 12.9%, respectively. Additionally, we discuss the influences of structure parameters on the sound absorption performance, and design two types of broadband compound units by combining 4 units with different central circular holes. The fractional bandwidth of the compound unit can be further enhanced to 18.7%. The measured sound absorption spectra agree well with the simulated ones.

DESIGN AND PERFORMANCES OF SOUND ABSORBER

Design of Unit

As schematically shown in **Figure 1A**, we propose an acoustic metasurface-based absorber consisting of periodic square

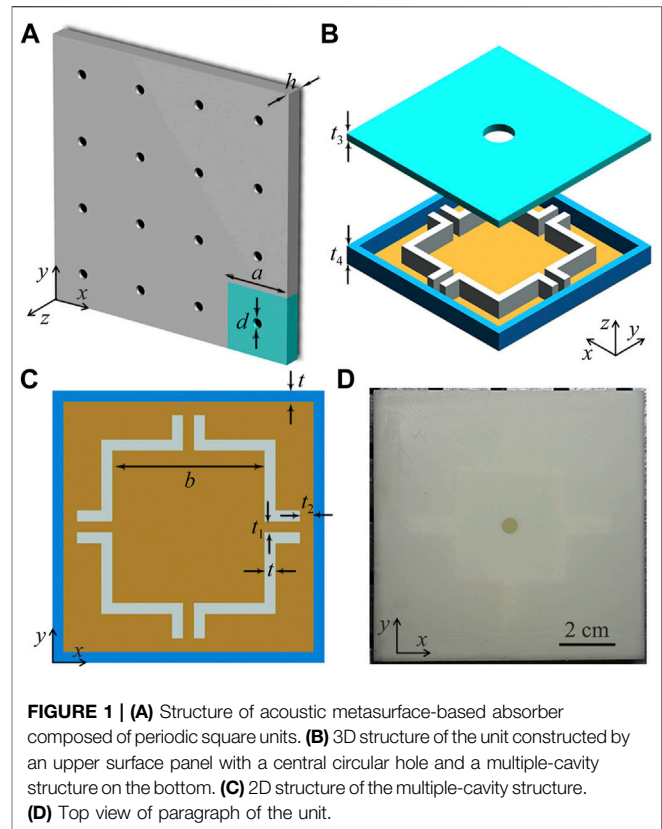
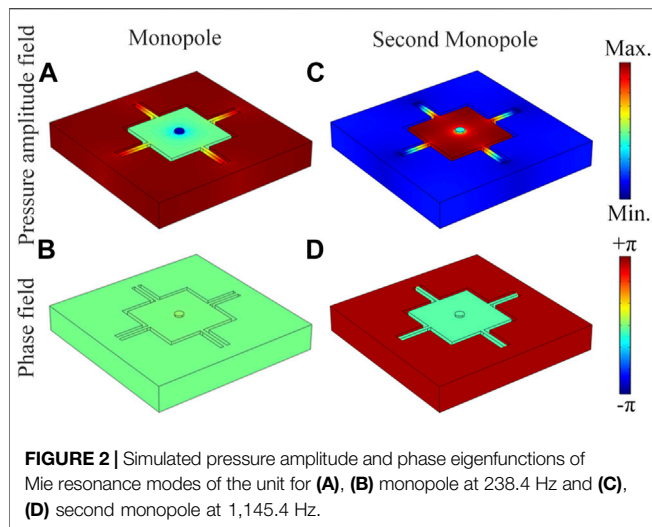


FIGURE 1 | (A) Structure of acoustic metasurface-based absorber composed of periodic square units. (B) 3D structure of the unit constructed by an upper surface panel with a central circular hole and a multiple-cavity structure on the bottom. (C) 2D structure of the multiple-cavity structure. (D) Top view of paragraph of the unit.

units with a length a and a thickness h . A central circular hole with a diameter d is located at the upper surface of the unit. Each unit is composed of an upper surface panel (with a thickness t_3) and a multiple-cavity structure (with a thickness t_4) on the bottom (**Figure 1B**). As shown in **Figure 1C**, the multiple-cavity structure consists of a central square cavity (with a length b) surrounded by four interconnected identical cavities which are divided by four narrow slits (with a width t_1), showing a high structure symmetry. The distance between the slits and the outer frame is t_2 , and the frames (with a thickness t) are made of epoxy resin based on 3D-printing technology. Here, the COMSOL Multiphysics software is used to numerically simulate sound absorption characteristics, and the structure parameters are selected as $a = 100$ mm, $b = 42$ mm, $d = 5$ mm, $t = t_1 = 2$ mm, $t_2 = 10$ mm, $t_3 = 1$ mm, and $t_4 = 15$ mm. In our work, the sound absorption is created by the thermoviscous loss of the unit structure, and we use the module of Thermoviscous Acoustic-Solid Interaction inside the unit, and the module of Acoustic Pressure outside the unit due to the huge computation load. In the simulations, the thermoviscous acoustic boundary is used for all the surfaces inside the unit (include the inner surface of the hole), and the acoustic-thermoviscous acoustic boundary is adopted for the interface between the hole and the external space. The parameters of epoxy resin are the density $\rho_e = 1,180$ kg/m³, the longitudinal wave velocity $c_l = 2,720$ m/s, and the transversal wave velocity $c_t = 1,460$ m/s, and those of air are calculated as $\rho_a = p_0 M / RT$ and $c_a = \sqrt{\gamma RT / M}$, in which the



ratio of the molar heat capacities γ , the molar mass M , and the temperature of air are 1.4, 28.97×10^{-3} kg/mol, and 293 K, respectively, the molar gas constant $R = 8.31$ J/(mol/K), and $p_0 = 101.325$ kPa. The paragraph of the unit is shown in Figure 1D.

Characteristics of Two Types of MMR Modes

Figure 2 shows the simulated pressure amplitude and phase eigenfunctions of the proposed unit. We can see that two types of eigenmodes present typical characteristics of the MMR, which are denoted as the monopole and second monopole. Additionally, due to high symmetry of the multiple-cavity structure, the Mie resonance of the dipole and quadrupole can also be observed (see **Supplementary Material**), showing rich Mie resonant modes of the unit. As shown in Figure 2A, for the MMR mode at 238.4 Hz, the sound energy is mainly concentrated into the surrounding four cavities, and the whole structure exhibits a collective in-phase characteristic (Figure 2B). But for the second MMR mode at 1,145.4 Hz, the sound energy is mainly in the central square cavity (Figure 2C), and an out-of-phase feature (Figure 2D) is observed between the internal and external cavities. Here, to further demonstrate the mechanism of both MMR modes, we simulate the pressure amplitude and phase eigenfunctions of the units with different number of surrounding cavities (see **Supplementary Material**). The results show that the eigenfrequencies of both MMR modes change greatly with different number of cavities, but their mode characteristics are almost the same.

Low-Frequency Sound Absorption Created by the MMR Mode

Next, we experimentally measure the absorption performance of low-frequency sound created by the MMR mode in Figure 2A. As shown in Figure 3A, in the experiment, the

sample (shown in Figure 1D) is placed at the right side in the straight waveguide which is made of acrylic plates to satisfy sound hard boundary condition. The experimental set-up is presented in the **Supplementary Material**. Figure 3B shows the measured and simulated sound absorption spectra created by the unit. We find that there exists a sound absorption peak at 239 Hz for both results, and the absorption coefficient can reach about 0.97, showing a near-perfect low-frequency sound absorption. Moreover, the bandwidth of sound absorption (black shaded region) is about 31 Hz, and its corresponding fractional bandwidth (the ratio of the bandwidth to the center frequency) can reach about 12.9%. The measured and simulated sound absorption spectra match well with each other. Beyond that, the thickness h of the unit is only 16 mm, which is equal to $\lambda/90$, exhibiting a deep subwavelength thickness of the proposed low-frequency sound absorber.

To explain the existence of the sound absorption peak, we introduce the relative acoustic impedance of the unit defined as $Z_r = \frac{\langle p \rangle}{Z_a \langle v_{\perp} \rangle}$ (Li et al., 2016), where $Z_a = \rho_a c_a$ is the acoustic impedance of air, p and v_{\perp} are the total acoustic pressure and the sound velocity normal to the surface, respectively, and $\langle \cdot \rangle$ represents averaging over the surface of the unit. The simulated real and imaginary parts of Z_r are shown in Figure 3C. We observe that, at the frequency of absorption peak, the real and imaginary parts of Z_r are about 1.35 and 0, respectively, indicating better impedance match between the proposed structure and air at 239 Hz. Therefore, the near-perfect sound absorption can be created by the unit structure.

Furthermore, we find that the frequency of sound absorption peak is almost the same as that of the MMR mode, and thus the sound absorption may arise from the MMR mode of the unit. To make a further insight into it, we simulate the distributions of the pressure amplitude and total thermal-viscous power loss density in the unit created by a normal incidence of sound at 239 Hz, which are shown in Figures 3D,E, respectively. Note that the excited pressure amplitude distribution of the unit (Figure 3D) agrees well with that of the MMR mode (Figure 2A), indicating that the low-frequency sound absorption is created by the MMR mode of the unit. Moreover, as shown in Figure 3E, there exist an obvious thermal-viscous sound loss around the central circular hole and four narrow slits, especially the central circular hole. Therefore, we deduce that the sound absorption of the unit arises from the thermoviscous loss around the central circular hole and four narrow slits under the excitation of the MMR mode. Beyond that, we also simulate the sound absorption spectra created by the MMR mode of the unit with different incident angles (θ), and the absorption spectra are relatively stable below $\theta = 60^\circ$. (see **Supplementary Material**).

Besides the sound absorption created by the MMR mode, we simulate the performances of sound absorption created by the second MMR mode of the unit. The results show that the sound absorption can also be created by the second MMR mode, but its absorption performance is reduced greatly due

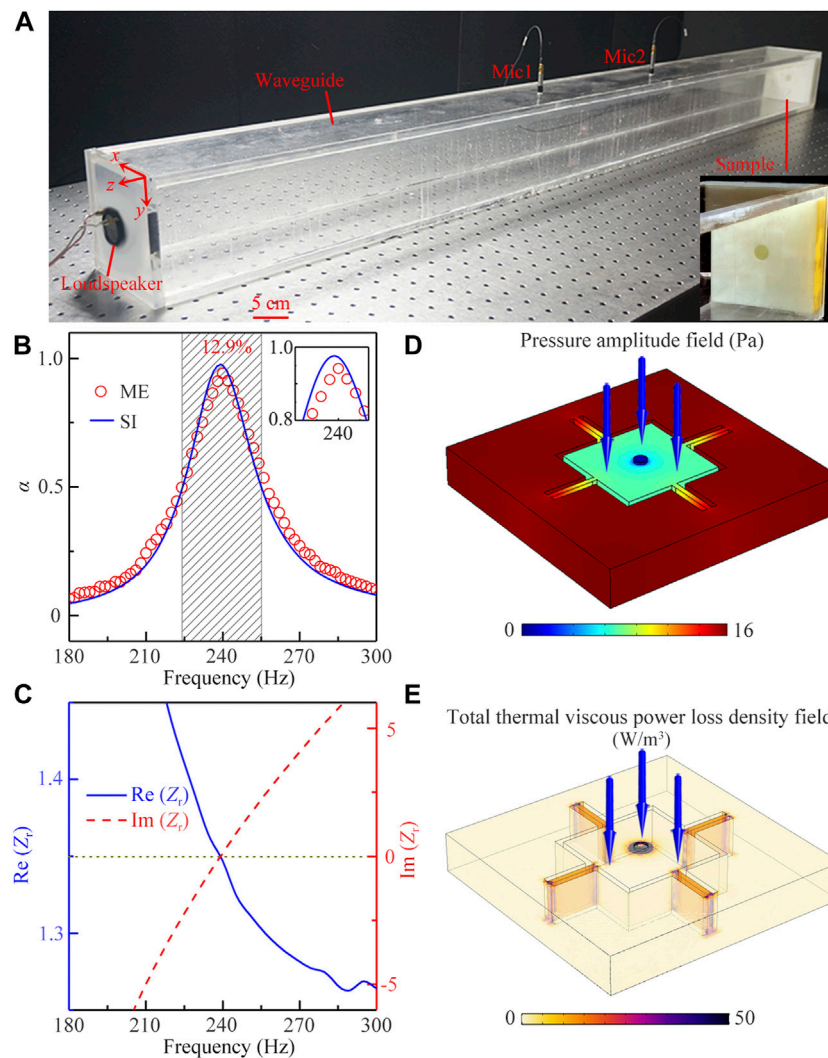


FIGURE 3 | (A) Experiment set-up of sound absorption. (B) Simulated (blue solid line) and measured (red open circles) sound absorption spectra of the unit. (C) Real and imaginary parts of relative acoustic impedance Z_r of the unit. Distributions of (D) the pressure amplitude and (E) total thermal viscous power loss density in the unit excited by a normal incident wave (blue solid arrows) at 239 Hz.

to the sound reflection created by the impedance mismatch (see **Supplementary Material**). Furthermore, we simulate the sound absorption spectra of the units with different number of surrounding cavities (see **Supplementary Material**), in which the results further demonstrates that the sound absorption of the unit arises from the excitation of both MMR modes.

BANDWIDTH OPTIMIZATION OF SOUND ABSORBER

Finally, we discuss the influences of the parameters b and d on the sound absorption and further optimize the working bandwidth of the sound absorber. **Figures 4A,B** show the simulated sound absorption spectra created by the MMR mode

as a function of the parameters b and d , respectively, in which other parameters remain unchanged. It is found that, with the decrease of both parameters, the working bandwidth moves to the low-frequency region with a high sound absorption coefficient. The corresponding measured results for the parameters b and d are displayed in **Figures 4C,D**, which agree well with the simulation ones. Thus, we can reduce the working frequency of the sound absorption by simply decreasing the values of b and d .

To further optimize the working bandwidth, we design two types of compound units A and B consisting of 4 units (2×2 array) with different values of d ($d = 8, 10$, and 12 mm for the units I, II and III), and experimentally measure sound absorption of both compound units. The experiment set-up is shown in **Figure 5A**, in which the width and height of the waveguide double those in **Figure 3A**, and the other

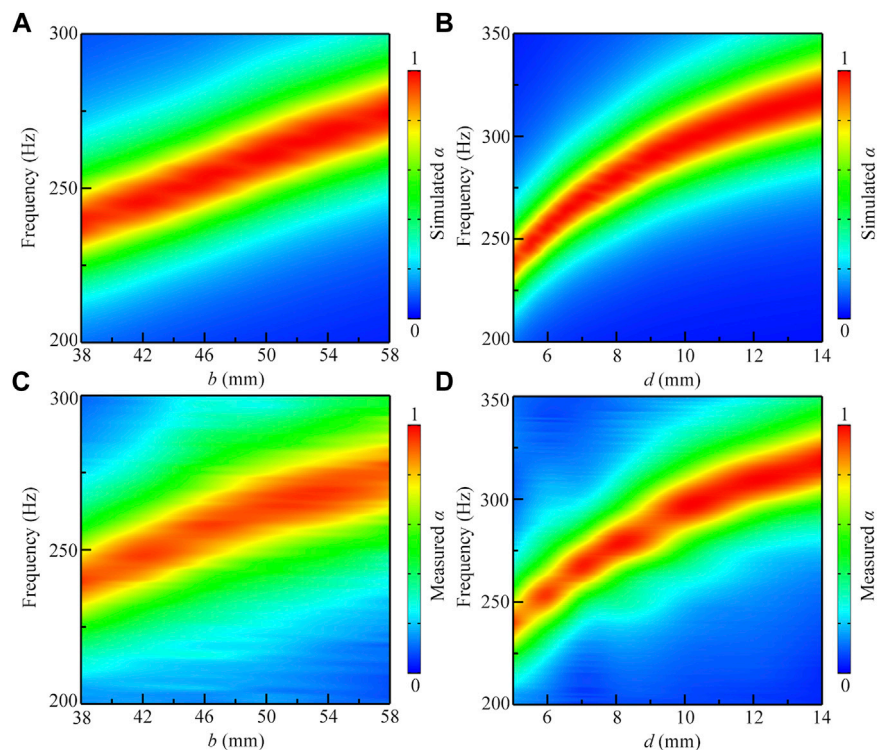


FIGURE 4 | Simulated sound absorption spectra as a function of parameters (A) b and (B) d , and the corresponding measured sound absorption spectra for the parameters (C) b and (D) d , in which the other parameters remain unchanged.

parameters are the same. As shown in **Figure 5B**, the compound unit A consists of two types of units (I and II), and the arrangement of 4 units is shown in the sample photograph (shown in bottom inset). Note that, by combining the units I and II, the fractional bandwidth of the compound unit A can reach about 16.4%, in which the working frequency range (266–313.5 Hz, black shaded region) can cover those of a single unit I or II. Compared with the result in **Figure 3B**, the maximum sound absorption coefficient decreases slightly, but the absorption peak becomes wide and flat due to their coupling effect of both types of units. Additionally, as shown in **Figure 5C**, the compound unit B is composed of three types of units (I, II and III). By introducing the unit III, the working band (266–321 Hz, black shaded region) of the compound unit B is further improved, and its fractional bandwidth can be enhanced to 18.7%, showing a broadband feature of the sound absorption. The measured sound absorption spectra for both compound units agree with the simulations. Therefore, by combining the units with different values of d , we can further enhance the working bandwidth of the proposed sound absorber. Furthermore, we simulate the sound absorption spectra of another two types of compound units C and D with different configurations (see **Supplementary Material**). Compared with the absorption performance of the compound units A and B, we demonstrate that the absorption performance of the compound unit is closely related to its configuration.

CONCLUSION

In conclusions, we have demonstrated a metasurface-based unit with near-perfect low-frequency sound absorption based on artificial Mie resonances. The results show that a series of artificial Mie resonance modes can be observed in the unit, including the MMR mode at 238.4 Hz and the second MMR mode at 1,145.4 Hz. Based on the excited MMR mode and the thermal-viscous loss around the circular hole and four narrow slits of the unit, the near-perfect low-frequency sound absorption is achieved at 239 Hz, the maximum absorption coefficient and fractional bandwidth of the proposed unit can reach 0.97 and 12.9%. It is noted that the thickness of the unit is only about $\lambda/90$, showing a deep subwavelength thickness of the proposed metasurface-based sound absorber. In addition, we discuss the influences of structure parameters b and d on the sound absorption in detail, and find that the working bandwidth moves to the low-frequency region with a high absorption coefficient by decreasing both parameters. Finally, we improve the working bandwidth of the sound absorption by combining 4 units with different values of b , and the fractional bandwidth of the compound unit B can be further enhanced to 18.7%. The measured and simulated sound absorption spectra match well with each other. The proposed multiple-cavity units with the near-perfect sound absorption and broadband feature provide diverse routes to design advanced sound absorption structures with great potential applications in low-frequency noise control, architectural acoustics and environmental protection.

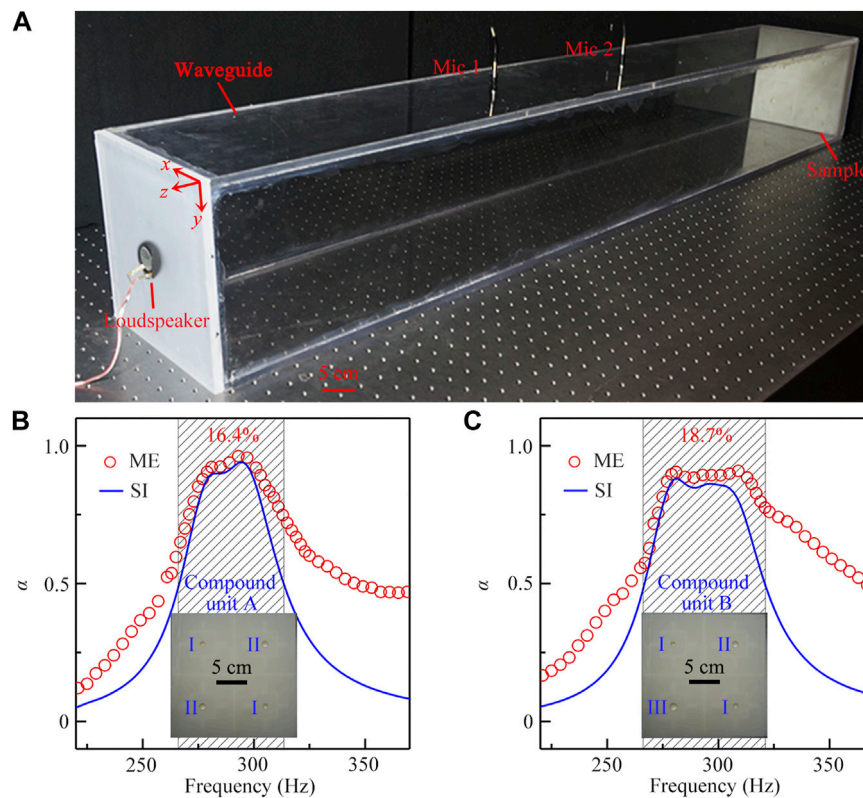


FIGURE 5 | (A) Experiment set-up of sound absorption for the compound unit. Simulated (blue solid lines) and measured (red open circles) sound absorption spectra of the compound units **(B)** A and **(C)** B. The arrangement of 4 units with different values of d ($d = 8, 10$, and 12 mm for the units I, II, and III) are shown in the paragraphs of the compound units A and B (shown as two insets on the bottom).

DATA AVAILABILITY STATEMENT

The original contributions presented in the study are included in the article/**Supplementary Material**, further inquiries can be directed to the corresponding authors.

AUTHOR CONTRIBUTIONS

Y-JG and YG contributed equally to this work.

REFERENCES

- Arenas, J. P., and Crocker, M. J. (2010). Recent Trends in Porous Sound-Absorbing Materials. *Sound Vib* 44, 12–17. doi:10.1007/s00397-010-0453-x
- Assouar, B., Liang, B., Wu, Y., Li, Y., Cheng, J.-C., and Jing, Y. (2018). Acoustic Metasurfaces. *Nat. Rev. Mater.* 3, 460–472. doi:10.1038/s41578-018-0061-4
- Biot, M. A. (1956). Theory of Propagation of Elastic Waves in a Fluid-Saturated Porous Solid. I. Low-Frequency Range. *The J. Acoust. Soc. America* 28, 168–178. doi:10.1121/1.1908239
- Cai, X., Guo, Q., Hu, G., and Yang, J. (2014). Ultrathin Low-Frequency Sound Absorbing Panels Based on Coplanar Spiral Tubes or Coplanar Helmholtz Resonators. *Appl. Phys. Lett.* 105, 121901. doi:10.1063/1.4895617

FUNDING

This work was supported by the National Natural Science Foundation of China (11774137, 51779107, 11834008, 61671314, 11974176, and 12174159).

SUPPLEMENTARY MATERIAL

The Supplementary Material for this article can be found online at: <https://www.frontiersin.org/articles/10.3389/fmats.2021.764338/full#supplementary-material>

- Cheng, Y., Li, W., and Mao, X. (2019). Triple-band Polarization Angle Independent 90° Polarization Rotator Based on Fermat's Spiral Structure Planar Chiral Metamaterial. *Pier* 165, 35–45. doi:10.2528/PIER18112603
- Cheng, Y., Zhou, C., Yuan, B. G., Wu, D. J., Wei, Q., and Liu, X. J. (2015). Ultra-sparse Metasurface for High Reflection of Low-Frequency Sound Based on Artificial Mie Resonances. *Nat. Mater* 14, 1013–1019. doi:10.1038/NMAT4393
- Christensen, J., and de Abajo, F. J. G. (2012). Anisotropic Metamaterials for Full Control of Acoustic Waves. *Phys. Rev. Lett.* 108, 124301. doi:10.1103/PhysRevLett.108.124301
- Cummer, S. A., Christensen, J., and Alù, A. (2016). Controlling Sound with Acoustic Metamaterials. *Nat. Rev. Mater.* 1, 16001. doi:10.1038/natrevmats.2016.1
- Donda, K., Zhu, Y., Fan, S.-W., Cao, L., Li, Y., and Assouar, B. (2019). Extreme Low-Frequency Ultrathin Acoustic Absorbing Metasurface. *Appl. Phys. Lett.* 115, 173506. doi:10.1063/1.5122704

- Duan, Y., Luo, J., Wang, G., Hang, Z. H., Hou, B., Li, J., et al. (2015). Theoretical Requirements for Broadband Perfect Absorption of Acoustic Waves by Ultra-thin Elastic Meta-Films. *Sci. Rep.* 5, 12139. doi:10.1038/srep12139
- Fang, N., Xi, D., Xu, J., Ambati, M., Srituravanich, W., Sun, C., et al. (2006). Ultrasonic Metamaterials with Negative Modulus. *Nat. Mater.* 5, 452–456. doi:10.1038/nmat1644
- Gao, N., Luo, D., Cheng, B., and Hou, H. (2020). Teaching-learning-based Optimization of a Composite Metastructure in the 0–10 kHz Broadband Sound Absorption Range. *J. Acoust. Soc. America* 148, EL125–EL129. doi:10.1121/10.0001678
- Gao, N., Tang, L., Deng, J., Lu, K., Hou, H., and Chen, K. (2021). Design, Fabrication and Sound Absorption Test of Composite Porous Metamaterial with Embedding I-Plates into Porous Polyurethane Sponge. *Appl. Acoust.* 175, 107845. doi:10.1016/j.apacoust.2020.107845
- Gao, N., Wu, J., Lu, K., and Zhong, H. (2021). Hybrid Composite Meta-Porous Structure for Improving and Broadening Sound Absorption. *Mech. Syst. Signal Process.* 154, 107504. doi:10.1016/j.ymssp.2020.107504
- Gao, W.-t., Xia, J.-p., Sun, H.-x., Yuan, S.-q., Ge, Y., and Liu, X.-j. (2019). Acoustic Energy Harvesting for Low-Frequency Airborne Sound Based on Compound Mie Resonances. *Appl. Phys. Express* 12, 044002. doi:10.7567/1882-0786/ab07e5
- Ge, Y., Sun, H.-x., Yuan, S.-q., and Lai, Y. (2019). Switchable Omnidirectional Acoustic Insulation through Open Window Structures with Ultrathin Metasurfaces. *Phys. Rev. Mater.* 3, 065203. doi:10.1103/PhysRevMaterials.3.065203
- Holloway, C. L., Kuester, E. F., and Haddab, A. H. (2019). Retrieval Approach for Determining Surface Susceptibilities and Surface Porosities of a Symmetric Metascreen from Reflection and Transmission Coefficients. *Pier* 166, 1–22. doi:10.2528/PIER19022305
- Jiménez, N., Huang, W., Romero-García, V., Pagneux, V., and Groby, J.-P. (2016). Ultra-thin Metamaterial for Perfect and Quasi-Omnidirectional Sound Absorption. *Appl. Phys. Lett.* 109, 121902. doi:10.1063/1.4962328
- Jiménez, N., Romero-García, V., Pagneux, V., and Groby, J.-P. (2017). Quasiperfect Absorption by Subwavelength Acoustic Panels in Transmission Using Accumulation of Resonances Due to Slow Sound. *Phys. Rev. B* 95, 014205. doi:10.1103/PhysRevB.95.014205
- Jiménez, N., Romero-García, V., Pagneux, V., and Groby, J.-P. (2017). Rainbow-trapping Absorbers: Broadband, Perfect and Asymmetric Sound Absorption by Subwavelength Panels for Transmission Problems. *Sci. Rep.* 7, 13595. doi:10.1038/s41598-017-13706-4
- Landi, M., Zhao, J., Prather, W. E., Wu, Y., and Zhang, L. (2018). Acoustic purcell Effect for Enhanced Emission. *Phys. Rev. Lett.* 120, 114301. doi:10.1103/PhysRevLett.120.114301
- Li, J., Fok, L., Yin, X., Bartal, G., and Zhang, X. (2009). Experimental Demonstration of an Acoustic Magnifying Hyperlens. *Nat. Mater.* 8, 931–934. doi:10.1038/NMAT2561
- Li, J., Wang, W., Xie, Y., Popa, B.-I., and Cummer, S. A. (2016). A Sound Absorbing Metasurface with Coupled Resonators. *Appl. Phys. Lett.* 109, 091908. doi:10.1063/1.4961671
- Li, Y., and Assouar, B. M. (2016). Acoustic Metasurface-Based Perfect Absorber with Deep Subwavelength Thickness. *Appl. Phys. Lett.* 108, 063502. doi:10.1063/1.4941338
- Li, Y., Liang, B., Gu, Z.-m., Zou, X.-y., and Cheng, J.-c. (2013). Reflected Wavefront Manipulation Based on Ultrathin Planar Acoustic Metasurfaces. *Sci. Rep.* 3, 2546. doi:10.1038/srep02546
- Liang, Z., and Li, J. (2012). Extreme Acoustic Metamaterial by Coiling up Space. *Phys. Rev. Lett.* 108, 114301. doi:10.1103/PhysRevLett.108.114301
- Liu, Z., Zhang, X. X., Mao, Y. W., Zhu, Y. Y., Yang, Z. Y., Chan, C. T., et al. (2000). Locally Resonant Sonic Materials. *Science* 289, 1734–1736. doi:10.1126/science.289.5485.1734
- Long, H., Cheng, Y., and Liu, X. (2017). Asymmetric Absorber with Multiband and Broadband for Low-Frequency Sound. *Appl. Phys. Lett.* 111, 143502. doi:10.1063/1.4998516
- Long, H., Gao, S., Cheng, Y., and Liu, X. (2018). Multiband Quasi-Perfect Low-Frequency Sound Absorber Based on Double-Channel Mie Resonator. *Appl. Phys. Lett.* 112, 033507. doi:10.1063/1.5013225
- Long, H., Shao, C., Liu, C., Cheng, Y., and Liu, X. (2019). Broadband Near-Perfect Absorption of Low-Frequency Sound by Subwavelength Metasurface. *Appl. Phys. Lett.* 115, 103503. doi:10.1063/1.5109826
- Lu, G., Ding, E., Wang, Y., Peng, X., Cui, J., Liu, X., et al. (2017). Realization of Acoustic Wave Directivity at Low Frequencies with a Subwavelength Mie Resonant Structure. *Appl. Phys. Lett.* 110, 123507. doi:10.1063/1.4979105
- Ma, G., Yang, M., Xiao, S., Yang, Z., and Sheng, P. (2014). Acoustic Metasurface with Hybrid Resonances. *Nat. Mater.* 13, 873–878. doi:10.1038/NMAT3994
- Maa, D.-Y. (1998). Potential of Microperforated Panel Absorber. *J. Acoust. Soc. America* 104, 2861–2866. doi:10.1121/1.423870
- Mei, J., Ma, G., Yang, M., Yang, Z., Wen, W., and Sheng, P. (2012). Dark Acoustic Metamaterials as Super Absorbers for Low-Frequency Sound. *Nat. Commun.* 3, 756. doi:10.1038/ncomms1758
- Quan, L., Sounas, D. L., and Alù, A. (2019). Nonreciprocal willis Coupling in Zero-index Moving media. *Phys. Rev. Lett.* 123, 064301. doi:10.1103/PhysRevLett.123.064301
- Quan, L., Zhong, X., Liu, X., Gong, X., and Johnson, P. A. (2014). Effective Impedance Boundary Optimization and its Contribution to Dipole Radiation and Radiation Pattern Control. *Nat. Commun.* 5, 3188. doi:10.1038/ncomms4188
- Ranjbar Nikkhar, M., Hiranandani, M., and Kishk, A. A. (2020). Rotman Lens Design with Wideband DRA Array. *Pier* 169, 45–57. doi:10.2528/PIER20050801
- Romero-García, V., Theocharis, G., Richoux, O., Merkel, A., Tournat, V., and Pagneux, V. (2016). Perfect and Broadband Acoustic Absorption by Critically Coupled Sub-wavelength Resonators. *Sci. Rep.* 6, 19519. doi:10.1038/srep19519
- Song, J. Z., Bai, P., Hang, Z. H., and Lai, Y. (2014). Acoustic Coherent Perfect Absorbers. *New J. Phys.* 16, 033026. doi:10.1088/1367-2630/16/3/033026
- Sun, Y. Y., Xia, J. P., Sun, H. X., Yuan, S. Q., Ge, Y., and Liu, X. J. (2019). Dual-Band Fano Resonance of Low-Frequency Sound Based on Artificial Mie Resonances. *Adv. Sci.* 6, 1901307. doi:10.1002/advs.201901307
- Tang, K., Qiu, C., Ke, M., Lu, J., Ye, Y., and Liu, Z. (2014). Anomalous Refraction of Airborne Sound through Ultrathin Metasurfaces. *Sci. Rep.* 4, 6517. doi:10.1038/srep06517
- Tang, Y., Xin, F., Huang, L., and Lu, T. (2017). Deep Subwavelength Acoustic Metamaterial for Low-Frequency Sound Absorption. *Epl* 118, 44002. doi:10.1209/0295-5075/118/44002
- Toyoda, M., Sakagami, K., Takahashi, D., and Morimoto, M. (2011). Effect of a Honeycomb on the Sound Absorption Characteristics of Panel-type Absorbers. *Appl. Acoust.* 72, 943–948. doi:10.1016/j.apacoust.2011.05.017
- Wei, P., Croëne, C., Tak Chu, S., and Li, J. (2014). Symmetrical and Anti-symmetrical Coherent Perfect Absorption for Acoustic Waves. *Appl. Phys. Lett.* 104, 121902. doi:10.1063/1.4869462
- Wu, X., Fu, C., Li, X., Meng, Y., Gao, Y., Tian, J., et al. (2016). Low-frequency Tunable Acoustic Absorber Based on Split Tube Resonators. *Appl. Phys. Lett.* 109, 043501. doi:10.1063/1.4959959
- Xia, J.-p., Sun, H.-x., Yuan, S.-q., and Zhang, S.-y. (2015). Extraordinary Acoustic Transmission Based on Source Pattern Enhancement and Reconstruction by Metal cylinder Structure. *Appl. Phys. Express* 8, 104301. doi:10.7567/APEX.8.104301
- Xie, B., Tang, K., Cheng, H., Liu, Z., Chen, S., and Tian, J. (2017). Coding Acoustic Metasurfaces. *Adv. Mater.* 29, 1603507. doi:10.1002/adma.201603507
- Xie, Y., Wang, W., Chen, H., Konneker, A., Popa, B.-I., and Cummer, S. A. (2014). Wavefront Modulation and Subwavelength Diffractive Acoustics with an Acoustic Metasurface. *Nat. Commun.* 5, 5553. doi:10.1038/ncomms6553
- Yang, M., Chen, S., Fu, C., and Sheng, P. (2017). Optimal Sound-Absorbing Structures. *Mater. Horiz.* 4, 673–680. doi:10.1039/c7mh00129k
- Yang, M., Li, Y., Meng, C., Fu, C., Mei, J., Yang, Z., et al. (2015). Sound Absorption by Subwavelength Membrane Structures: A Geometric Perspective. *Comptes Rendus Mécanique* 343, 635–644. doi:10.1016/j.crme.2015.06.008
- Yang, M., Meng, C., Fu, C., Li, Y., Yang, Z., and Sheng, P. (2015). Subwavelength Total Acoustic Absorption with Degenerate Resonators. *Appl. Phys. Lett.* 107, 104104. doi:10.1063/1.4930944
- Zarek, J. H. B. (1978). Sound Absorption in Flexible Porous Materials. *J. Sound Vibration* 61, 205–234. doi:10.1016/0022-460X(78)90004-4
- Zhang, C., and Hu, X. (2016). Three-dimensional Single-Port Labyrinthine Acoustic Metamaterial: Perfect Absorption with Large Bandwidth and Tunability. *Phys. Rev. Appl.* 6, 064025. doi:10.1103/PhysRevApplied.6.064025

- Zhang, J., Cheng, Y., and Liu, X. (2017). Extraordinary Acoustic Transmission at Low Frequency by a Tunable Acoustic Impedance Metasurface Based on Coupled Mie Resonators. *Appl. Phys. Lett.* 110, 233502. doi:10.1063/1.4985154
- Zhou, C., Yuan, B., Cheng, Y., and Liu, X. (2016). Precise Rainbow Trapping for Low-Frequency Acoustic Waves with Micro Mie Resonance-Based Structures. *Appl. Phys. Lett.* 108, 063501. doi:10.1063/1.4941664
- Zhu, Y., and Assouar, B. (2019). Multifunctional Acoustic Metasurface Based on an Array of Helmholtz Resonators. *Phys. Rev. B* 99, 174109. doi:10.1103/PhysRevB.99.174109

Conflict of Interest: The authors declare that the research was conducted in the absence of any commercial or financial relationships that could be construed as a potential conflict of interest.

Publisher's Note: All claims expressed in this article are solely those of the authors and do not necessarily represent those of their affiliated organizations, or those of the publisher, the editors, and the reviewers. Any product that may be evaluated in this article, or claim that may be made by its manufacturer, is not guaranteed or endorsed by the publisher.

Copyright © 2021 Guan, Ge, Sun, Yuan, Lai and Liu. This is an open-access article distributed under the terms of the Creative Commons Attribution License (CC BY). The use, distribution or reproduction in other forums is permitted, provided the original author(s) and the copyright owner(s) are credited and that the original publication in this journal is cited, in accordance with accepted academic practice. No use, distribution or reproduction is permitted which does not comply with these terms.



Enhanced Energy Harvesting of Flexural Waves in Elastic Beams by Bending Mode of Graded Resonators

Jacopo Maria De Ponti^{1*†}, Luca Iorio^{1†}, Emanuele Riva^{2†}, Francesco Braghin^{2†}, Alberto Corigliano^{1†} and Raffaele Ardito^{1†}

¹Department of Civil and Environmental Engineering, Politecnico di Milano, Milano, Italy, ²Department of Mechanical Engineering, Politecnico di Milano, Milano, Italy

OPEN ACCESS

Edited by:

Fuyin Ma,
Xi'an Jiaotong University, China

Reviewed by:

Ming Yuan,
Nanjing University of Posts and
Telecommunications, China
Xiao-shuang Li,
Hebei University, China

*Correspondence:

Jacopo Maria De Ponti
jacopomaria.deponti@polimi.it

†ORCID ID:

Jacopo Maria De Ponti
orcid.org/0000-0002-6155-2031
Luca Iorio
orcid.org/0000-0002-9515-9334
Emanuele Riva
orcid.org/0000-0001-6773-9000
Francesco Braghin
orcid.org/0000-0002-0476-4118
Alberto Corigliano
orcid.org/0000-0002-1285-2724
Raffaele Ardito
orcid.org/0000-0002-4271-9190

Specialty section:

This article was submitted to
Metamaterials,
a section of the journal
Frontiers in Materials

Received: 21 July 2021

Accepted: 04 October 2021

Published: 05 November 2021

Citation:

De Ponti JM, Iorio L, Riva E, Braghin F,
Corigliano A and Ardito R (2021)
Enhanced Energy Harvesting of
Flexural Waves in Elastic Beams by
Bending Mode of Graded Resonators.
Front. Mater. 8:745141.
doi: 10.3389/fmats.2021.745141

We show efficient elastic energy transfer and wave confinement through a graded array of resonators attached to an elastic beam. Experiments demonstrate that flexural resonators of increasing lengths allow to reduce wave scattering and to achieve the rainbow effect with local wavefield amplifications. We show that the definition of a monotonically decreasing distribution of the natural frequencies of the resonators along the wave propagation direction, is the preferable choice to increase the energy efficiency of the system. The proposed configuration is suitable for micro-fabrication, envisaging practical applications for micro-scale vibration energy harvesting.

Keywords: metamaterials, piezoelectricity, energy harvesting, resonators, rainbow effect

1 INTRODUCTION

The study of novel metamaterial devices has attracted growing interest within the research community working in several fields of physics, such as electromagnetism (Pendry et al., 1999; Pendry, 2000) acoustics (Liu et al., 2000; Craster and Guenneau, 2013) and elasticity (Craster and Guenneau, 2017), amongst others. In the context of elastic waves, early designs based on Bragg scattering behavior due to material contrast were used to create bandgaps (Kushwaha et al., 1993; Vasseur et al., 2001; Khelif et al., 2003; Pennec et al., 2011; Laude, 2015) and to tailor specific wave behaviors often drawing ideas from the photonic crystal community. To push the operational regime of such systems toward lower frequencies, the exploitation of local resonance has received considerable attention (Liu et al., 2000; Miroshnichenko et al., 2010; Lemoult et al., 2011; Williams et al., 2015), especially for applications in geophysics, mechanical and civil engineering (Colombi et al., 2016a; Miniaci et al., 2016; Achaoui et al., 2017) involving common ambient spectra. While the concept was initially employed for vibration isolation purposes, it was later linked to a variety of phenomena including lensing (Colombi, 2016; Chaplain and Craster, 2019; Fuentes-Domínguez et al., 2021), localisation (Lott et al., 2020) or topological edge states (Pal and Ruzzene, 2017; Xia et al., 2020).

To capitalize on these recent metamaterial designs, energy harvesting is an attractive application: vibration-based energy harvesting has received considerable attention over the last 2 decades, aiming at powering devices using vibrational energy. A practical example consists in the opportunity to harvest energy from the environment to potentially remove the cost associated with battery replacement and avoid the waste of conventional batteries (Erturk and Elvin, 2013). Among the various possible energy harvesting methods, the ones based on piezoelectric materials are widely used due to their large power densities and ease of application (Anton and Sodano, 2007; Erturk and Inman, 2011). A recent line of work in this context exploits methods to locally concentrate the

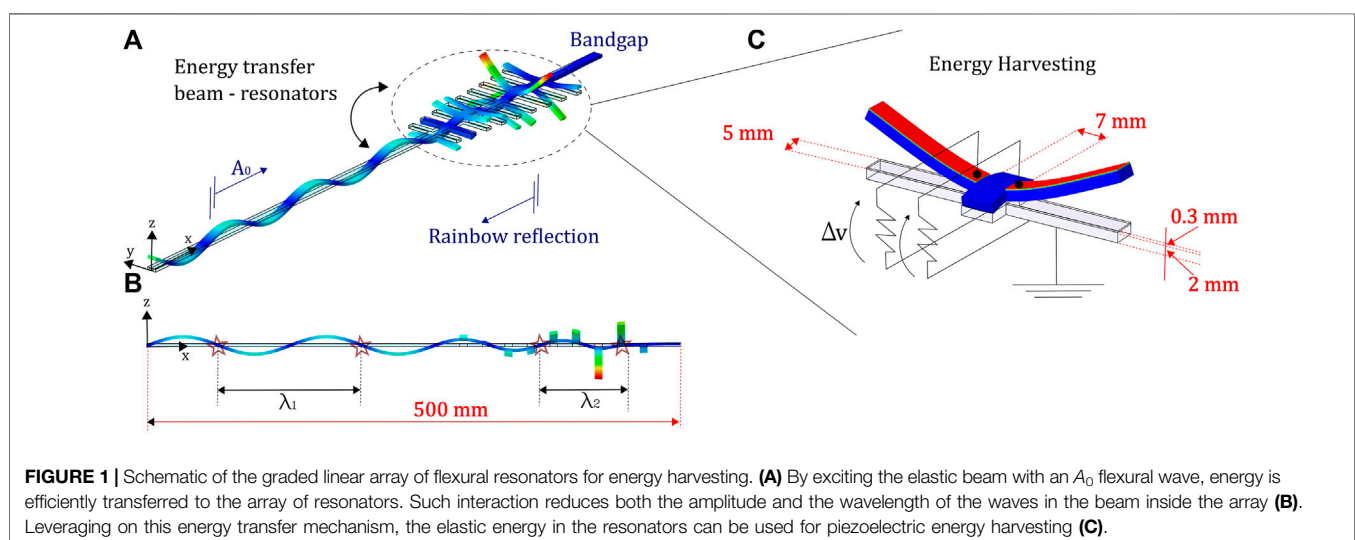
vibrational energy in the attempt to enhance the efficiency of piezoelectric devices. For instance, this can be achieved by focusing or localising acoustic/elastic wave energy in correspondence of the harvester using elastic mirrors, funnels (Carrara et al., 2013) defect modes (Qi et al., 2016), lenses (Tol et al., 2017; Allam et al., 2021), or black holes (Zhao et al., 2014). Another approach to amplify the wavefield relies on the rainbow effect, that effectively slows down waves and spatially separates frequency components. These systems are based on gradually varying periodic arrays of resonators to take advantage of local band-gaps to control wave propagation. The underlying physics, capable of inducing spatial segregation of frequency components, relies on the ability to locally decrease the propagation speed along the array. A similar wave speed reduction can be achieved through black-hole configurations that, however, rely on thickness modulations which reflect on a local stiffness decrease of the host medium, often undesired from the engineering perspective.

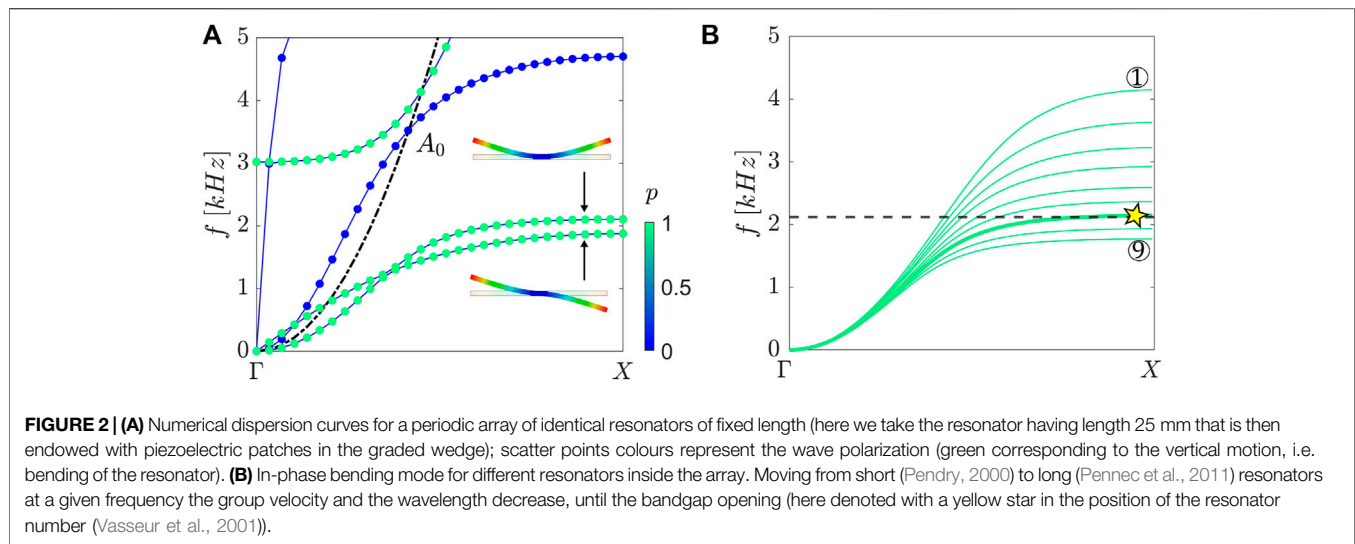
A graded array is instead formed by smoothly varying a particular parameter in space through a specific design of consecutive unit cells. Originally discovered in electromagnetism using axially non-uniform, linearly tapered, planar waveguides with cores of negative index material (Tsakmakidis et al., 2007), there has been a flurry of intensive research translating the rainbow effect into all flavors of classical wave propagation fields including acoustics (Romero-García et al., 2013; Zhu et al., 2013; Cebrecos et al., 2014; Chen et al., 2014), water waves (Bennetts et al., 2018) and fluid loaded elastic plates (Skelton et al., 2018), amongst others. Particular advances have been recently reported in elastic devices made of arrays of resonant rods for deep elastic substrates (Colombi et al., 2016b; Colombi et al., 2017; Colquitt et al., 2017; Chaplain et al., 2020a) to mode convert Rayleigh (*R*) into Shear (*S*) or Pressure (*P*) waves. Such graded line arrays of resonators have been theorised, designed and manufactured also for energy harvesting applications (Chaplain et al., 2020b; De Ponti et al., 2020; Alshaqqa and Erturk, 2021; De Ponti, 2021). In this context,

rainbow reflection and trapping mechanisms are employed to enhance the interaction time between waves and the harvesting system, reporting higher power output as compared to ungraded designs. A straightforward implementation consists into a set of rod resonators of increasing height, which effectively couple with the motion of the A_0 mode, with particularly strong interaction at the longitudinal resonance frequency of the rods (De Ponti et al., 2020). Even if the efficiency of the proposed designs has been verified numerically and experimentally, the use of axial resonators could be a problem for both fabrication and proper connection of the piezoelectric patches. Here, in contrast, we develop a more compact configuration based on a planar geometry with cantilever resonators. This system is also suitable for a piezoelectric deposition processes on the entire structure, yielding an overall smaller device with broadband features. In order to quantify the potential advantages of such rainbow device, we compare its performance to the case of a single resonating element and to an array with the same length and random grading law. We show that a monotonically decreasing distribution of the natural frequencies of the resonators yields stronger wavefield amplifications, which reflect on enhanced energy harvesting performance.

2 RAINBOW REFLECTION MECHANICS

We consider the system depicted in **Figure 1A** made of an elastic beam with attached an array of cantilevers of linearly increasing lengths. Due to the cross section symmetry, we focus the analysis on the wave propagation of the A_0 flexural mode. It is worth to mention that a symmetry-broken cross-section or a non-null coupling between consecutive resonators may trigger different phenomena involving the excitation of waves with different polarization (De Ponti et al., 2021). Herein, we limit the analysis to the A_0 mode and we consider all other supported modes as orthogonal to the excitation mechanism. The beam and the resonators are made of aluminium with Young modulus $E_a = 70 \text{ GPa}$, Poisson ratio $\nu_a =$





0.33 and density $\rho_a = 2710 \text{ kg/m}^3$. The beam is 500 mm long, 7 mm wide and 2 mm thick. The array is made of 9 unit cells of size $a = 15 \text{ mm}$, with a linear grading law for the lengths of the resonators, from 16.75 to 27.75 mm, resulting in a grading angle of approximately 5.2° . By spatially varying the resonance frequency of the resonators attached to the beam (De Ponti et al., 2020; De Ponti, 2021) waves slow down with a reduction of both amplitude and wavelength (Figure 1B). Differently with respect to the acoustic wave compression (Chen et al., 2014), the array of resonators progressively absorbs energy from the beam, allowing for a wave amplitude reduction in the beam inside the array (De Ponti, 2021). We remark that there is a difference between rainbow reflection (hereafter implemented) and rainbow trapping, as delineated in Chaplain et al. (2020b). Rainbow reflection occurs when zero group velocity modes are met at band edge, while rainbow trapping when zero group velocity modes arises within the first Brillouin Zone due to the coupling between crossing modes. In both cases, the concurrent amplitude and wavelength reduction is a hallmark of energy transfer between the main structure and the resonators, and is used here for energy harvesting purposes. That is, our implementation in Figure 1C shows the arrangement of a set of piezoelectric patches and the electric circuit employed to transduce electric energy due to resonator motion in a tailored position along the beam. In here, we exploit the 31-mode of the piezoelectric patches connected to a resistive load to effectively harvest the elastic energy stored inside the target resonators.

The wave propagation properties of the system can be rigorously inferred by looking at the dispersion curves of a given cell inside the array. Provided the grading is gentle enough and provided the number of unit cells is sufficient, the global behaviour of the whole array can be deduced from the local dispersion curves of the constituent elements (Colombi et al., 2016b); in this way, the desired spatial selection by frequency properties, i.e. the rainbow behaviour of the system, is determined from the locally periodic structure at a given position. Figure 2A shows the numerical dispersion curves for the cell number 7 (where the cell numbering in the array goes from 1 for the shortest resonators

to 9 for the longest). These dispersion curves are computed along the 1D irreducible Brillouin Zone using the finite elements software Abaqus (Smith, 2009), that incorporates the Bloch phase shift via Bloch-Floquet periodic boundary conditions in the attempt to study the unit cell containing two resonators. The resonators, later used for energy harvesting purposes, are 5 mm wide and 25 mm long. These values and the geometry of the attachments are chosen to ease the manufacturing of the specimen, but we remark that dynamically equivalent configurations can be achieved matching the desired natural frequency and the participating mass (Sugino et al., 2016). By inspecting the dispersion curves related to the bending of the resonators, we identify an in-phase and an out-of-phase mode, as shown in the inset in Figure 2A. This behaviour, which comes from having two resonators per cell, does not affect the response of the array since the antisymmetric mode cannot be excited with the symmetric A_0 input. The spatial properties of the wavefield can be deduced from the local dispersion curves at a given frequency, as shown in Figure 2B. By increasing the length of the resonators along the spatial dimension, i.e. moving from (Pendry, 2000) to (Pennec et al., 2011), the dispersion curves shift towards lower frequencies. As a result, by fixing the frequency, the group velocity, $v_g = \partial\omega/\partial k$, smoothly reduces until zero. Such effect allows to slow down elastic waves inside the array and to confine waves in different positions depending on frequency. In addition, since the zero group velocity mode occurs at the band edge, it can couple with a backward propagating mode, which is typical of rainbow reflection (Chaplain et al., 2020b).

To provide further insights on the energy transfer mechanism related to rainbow reflection, we compare the linear graded array to the case of a single cell, and to an array with a random grading law. The cells involved in the random configuration are the same adopted for the linear array but with a different arrangement of attachments, except for the target one. Figure 3 shows the three configurations, in which the target resonator, i.e. the one with the first flexural mode corresponding to the input frequency, is marked with a yellow star. We quantify the efficiency of each configuration

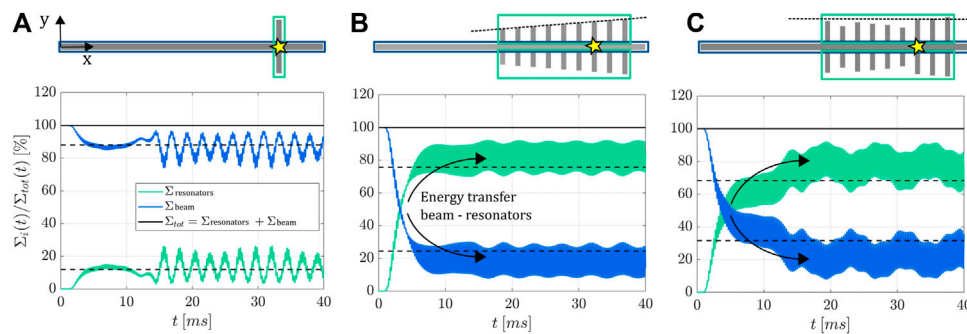


FIGURE 3 | Total energy density distributions in time for the single cell **(A)**, linear **(B)** and random array **(C)**. Each system is forced using a tone burst of 15 ms at 2 kHz, able to excite the flexural resonance of the resonators in the cell marked with a yellow star. For the lone cell **(A)**, weak energy transfer between the beam and the resonators is achieved. Adding a linear array of resonators **(B)** allows to increase the efficiency of energy transfer, providing strong energy confinement inside the resonators. A similar behaviour, but less efficient, is shown for the random array **(C)**. To outline the differences in term of performance, the mean energy density along time is also reported with dashed black lines.

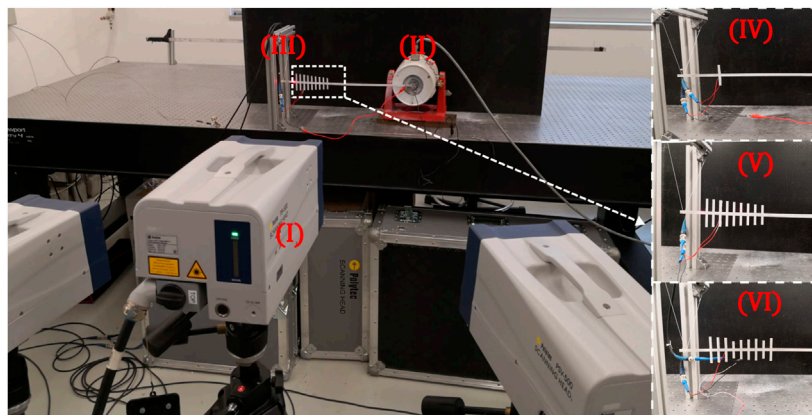


FIGURE 4 | Experimental setup. The wavefield is measured using a 3D laser vibrometer **(I)**. The beam is forced using an electrodynamic shaker **(II)**, while the opposite side is suspended through elastic cables **(III)**. A zoomed-in view of the lone cell **(IV)**, linear array **(V)** and random array **(VI)** is reported in the right insets.

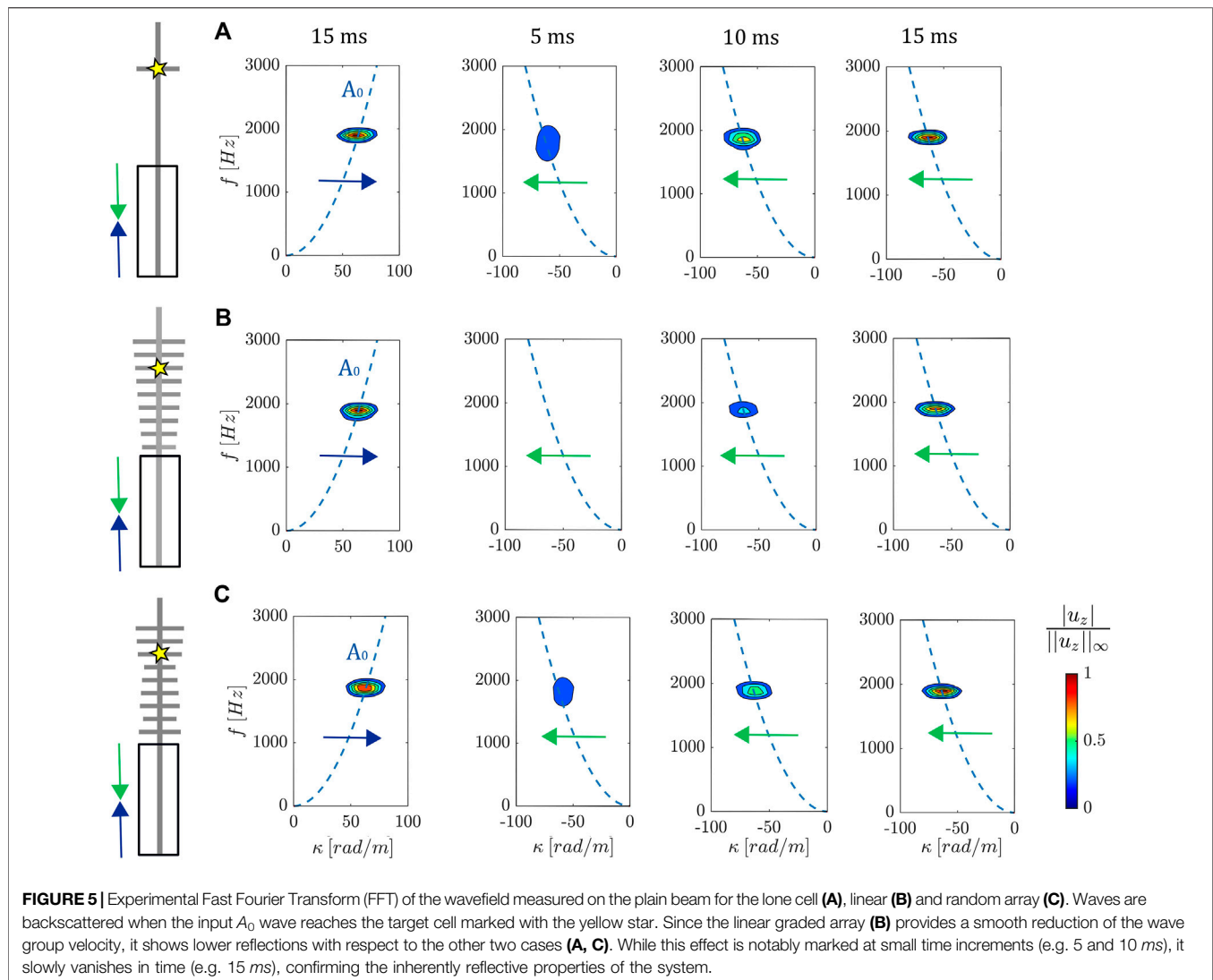
by looking at the total energy density distributions along time, as shown in **Figure 3**. Such energy, denoted with Σ , can be decomposed in the contribution of the beam, Σ_{beam} , and the resonators $\Sigma_{resonators}$. Each configuration is excited using a narrowband source at central frequency of 2 kHz, width $\Delta f = 0.14$ kHz, and time duration $T = 15$ ms. The numerical model employed is based on a finite element discretization of the system through Abaqus (Smith, 2009), using full 3D stress quadratic elements (C3D20). The analysis is performed opting for an implicit analysis based on the Hilber-Hughes-Taylor operator, with a constant time increment $dt = 0.01$ ms. The energy density for the beam and the resonators is obtained summing the strain and kinetic energy densities of the corresponding individual finite elements (FE) for each time instant. We notice that when a single cell is introduced on the elastic beam, low energy transfer is achieved (**Figure 3A** with a mean local energy density percentage in the resonators of about 12%). The linear array shows (**Figure 3B**) the strongest energy transfer, with a mean local energy density percentage in the

resonators of about 76%. Finally, the random array shows a mean local energy density percentage in the resonators of about 68%.

3 EXPERIMENTS ON SLOW WAVES FOR ENERGY HARVESTING

A peculiar property of the rainbow reflection device is the capability to slow down array guided waves as they transverse the array. Such phenomenon allows for a longer interaction between the wave and the resonators, locally increasing the amplitude of the wavefield inside the resonators (De Ponti et al., 2020; De Ponti, 2021). To validate this effect, and the implications in terms of energy harvesting, we perform experimental tests in narrow and broad-band frequency regime. **Figure 4** shows the experimental setup used for testing.

At the right boundary, a LDS v406 electrodynamic shaker is rigidly connected to the beam through a thick aluminium plate with



high strength adhesive, to provide excitation. At the opposite boundary, the structure is suspended through elastic cables that do not affect the dynamics of the system. The wavefield on the elastic beam is measured through a Polytec 3D Scanner Laser Doppler Vibrometer (SLDV), which is able to separate the out-of-plane velocity field in both space and time. The same narrow-band excitation input used in the numerical model is synchronously started with the acquisition which, in turn, is averaged in time to decrease the noise. **Figure 5** shows the experimental Fast Fourier Transform (FFT) of the wavefield for the single cell (**Figure 5A**), the linear (**Figure 5B**) and random array (**Figure 5C**) at different time instants. The corresponding input (blue arrow) and reflected waves (green arrow) measured for different time instants along the plain beam before the resonators are reported for the different configurations. It can be noticed that a stronger slowing effect is achieved for the linear array, since the wave reflection is not visible before the array at 5 ms. After a certain amount of time, such effect vanishes and the three configurations are similar in terms of wave reflection.

We experimentally show the rainbow effect in the linear array by applying a broadband frequency sweep in the range 1.6–4.2 kHz. **Figure 6A** shows a space-frequency analysis of the experimental data. Depending on the frequency, waves stop at different spatial positions, corresponding to the bandgap opening. Moreover, we notice that the amplitude and the wavelength of the mode shapes decrease inside the array, until the amplitude vanishes in correspondence of the position of the resonating element, which is well predicted by numerical results (dashed white line). We then quantify the advantages of such mechanism for energy harvesting by placing piezoelectric PZT-5H patches ($E_p = 61 \text{ GPa}$, $\nu_p = 0.31$, $\rho_p = 7800 \text{ kg/m}^3$, dielectric constant $\epsilon_{33}^T/\epsilon_0 = 3500$, and piezoelectric coefficient $e_{31} = -9.2 \text{ C/m}^2$) at the position of the 7th cell, denoted with the white star in **Figure 6A**. **Figure 6B** shows the mean output open circuit voltage for the single cell, random and linear arrays normalized by the measured input velocity, to make sure that the results are displayed under the same conditions. Moreover, the extra stiffness due to the piezoelectric layer is considered in the evaluation of the natural frequency of the resonator. We observe that the graded linear array gives a mean

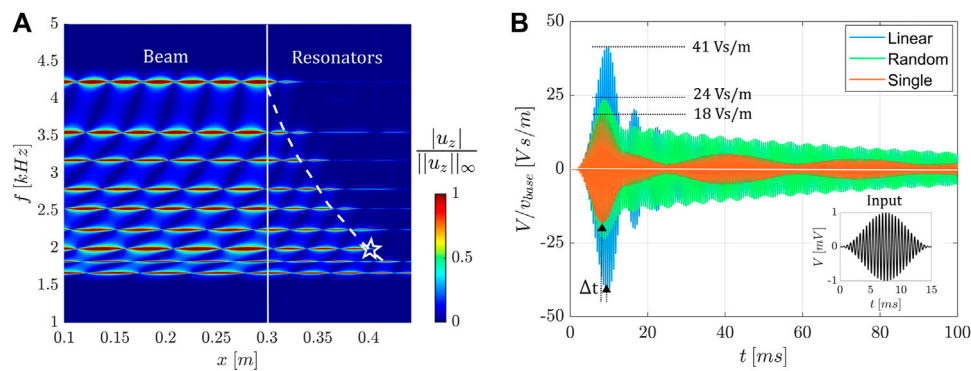


FIGURE 6 | (A) Space-frequency analysis of the experimental data superimposed to numerical predictions (dashed white line) from dispersion curves. **(B)** Open circuit output voltage for the linear, random and single cell configuration, corresponding to the input excitation frequency marked with the white star in **(A)**. The linear grading provides the maximum output voltage and time delay.

normalized peak voltage of 41 Vs/m which is 56% higher than the single cell and 41% higher than the random array. We notice that such peak is reached with a delay Δt of approximately 1.3 ms, which is justified by the smooth reduction of the group velocity inside the linear array. Both the linear and random arrays provide a strong time spreading of the input, as can be noticed by comparing the input signal reported in the inset of **Figure 6B** with the response of the resonators for long time periods.

4 CONCLUSION

In conclusion, we have demonstrated potential advantages in using graded arrays of flexural resonators for efficient elastic energy confinement. The array capability of slowing down waves enables a strong energy transfer to the resonators, which then reflects in enhanced energy harvesting performances. This effect is stronger for a monotonically decreasing distribution of the natural frequencies of the resonators, due to the longest interaction time between the wave and the array. We remark that the system can be frequency-tuned simply by adding masses at the tip of the cantilever resonators: this design can be employed to match applications and scenarios characterized low frequency ambient spectra. Also, we remark that the present configuration can be suitably employed for energy harvesting applications and can be scaled at the micro-scale for the implementation of next generation vibration energy harvesting devices.

REFERENCES

- Achaoui, Y., Antonakakis, T., Brûlé, S., Craster, R. V., Enoch, S., and Guenneau, S. (2017). Clamped Seismic Metamaterials: Ultra-low Frequency Stop Bands. *New J. Phys.* 19, 063022. doi:10.1088/1367-2630/aa6e21
- Allam, A., Sabra, K., and Erturk, A. (2021). Sound Energy Harvesting by Leveraging a 3D-Printed Phononic crystal Lens. *Appl. Phys. Lett.* 118, 103504. doi:10.1063/5.0030698
- Alshaq, M., and Erturk, A. (2021). Graded Multifunctional Piezoelectric Metastructures for Wideband Vibration Attenuation and Energy Harvesting. *Smart Mater. Struct.* 30, 015029. doi:10.1088/1361-665x/abc7fa

DATA AVAILABILITY STATEMENT

The original contributions presented in the study are included in the article/Supplementary Material, further inquiries can be directed to the corresponding author.

AUTHOR CONTRIBUTIONS

JMDP, AC, and RA initiated the project. JMDP and LI carried out the numerical studies and created the figures. ER and FB helped with the laboratory experiment. JMDP wrote the article. All the authors contributed to the editing of the article.

FUNDING

The support of the H2020 FET-proactive project MetaVEH under grant agreement No. 952039.

ACKNOWLEDGMENTS

We also gratefully acknowledge the Italian Ministry of Education, University and Research for the support provided through the Project “Department of Excellence LIS4.0—Lightweight and Smart Structures for Industry 4.0.”

- Anton, S. R., and Sodano, H. A. (2007). A Review of Power Harvesting Using Piezoelectric Materials (2003-2006). *Smart Mater. Struct.* 16, R1–R21. doi:10.1088/0964-1726/16/3/r01
- Bennetts, L. G., Peter, M. A., and Craster, R. V. (2018). Graded Resonator Arrays for Spatial Frequency Separation and Amplification of Water Waves. *J. Fluid Mech.* 854, R4. doi:10.1017/jfm.2018.648
- Carrara, M., Cacan, M. R., Toussaint, J., Leamy, M. J., Ruzzene, M., and Erturk, A. (2013). Metamaterial-inspired Structures and Concepts for Elastoacoustic Wave Energy Harvesting. *Smart Mater. Struct.* 22, 065004. doi:10.1088/0964-1726/22/6/065004
- Cebrecos, A., Picó, R., Sánchez-Morcillo, V. J., Staliunas, K., Romero-García, V., and Garcia-Raffi, L. M. (2014). Enhancement of Sound by Soft Reflections in Exponentially Chirped Crystals. *AIP Adv.* 4, 124402. doi:10.1063/1.4902508

- Chaplain, G. J., De Ponti, J. M., Colombi, A., Fuentes-Dominguez, R., Dryburg, P., Pieris, D., et al. (2020). Tailored Elastic Surface to Body Wave Umklapp Conversion. *Nat. Commun.* 11, 3267, 1–8. doi:10.1038/s41467-020-17021-x
- Chaplain, G. J., and Craster, R. V. (2019). Flat Lensing by Graded Line Meta-Arrays. *Phys. Rev. B* 99 (R), 220102. doi:10.1103/physrevb.99.220102
- Chaplain, G. J., Pajer, D., De Ponti, J. M., and Craster, R. V. (2020). Delineating Rainbow Reflection and Trapping with Applications for Energy Harvesting. *New J. Phys.* 22, 063024. doi:10.1088/1367-2630/ab8cae
- Chen, Y., Liu, H., Reilly, M., Bae, H., and Yu, M. (2014). Enhanced Acoustic Sensing through Wave Compression and Pressure Amplification in Anisotropic Metamaterials. *Nat. Commun.* 5, 5247. doi:10.1038/ncomms6247
- Colombi, A., Colquitt, D., Roux, P., Guenneau, S., and Craster, R. V. (2016). A Seismic Metamaterial: The Resonant Metawedge. *Sci. Rep.* 6 (1), 27717, 1–6. doi:10.1038/srep27717
- Colombi, A., Ageeva, V., Smith, R. J., Clare, A., Patel, R., Clark, M., et al. (2017). Enhanced Sensing and Conversion of Ultrasonic Rayleigh Waves by Elastic Metasurfaces. *Sci. Rep.* 7 (1), 6750. doi:10.1038/s41598-017-07151-6
- Colombi, A. (2016). Resonant Metalenses for Flexural Waves in Plates. *The J. Acoust. Soc. America* 140, EL423–EL428. doi:10.1121/1.4967179
- Colombi, A., Roux, P., Guenneau, S., Gueguen, P., and Craster, R. V. (2016). Forests as a Natural Seismic Metamaterial: Rayleigh Wave Bandgaps Induced by Local Resonances. *Sci. Rep.* 6, 19238. doi:10.1038/srep19238
- Colquitt, D. J., Colombi, A., Craster, R. V., Roux, P., and Guenneau, S. R. L. (2017). Seismic Metasurfaces: Sub-wavelength Resonators and Rayleigh Wave Interaction. *J. Mech. Phys. Sol.* 99, 379–393. doi:10.1016/j.jmps.2016.12.004
- Craster, R. V., and Guenneau, S. (2013). *Acoustic Metamaterials, Negative Refraction, Imaging, Lensing and Cloaking*. Springer Series in Materials Science, 1–324.
- Craster, R. V., and Guenneau, S. (2017). *World Scientific Handbook of Metamaterials and Plasmonics: Volume 2: Elastic, Acoustic and Seismic Metamaterials*. Singapore: World Scientific.
- De Ponti, J. M., Colombi, A., Riva, E., Ardito, R., Braghin, F., Corigliano, A., et al. (2020). Experimental Investigation of Amplification, via a Mechanical Delay-Line, in a Rainbow-Based Metamaterial for Energy Harvesting. *Appl. Phys. Lett.* 117, 143902. doi:10.1063/5.0023544
- De Ponti, J. M. (2021). *Graded Elastic Metamaterials for Energy Harvesting*. Springer.
- De Ponti, J. M., Iorio, L., Riva, E., Ardito, R., Braghin, F., and Corigliano, A. (2021). Selective Mode Conversion and Rainbow Trapping via Graded Elastic Waveguides. *Phys. Rev. Appl.* 16, 034028. doi:10.1103/physrevapplied.16.034028
- Erturk, A., and Elvin, N. (2013). *Advances in Energy Harvesting Methods*. Springer.
- Erturk, A., and Inman, D. J. (2011). *Piezoelectric Energy*. Wiley.
- Fuentes-Dominguez, R., Yao, M., Colombi, A., Dryburgh, P., Pieris, D., Jackson-Crisp, A., et al. (2021). Design of a Resonant Luneburg Lens for Surface Acoustic Waves. *Ultrasonics* 111, 106306. doi:10.1016/j.ultras.2020.106306
- Khelif, A., Djafari-Rouhani, B., Vasseur, J. O., and Deymier, P. A. (2003). Transmission and Dispersion Relations of Perfect and Defect-Containing Waveguide Structures in Phononic Band gap Materials. *Phys. Rev. B* 68, 024302. doi:10.1103/physrevb.68.024302
- Kushwaha, M. S., Halevi, P., Dobrzynski, L., and Djafari-Rouhani, B. (1993). Acoustic Band Structure of Periodic Elastic Composites. *Phys. Rev. Lett.* 71, 2022–2025. doi:10.1103/physrevlett.71.2022
- Laude, V. (2015). *Phononic Crystals Artificial Crystals for Sonic, Acoustic, and Elastic Waves*. Berlin: De Gruyter.
- Lemoult, F., Fink, M., and Lerosey, G. (2011). Acoustic Resonators for Far-Field Control of Sound on a Subwavelength Scale. *Phys. Rev. Lett.* 107, 064301. doi:10.1103/PhysRevLett.107.064301
- Liu, Z., Zhang, X., Mao, Y., Zhu, Y. Y., Yang, Z., Chan, C. T., et al. (2000). Locally Resonant Sonic Materials. *Science* 289, 1734–1736. doi:10.1126/science.289.5485.1734
- Lott, M., Roux, P., Seydoux, L., Tallon, B., Pelat, A., Skipetrov, S., et al. (2020). Localized Modes on a Metasurface through Multiwave Interactions. *Phys. Rev. Mater.* 4, 065203. doi:10.1103/physrevmaterials.4.065203
- Miniati, M., Krushynska, A., Bosia, F., and Pugno, N. M. (2016). Large Scale Mechanical Metamaterials as Seismic Shields. *New J. Phys.* 18, 083041. doi:10.1088/1367-2630/18/8/083041
- Miroshnichenko, A. E., Flach, S., and Kivshar, Y. S. (2010). Fano Resonances in Nanoscale Structures. *Rev. Mod. Phys.* 82, 2257–2298. doi:10.1103/revmodphys.82.2257
- Pal, R. K., and Ruzzene, M. (2017). Edge Waves in Plates with Resonators: an Elastic Analogue of the Quantum valley Hall Effect. *New J. Phys.* 19, 025001. doi:10.1088/1367-2630/aa56a2
- Pendry, J. B., Holden, A. J., Robbins, D. J., and Stewart, W. J. (1999). Magnetism from Conductors and Enhanced Nonlinear Phenomena. *IEEE Trans. Microwave Theor. Techn.* 47, 2075–2084. doi:10.1109/22.798002
- Pendry, J. B. (2000). Negative Refraction Makes a Perfect Lens. *Phys. Rev. Lett.* 85, 3966–3969. doi:10.1103/physrevlett.85.3966
- Pennec, Y., Rouhani, B. D., Li, C., Escalante, J. M., Martinez, A., Benchabane, S., et al. (2011). Band Gaps and Cavity Modes in Dual Phononic and Photonic Strip Waveguides. *AIP Adv.* 1, 041901. doi:10.1063/1.3675799
- Qi, S., Oudich, M., Li, Y., and Assouar, B. (2016). Acoustic Energy Harvesting Based on a Planar Acoustic Metamaterial. *Appl. Phys. Lett.* 108, 263501. doi:10.1063/1.4954987
- Romero-García, V., Picó, R., Cebrecos, A., Sánchez-Morcillo, V. J., and Staliunas, K. (2013). Enhancement of Sound in Chirped Sonic Crystals. *Appl. Phys. Lett.* 102, 091906. doi:10.1063/1.4793575
- Skelton, E. A., Craster, R. V., Colombi, A., and Colquitt, D. J. (2018). The Multi-Physics Metawedge: Graded Arrays on Fluid-Loaded Elastic Plates and the Mechanical Analogues of Rainbow Trapping and Mode Conversion. *New J. Phys.* 20, 053017. doi:10.1088/1367-2630/aabecf
- Smith, M. (2009). *ABAQUS/Standard User's Manual, Version 6.9*. Providence, RI: Dassault Systèmes Simulia Corp.
- Sugino, C., Leadenham, S., Ruzzene, M., and Erturk, A. (2016). On the Mechanism of Bandgap Formation in Locally Resonant Finite Elastic Metamaterials. *J. Appl. Phys.* 120, 134501. doi:10.1063/1.4963648
- Tol, S., Degertekin, F. L., and Erturk, A. (2017). Phononic crystal Luneburg Lens for Omnidirectional Elastic Wave Focusing and Energy Harvesting. *Appl. Phys. Lett.* 111, 013503. doi:10.1063/1.4991684
- Tsakmakidis, K. L., Boardman, A. D., and Hess, O. (2007). 'Trapped Rainbow' Storage of Light in Metamaterials. *Nature* 450, 397–401. doi:10.1038/nature06285
- Vasseur, J. O., Deymier, P. A., Chenni, B., Djafari-Rouhani, B., Dobrzynski, L., and Prevost, D. (2001). Experimental and Theoretical Evidence for the Existence of Absolute Acoustic Band Gaps in Two-Dimensional Solid Phononic Crystals. *Phys. Rev. Lett.* 86, 3012–3015. doi:10.1103/physrevlett.86.3012
- Williams, E. G., Roux, P., Rupin, M., and Kuperman, W. A. (2015). Theory of Multiresonant Metamaterials for A0 Lamb Waves. *Phys. Rev. B* 91, 104307. doi:10.1103/physrevb.91.104307
- Xia, Y., Erturk, A., and Ruzzene, M. (2020). Topological Edge States in Quasiperiodic Locally Resonant Metastructures. *Phys. Rev. Appl.* 13, 014023. doi:10.1103/physrevapplied.13.014023
- Zhao, L., Conlon, S. C., and Semperlotti, F. (2014). Broadband Energy Harvesting Using Acoustic Black Hole Structural Tailoring. *Smart Mater. Struct.* 23, 065021. doi:10.1088/0964-1726/23/6/065021
- Zhu, J., Chen, Y., Zhu, X., Garcia-Vidal, F. J., Yin, X., Zhang, W., et al. (2013). Acoustic Rainbow Trapping. *Sci. Rep.* 3, 1728. doi:10.1038/srep01728

Conflict of Interest: The authors declare that the research was conducted in the absence of any commercial or financial relationships that could be construed as a potential conflict of interest.

Publisher's Note: All claims expressed in this article are solely those of the authors and do not necessarily represent those of their affiliated organizations, or those of the publisher, the editors and the reviewers. Any product that may be evaluated in this article, or claim that may be made by its manufacturer, is not guaranteed or endorsed by the publisher.

Copyright © 2021 De Ponti, Iorio, Riva, Braghin, Corigliano and Ardito. This is an open-access article distributed under the terms of the Creative Commons Attribution License (CC BY). The use, distribution or reproduction in other forums is permitted, provided the original author(s) and the copyright owner(s) are credited and that the original publication in this journal is cited, in accordance with accepted academic practice. No use, distribution or reproduction is permitted which does not comply with these terms.



Hybrid Bandgaps in Mass-coupled Bragg Atomic Chains: Generation and Switching

Shao-Feng Xu¹, Zhu-Long Xu¹ and Kuo-Chih Chuang^{1,2*}

¹Key Laboratory of Soft Machines and Smart Devices of Zhejiang Province, School of Aeronautics and Astronautics, Institute of Applied Mechanics, Zhejiang University, Hangzhou, China, ²State Key Laboratory for Strength and Vibration of Mechanical Structures, School of Aerospace Engineering, Xi'an Jiaotong University, Xi'an, China

OPEN ACCESS

Edited by:

Yan-Feng Wang,
Tianjin University, China

Reviewed by:

Yabin Jin,
Tongji University, China
Yongquan Liu,
Xi'an Jiaotong University, China

*Correspondence:

Kuo-Chih Chuang
chuangkc@zju.edu.cn

Specialty section:

This article was submitted to
Metamaterials,
a section of the journal
Frontiers in Materials

Received: 12 September 2021

Accepted: 27 September 2021

Published: 30 November 2021

Citation:

Xu S-F, Xu Z-L and Chuang K-C (2021)
Hybrid Bandgaps in Mass-coupled
Bragg Atomic Chains: Generation
and Switching.
Front. Mater. 8:774612.
doi: 10.3389/fmats.2021.774612

In this work, without introducing mass-in-mass units or inertial amplification mechanisms, we show that two Bragg atomic chains can form an acoustic metamaterial that possesses different types of bandgaps other than Bragg ones, including local resonance and inertial amplification-like bandgaps. Specifically, by coupling masses of one monatomic chain to the same masses of a diatomic or triatomic chain, hybrid bandgaps can be generated and further be switched through the adjustment of the structural parameters. To provide a tuning guidance for the hybrid bandgaps, we derived an analytical transition parameter (p -value) for the mass-coupled monatomic/diatomic chain and analytical discriminants for the mass-coupled monatomic/triatomic chain. In our proposed mass-coupled monatomic/triatomic chain system, each set of analytical discriminants determines a hybrid bandgap state and a detailed examination reveals 14 different bandgap states. In addition to bandgap switching, the analytical p -value and discriminants can also be used as a guide for designing the coupled-chain acoustic metamaterials. The relations between the mass-coupled monatomic/triatomic chain system and a three-degree-of-freedom (DOF) inertial amplification system further indicate that the band structure of the former is equivalent to that of the latter through coupling masses by negative dynamic stiffness springs.

Keywords: metamaterials, atomic chains, bandgaps, local resonance, inertial amplification, phononic crystal

INTRODUCTION

Being classic textbook models that can explain lattice vibrations in solid state physics, one-dimensional atomic chains can capture the most fundamental properties of phononic crystals (PCs) (Kittel et al., 1996; Hofmann, 2015), which are known for having Bragg bandgaps that can suppress the propagation of mechanical waves (Deymier, 2013; Khelif and Adibi, 2015). Over the past decade, based on PCs that contain the simplest spring-mass systems in a unit cell, some important advances in the domains of nonlinear wave guides (Narisetti et al., 2010; Porubov and Andrianov, 2013; Ganesh and Gonella, 2015; Fang et al., 2016), topological edge states (Pal et al., 2018; Al Ba'ba'a et al., 2019), and diode-like acoustic structures (Vila et al., 2017; Attarzadeh et al., 2018) have been achieved. The atomic chains have also been used to explain nonlocal interactions of the panels of origami metamaterials (Pratapa et al., 2018). Despite being an idealized spring-mass lattice system, the simplest atomic chains can capture the bandgap phenomenon of PCs and to which other bandgap-generation mechanisms can be introduced.

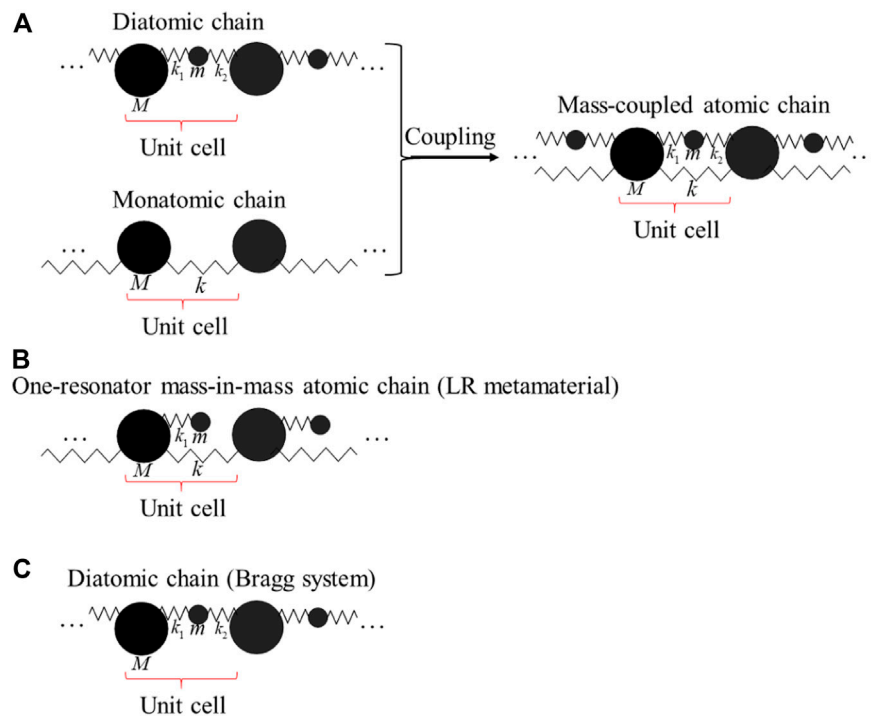


FIGURE 1 | (A) The mass-coupled atomic chain coupled by a diatomic chain and a monatomic chain. **(B)** One-resonator mass-in-mass atomic chain. **(C)** Diatomic chain.

Since the properties of the Bragg bandgaps depend heavily on the lattice constant, it is difficult to achieve low-frequency bandgaps if not increasing the size of the periodic cell. By introducing mass-in-mass units to a monatomic lattice system, acoustic metamaterials exhibiting local resonance (LR) bandgaps independent of the spatial periodicity can be obtained (Huang et al., 2009). Acoustic metamaterials have attracted significant interest due to their unusual mechanical properties such as subwavelength bandgaps, negative effective mass density, or negative effective modulus (Liu et al., 2000; Li and Chan, 2004; Fang et al., 2006; Lazarov and Jensen, 2007; Yao et al., 2008; Huang and Sun, 2010; Huang and Sun, 2012). The concept of infinite mass-in-mass atomic chains have been extended to the design of continuum structures such as elastic metamaterial rods (i.e., through the homogenization method), beams, plates or pillared metamaterial (i.e., surfaces that consist of pillars or branching substructures) in which longitudinal, lateral or flexural vibrations can be suppressed (Yu et al., 2006; Kundu et al., 2014; Zhu et al., 2014; Liu et al., 2015; MuhammadLim, 2019; Jin et al., 2021). Although LR bandgaps are low-frequency ones compared to Bragg bandgaps, several researchers have attempted to further push the bandgaps to lower frequencies without adding extra masses. By introducing internal couplings to mass-in-mass lattices through negative stiffness springs, Hu et al. recently showed that multiple bandgaps and ultra-low resonance bandgaps can be achieved without adding extra masses (Hu et al., 2017; Hu et al., 2019). In addition to mass-in-mass units, inertial amplification mechanisms have also been

introduced to mass-spring chains to generate wide and deep low-frequency bandgaps (Yilmaz et al., 2007; Yilmaz and Hulbert, 2010; Taniker and Yilmaz, 2013; Yilmaz et al., 2017). Frandsen et al. investigated an elastic rod with a periodically attached inertial amplification mechanism and found the characteristic double-peak phenomenon in bandgap regions (Frandsen et al., 2016). Through deriving the effective mass of a modified monatomic chain with a lightweight attached mass-link system, Bennetts et al. obtained its low-frequency vibration-isolation properties (Bennetts et al., 2019). Recently, Li and Zhou proposed a periodic mass-spring-truss chain based on a scissor-like structure and inertial amplification to achieve low-frequency vibration attenuation (Li and Zhou, 2021). One interesting question arises: Can we generate local resonance or inertial amplification bandgaps in the band structures of atomic chains without mass-in-mass units or inertial amplification mechanisms?

To solve the above question, we introduce mass coupling to two Bragg atomic chains at certain masses. Specifically, as illustrated in Figure 1A, considering a fundamental configuration of a mass-coupled atomic chain, where a diatomic chain is coupled to a monatomic chain. It is well known that, depending on the existence of certain springs, the mass-coupled atomic chain can be degenerated to a local resonant (LR) acoustic metamaterial with mass-in-mass units (see Figure 1B) or an alternating mass-spring Bragg system (i.e., also known as phononic crystal) showed in Figure 1C. What we are going to demonstrate is that the local resonance, as

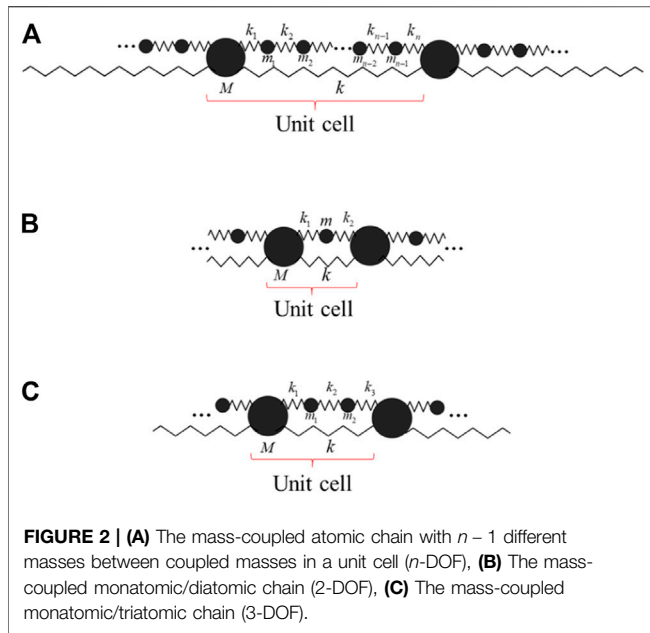


FIGURE 2 | (A) The mass-coupled atomic chain with $n-1$ different masses between coupled masses in a unit cell (n -DOF), **(B)** The mass-coupled monatomic/diatomic chain (2-DOF), **(C)** The mass-coupled monatomic/triatomic chain (3-DOF).

well as the inertial amplification-like (IA-like) bandgaps can be opened through adjusting parameters without altering system configuration (i.e., without performing mechanical cutting of certain springs or arranging the inertial amplification mechanisms).

In this work, we first obtain the governing equations of the mass-coupled atomic chain with n -degree-of-freedom (DOF) by analytical mechanics. Then, the analytical expressions of band structures, anti-resonant frequencies, and edge frequencies of passbands are deduced. In **Section 3.1**, through discussions about mass-coupled monatomic/diatomic chain, we show that LR bandgaps can be generated simply by performing parametric switching, which is characterized by an inherent transition parameter (p -value). The different bandgap behaviors of mass-coupled monatomic/triatomic chain are classified by different sets of discriminants in **Section 3.2**. Finally, the relations between the mass-coupled monatomic/triatomic chain system and a 3-DOF inertial amplification system are further discussed in **Section 3.3**.

MODEL DESCRIPTIONS AND TRANSITION CONDITIONS OF HYBRID BANDGAPS

The mass-coupled atomic chain, as illustrated in **Figure 1A**, can be generalized as a model shown in **Figure 2A**, where a polyatomic chain is coupled to a monatomic chain. There are arbitrary $n-1$ ($n \geq 2$) masses connected by n different springs between coupled masses in a unit cell. Obviously, there are n degrees of freedom in this system, the displacements of the coupled mass M_j and other masses $m_{i,j}$ ($1 \leq i \leq n-1$) are respectively marked as U_j and $u_{i,j}$ for the j -th unit cell.

The band structures of this infinite mass-coupled atomic chain can be deduced as follows. First, we list all expressions about kinetic and potential energies related to the displacements:

$$\begin{cases} T = \frac{1}{2} m_{1,j} \dot{u}_{1,j}^2 \\ V = \frac{1}{2} k_1 (u_{1,j} - U_j)^2 + \frac{1}{2} k_2 (u_{1,j} - u_{2,j})^2, \text{ for } i = 1, \end{cases} \quad (1)$$

$$\begin{cases} T = \frac{1}{2} m_{i,j} \dot{u}_{i,j}^2 \\ V = \frac{1}{2} k_i (u_{i,j} - u_{i-1,j})^2 + \frac{1}{2} k_{i+1} (u_{i,j} - u_{i+1,j})^2, \text{ for } 2 \leq i \leq n-2, \end{cases} \quad (2)$$

$$\begin{cases} T = \frac{1}{2} m_{n-1,j} \dot{u}_{n-1,j}^2 \\ V = \frac{1}{2} k_n (u_{n-1,j} - U_{j+1})^2 + \frac{1}{2} k_{n-1} (u_{n-1,j} - u_{n-2,j})^2, \text{ for } i = n-1, \end{cases} \quad (3)$$

And

$$\begin{cases} T = \frac{1}{2} M_j \dot{U}_j^2 \\ V = \frac{1}{2} k_1 (U_j - u_{1,j})^2 + \frac{1}{2} k_n (U_j - u_{n-1,j-1})^2 + \frac{1}{2} k (U_j - U_{j-1})^2 + \frac{1}{2} k (U_j - U_{j+1})^2. \end{cases} \quad (4)$$

According to the Lagrange equation for conservative systems, i.e.,

$$\frac{\partial L}{\partial \bar{u}} - \frac{d}{dt} \left(\frac{\partial L}{\partial \dot{\bar{u}}} \right) = 0, \quad (5)$$

Where $L = T - V$ is Lagrangian, \bar{u} is generalized displacement, and $\dot{\bar{u}}$ is generalized velocity, the governing equations can be derived as

$$\begin{cases} m_{1,j} \ddot{u}_{1,j} + k_1 (u_{1,j} - U_j) + k_2 (u_{1,j} - u_{2,j}) = 0 \\ m_{i,j} \ddot{u}_{i,j} + k_i (u_{i,j} - u_{i-1,j}) + k_{i+1} (u_{i,j} - u_{i+1,j}) = 0 \quad (2 \leq i \leq n-2) \\ m_{n-1,j} \ddot{u}_{n-1,j} + k_n (u_{n-1,j} - U_{j+1}) + k_{n-1} (u_{n-1,j} - u_{n-2,j}) = 0 \\ M_j \ddot{U}_j + k_1 (U_j - u_{1,j}) + k_n (U_j - u_{n-1,j-1}) + k (2U_j - U_{j-1} - U_{j+1}) = 0. \end{cases} \quad (6)$$

Then the band structures can be obtained by solving the following eigenvalue problem according to Bloch theorem (Huang et al., 2009; Hu et al., 2017; Hu et al., 2019):

$$[\mathbf{K} - \omega^2 \mathbf{M}] = 0, \quad (7)$$

Where

$$\mathbf{K} = \begin{bmatrix} 2k(1 - \cos(qa)) + k_1 + k_n & -k_1 & 0 & \cdots & 0 & -k_n e^{-iqa} \\ -k_1 & k_1 + k_2 & -k_2 & \cdots & \cdots & 0 \\ 0 & -k_2 & \ddots & \ddots & \cdots & \vdots \\ \vdots & \cdots & \ddots & \ddots & \ddots & 0 \\ 0 & \cdots & \cdots & -k_{n-2} & k_{n-2} + k_{n-1} & -k_{n-1} \\ -k_n e^{iqa} & 0 & \cdots & 0 & -k_{n-1} & k_{n-1} + k_n \end{bmatrix}, \quad (8)$$

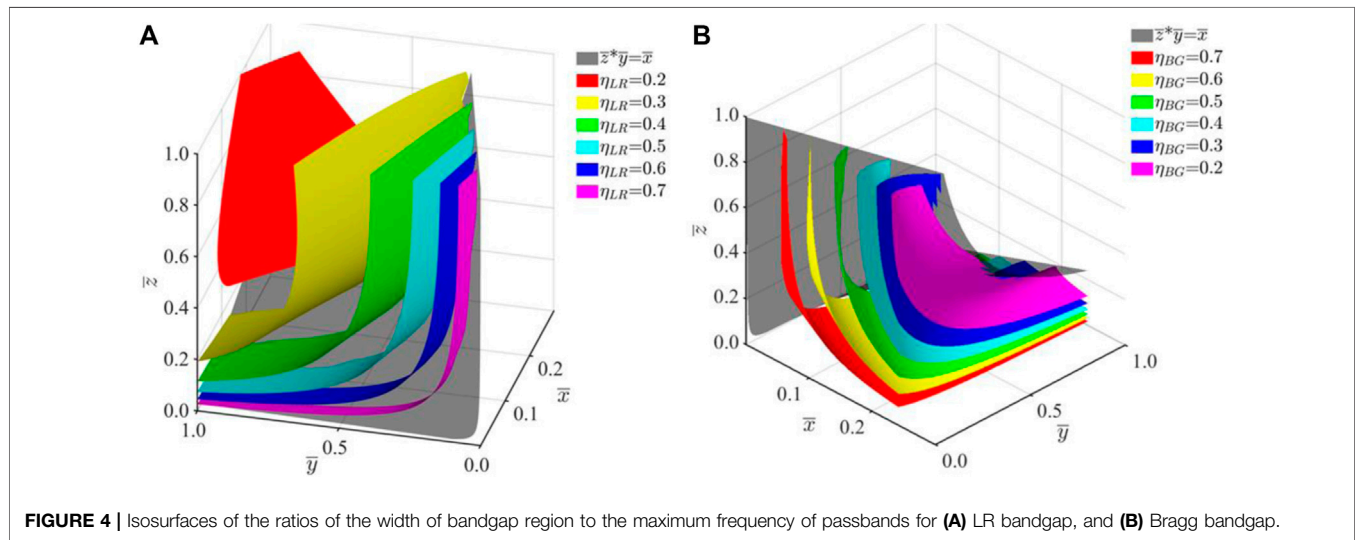
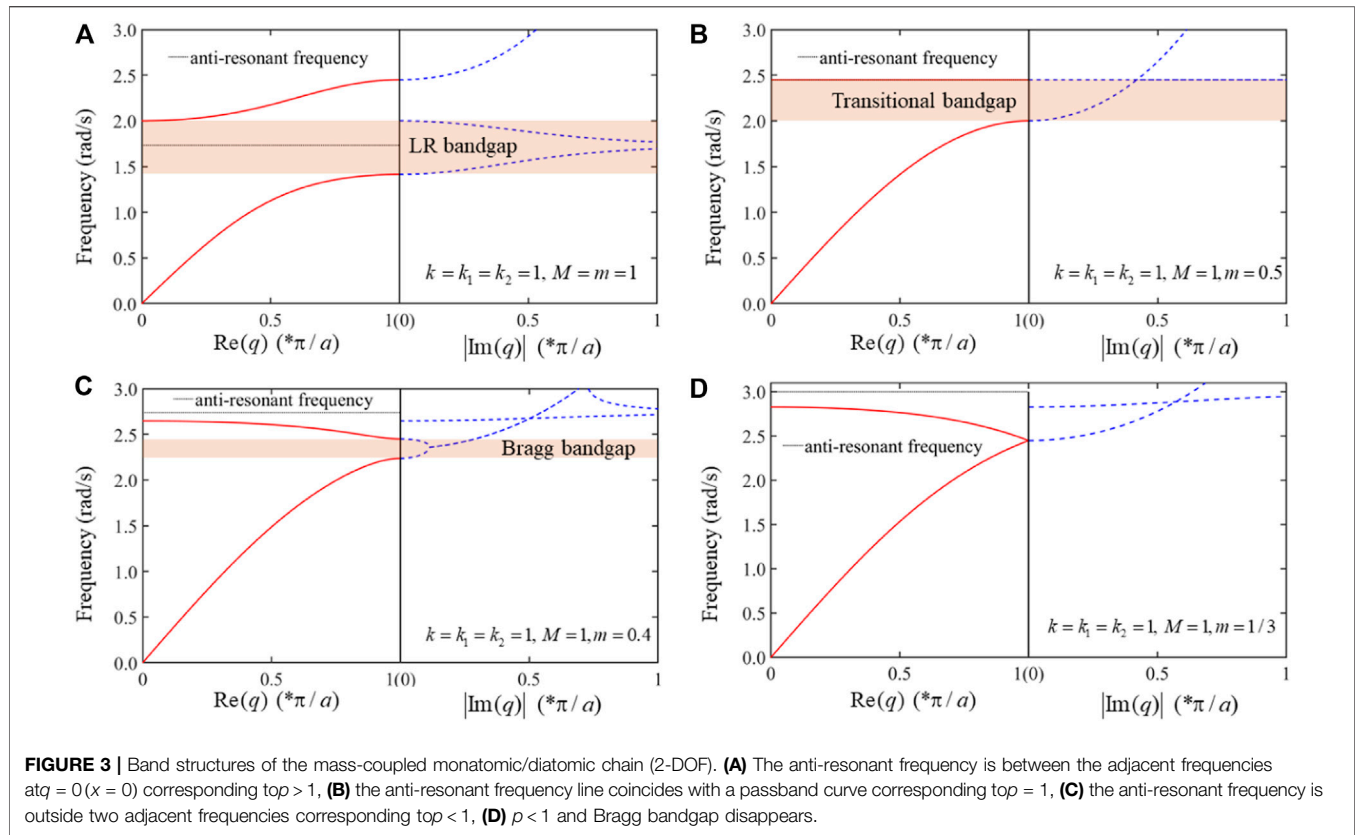
$$\mathbf{M} = \begin{bmatrix} M_j & 0 & 0 & \cdots & 0 & 0 \\ 0 & m_{1,j} & 0 & \cdots & \cdots & 0 \\ 0 & 0 & \ddots & \ddots & \cdots & \vdots \\ \vdots & \cdots & \ddots & \ddots & 0 & 0 \\ 0 & \cdots & \cdots & 0 & m_{n-2,j} & 0 \\ 0 & 0 & \cdots & 0 & 0 & m_{n-1,j} \end{bmatrix},$$

q is the Bloch wave vector, ω is circular frequency, and a is lattice constant.

The coefficient polynomial of **Eq. 7** can be expressed as

$$2x \left[\prod_{i=1}^n k_i + k \left(\prod_{i=1}^{n-1} m_i \right) \right] f_1(\omega) - \omega^2 \left(\prod_{i=1}^n m_i \right) f_2(\omega) = 0, \quad (9)$$

Where



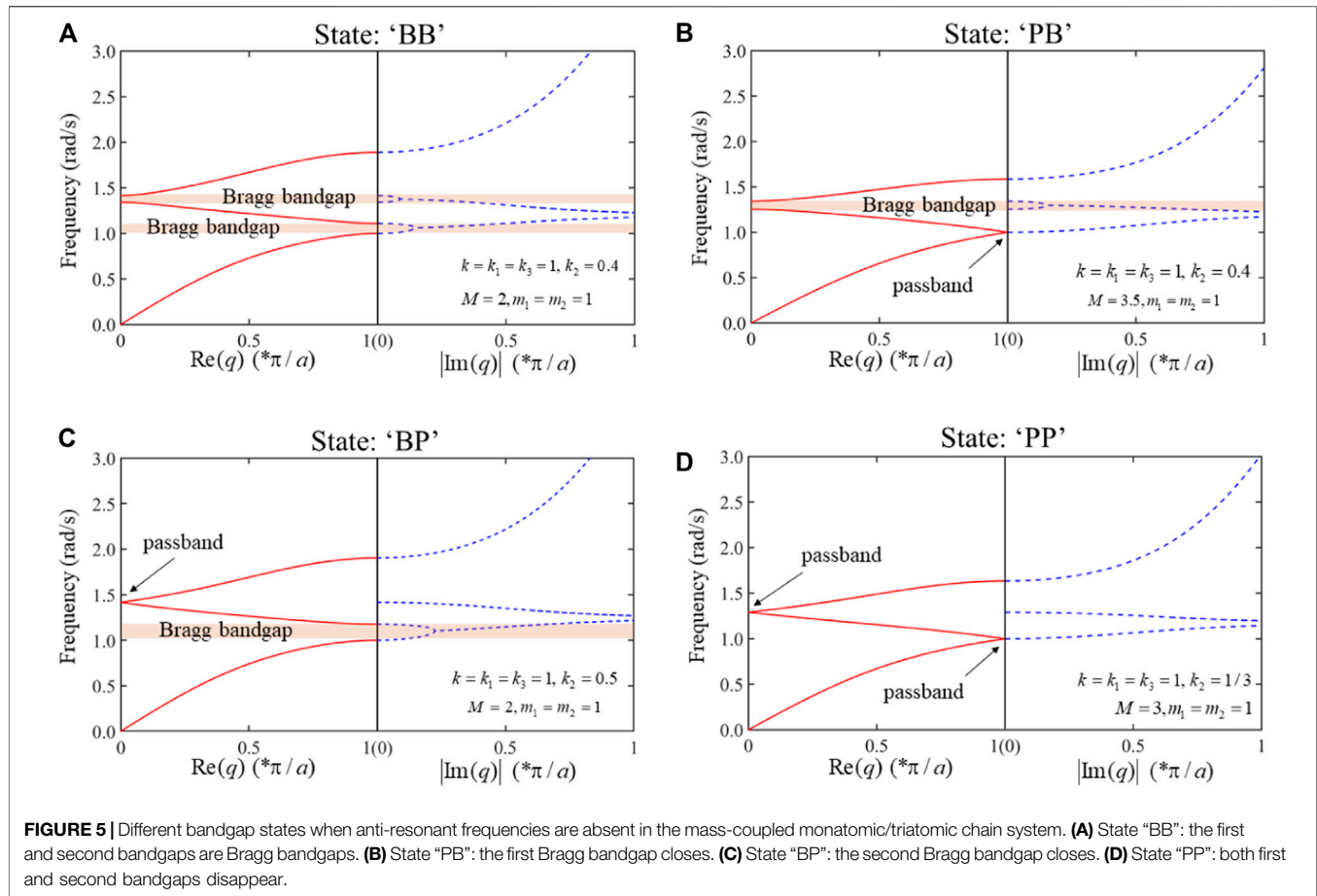
$$\begin{cases} x = 1 - \cos(qa) \\ m_i = m_{i,j} \ (1 \leq i \leq n-1), \\ m_n = M = M_j \end{cases} \quad (10)$$

And the analytical formulas of $f_1(\omega)$ and $f_2(\omega)$ are listed in **Appendix A**. Coefficient polynomial of x determines the existence of the anti-resonant frequencies as well as their values according to **Eq. 9** (Hu et al., 2017; Yilmaz et al., 2017; Bennetts et al., 2019; Hu et al., 2019; Li and Zhou, 2021).

So anti-resonant frequencies are acquired by solving the following expression:

$$\prod_{i=1}^n k_i + k \left(\prod_{i=1}^{n-1} m_i \right) f_1(\omega) = 0. \quad (11)$$

It is worth noting that in band structures any single curve of passbands is continuous when $q \in (0, \frac{\pi}{a})$ ($x \in (0, 2)$). Meanwhile,



the passbands will not intersect with the anti-resonant frequency line. According to Eq. 9, if an anti-resonant frequency solved by Eq. 11 is simultaneously the solution of edge frequency of passband, the corresponding passband will be a straight-line coinciding with this anti-resonant frequency line. Therefore, one can determine whether a bandgap is LR bandgap by comparing the roots of Eq. 11 with edge frequencies of the passbands. The edge frequencies can be obtained by Eq. 9:

$$\begin{cases} \omega^2 \left(\prod_{i=1}^n m_i \right) f_2(\omega) = 0, & x = 0 \\ 4 \left[\prod_{i=1}^n k_i + k \left(\prod_{i=1}^{n-1} m_i \right) f_1(\omega) \right] - \omega^2 \left(\prod_{i=1}^n m_i \right) f_2(\omega) = 0, & x = 2. \end{cases}$$

There is a LR bandgap around a root if the root of Eq. 11 is between the adjacent two solutions of $\omega^2 f_2(\omega) = 0$.

Based on the above inference, by comparing distributions of solutions corresponding to Eqs 11, 12, we can derive an analytical parameter (p -value) or analytical discriminants describing the transition conditions between the LR bandgaps and Bragg bandgaps. The bandgap transition p -value will be defined and its analytical expression will be given in the next section (Section 3.1). The discriminants for a monatomic/triatomic chain will also be given in the next section (Section 3.2).

RESULTS AND DISCUSSION

P -value in Mass-coupled Monatomic/Diatomic Chain

Let's first discuss the simplest 2-DOF case where a monatomic chain is coupled to a diatomic chain as illustrated in Figure 2B. According to theories in Section 2 and Eq. (A3) in Appendix A, the transition condition from the LR bandgap to Bragg bandgap can be written as

$$\sqrt{\frac{(M+m)(k_1+k_2)}{Mm}} < \sqrt{\frac{k_1k_2+kk_1+kk_2}{km}}, \quad (13)$$

i.e.,

$$p = \frac{k(k_1+k_2)(M+m)}{(k_1k_2+kk_1+kk_2)M} < 1, \quad (14)$$

Where p is defined as the bandgap transition parameter (p -value). If $p < 1$, there is a Bragg bandgap. Bragg bandgap turns into LR bandgap when $p > 1$.

The expression of p can be simplified as

$$p = 1 + \frac{\frac{k}{M} - \frac{k_1k_2}{(k_1+k_2)m}}{\frac{k}{m} + \frac{k_1k_2}{(k_1+k_2)m}} = 1 + \frac{\frac{k}{M} - \frac{k_{eff}}{m}}{\frac{k}{m} + \frac{k_{eff}}{m}}, \quad (15)$$

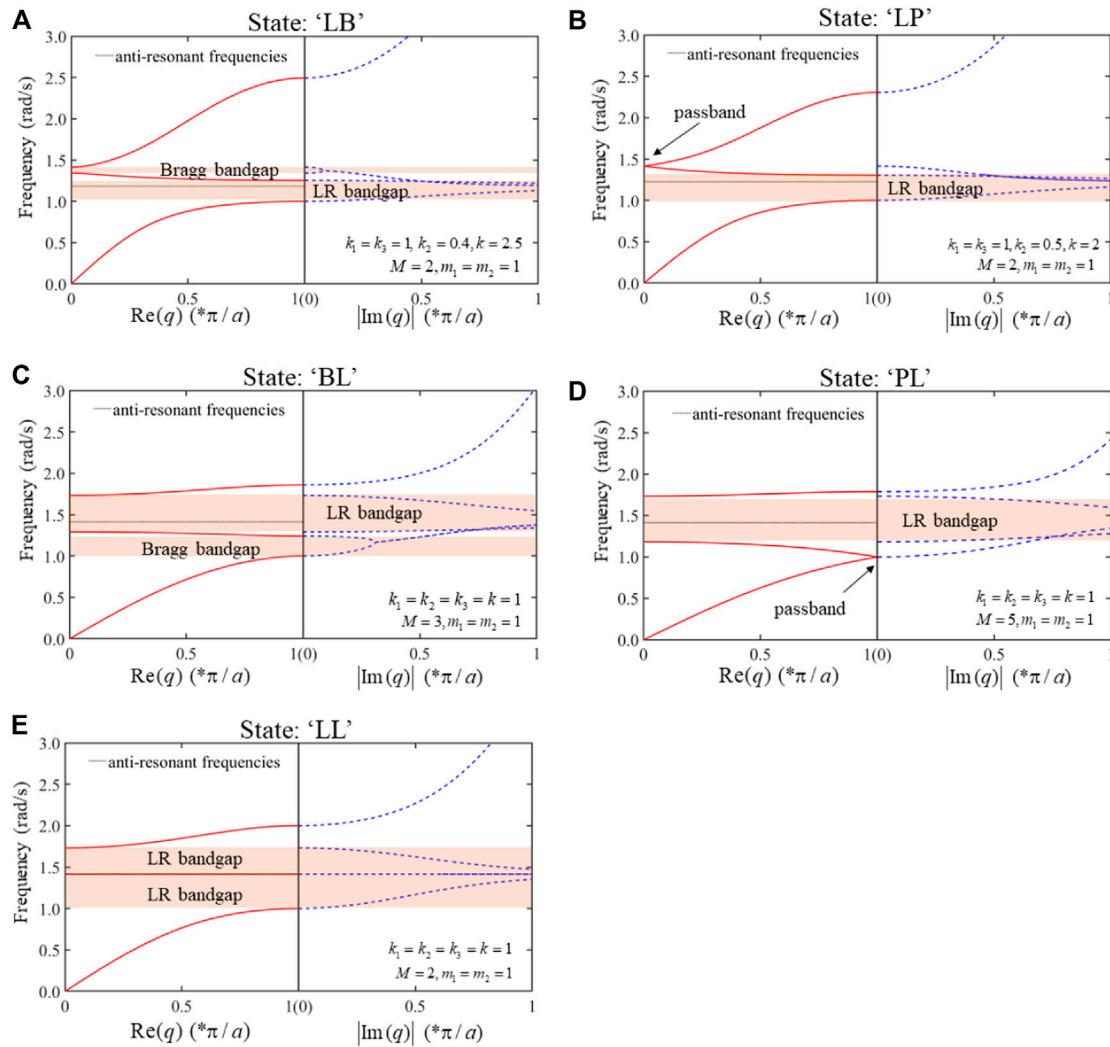


FIGURE 6 | Different bandgap states when there is only one anti-resonant frequency in the mass-coupled monatomic/triatomic chain system. **(A)** State “LB”: the first bandgap is LR bandgap and second one is Bragg bandgap. **(B)** State “LP”: the second Bragg bandgap disappears. **(C)** State “BL”: the first bandgap is Bragg bandgap and second one is LR bandgap. **(D)** State “PL”: the first Bragg bandgap has vanished and only the LR bandgap is left. **(E)** State “LL”: the anti-resonant frequency line coincides with a curve of passband, which generates an enlarged LR bandgap.

Where k_{eff} is effective stiffness. It is obvious that bandgaps can be switched to different types depending on

$$\begin{cases} \frac{k}{M} > \frac{k_{eff}}{m}, & \text{Bragg bandgap to LR bandgap} \\ \frac{k}{M} < \frac{k_{eff}}{m}, & \text{LR bandgap to Bragg bandgap} \end{cases} \quad (16)$$

In classical acoustic metamaterials with local resonators, as shown in **Figure 1B**, the value of k_{eff} is zero ($k_1 = 0$ or $k_2 = 0$), on the contrary, we get $k = 0$ in a Bragg system (see **Figure 1C**).

Figure 3 shows the transition process from LR bandgap to Bragg bandgap with respect to the change of p -value. If $p > 1$, the anti-resonant frequency is between the adjacent frequencies of passbands at $q = 0$ ($x = 0$), which leads to the occurrence of an

anti-resonant peak in the bandgap region. Bragg bandgap appears when the anti-resonant frequency is outside the adjacent passband frequencies corresponding to $p < 1$. As shown in **Figure 3D**, Bragg bandgap will vanish in some situations due to the fact that the spring with stiffness k acts as a waveguide that counteracts and diminishes the Bragg scattering effect compared to the Bragg system.

In addition, when there is a LR bandgap, the ratio of the width of bandgap region to the maximum frequency of passbands in band structure can be calculated by

$$\eta_{LR} = \frac{\sqrt{2} - \sqrt{1 + \frac{4mk}{(M+m)(k_1+k_2)}} - \sqrt{\left(1 + \frac{4mk}{(M+m)(k_1+k_2)}\right)^2 - \frac{16Mm[k_1k_2+k(k_1+k_2)]}{(M+m)^2(k_1+k_2)^2}}}{\sqrt{\left(1 + \frac{4mk}{(M+m)(k_1+k_2)}\right)^2 - \frac{16Mm[k_1k_2+k(k_1+k_2)]}{(M+m)^2(k_1+k_2)^2}} + \sqrt{\left(1 + \frac{4mk}{(M+m)(k_1+k_2)}\right)^2 - \frac{16Mm[k_1k_2+k(k_1+k_2)]}{(M+m)^2(k_1+k_2)^2}}} \quad (17)$$

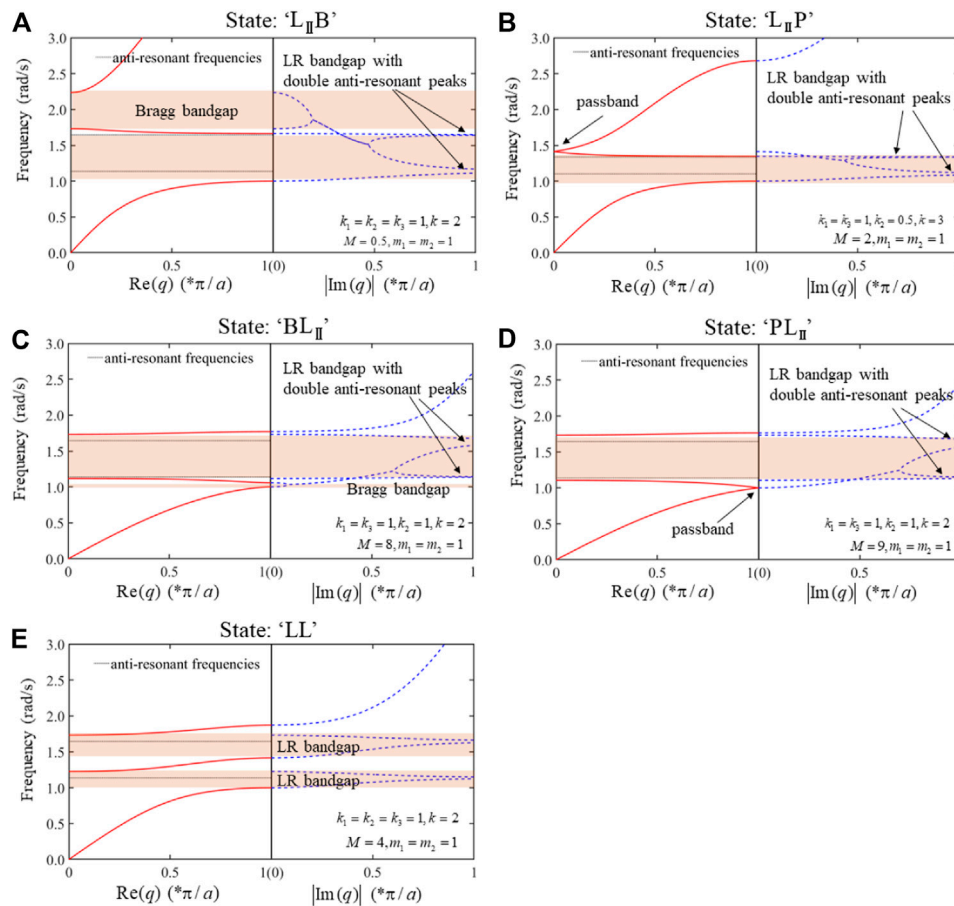


FIGURE 7 | Different bandgap states when there are two anti-resonant frequencies in the mass-coupled monatomic/triatomic chain system. **(A)** State “L_{II}B”: the first bandgap is a LR bandgap with double anti-resonant peaks and second one is Bragg bandgap. **(B)** State “L_{II}P”: the second Bragg bandgap becomes a passband. **(C)** State “BL_{II}”: Bragg bandgap and LR bandgap with double anti-resonant peaks. **(D)** State “PL_{II}”: the first Bragg bandgap vanishes. **(E)** State “LL”: there are two LR bandgaps.

But for Bragg bandgap, the ratio becomes

$$\eta_{BG} = \frac{\sqrt{1 + \frac{4mk}{(M+m)(k_1+k_2)}} + \sqrt{\left(1 + \frac{4mk}{(M+m)(k_1+k_2)}\right)^2 - \frac{16Mm[k_1k_2 + k(k_1+k_2)]}{(M+m)^2(k_1+k_2)^2}}}{\sqrt{2}} \quad (18)$$

Noting that Eq. 17 or Eq. 18 can be expressed by three independent variables,

$$\bar{x} = \frac{k_1k_2}{(k_1+k_2)^2}, \bar{y} = \frac{k}{(k_1+k_2)}, \bar{z} = \frac{m}{M}, \quad (19)$$

So Eqs 17, 18 can be rewritten as

$$\left\{ \begin{aligned} \eta_{LR} &= \frac{\sqrt{2}\sqrt{1+\bar{z}} - \sqrt{1+\bar{z}+4\bar{z}\bar{y}} - \sqrt{(1+\bar{z}+4\bar{z}\bar{y})^2 - 16\bar{z}(\bar{x}+\bar{y})}}{\sqrt{1+\bar{z}+4\bar{z}\bar{y}} + \sqrt{(1+\bar{z}+4\bar{z}\bar{y})^2 - 16\bar{z}(\bar{x}+\bar{y})}} \\ \eta_{BG} &= \frac{\sqrt{1+\bar{z}+4\bar{z}\bar{y}} + \sqrt{(1+\bar{z}+4\bar{z}\bar{y})^2 - 16\bar{z}(\bar{x}+\bar{y})}}{-\sqrt{1+\bar{z}+4\bar{z}\bar{y}} - \sqrt{(1+\bar{z}+4\bar{z}\bar{y})^2 - 16\bar{z}(\bar{x}+\bar{y})}} \end{aligned} \right. \quad (20)$$

The discriminant of Eq. 16 turns to

$$\left\{ \begin{aligned} \bar{z}\bar{y} > \bar{x}, & \text{Bragg bandgap to LR bandgap} \\ \bar{z}\bar{y} < \bar{x}, & \text{LR bandgap to Bragg bandgap} \end{aligned} \right. \quad (21)$$

Hence the bandgap transition condition is separated by a hyperbolic paraboloid. The isosurfaces of ratios for LR bandgap and Bragg bandgap are plotted in Figure 4 respectively. One can

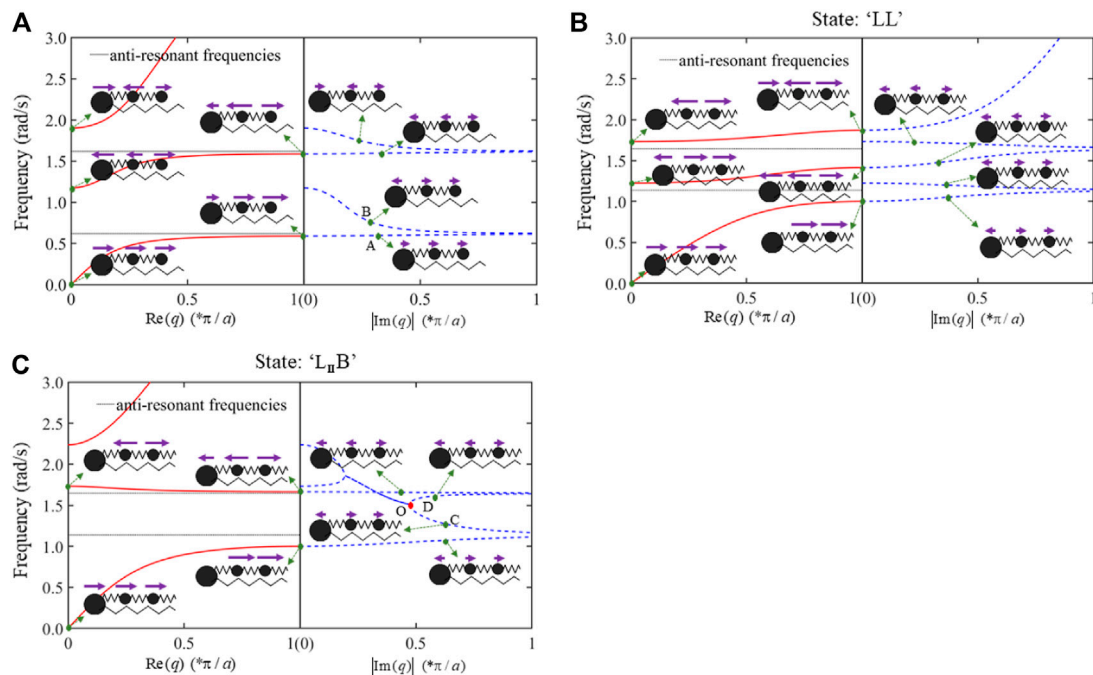


FIGURE 8 | Vibration modes of a unit cell at certain points in band structures for the (A) LR acoustic metamaterial with two resonators in series ($k_1 = k_2 = 1$, $k_3 = 0$, $k = 2$, $M = 0.5$, $m_1 = m_2 = 1$), (B) State “LL” ($k_1 = k_2 = k_3 = 1$, $k = 2$, $M = 4$, $m_1 = m_2 = 1$), and (C) State “L_BB” ($k_1 = k_2 = k_3 = 1$, $k = 2$, $M = 0.5$, $m_1 = m_2 = 1$). The purple arrows indicate the vibration directions and the lengths of the arrows represent the relative amplitudes. The corresponding amplitudes are zero when there are no arrows above the masses.

construct a wide bandgap at low frequency through changing the material parameters according to the isosurfaces.

Bandgap States of Mass-coupled Monatomic/triatomic Chain Classified by Discriminants

In this section, we study the 3-DOF mass-coupled monatomic/triatomic chain as shown in **Figure 2C**. Here the transition parameter p -value will turn to several sets of discriminants determining the transition conditions between LR bandgaps and Bragg bandgaps. We note that as the number of degrees of freedom further increases, the complexity of the problem sharply arises despite the number of material parameters only increase by two compared to the 2-DOF system.

According to **Eqs 9, 11, 12** and **Eq. (A4)**, the equations about nonzero edge frequencies of passbands can be obtained,

$$Mm_1m_2\omega^4 - ((k_1 + k_3)m_1m_2 + M(k_1m_2 + k_2(m_1 + m_2) + k_3m_1))\omega^2 + (k_1k_2 + k_1k_3 + k_2k_3)(m_1 + m_2 + M) = 0 \quad (\text{at } x = 0), \quad (22)$$

$$Mm_1m_2\omega^6 - [(k_1 + k_3 + 4k)m_1m_2 + M(k_1m_2 + k_2(m_1 + m_2) + k_3m_1)]\omega^4 + [(k_1k_2 + k_1k_3 + k_2k_3)(m_1 + m_2 + M) + 4k(k_1m_2 + k_2(m_1 + m_2) + k_3m_1)]\omega^2 - 4(k_1k_2k_3 + k(k_1k_2 + k_1k_3 + k_2k_3)) = 0 \quad (\text{at } x = 2), \quad (23)$$

And anti-resonant frequencies can be acquired by

$$m_1m_2\omega^4 - (k_1m_2 + k_2(m_1 + m_2) + k_3m_1)\omega^2 + \left(\frac{k_1k_2k_3}{k} + (k_1k_2 + k_1k_3 + k_2k_3)\right) = 0. \quad (24)$$

The distribution of solutions of these equations are discussed in detail in **Appendix B**. There are total 14 different bandgap behaviors, referred to as bandgap states, in our mass-coupled monatomic/triatomic chain according to **Eq. (B16)**. For the sake of convenience, we use “L,” “B,” and “P” to represent the normal LR bandgap, the Bragg bandgap, and the passband, respectively. When the values of anti-resonant frequencies solved by **Eq. 24** are conjugate imaginary numbers (i.e., anti-resonant frequencies don’t actually exist), there are four different states as shown in **Figure 5**. The states from (a) to (d) correspond to sets of discriminants from (1) to (4) in **Eq. (B16)**, respectively. Obviously, there are no LR bandgaps due to non-existence of anti-resonant frequencies.

Figure 6 shows five bandgap states, corresponding to sets of discriminants from (5) to (9) in **Eq. (B16)**, where there is only one anti-resonant frequency. In **Figure 6A**, the anti-resonant frequency lies between edge frequencies of passbands, which leads to the formation of LR bandgap. The second bandgap can turn into LR bandgap with tuning of parameters as shown in **Figures 6C,D**. A widened LR bandgap is generated in **Figure 6E** due to coincidence of the anti-resonant frequency line and a dispersion curve.

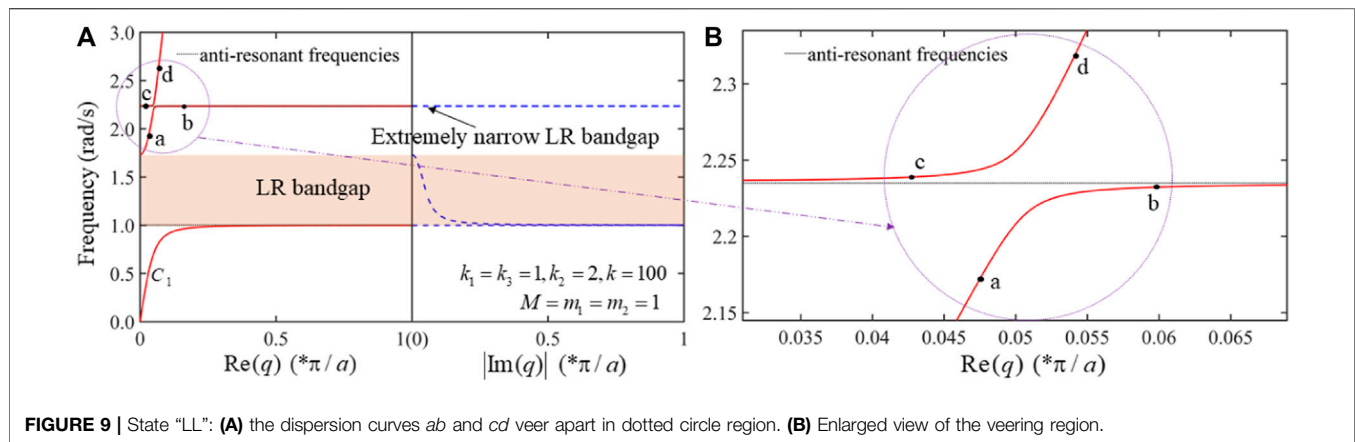


FIGURE 9 | State “LL”: (A) the dispersion curves ab and cd veer apart in dotted circle region. (B) Enlarged view of the veering region.

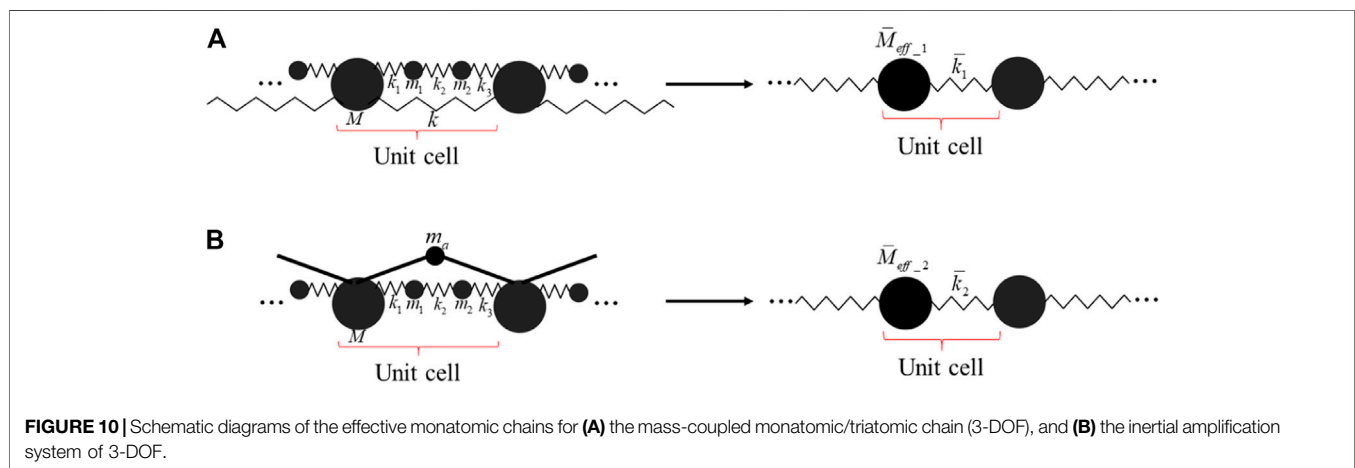


FIGURE 10 | Schematic diagrams of the effective monatomic chains for (A) the mass-coupled monatomic/triatomic chain (3-DOF), and (B) the inertial amplification system of 3-DOF.

When there are two anti-resonant frequencies, other five bandgap states arise as shown in **Figure 7**, corresponding to sets of discriminants from (10) to (14) in **Eq. (B16)**. A LR bandgap with double anti-resonant peaks is observed in **Figures 7A–D**. In order to distinguish the LR bandgap with double anti-resonant peaks from the normal LR bandgap, which is labeled as “L,” the former is represented by the symbol “L_{II}.” In addition, to further reveal the differences between the LR bandgap with double anti-resonant peaks and a normal one, vibration modes of a unit cell at certain points in band structures are plotted in **Figure 8**. In the LR metamaterial with two resonators in series, the anti-resonant frequencies separate two different vibration modes as shown in **Figure 8A**. Although the vibrations are attenuated and weak, all the masses vibrate in one direction at point A while the vibration direction of the coupled mass is different from those of the resonators at point B. In the state “LL” of the monatomic/triatomic chain system, the relative vibration directions of the masses are the same on both sides of the gap separated by the anti-resonant frequency as shown in **Figure 8B**. In the LR bandgap region with double anti-resonant peaks as shown in **Figure 8C**, two dispersion curves CO and DO that represent evanescent waves come close as frequency increases until the two curves lock

together at point O , forming a pair of attenuating oscillatory waves, which later unlock into a pair of evanescent waves (Mace and Manconi, 2012). The relative vibration directions of the masses change at point O , so the vibration modes will ultimately change while passing through the LR bandgap region with double anti-resonant peaks.

In addition, the weak coupling phenomenon, known as veering that occurs when branches of the dispersion curves interact in coupled periodic waveguide system, is also observed in band structures in **Figure 9** (Mace and Manconi, 2012). As shown in **Figure 9**, two dispersion curves ab and cd come close together as frequency increases then the curves veer apart, which results in an extremely narrow LR bandgap.

Relations Between the Mass-coupled Monatomic/triatomic Chain and Inertial Amplification System

In the previous section, we find that under certain parameters there is a double anti-resonant peak in the LR bandgap region of the mass-coupled monatomic/triatomic chain, which is also a representative characteristic of the bandgap behaviors possessed in a periodic structure with inertial amplification mechanisms (Frandsen et al., 2016). Next, we will show that IA-like bandgaps

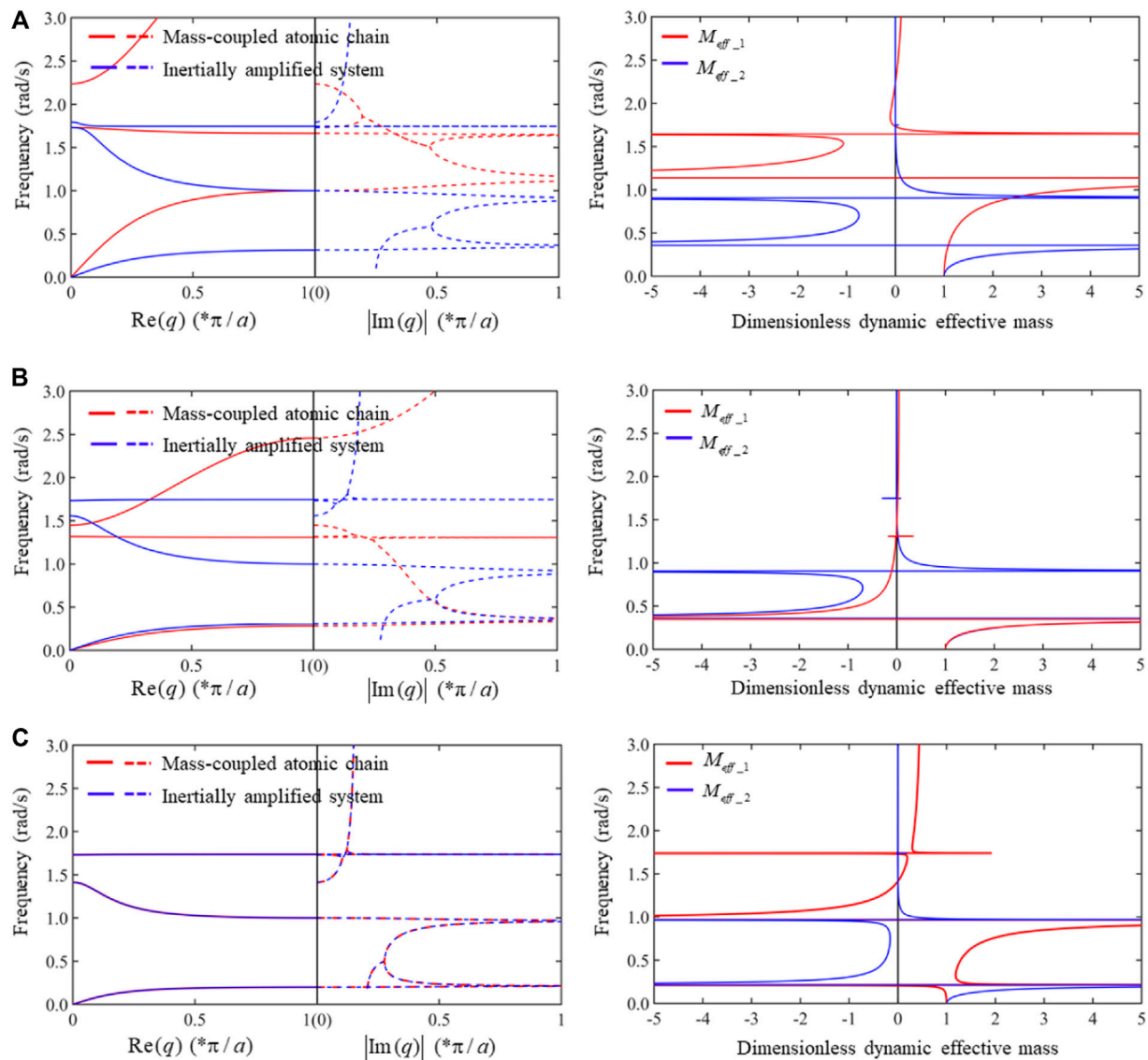


FIGURE 11 | Band structures of the mass-coupled monatomic/triatomic chains and inertial amplification systems of 3-DOF and their corresponding dimensionless dynamic effective masses. The parameters are listed as follows: **(A)** $k_1 = k_2 = k_3 = 1, k = 2, M = 0.5, m_1 = m_2 = 1, m_a = 0.4, \theta = \pi/18$, **(B)** $k_1 = k_3 = k = 1, k_2 = 10, M = 1, m_1 = 15, m_2 = 10$ for the mass-coupled atomic chain and $k_1 = k_2 = k_3 = 1, M = m_1 = m_2 = 1, m_a = 0.4, \theta = \pi/18$ for the inertial amplification system, **(C)** $k_1 = k_2 = k_3 = 1, k = \frac{1}{4}(1 - \cot^2(\pi/18))\omega^2, M = 2, m_1 = m_2 = 1$ for the mass-coupled atomic chain and $k_1 = k_2 = k_3 = 1, M = m_1 = m_2 = 1, m_a = 1, \theta = \pi/18$ for the inertial amplification system.

can exist in band structures of mass-coupled monatomic/triatomic chain.

As shown in **Figure 10B**, in a classical 3-DOF inertial amplification system (Yilmaz et al., 2017), an added mass m_a is connected to the coupled masses by two massless rigid rods in a unit cell with a very small angle θ between the rigid rods and the horizontal line. The characteristic determinant of band structure is

$$\begin{vmatrix} k_1 + k_3 - \left(M + \frac{1}{2}m_a[1 + \cos qa + \cot^2 \theta(1 - \cos qa)]\right)\omega^2 & -k_1 & -k_3 e^{-iqa} \\ -k_1 & k_1 + k_2 - m_1 \omega^2 & -k_2 \\ -k_3 e^{iqa} & -k_2 & k_2 + k_3 - m_2 \omega^2 \end{vmatrix} = 0, \quad (25)$$

Which can be rewritten as

$$\begin{aligned} & \left[M + \frac{1}{2}m_a(1 + \cot^2 \theta)\right][m_1 m_2 \omega^6 - (k_1 m_2 + k_2(m_1 + m_2) \\ & + k_3 m_1)\omega^4 + (k_1 k_2 + k_1 k_3 + k_2 k_3)\omega^2] - (k_1 + k_3)m_1 m_2 \omega^4 \\ & + (k_1 k_2 + k_1 k_3 + k_2 k_3)(m_1 + m_2)\omega^2 - 2k_1 k_2 k_3 \\ & + \left(\frac{1}{2}m_a(1 - \cot^2 \theta)[m_1 m_2 \omega^6 - (k_1 m_2 + k_2(m_1 + m_2) \right. \\ & \left. + k_3 m_1)\omega^4 + (k_1 k_2 + k_1 k_3 + k_2 k_3)\omega^2] + 2k_1 k_2 k_3\right) \cos qa = 0. \end{aligned} \quad (26)$$

The mass-coupled atomic chain and the inertial amplification system can be simplified as effective monatomic chains. The effective stiffness and mass for the mass-coupled atomic chain are listed as

$$\left\{ \begin{array}{l} \bar{k}_1 = \frac{k_1 k_2 k_3}{(k_1 k_2 + k_1 k_3 + k_2 k_3)} + k \\ \bar{M}_{eff-1} = \frac{M m_1 m_2 \omega^4 - [M(k_1 m_2 + k_2(m_1 + m_2) + k_3 m_1) + (k_1 + k_3) m_1 m_2] \omega^2 + (k_1 k_2 + k_1 k_3 + k_2 k_3)(M + m_1 + m_2)}{k m_1 m_2 \omega^4 - k(k_1 m_2 + k_2(m_1 + m_2) + k_3 m_1) \omega^2 + k(k_1 k_2 + k_1 k_3 + k_2 k_3) + k_1 k_2 k_3} \bar{k}_1 \end{array} \right. \quad (27)$$

And

$$\left\{ \begin{array}{l} \bar{k}_2 = \frac{k_1 k_2 k_3}{k_1 k_2 + k_1 k_3 + k_2 k_3} \\ \bar{M}_{eff-2} = \frac{(M + m_a) m_1 m_2 \omega^4 - [(M + m_a)(k_1 m_2 + k_2(m_1 + m_2) + k_3 m_1) + (k_1 + k_3) m_1 m_2] \omega^2 + (k_1 k_2 + k_1 k_3 + k_2 k_3)(M + m_a + m_1 + m_2)}{\frac{1}{4} m_a (1 - \cot^2 \theta) [m_1 m_2 \omega^6 - (k_1 m_2 + k_2(m_1 + m_2) + k_3 m_1) \omega^4 + (k_1 k_2 + k_1 k_3 + k_2 k_3) \omega^2] + k_1 k_2 k_3} \bar{k}_2 \end{array} \right. \quad (28)$$

For the inertial amplification system. The dimensionless dynamic effective masses are

$$\left\{ \begin{array}{l} M_{eff-1} = \frac{\bar{M}_{eff-1}}{M + m_1 + m_2} \\ M_{eff-2} = \frac{\bar{M}_{eff-2}}{M + m_a + m_1 + m_2} \end{array} \right. \quad (29)$$

Besides double anti-resonant peaks, the mass-coupled atomic chain can also offer high attenuation in the bandgap regions and similar width of bandgaps compared to the inertial amplification system by adjusting material parameters (see **Figure 11A**). As shown in **Figures 11A,B**, a wide bandgap in low frequency can also be opened in mass-coupled atomic chain.

In fact, the band structures of the mass-coupled atomic chain can be exactly the same as that of an inertial amplification system through introducing a negative dynamic stiffness k , i.e., let

$$\left\{ \begin{array}{l} k = \frac{1}{4} m_a (1 - \cot^2 \theta) \omega^2 \\ \bar{M} = M + m_a \end{array} \right. \quad (30)$$

As seen in **Figure 11C**, the band structures are identical for these two atomic chains. The effective dynamic masses are not exactly the same because the effective stiffnesses are different when these two systems are simplified to monatomic chains according to **Eqs 27, 28**. Thus far, we have shown that IA-like bandgaps can exist in band structures of mass-coupled monatomic/triatomic chain.

CONCLUSION

In this work, we propose an acoustic metamaterial formed by two coupled Bragg atomic chains that can possess various bandgap behaviors through the adjustment of parameters. The transition condition between LR bandgaps and Bragg bandgaps in the mass-coupled monatomic/diatomic chain can be characterized by an analytical transition parameter, referred to as p -value. If $p < 1$, there is a Bragg bandgap, but the Bragg bandgap turns into LR bandgap when $p > 1$. The ratio of the bandgap width to the maximum frequency of passbands is determined by three independent variables and the bandgap transition condition is separated by a hyperbolic paraboloid. A wide bandgap at low frequency can be constructed through changing the material parameters according to the isosurfaces.

The transition p -value turns to several sets of discriminants when considering bandgap states for mass-coupled monatomic/triatomic chain due to the increase of the degrees of freedom. After careful classification, we find that there are 14 different sets of discriminants, which correspond to 14 possible bandgap states. In addition, the weak coupling phenomenon termed veering which occurs in coupled periodic elastic systems is observed in the band structures. The veering phenomenon can be used to construct an extremely narrow LR bandgap. IA-like bandgaps can be opened by adjusting parameters without requirement of changing structural topological properties. Moreover, through coupling masses by a negative dynamic stiffness spring, the band structure of mass-coupled monatomic/triatomic chain system is equivalent to that of the 3-DOF inertial-amplification periodic system.

DATA AVAILABILITY STATEMENT

The raw data supporting the conclusions of this article will be made available by the authors, without undue reservation.

AUTHOR CONTRIBUTIONS

SX and K-CC conceived and designed the main ideas together; SX, ZX, and K-CC performed theoretical analysis; SX and K-CC wrote the paper draft. All authors conducted subsequent improvements to the manuscript.

FUNDING

Financial support from the National Natural Science Foundation of China (No. 11972318) and the Opening Project of State Key Laboratory for Strength and Vibration of Mechanical Structures (No. SV2020-KF-16), Xi'an Jiaotong University is gratefully acknowledged.

REFERENCES

- Al Ba'ba'a, H., Nouh, M., and Singh, T. (2019). Dispersion and Topological Characteristics of Permutative Polyatomic Phononic Crystals. *Proc. R. Soc. A: Math. Phys. Eng. Sci.* 475 2226. doi:10.1098/rspa.2019.0022
- Attarzadeh, M. A., Al Ba'ba'a, H., and Nouh, M. (2018). On the Wave Dispersion and Non-reciprocal Power Flow in Space-Time Traveling Acoustic Metamaterials. *Appl. Acoust.* 133, 210–214. doi:10.1016/j.apacoust.2017.12.028
- Bennetts, L. G., Peter, M. A., Dylejko, P., and Skvortsov, A. (2019). Effective Properties of Acoustic Metamaterial Chains with Low-Frequency Bandgaps Controlled by the Geometry of Lightweight Mass-Link Attachments. *J. Sound Vibration* 456, 1–12. doi:10.1016/j.jsv.2019.05.022
- Deymier, P. A. (2013). *Acoustic Metamaterials and Phononic Crystals*. Berlin: Springer Science and Business Media.
- Fang, N., Xi, D., Xu, J., Ambati, M., Srituravanich, W., Sun, C., et al. (2006). Ultrasonic Metamaterials with Negative Modulus. *Nat. Mater* 5 (6), 452–456. doi:10.1038/nmat1644
- Fang, X., Wen, J., Yin, J., and Yu, D. (2016). Wave Propagation in Nonlinear Metamaterial Multi-Atomic Chains Based on Homotopy Method. *AIP Adv.* 6 (12), 121706. doi:10.1063/1.4971761
- Frandsen, N. M. M., Bilal, O. R., Jensen, J. S., and Hussein, M. I. (2016). Inertial Amplification of Continuous Structures: Large Band Gaps from Small Masses. *J. Appl. Phys.* 119 (12), 124902. doi:10.1063/1.4944429
- Ganesh, R., and Gonella, S. (2015). From Modal Mixing to Tunable Functional Switches in Nonlinear Phononic Crystals. *Phys. Rev. Lett.* 114 (5), 054302. doi:10.1103/PhysRevLett.114.054302
- Hofmann, P. (2015). *Solid State Physics: An Introduction*. Hoboken, NJ: John Wiley & Sons.
- Hu, G., Tang, L., Das, R., Gao, S., and Liu, H. (2017). Acoustic Metamaterials with Coupled Local Resonators for Broadband Vibration Suppression. *AIP Adv.* 7, 2. doi:10.1063/1.4977559
- Hu, G., Tang, L., Xu, J., Lan, C., and Das, R. (2019). Metamaterial with Local Resonators Coupled by Negative Stiffness Springs for Enhanced Vibration Suppression. *J. Appl. Mech.* 86, 8. doi:10.1115/1.4043827
- Huang, G. L., and Sun, C. T. (2010). Band Gaps in a Multiresonator Acoustic Metamaterial. *J. Vibration Acoust.* 132, 3. doi:10.1115/1.4000784
- Huang, H. H., and Sun, C. T. (2012). Anomalous Wave Propagation in a One-Dimensional Acoustic Metamaterial Having Simultaneously Negative Mass Density and Young's Modulus. *The J. Acoust. Soc. America* 132 (4), 2887–2895. doi:10.1121/1.4744977
- Huang, H. H., Sun, C. T., and Huang, G. L. (2009). On the Negative Effective Mass Density in Acoustic Metamaterials. *Int. J. Eng. Sci.* 47 (4), 610–617. doi:10.1016/j.jengsci.2008.12.007
- Jin, Y., Pennec, Y., Bonello, B., Honarvar, H., Dobrzynski, L., Djafari-Rouhani, B., et al. (2021). Physics of Surface Vibrational Resonances: Pillared Phononic Crystals, Metamaterials, and Metasurfaces. *Rep. Prog. Phys.* 84, 8. doi:10.1088/1361-6633/abdab8
- Khelif, A., and Adibi, A. (2015). *Phononic Crystals*. Berlin: Springer.
- Kittel, C., McEuen, P., and McEuen, P. (1996). *Introduction to Solid State Physics*. New York, NY: Wiley.
- Kundu, T., Nouh, M., Aldraihem, O., and Baz, A. (2014). Metamaterial Structures with Periodic Local Resonances. San Diego, CA: Health Monitoring of Structural and Biological Systems.
- Lazarov, B. S., and Jensen, J. S. (2007). Low-frequency Band Gaps in Chains with Attached Non-linear Oscillators. *Int. J. Non-Linear Mech.* 42 (10), 1186–1193. doi:10.1016/j.ijnonlinmec.2007.09.007
- Li, J., and Chan, C. T. (2004). Double-negative Acoustic Metamaterial. *Phys. Rev. E Stat. Nonlin Soft Matter Phys.* 70 (5 Pt 2), 055602. doi:10.1103/PhysRevE.70.055602
- Li, Y., and Zhou, W. (2021). Bandgap and Vibration Transfer Characteristics of Scissor-like Periodic Metamaterials. *J. Appl. Phys.* 130 (2). doi:10.1063/5.0047119
- Liu, Y., Su, X., and Sun, C. T. (2015). Broadband Elastic Metamaterial with Single Negativity by Mimicking Lattice Systems. *J. Mech. Phys. Sol.* 74, 158–174. doi:10.1016/j.jmps.2014.09.011
- Liu, Z., Zhang, X., Mao, Y., Zhu, Y. Y., Yang, Z., Chan, C. T., et al. (2000). Locally Resonant Sonic Materials. *Science* 289 (5485), 1734–1736. doi:10.1126/science.289.5485.1734
- Mace, B. R., and Manconi, E. (2012). Wave Motion and Dispersion Phenomena: Veering, Locking and strong Coupling Effects. *J. Acoust. Soc. America* 131 (2), 1015–1028. doi:10.1121/1.3672647
- Muhammad and Lim, C. W. (2019). Elastic Waves Propagation in Thin Plate Metamaterials and Evidence of Low Frequency Pseudo and Local Resonance Bandgaps. *Phys. Lett. A* 383 (23), 2789–2796. doi:10.1016/j.physleta.2019.05.039
- Narisetti, R. K., Leamy, M. J., and Ruzzene, M. (2010). A Perturbation Approach for Predicting Wave Propagation in One-Dimensional Nonlinear Periodic Structures. *J. Vibration Acoust.* 132 (3). doi:10.1115/1.4000775
- Pal, R. K., Vila, J., Leamy, M., and Ruzzene, M. (2018). Amplitude-dependent Topological Edge States in Nonlinear Phononic Lattices. *Phys. Rev. E* 97 (3-1), 032209. doi:10.1103/PhysRevE.97.032209
- Porubov, A. V., and Andrianov, I. V. (2013). Nonlinear Waves in Diatomic Crystals. *Wave Motion* 50 (7), 1153–1160. doi:10.1016/j.wavemoti.2013.03.009
- Pratapa, P. P., Suryanarayana, P., and Paulino, G. H. (2018). Bloch Wave Framework for Structures with Nonlocal Interactions: Application to the Design of Origami Acoustic Metamaterials. *J. Mech. Phys. Sol.* 118, 115–132. doi:10.1016/j.jmps.2018.05.012
- Taniker, S., and Yilmaz, C. (2013). Phononic Gaps Induced by Inertial Amplification in BCC and FCC Lattices. *Phys. Lett. A* 377 (31-33), 1930–1936. doi:10.1016/j.physleta.2013.05.022
- Vila, J., Pal, R. K., Ruzzene, M., and Trainiti, G. (2017). A Bloch-Based Procedure for Dispersion Analysis of Lattices with Periodic Time-Varying Properties. *J. Sound Vibration* 406, 363–377. doi:10.1016/j.jsv.2017.06.011
- Yao, S., Zhou, X., and Hu, G. (2008). Experimental Study on Negative Effective Mass in a 1D Mass-spring System. *New J. Phys.* 10, 4. doi:10.1088/1367-2630/10/4/043020
- Yilmaz, C., and Hulbert, G. M. (2017). “Dynamics of Locally Resonant and Inertially Amplified Lattice Materials,” in *Dynamics of Lattice Materials*. Editors A. S. Phani and M. I. Hussein, 233–258. doi:10.1002/9781118729588.ch11
- Yilmaz, C., Hulbert, G. M., and Kikuchi, N. (2007). Phononic Band Gaps Induced by Inertial Amplification in Periodic media. *Phys. Rev. B* 76, 5. doi:10.1103/physrevb.76.054309
- Yilmaz, C., and Hulbert, G. M. (2010). Theory of Phononic Gaps Induced by Inertial Amplification in Finite Structures. *Phys. Lett. A* 374 (34), 3576–3584. doi:10.1016/j.physleta.2010.07.001
- Yu, D., Liu, Y., Wang, G., Zhao, H., and Qiu, J. (2006). Flexural Vibration Band Gaps in Timoshenko Beams with Locally Resonant Structures. *J. Appl. Phys.* 100, 12. doi:10.1063/1.2400803
- Zhu, R., Liu, X. N., Hu, G. K., Sun, C. T., and Huang, G. L. (2014). A Chiral Elastic Metamaterial Beam for Broadband Vibration Suppression. *J. Sound Vibration* 333 (10), 2759–2773. doi:10.1016/j.jsv.2014.01.009
- Zucker, I. J. (2016). 92.34 The Cubic Equation - A New Look at the Irreducible Case. *Math. Gaz.* 92 (524), 264–268. doi:10.1017/s0025557200183135

Conflict of Interest: The authors declare that the research was conducted in the absence of any commercial or financial relationships that could be construed as a potential conflict of interest.

Publisher's Note: All claims expressed in this article are solely those of the authors and do not necessarily represent those of their affiliated organizations, or those of the publisher, the editors and the reviewers. Any product that may be evaluated in this article, or claim that may be made by its manufacturer, is not guaranteed or endorsed by the publisher.

Copyright © 2021 Xu, Xu and Chuang. This is an open-access article distributed under the terms of the Creative Commons Attribution License (CC BY). The use, distribution or reproduction in other forums is permitted, provided the original author(s) and the copyright owner(s) are credited and that the original publication in this journal is cited, in accordance with accepted academic practice. No use, distribution or reproduction is permitted which does not comply with these terms.

APPENDIX A

(Note: All material parameters discussed in Appendix A and B are positive by default.)

The analytical formulas of $f_1(\omega)$ and $f_2(\omega)$ in Eq. 9 are expressed as

$$\begin{cases} f_1(\omega) = \sum_{i=1}^n (-1)^{i-1} \left(\sum_{\substack{z_1, z_2, \dots, z_{n-i} \in [1, n-1] \\ z_1 < z_2 < \dots < z_{n-i}}} \frac{\sum_{\substack{k_{t_s} \in \{k_{z_s}, k_{z_s+1}\} \\ t_1 < t_2 < \dots < t_{n-i}}} \left(\prod_{s=1}^{n-i} k_{t_s} \right)}{\prod_{s=1}^{n-i} m_{z_s}} \right) \omega^{2(i-1)} \\ f_2(\omega) = \sum_{i=1}^n (-1)^{i-1} \left(\sum_{\substack{z_1, z_2, \dots, z_{n-i} \in [1, n] \\ z_1 < z_2 < \dots < z_{n-i}}} \frac{\sum_{\substack{k_{t_s} \in \{k_{z_s}, k_{z_s+1}\} \\ t_1 < t_2 < \dots < t_{n-i}}} \left(\prod_{s=1}^{n-i} k_{t_s} \right)}{\prod_{s=1}^{n-i} m_{z_s}} \right) \omega^{2(i-1)} \end{cases}, \quad (\text{A1})$$

where

$$m_n = M, \quad k_{n+1} = k_1, \quad (\text{A2})$$

noting that value range of z_s is $[1, n-1]$ in $f_1(\omega)$ but that of z_s is $[1, n]$ in $f_2(\omega)$. This is because there is one more component (i.e., coupled mass M) in $f_2(\omega)$.

Some concrete expressions are as follows:

$$\begin{cases} f_1(\omega) = -\omega^2 + \frac{k_1 + k_2}{m_1} \\ f_2(\omega) = -\omega^2 + \frac{(M + m_1)}{Mm_1} (k_1 + k_2) \end{cases} \quad \text{for } n = 2, \quad (\text{A3})$$

When $n = 3$,

$$\begin{cases} f_1(\omega) = \omega^4 - \frac{(k_1m_2 + k_2(m_1 + m_2) + k_3m_1)}{m_1m_2} \omega^2 + \frac{(k_1k_2 + k_1k_3 + k_2k_3)}{m_1m_2} \\ f_2(\omega) = \omega^4 - \left(\frac{k_1 + k_3}{M} + \frac{(k_1m_2 + k_2(m_1 + m_2) + k_3m_1)}{m_1m_2} \right) \omega^2 \\ \quad + (k_1k_2 + k_1k_3 + k_2k_3) \frac{(m_1 + m_2 + M)}{Mm_1m_2} \end{cases}, \quad (\text{A4})$$

when $n = 4$,

$$\begin{aligned} f_1(\omega) = & -\omega^6 + \left(\frac{k_1m_2m_3 + k_2(m_1 + m_2)m_3}{m_1m_2m_3} + \frac{m_1(k_2k_3 + k_2k_4 + k_3k_4)}{m_1m_2m_3} \right. \\ & \left. + \frac{m_2(k_1k_3 + k_1k_4 + k_2k_3 + k_2k_4)}{m_1m_2m_3} + \frac{m_3(k_1k_2 + k_1k_3 + k_2k_3)}{m_1m_2m_3} \right) \omega^4 \\ & - \left(\frac{k_1k_2k_3 + k_1k_2k_4 + k_1k_3k_4 + k_2k_3k_4}{m_1m_2m_3} \right) \omega^2, \end{aligned} \quad (\text{A5})$$

$$\begin{aligned} f_2(\omega) = & -\omega^6 + \left(\frac{(k_1 + k_4)}{M} + \frac{k_1m_2m_3 + k_2(m_1 + m_2)m_3}{m_1m_2m_3} \right) \omega^4 \\ & - \left(\frac{m_1(k_2k_3 + k_2k_4 + k_3k_4) + m_2(k_1k_3}{m_1m_2m_3} + \frac{k_1k_4 + k_2k_3 + k_2k_4)}{m_1m_2m_3} + \frac{m_3(k_1k_2 + k_1k_3 + k_2k_3)}{m_1m_2m_3} \right. \\ & \left. + \frac{(k_1k_3 + k_1k_4 + k_3k_4)}{Mm_3} + \frac{(k_1k_2 + k_2k_4 + k_1k_3 + k_3k_4)}{Mm_2} + \frac{(k_1k_2 + k_1k_4 + k_2k_4)}{Mm_1} \right) \omega^2 \\ & + (k_1k_2k_3 + k_1k_2k_4 + k_1k_3k_4 + k_2k_3k_4) \frac{(m_1 + m_2 + m_3 + M)}{Mm_1m_2m_3}. \end{aligned} \quad (\text{A6})$$

APPENDIX B

We will solve Eq. 22 as well as Eq. 24 and make a thorough classified discussion to obtain the discriminants about bandgap transitions.

The criterion on existence of solutions of Eq. 22 is:

$$\begin{aligned} \Delta_1 = & ((k_1 + k_3)m_1m_2 + M(k_1m_2 + k_2(m_1 + m_2) + k_3m_1))^2 \\ & - 4Mm_1m_2(k_1k_2 + k_1k_3 + k_2k_3)(m_1 + m_2 + M), \end{aligned} \quad (\text{B1})$$

and for Eq. 24 it becomes

$$\begin{aligned} \Delta_2 = & (k_1m_2 + k_2(m_1 + m_2) + k_3m_1)^2 - 4m_1m_2 \left(\frac{k_1k_2k_3}{k} + (k_1k_2 \right. \\ & \left. + k_1k_3 + k_2k_3) \right). \end{aligned} \quad (\text{B2})$$

First, we will confirm that Eq. (B1) is always greater than or equal to zero, i.e.,

$$\Delta_1 \geq 0. \quad (\text{B3})$$

The Eq. (B1) can be written as function of M :

$$\begin{aligned} f(M) = & M^2((-k_1m_2 + k_2m_1 - k_2m_2 + k_3m_1)^2 + 4k_2^2m_1m_2) \\ & + 2M(k_1^2m_1m_2^2 + k_3^2m_1^2m_2 - (k_1k_2 + k_1k_3 \\ & + k_2k_3)(m_1^2m_2 + m_1m_2^2)) \\ & + (k_1 + k_3)^2m_1^2m_2^2, \end{aligned} \quad (\text{B4})$$

then the criterion on roots of this quadratic function is

$$\bar{\Delta}_1 = -4(k_1k_2 + k_1k_3 + k_2k_3)(k_1m_2 - k_3m_1)^2 \leq 0. \quad (\text{B5})$$

Therefore, Eq. (B3) has been proven to be correct for all situations.

Next, we will discuss the following six situations:

$$\left\{ \begin{array}{l} \Delta_1 > 0 \\ \Delta_2 < 0 \end{array} \right\}, \left\{ \begin{array}{l} \Delta_1 = 0 \\ \Delta_2 < 0 \end{array} \right\}, \left\{ \begin{array}{l} \Delta_1 > 0 \\ \Delta_2 = 0 \end{array} \right\}, \left\{ \begin{array}{l} \Delta_1 = 0 \\ \Delta_2 = 0 \end{array} \right\}, \left\{ \begin{array}{l} \Delta_1 > 0 \\ \Delta_2 > 0 \end{array} \right\}, \text{ and } \left\{ \begin{array}{l} \Delta_1 = 0 \\ \Delta_2 > 0 \end{array} \right\}. \quad (\text{B6})$$

The equivalent formulas below can be derived:

$$\Delta_1 = 0 \Leftrightarrow (k_1 m_2 - k_3 m_1)^2 + \left[(k_1 + k_3) \frac{m_1 m_2}{M} - k_2 (m_1 + m_2) \right]^2 = 0 \quad (\text{B7})$$

and

$$\Delta_2 = 0 \Leftrightarrow (-k_1 m_2 + k_2 m_1 - k_2 m_2 + k_3 m_1)^2 + 4k_2^2 m_1 m_2 - 4m_1 m_2 \frac{k_1 k_2 k_3}{k} = 0. \quad (\text{B8})$$

Solutions of Eq. 22 can be expressed as

$$\bar{\omega}_{1,2} = \sqrt{\frac{(k_1 + k_3)m_1 m_2 + M(k_1 m_2 + k_2(m_1 + m_2) + k_3 m_1) \pm \sqrt{\Delta_1}}{2Mm_1 m_2}}, \quad (\text{B9})$$

and those of Eq. 24 are

$$\bar{\omega}_{LR1,LR2} = \sqrt{\frac{k_1 m_2 + k_2(m_1 + m_2) + k_3 m_1 \pm \sqrt{\Delta_2}}{2m_1 m_2}}. \quad (\text{B10})$$

For every situation in Eq. (B6), the classified discussions are carried forward by comparing the distribution between solutions of Eq. 22 and that of Eq. 24. Several sets of discriminants, which are used to distinguish different bandgap behaviors, of all possible results of discussions are listed below,

$$\begin{aligned} & \left\{ \begin{matrix} g_1 > 0 \\ g_2 < 0 \end{matrix} \right\}, \quad \left\{ \begin{matrix} g_1 = 0 \\ g_2 < 0 \end{matrix} \right\}, \quad \left\{ \begin{matrix} g_1 > 0 \\ g_2 = 0 \\ g_3 < 0 \end{matrix} \right\}, \quad \left\{ \begin{matrix} g_1 > 0 \\ g_2 = 0 \\ g_3 = 0 \end{matrix} \right\}, \quad \left\{ \begin{matrix} g_1 > 0 \\ g_2 = 0 \\ g_3 > 0 \end{matrix} \right\}, \\ & \left\{ \begin{matrix} g_1 = 0 \\ g_2 = 0 \end{matrix} \right\}, \quad \left\{ \begin{matrix} g_1 = 0 \\ g_2 > 0 \end{matrix} \right\}, \quad \left\{ \begin{matrix} g_1 > 0 \\ g_2 > 0 \\ g_3 \leq 0 \end{matrix} \right\}, \quad \left\{ \begin{matrix} g_1 > 0 \\ g_2 > 0 \\ g_3 > 0 \end{matrix} \right\}, \quad \left\{ \begin{matrix} g_1 > 0 \\ g_2 > 0 \\ g_3 < 0 \\ g_4 > 0 \end{matrix} \right\}, \end{aligned} \quad (\text{B11})$$

where g_i ($i = 1, 2, 3, 4$) are functions of material parameters:

$$\begin{aligned} & g_1(M, k_1, k_2, k_3, m_1, m_2) = (k_1 m_2 - k_3 m_1)^2 \\ & \quad + \left[(k_1 + k_3) \frac{m_1 m_2}{M} - k_2 (m_1 + m_2) \right]^2 \\ & g_2(k, k_1, k_2, k_3, m_1, m_2) = (-k_1 m_2 + k_2 m_1 - k_2 m_2 + k_3 m_1)^2 \\ & \quad + 4k_2^2 m_1 m_2 - 4m_1 m_2 \frac{k_1 k_2 k_3}{k} \\ & g_3(M, k_1, k_2, k_3, m_1, m_2) \\ & \quad = M((-k_1 m_2 + k_2 m_1 - k_2 m_2 + k_3 m_1)^2 + 4k_2^2 m_1 m_2) \\ & \quad - 2m_1 m_2 [(k_1 k_2 + k_1 k_3 + k_2 k_3)(m_1 + m_2) \\ & \quad - (k_1^2 m_2 + k_3^2 m_1)] g_4(k, M, k_1, k_2, k_3, m_1, m_2) \\ & \quad = \left(\frac{k_1 k_2 k_3}{k} \right)^2 M^2 - \frac{k_1 k_2 k_3}{k} M [(k_1 k_2 + k_1 k_3 + k_2 k_3)(m_1 + m_2) \\ & \quad - (k_1^2 m_2 + k_3^2 m_1)] \\ & \quad + (k_1 + k_3)^2 \frac{k_1 k_2 k_3}{k} m_1 m_2 - (k_1 k_2 + k_1 k_3 + k_2 k_3)(k_1 m_2 - k_3 m_1)^2. \end{aligned} \quad (\text{B12})$$

The above results have not included the influence of frequencies of passbands at another edge (i.e., $q = \pi/a, x = 2$).

In fact, the distribution of frequencies at $x = 2$ only affects whether the Bragg bandgaps are opened or not after we have determined locations of LR bandgaps. Then we will deal with equation about edge ($x = 2$) frequencies of passbands (i.e., Eq. 23). According to theories about solutions of cubic equation (Zucker, 2016), its discriminants of the roots are:

$$\begin{cases} \Delta_{r1} = 18\bar{a}\bar{b}\bar{c}\bar{d} - 4\bar{b}^3\bar{d} + \bar{b}^2\bar{c}^2 - 4\bar{a}\bar{c}^3 - 27\bar{a}^2\bar{d}^2, \\ \Delta_{r2} = \bar{b}^2 - 3\bar{a}\bar{c} \end{cases}, \quad (\text{B13})$$

where

$$\begin{cases} \bar{a} = Mm_1 m_2 \\ \bar{b} = -[(k_1 + k_3 + 4k)m_1 m_2 + M(k_1 m_2 + k_2(m_1 + m_2) + k_3 m_1)] \\ \bar{c} = (k_1 k_2 + k_1 k_3 + k_2 k_3)(m_1 + m_2 + M) \\ \quad + 4k(k_1 m_2 + k_2(m_1 + m_2) + k_3 m_1) \\ \bar{d} = -4(k_1 k_2 k_3 + k(k_1 k_2 + k_1 k_3 + k_2 k_3)). \end{cases} \quad (\text{B14})$$

Adopting similar approaches on proving Eq. (B3), one can ascertain the following inequalities

$$\begin{cases} \Delta_{r1} \geq 0 \\ \Delta_{r2} > 0 \end{cases} \quad (\text{B15})$$

are true for any material parameters. It means that Eq. (B13) has three distinct real roots or has a double real root as well as a single real root. The Bragg bandgaps at $x = 2$ ($q = \pi/a$) will be opened when $\Delta_{r1} > 0$ and will be closed when $\Delta_{r1} = 0$.

The final sets of discriminants are as follows after above discussion:

$$\begin{aligned} & (1) \left\{ \begin{matrix} g_1 > 0 \\ g_2 < 0 \\ \Delta_{r1} > 0 \end{matrix} \right\}, (2) \left\{ \begin{matrix} g_1 > 0 \\ g_2 < 0 \\ \Delta_{r1} = 0 \end{matrix} \right\}, (3) \left\{ \begin{matrix} g_1 = 0 \\ g_2 < 0 \\ \Delta_{r1} > 0 \end{matrix} \right\}, \\ & (4) \left\{ \begin{matrix} g_1 = 0 \\ g_2 < 0 \\ \Delta_{r1} = 0 \end{matrix} \right\}, (5) \left\{ \begin{matrix} g_1 > 0 \\ g_2 = 0 \\ g_3 < 0 \end{matrix} \right\}, (6) \left\{ \begin{matrix} g_1 = 0 \\ g_2 = 0 \end{matrix} \right\}, \\ & (7) \left\{ \begin{matrix} g_1 > 0 \\ g_2 = 0 \\ g_3 > 0 \\ \Delta_{r1} > 0 \end{matrix} \right\}, (8) \left\{ \begin{matrix} g_1 > 0 \\ g_2 = 0 \\ g_3 > 0 \\ \Delta_{r1} = 0 \end{matrix} \right\}, (9) \left\{ \begin{matrix} g_1 > 0 \\ g_2 = 0 \\ g_3 = 0 \end{matrix} \right\}, \\ & (10) \left\{ \begin{matrix} g_1 > 0 \\ g_2 > 0 \\ g_3 < 0 \\ g_4 > 0 \end{matrix} \right\}, (11) \left\{ \begin{matrix} g_1 = 0 \\ g_2 > 0 \end{matrix} \right\}, \\ & (12) \left\{ \begin{matrix} g_1 > 0 \\ g_2 > 0 \\ g_3 \geq 0 \\ g_4 > 0 \\ \Delta_{r1} > 0 \end{matrix} \right\}, (13) \left\{ \begin{matrix} g_1 > 0 \\ g_2 > 0 \\ g_3 \geq 0 \\ g_4 > 0 \\ \Delta_{r1} = 0 \end{matrix} \right\}, (14) \left\{ \begin{matrix} g_1 > 0 \\ g_2 > 0 \\ g_4 \leq 0 \end{matrix} \right\}, \end{aligned} \quad (\text{B16})$$

where each set of discriminants corresponds to a bandgap behavior in the mass-coupled monatomic/triatomic chain system.



Acoustic Slow-Wave Effect Metamaterial Muffler for Noise Control of HVDC Converter Station

Dingge Yang¹, Quanyuan Jiang², Jingfeng Wu¹, Yanhua Han¹, Bin Ding¹, Bo Niu¹ and Guolin Xie^{2*}

¹State Grid Shaanxi Electric Power Research Institute, Xi'an, China, ²State Key Laboratory for Strength and Vibration of Mechanical Structures, School of Mechanical Engineering, Xi'an Jiaotong University, Xi'an, China

Aiming at the noise control of the HVDC converter station, a one-dimensional two-port metamaterial muffler based on the acoustic slow-wave effect is designed and manufactured. The metamaterial muffler achieves a broadband quasi-perfect absorption of noise from 600 to 900 Hz while ensuring a certain ventilation capacity. In addition, the internal equivalent sound velocity curve and the sound pressure and velocity field of the muffler are used to reveal the mechanism of its broadband quasi-perfect sound absorption. The performance of the muffler was verified by theoretical, numerical, and experimental models. The work in this paper is of guiding significance for solving the noise problem in HVDC converter stations.

OPEN ACCESS

Edited by:

Han Jia,
Institute of Acoustics (CAS), China

Reviewed by:

Xin-Ye Zou,
Nanjing University, China
Chen Shen,
Rowan University, United States

*Correspondence:

Guolin Xie
guolinxie@foxmail.com

Specialty section:

This article was submitted to
Metamaterials,
a section of the journal
Frontiers in Materials

Received: 29 October 2021

Accepted: 06 December 2021

Published: 03 January 2022

Citation:

Yang D, Jiang Q, Wu J, Han Y, Ding B,
Niu B and Xie G (2022) Acoustic Slow-
Wave Effect Metamaterial Muffler
for Noise Control of HVDC
Converter Station.
Front. Mater. 8:804302.
doi: 10.3389/fmats.2021.804302

Keywords: metamaterial, muffler, acoustic slow-wave effect, high voltage direct current, noise control

1 INTRODUCTION

In the power grid system, the high-voltage direct current (HVDC) converter station is a kind of important power conversion equipment. Its primary function is to convert high-voltage alternating current into direct current or vice versa. The HVDC converter station mainly includes transformers, reactors, thyristors, AC and DC side filters, and cooling equipment. With the improvement of people's living standards, the noise problem in HVDC converter stations has attracted more and more attention. According to previous research, the main noise in HVDC converter station is in the low-medium frequency band which will cause serious harm to personnel exposed to this environment (Li et al., 2016; Zhu et al., 2017; Wang et al., 2020). The commonly used noise reduction methods are mainly through changing the structure of the main equipment, traditional sound barriers, and active noise reduction technologies. The muffler is also a widely used noise reduction tool. It can allow airflow to achieve the purpose of heat dissipation and prevent the continued propagation of noise, which can better solve the noise and heat dissipation problems of HVDC.

The sound absorption performance of traditional dissipative mufflers (like porous materials) is closely related to their thickness, and their ventilation efficiency is not high. While reactive mufflers (like expansion chambers) are often larger, although they have better ventilation efficiency (Morse and Ingard, 1968; Munjal, 1987; Yang and Sheng, 2017). In recent years, the emergence of acoustic metamaterials has made it possible to better solve the noise problem of HVDC. The structure of the metamaterial mufflers is simple and light. Moreover, they can achieve quasi-perfect sound absorption of low frequency and broadband under the sub-wavelength size compared with the traditional mufflers. Also, they have better ventilation efficiency. Huang et al. proposed a drum muffler with a membrane structure that uses a tensioned diaphragm to form sound reflection by

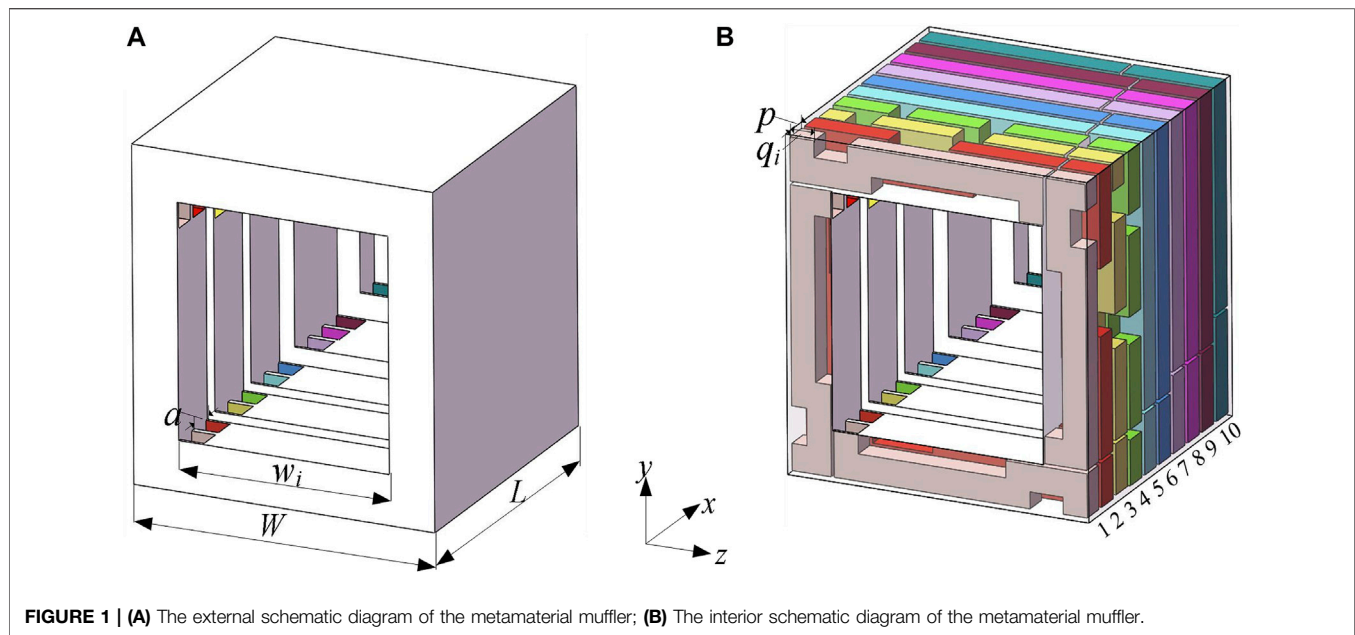


FIGURE 1 | (A) The external schematic diagram of the metamaterial muffler; **(B)** The interior schematic diagram of the metamaterial muffler.

coupling a flexible wall and sound waves (Huang, 2002). Wang et al. proposed a composite elastic plate muffler by combining sound-absorbing materials and elastic plates (Wang et al., 2007; Wang and Huang, 2007). Li et al. designed a broadband double-layer micro-perforated ventilation muffler, which can achieve a sound absorption coefficient of more than 0.5 in the mid-frequency range (850–1000 Hz) on the basis of 70% ventilation efficiency (Li et al., 2018). Kumar et al. proposed a sound-absorbing muffler with a perforated neck and cavity that can be ventilated, achieving a sound absorption coefficient of 0.96 (1,000 Hz) at 45% of the opening area (Kumar et al., 2020). Kumar and Lee designed a wide-band ventilated sound-absorbing muffler using six folded channels (Kumar and Lee, 2020). Cheng et al. proposed a Mie resonator formed by eight symmetrical coiled cavities to achieve “slow sound velocity” noise reduction. (Cheng et al., 2015). Raze et al. introduced the Fano resonance concept into acoustics and proposed a spiral ventilation muffler (Raze et al., 2019).

At present, in addition to traditional mufflers, membrane-type mufflers and metamaterial mufflers are more researched. However, membrane-type mufflers face problems in terms of installation and durability. In contrast, metamaterial mufflers mostly rely on sound absorption and sound reflection to achieve narrow-band perfect absorption or broadband low-absorption coefficient goals. Furthermore, most mufflers have not studied the balance between acoustic and ventilation performance, making these structures unusable in some scenes requiring ventilation and heat dissipation. Therefore, a muffler with a wide frequency band, high absorption coefficient, and good ventilation efficiency is urgently needed to solve the noise problem of HVDC.

In this work, aiming at the noise problem of HVDC, we design a metamaterial muffler based on the acoustic slow-wave effect. The muffler is composed of multiple arrays of Fabry-Pérot (F-P)

resonators, which can achieve broadband quasi-perfect absorption of sound waves in the middle and low-frequency bands and ensure a certain ventilation capacity. At the same time, compared with the traditional two-side open mufflers, the metamaterial muffler breaks the limitation of the sound absorption coefficient of less than 0.5. It can better solve the noise problem and heat dissipation problem of HVDC.

The remainder of this paper is structured as follows: **Section 2** describes the metamaterial muffler design and the theory; **Section 3** and **Section 4** respectively verify the sound absorption performance of the muffler and analyze the mechanism of noise reduction; the study is concluded with final remarks in **Section 5**.

2 STRUCTURE AND THEORY

Most of the existing mufflers can be used for theoretical analysis of their acoustic response with a one-dimensional two-port acoustic waveguide model (Merkel et al., 2015). This type of system mainly relies on the acoustic wave loss structure placed on the edge of the air duct to dissipate the energy of the grazing sound wave. This model can be simplified as a point-symmetric scattering structure, and the sound absorption coefficients are all less than 0.5. According to Merkel’s research, if we can adjust the size to make the transmission coefficient and reflection coefficient at the target frequency equal to 0.5, the sound absorption coefficient can be set to 1. Considering that many dimensions affect the transmission coefficient and reflection coefficient of the Helmholtz resonator, the adjustment is more complicated, so we chose the F-P resonator as the basic structure to design the metamaterial muffler. Because the sound absorption performance of the F-P resonator is only related to the side length of the cross-section, and the resonance frequency is only

TABLE 1 | Dimensions of each unit.

i	p /mm	q_i /mm	w_i /mm	h_i /mm
1	8.0	8.0	70	94
2	8.0	8.0	70	99
3	8.0	8.5	65	104
4	8.0	8.5	65	109
5	8.0	8.5	60	114
6	8.0	9.0	60	119
7	8.0	9.0	50	124
8	8.0	9.5	50	129
9	8.0	10.0	50	134
10	8.0	10.0	35	140

related to the length of the resonator, which is more convenient to control (Xie and Wang, 2021).

Figure 1 shows the external and internal specific structures of the designed metamaterial muffler. **Figure 1A** shows the external dimensions of the muffler. The length W , width L , and height of the muffler are all 100 mm. **Figure 1B** shows the internal details of the muffler. The entire muffler is divided into ten units, arranged in sequence along the x direction. The ventilation holes are located in the center of the structure. Each unit is composed of four identical coiled F-P tubes. The cross-sectional side lengths of the F-P tube are p and q_i . And the length is h_i . The thickness t of the partition between the unit is 1 mm. The thickness a of the unit is $p + 2t$, and the side length of the ventilation hole is w_i . Here the subscript i represents the unit number.

The size parameters of each unit are shown in **Table 1**.

In order to derive the theoretical model of the muffler, we simplify **Figure 1** as a 1/2 cross-sectional view of the x - y plane of the muffler in **Figure 2**. To facilitate the visual display of the height difference of the F-P tubes of each unit, we replace the coiled pipes with long straight tubes. It can be seen that the cross-sectional size and length of the four F-P tubes of the same unit are the same. The length h of the F-P tubes of each unit changes gradually, from 94 mm ($i = 1$) to 140 mm ($i = 10$) uniformly.

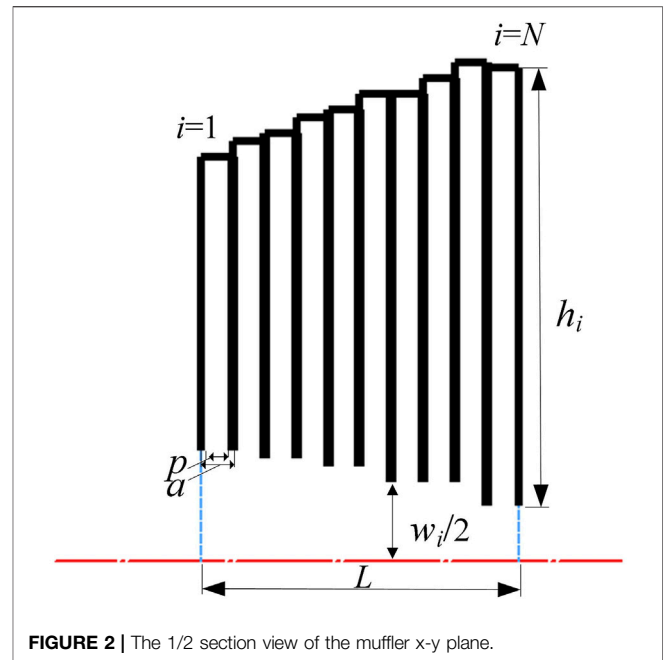
Next, we use the transfer matrix method to derive the theoretical model of the muffler. We define the sound pressure of the sound wave as p , and the normalized sound velocity in the horizontal direction as v_x . Assuming that there are only plane waves in the waveguide, according to the continuous boundary conditions of sound pressure and velocity, we can get,

$$\begin{bmatrix} p \\ v_x \end{bmatrix}_{x=0} = T \begin{bmatrix} p \\ v_x \end{bmatrix}_{x=L} = \begin{bmatrix} T_{11} & T_{12} \\ T_{21} & T_{22} \end{bmatrix} \begin{bmatrix} p \\ v_x \end{bmatrix}_{x=L},$$

where T is the system transfer matrix. T can be derived from the transfer matrix of N central through holes of different sizes and the F-P tubes coiled around. As shown in the following formula,

$$T = M_{\Delta d}^{[i]} \prod_{i=1}^{i=10} M_d^{[i]} M_{FP}^{[i]} M_{\Delta d}^{[i+1]},$$

where $M_d^{[i]}$ is the transfer matrix of the central through hole of the i -th unit, $M_{FP}^{[i]}$ is the transfer matrix of the F-P tubes of the i -th

**FIGURE 2** | The 1/2 section view of the muffler x - y plane.

unit, $M_{\Delta d}^{[i]}$ is the modified transfer matrix item of the central through hole of the i -th unit considering the radiation effect.

Due to the small cross-sectional area of the central through-hole and the F-P tube, we should consider the visco-thermal losses. So, we introduce the equivalent complex index. The medium is air with mass density $\rho_0 = 1.213 \text{ kg/m}^3$, sound speed $c_0 = 343 \text{ m/s}$, atmospheric pressure $P_0 = 101325 \text{ Pa}$, dynamic viscosity $\eta = 1.79 \times 10^{-5} \text{ kg/(m} \cdot \text{s)}$, specific heat ratio $\gamma = 1.4$, Prandtl number $Pr = 0.7167$. The equivalent complex density $\rho_d^{[i]}$ and equivalent bulk modulus $\kappa_d^{[i]}$ of the central through-hole air can be expressed as (Jimenez et al., 2017),

$$\rho_d^{[i]} = \rho_0 \left[1 - \frac{\tanh\left(\frac{\omega_i}{2} G_p\right)}{\frac{\omega_i}{2} G_p} \right]^{-1},$$

$$\kappa_d^{[i]} = k_0 \left[1 - (\gamma - 1) \frac{\tanh\left(\frac{\omega_i}{2} G_\kappa\right)}{\frac{\omega_i}{2} G_\kappa} \right]^{-1},$$

where $G_p = \sqrt{i\omega\rho_0/\eta}$, $G_\kappa = \sqrt{i\omega Pr\rho_0/\eta}$, the air bulk modulus $\kappa_0 = \gamma P_0$.

Next, we can get the transfer matrix of the central through hole of the i -th unit $M_d^{[i]}$,

$$M_d^{[i]} = \begin{bmatrix} \cos\left(k_d^{[i]} \frac{a_i}{2}\right) & iZ_d^{[i]} \sin\left(k_d^{[i]} \frac{a_i}{2}\right) \\ \frac{i}{Z_d^{[i]}} \sin\left(k_d^{[i]} \frac{a_i}{2}\right) & \cos\left(k_d^{[i]} \frac{a_i}{2}\right) \end{bmatrix},$$

where $k_d^{[i]}$ is the equivalent complex wave number of the central through hole of the i -th unit, $Z_d^{[i]} = \sqrt{\kappa_d^{[i]} \rho_d^{[i]} / S_d^{[i]}}$ is the normalized equivalent impedance of the central through hole of the i -th unit, $S_d^{[i]} = w_d^{[i]} \times w_d^{[i]}$ is the cross-sectional area of the central through hole of the i -th unit.

According to the existing thermal viscosity expression, the equivalent complex density $\rho_d^{[i]}$ and equivalent bulk modulus $\kappa_d^{[i]}$ of the F-P tube of the i -th unit can be expressed as (Jimenez et al., 2017),

$$\rho_{FP}^{[i]} = -\frac{\rho_0 p^2 q_i^2}{4G_\rho^2 \sum_{m \in N} \sum_{n \in N} [\alpha_m^2 \beta_n^2 (\alpha_m^2 + \beta_n^2 - G_\rho^2)]^{-1}},$$

$$\kappa_{FP}^{[i]} = \frac{\kappa_0}{\gamma + \frac{4(\gamma-1)G_k^2}{p^2 q_i^2} \sum_{m \in N} \sum_{n \in N} [\alpha_m^2 \beta_n^2 (\alpha_m^2 + \beta_n^2 - G_k^2)]^{-1}},$$

where $\alpha_m = 2(m + 1/2)\pi/p$, $\beta_n = 2(n + 1/2)\pi/q_i$.

Similarly, the transfer matrix of the F-P tube of the i -th unit $M_{FP}^{[i]}$ is

$$M_{FP}^{[i]} = \begin{bmatrix} 1 & 0 \\ \frac{1}{Z_{FP}^{[i]}} & 1 \end{bmatrix}.$$

Because of the sudden area change between unit 10 and the pipe, we also need to consider the error caused by the sound wave radiating from the waveguide to the free space. The equivalent length correction term can be expressed as (Jimenez et al., 2017),

$$\Delta l_d^{[N]} = \sigma \omega_N \sum_{m=1}^N \frac{\sin^2(m\pi\sigma)}{(m\pi\sigma)^3},$$

where $\sigma = \frac{\omega}{W}$. Then, the radiation impedance $Z_{\Delta d}^{[N]}$ between the central through hole of unit 10 and the free space can be expressed as:

$$Z_{\Delta d}^{[N]} = -i\omega \Delta l_d^{[N]} \rho_0 \sigma / W^2.$$

Due to the different cross-sectional area sizes of the central through holes between different units, there are discontinuities in the area. So it is also necessary to introduce a correction term to correct the radiation term of the sound wave. The radiation correction length from unit 1 to unit 9 can be expressed as:

$$\Delta l_d^{[i]} = 0.82 \left[1 - 1.35 \frac{\omega_i}{\omega_{i-1}} + 0.31 \left(\frac{\omega_i}{\omega_{i-1}} \right)^3 \right] \omega_i.$$

Therefore, we can get the radiation correction impedance of each unit $Z_{\Delta d}^{[i]}$, then, the central through-hole radiation correction transfer matrix of the i -th unit $M_{\Delta d}^{[i]}$ can be obtained.

$$Z_{\Delta d}^{[i]} = -i\omega \Delta l_d^{[i]} \rho_0 \sigma_i / w_i^2,$$

$$M_{\Delta d}^{[i]} = \begin{bmatrix} 1 & Z_{\Delta d}^{[i]} \\ 0 & 1 \end{bmatrix}.$$

After obtaining $M_d^{[i]}$, $M_{FP}^{[i]}$ and $M_{\Delta d}^{[i]}$, it is easy to get the system transfer matrix and then the system equivalent wavenumber k_e , equivalent impedance Z_e , equivalent sound velocity c_e , sound energy transmission coefficient T , reflection coefficient R and sound absorption coefficient A can be calculated.

$$k_e = \frac{a}{L} \cos\left(\frac{T_{11} + T_{22}}{2}\right)$$

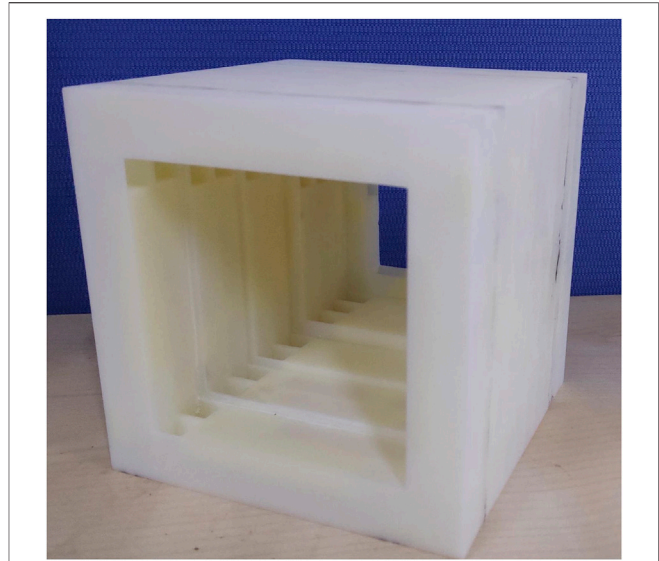


FIGURE 3 | Experimental sample of the metamaterial muffler.

$$Z_e = \frac{\sqrt{T_{11}/T_{21}}}{Z_0}$$

$$c_e = \text{Re} \left[\frac{w}{k_e} \right]$$

$$T = \left| \frac{T_{11} + T_{12}}{Z_0} + (T_{21} + T_{22})Z_0 \right|^2$$

$$R = \left| \frac{T_{11} + T_{12}/Z_0 - T_{21}Z_0 - T_{22}}{T_{11} + T_{12}/Z_0 + T_{21}Z_0 + T_{22}} \right|^2$$

$$A = 1 - T - R,$$

where the free space air impedance $Z_0 = \rho_0 c_0$.

3 SIMULATION AND EXPERIMENT

To analyze the acoustic performance of the proposed metamaterial muffler, a theoretical model, a numerical simulation model, and experiments were used for verification.

The theoretical model was established in MATLAB. The reflection coefficient and the sound energy transmission coefficient can be expressed by the system transfer matrix, and the sound absorption coefficient can then be expressed.

The numerical simulation model was established using the commercial finite element software COMSOL Multiphysics 5.4. The pressure acoustic module and the thermoacoustic module were adopted. The finite element simulation model consists of the upstream duct air domain, the metamaterial muffler air domain, and the downstream duct air domain. The pressure acoustic modules were used in the upstream duct air domain, downstream duct air domain, and the middle through-hole of the metamaterial muffler. The thermoacoustic module was used in the air domain of the coiled F-P tube. The boundaries of the air domain were considered as acoustic hard boundaries, and boundary-layer meshes with five layers were applied on the walls of the F-P tube. The incident

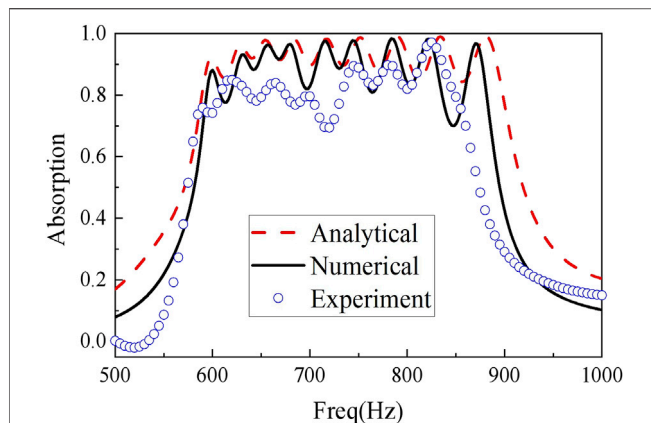


FIGURE 4 | Comparison of theoretical, numerical, and experimental sound absorption coefficient curves of the sample.

sound wave was a plane wave with unit amplitude incident on the vertical metamaterial muffler. When the sound waves propagate to the muffler structure, part is reflected, part is absorbed and dissipated in the F-P tube, and part is transmitted from the muffler into the downstream duct. After expressing the reflection coefficient and transmission coefficient, the sound absorption coefficient of the muffler can be obtained. In addition, since the thermoacoustic simulation has more degrees of freedom and is limited by computer hardware conditions, the coiled F-P tube is equivalent to a long straight F-P tube.

In the experimental study, the metamaterial muffler was installed in a square impedance-tube system with a cross-sectional size is 100 mm × 100 mm. The upper limit frequency is 1700 Hz. We installed the muffler between the upstream and downstream standing wave tubes, and the end of the downstream standing wave tube was filled with a sponge. The sound absorption coefficient was measured by the standard transfer-function method. The experimental sample of the metamaterial muffler is shown in **Figure 3**. The material of the muffler is PLA resin, and its density, elastic modulus, and Poisson's ratio are 1,160 kg/m³, 2.37 GPa and 0.41 respectively. The speed of sound waves propagating in it is 2230 m/s. Since the acoustic impedance of sound waves propagating in solid structures is much greater than that in air, the muffler can be regarded as an acoustic hard boundary. Even if its wall thickness is only 1 mm, it is sufficiently “hard” compared to air.

The sound absorption coefficient curves of the sample obtained by the theoretical, numerical, and experimental models are shown in **Figure 4**.

The red dotted line in the figure is the result obtained from the theoretical model. The black solid line is the result obtained from the numerical simulation model. The last blue circle line is the result obtained from experimental measurements. The theoretical and simulation results show that the sound absorption coefficient is mostly maintained above 0.9 in the 600–900 Hz frequency band. Moreover, the sound absorption coefficient curve has nine sound absorption peaks. A valley value of the sound absorption coefficient appears between two adjacent sound absorption peaks. However, through a reasonable adjustment of the size between the muffler

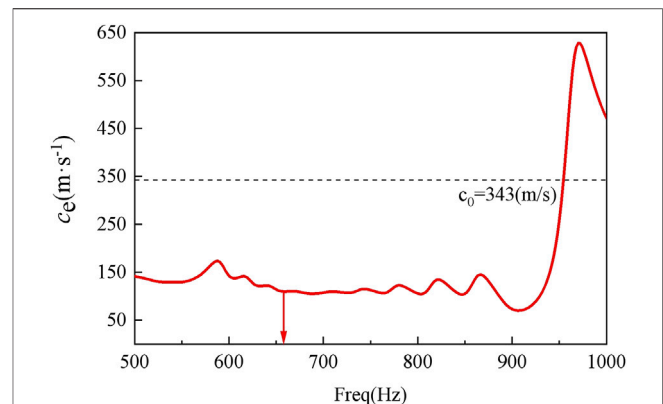


FIGURE 5 | Internal equivalent sound velocity curve of the muffler.

units, the valley value is also basically higher than 0.8. Combined with the experimental curves, the overall trend, amplitude, and position of the critical frequency of the three curves are basically the same, so it can be considered that the analytical solutions, simulation values, and experimental values are basically consistent. There is a certain difference between the experimental value of the sound absorption coefficient in the individual frequency bands (500–550 Hz, 700–750 Hz) and the simulated value, and the maximum error value does not exceed 0.2.

The experimental error is mainly because the accuracy of 3D printing is not high enough (± 0.1 mm). Moreover, the experimental boundary conditions are difficult to ensure the same as the ideal conditions in the simulation. In addition, because the side length of the channel in the self-made impedance tube is fixed at 100 mm, the sample size is slightly smaller than 100 mm, and there is a certain amount of acoustic leakage. Based on the above factors, the sound absorption coefficient curve of the muffler obtained by the experiment is lower than the ideal state of silent leakage in the theory and simulation.

After verifying the acoustic performance of the above metamaterial muffler, we can use this structure to reduce noise against the noise source of the HVDC converter station. Considering that the main transformer and high-voltage reactor are the main noise sources, we can use many designed metamaterial mufflers to form a wall to surround them to reduce noise. Of course, we can also apply it to other places where the noise is prominent.

4 ANALYSIS AND DISCUSSION

In order to further analyze the mechanism of the muffler, first draw the internal equivalent sound velocity curve of the muffler, as shown in **Figure 5**. In the 500–950 Hz frequency band, the internal equivalent sound velocity of the muffler is much smaller than the free space sound velocity of 343 m/s, and an equivalent “slow-wave” is formed inside the muffler. This “slow-wave” is produced because the center hole of the muffler can be equivalent to a slit. The slit is surrounded by a plurality of F-P tube circumferential arrays, and the propagation of sound waves in each slit is strongly dispersive. The resonant frequency bandgap of the resonant structure continuously

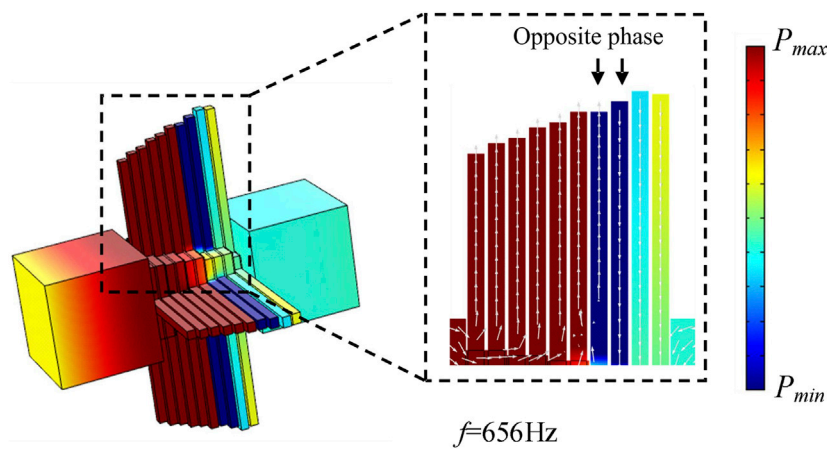


FIGURE 6 | The muffler pressure/velocity cloud graph at $f = 656$ Hz.

accumulates and reaches a phase velocity close to zero above the highest resonant frequency. In addition, due to the existence of the slow-wave effect inside the muffler, the ratio of λ/L is significantly reduced, which dramatically reduces the length of the F-P tube required to reach the resonance frequency. Therefore, this muffler exhibits the effect of a sub-wavelength resonator.

In order to more intuitively explore the causes of slow waves, the pressure and velocity fields of the muffler are analyzed, and the results are shown in **Figure 6**. The figure shows the pressure velocity cloud diagram of the muffler when $f = 656$ Hz, that is, when unit 7 reaches resonance. It can be seen that since the sound waves of the inflow unit 7 and the outflow unit 8 are in anti-phase, the two interfere in the central through-hole and cancel each other. Most of the sound waves no longer propagate downstream, resulting in a reduction in the equivalent phase velocity of the sound waves. In the same way, at the resonance frequency of other units, the resonance unit, and adjacent units will also interfere with sound waves, resulting in a “slow-wave” phenomenon in a relatively wide frequency band.

According to the currently designed structure, the unit with the smallest side length of the middle through-hole is unit 10, and its side length is 35 mm, so there is only 12.25% of the ventilation area. We sacrificed the ventilation area to obtain a wider sound absorption bandwidth and a higher sound absorption coefficient in the design. If we abandon unit 10 (sacrifice a peak at the low frequency), the minimum side length of the middle through-hole becomes 50 mm. The ventilation area becomes 25%. In addition, if the remaining space of the muffler is better utilized and the shape of the middle through-hole is optimized, the ventilation performance can be further improved. In this article, we only ensure a certain ventilation performance. The balance of acoustic performance and ventilation performance will be one of our main tasks in the future.

5 CONCLUSION

In short, we propose and manufacture a metamaterial muffler based on the slow-wave effect. Through ten specially designed units, the muffler breaks through the limitation that the sound

absorption coefficient of the traditional two-side open muffler is less than 0.5. Moreover, we realize the broadband quasi-perfect absorption from 600 to 900 Hz while ensuring a certain ventilation capacity. We use finite element simulation and experiment to verify the noise reduction performance of the muffler, and the theoretical, simulation, and experimental results are in good agreement. In addition, through the internal sound pressure and velocity cloud diagram of the muffler, we found that the sound waves of the resonant unit and the adjacent unit are in opposite phases at the resonance frequency, causing the interference of the sound waves to cancel, achieving the purpose of noise elimination. At the same time, this also leads to a reduction in the equivalent phase velocity of the acoustic wave, resulting in a “slow-wave” phenomenon in a relatively wide frequency band.

DATA AVAILABILITY STATEMENT

The original contributions presented in the study are included in the article/Supplementary Material, further inquiries can be directed to the corresponding author.

AUTHOR CONTRIBUTIONS

DY and QJ have substantial contributions to the conception or design of the work; BD and YH worked for the acquisition, analysis or interpretation of data; BN and GX wrote the work and revised it critically for important intellectual content; JW was responsible for responding to reviewers' comments, follow-up work on paper production, and determining the final version to be published.

FUNDING

This work is supported by the State Grid Shaanxi Electric Power Company Technology Project (5226KY20001G).

REFERENCES

- Cheng, Y., Zhou, C., Yuan, B. G., Wu, D. J., Wei, Q., and Liu, X. J. (2015). Ultra-Sparse Metasurface for High Reflection of Low-Frequency Sound Based on Artificial Mie Resonances. *Nat. Mater.* 14 (10), 1013–1019. doi:10.1038/Nmat4393
- Huang, L. (2002). Modal Analysis of a Drumlike Silencer. *J. Acoust. Soc. Am.* 112 (5 Pt 1), 2014–2025. doi:10.1121/1.1508778
- Jimenez, N., Romero-Garcia, V., Pagneux, V., and Groby, J. P. (2017). Quasi-Perfect Absorption by Subwavelength Acoustic Panels in Transmission Using Accumulation of Resonances Due to Slow Sound. *Phys. Rev. B* 95 (1), 014205. doi:10.1103/physrevb.95.014205
- Kumar, S., and Lee, H. P. (2020). Labyrinthine Acoustic Metastructures Enabling Broadband Sound Absorption and Ventilation. *Appl. Phys. Lett.* 116 (13), 134103. doi:10.1063/5.0004520
- Kumar, S., Xiang, T., and Lee, H. P. (2020). Ventilated Acoustic Metamaterial Window Panels for Simultaneous Noise Shielding and Air Circulation. *Appl. Acoust.* 159, 107088. doi:10.1016/j.apacoust.2019.107088
- Li, J., Ji, S., Zhu, L., Wu, P., and Cao, T. (2016). Vibration Characteristics of Filter Capacitors Used in HVDC Converter Stations. *IEEE Trans. Power Deliv.* 31 (5), 2045–2053. doi:10.1109/TPWRD.2015.2483638
- Li, L., Zheng, B., Zhong, L., Yang, J., Liang, B., and Jian, C. (2018). Broadband Compact Acoustic Absorber with High-Efficiency Ventilation Performance. *Appl. Phys. Lett.* 113 (10), 103501. doi:10.1063/1.5038184
- Merkel, A., Theocharis, G., Richoux, O., Romero-Garcia, V., and Pagneux, V. (2015). Control of Acoustic Absorption in One-Dimensional Scattering by Resonant Scatterers. *Appl. Phys. Lett.* 107 (24), 244102. doi:10.1063/1.4938121
- Morse, P. M., and Ingard, K. U. (1968). *Theoretical Acoustics*. MCGRAW-HILL BOOK COMPANY.
- Munjal, M. L. (1987). *Acoustic of Ducts and Mufflers with Application to Exhaust and Ventilation System Design*. Hoboken, New Jersey: Wiley press.
- Raze, G., Nikolajczyk, J., Anderson, S., and Zhang, X. (2019). Ultra-Open Acoustic Metamaterial Silencer Based on Fano-like Interference. *Phys. Rev. B* 99 (2), 024302. doi:10.1103/PhysRevB.99.024302
- Wang, C., and Huang, L. (2007). Analysis of Absorption and Reflection Mechanisms in a Three-Dimensional Plate Silencer. *J. Sound Vibration* 313 (3), 510–524. doi:10.1016/j.jsv.2007.12.027
- Wang, C., Han, J., and Huang, L. (2007). Optimization of a Clamped Plate Silencer. *J. Acoust. Soc. Am.* 121 (2), 949–960. doi:10.1121/1.2427126
- Wang, L., Wu, J., Wei, J., Zhou, H., Geng, M., and Bai, X. (2020). “Study on Audible Noise Characteristics of Filter Capacitors and Reactors in HVDC Converter Stations by Using Sound Signal Processing Array Technique,” in 2020 5th Asia Conference on Power and Electrical Engineering (ACPEE), Chengdu, China, June, 2020, 1281–1285.
- Xie, G., and Wang, X. (2021). Optimal Size Design of Fabry-Perot Sound Absorbers Based on the Loss Equation. *J. Appl. Phys.* 130 (1), 015111. doi:10.1063/5.0050502
- Yang, M., and Sheng, P. (2017). Sound Absorption Structures: From Porous Media to Acoustic Metamaterials. *Annu. Rev. Mater. Res.* 47, 83–114. doi:10.1146/annurev-matsci-070616-124032
- Zhu, L., Li, J., Shi, Y., Rehman, H., and Ji, S. (2017). Audible Noise Characteristics of Filter Capacitors Used in HVDC Converter Stations. *IEEE Trans. Power Deliv.* 32 (5), 2263–2271. doi:10.1109/tpwr.2016.2587638

Conflict of Interest: DY, JW, YH, BD, and BN were employed by the State Grid Shaanxi Electric Power Research Institute.

The remaining authors declare that the research was conducted in the absence of any commercial or financial relationships that could be construed as a potential conflict of interest.

Publisher’s Note: All claims expressed in this article are solely those of the authors and do not necessarily represent those of their affiliated organizations, or those of the publisher, the editors and the reviewers. Any product that may be evaluated in this article, or claim that may be made by its manufacturer, is not guaranteed or endorsed by the publisher.

Copyright © 2022 Yang, Jiang, Wu, Han, Ding, Niu and Xie. This is an open-access article distributed under the terms of the Creative Commons Attribution License (CC BY). The use, distribution or reproduction in other forums is permitted, provided the original author(s) and the copyright owner(s) are credited and that the original publication in this journal is cited, in accordance with accepted academic practice. No use, distribution or reproduction is permitted which does not comply with these terms.



Broadband Sound Absorption of Subwavelength Porous Meta-Liner

Heye Xiao^{1†}, Tianyue Yuan^{2†}, Xiang Song², Junli Chen², Jie Zhou², Dan Sui^{2*} and Jintao Gu³

¹Unmanned System Research Institute, Northwestern Polytechnical University, Xi'an, China, ²School of Aeronautics, Northwestern Polytechnical University, Xi'an, China, ³First Aircraft Design and Research Institute, Aviation Industry Corporation of China Ltd., Xi'an, China

OPEN ACCESS

Edited by:

Yong Xiao,
National University of Defense
Technology, China

Reviewed by:

Bu Huanxian,
Hong Kong University of Science and
Technology, Hong Kong SAR, China
Chongrui Liu,
Xi'an Jiaotong University, China

*Correspondence:

Dan Sui
suidan@nwpu.edu.cn

[†]These authors have contributed
equally to this work

Specialty section:

This article was submitted to
Metamaterials,
a section of the journal
Frontiers in Materials

Received: 30 December 2021

Accepted: 14 January 2022

Published: 07 February 2022

Citation:

Xiao H, Yuan T, Song X, Chen J,
Zhou J, Sui D and Gu J (2022)
Broadband Sound Absorption of
Subwavelength Porous Meta-Liner.
Front. Mater. 9:845597.
doi: 10.3389/fmats.2022.845597

This work proposes a subwavelength porous meta-liner with broadband sound absorption from 900 to 1,200 Hz. The meta-liner consists of four subunits, which are made up of porous material and hollow coiling slit embedded in it. Each subunit is designed by adjusting the length of its coiling slit to achieve resonance in the target frequency and examined by the finite element method (FEM). These subunits are arranged in an axial direction uniformly and radial direction periodically to propose a meta-liner duct. Then, the noise reduction of the propeller system with the meta-liner duct is measured by the microphone array. The result shows that the propeller with the meta-liner duct can reduce the noise level of the ducted propeller between 3.6 and 5.5 dB in the design frequency range, which also effectively reduces the noise level in the broadband frequency range. Therefore, the meta-liner shows a good application prospect in the noise reduction of the propeller.

Keywords: porous meta-liner, subwavelength, duct, propeller noise reduction, finite element method

INTRODUCTION

The noise reduction problem of small-scale unmanned aerial vehicles (UAVs) is widely researched for the improvement of the competitiveness in the civil market and the increase of the concealment in the military application (Mueller, 2001; Christian and Cabell, 2017). The primary noise source of the UAVs is the propeller noise (Zhou and Fattah, 2017). The propeller emission noise may be divided into broadband noise and tonal noise (Kemp, 1932; Kurtz and Marte, 1970). The broadband noise results from the turbulence generated by the interaction between the air and the propeller blade, and the tonal noise comes from the motion of the rotor.

Usually, the tonal noise is a significant noise source, which is most prominent at the harmonics of the passing frequency of the propeller blade. In order to control the noise of the propeller, several techniques have been utilized to reduce the noise level both in the generation and propagation of the noise. For example, the serrated trailing edge blades can reduce the broadband noise and the ducted propeller. Except for reducing the noise level of the propeller, the ducted propeller can also improve the aerodynamic efficiency of the UAVs and protect the propeller blade from damage.

Meanwhile, Pereira et al. pointed out that a hard wall duct can result in a slight increment of noise if the duct is not designed well (Pereira, 2008). Malgouezar et al. investigated the characteristics of the noise of the propeller with a rigid duct according to the experiment (Malgouezar et al., 2019). They found the introduction of the duct will result in the increase of the broadband noise, a decrease of the first harmonics, and an overall decrease in the noise level. Furthermore, Lu et al. investigated the acoustic performance of the rigid duct and a micro-perforated duct. Their acoustic benefits were not as high as expected (Lu et al., 2016). Guo et al. designed a lined duct using a Helmholtz resonator with an extended neck and achieved approximately 3 dB noise reduction in the range of 700–1,000 Hz

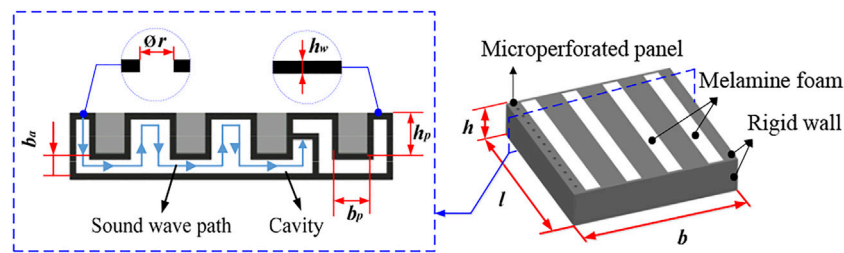


FIGURE 1 | Structure of acoustic liner and its subunit.

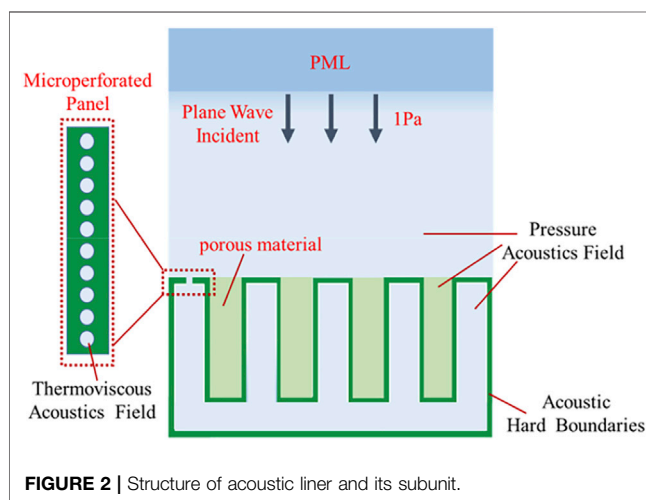


FIGURE 2 | Structure of acoustic liner and its subunit.

(Guo et al., 2021). In general, a ducted propeller can significantly increase the aerodynamic and acoustic performance if the duct is designed properly. There is still a lack of design for the new ducted propellers to reduce the propeller noise in the wider frequency. Moreover, it is significant to control the weight of the ducted propellers to meet the lightweight requirement of the aircraft (Reducing the weight of ai, 2014). Therefore, a new lightweight duct occupying a small space, which also has excellent acoustic performance both in low and high frequencies, needs to be studied and designed.

Traditional Helmholtz resonator (HR)-type acoustic liners, composed of a honeycomb layer placed between a perforated plate and a rigid back-plate (Nark and Jones, 2017), are commonly used to control noise in many duct sound suppression problems (e.g., aero-engines and air-conditioning ducts). This type of liner is effective across a narrow band of frequencies (Durau, 2012), thus making it unsuitable for broadband noise reduction. Fortunately, new acoustic metamaterials offer greater potential for noise control. Most metamaterials for sound absorption have only been studied in lab tests (Li and Assouar, 2016; Zhou et al., 2017; Fang et al., 2018a; Fang et al., 2018b; Wang et al., 2018; Wang et al., 2019; Wu et al., 2019; Li et al., 2020; Liu et al., 2020; Zhao et al., 2020; Liang et al., 2021; Liu et al., 2021), leaving a research gap of their applications to aeroacoustic

problems. In this article, we present the numerical and experimental investigations on sound absorption of subwavelength porous meta-liner. The coiling slit with rigid walls is embedded in the porous material to build the subunit of the meta-liner. The sound absorption of each subunit in the meta-liner is examined by using the finite element method (FEM). Then, the designed meta-liner, which is composed of several subunits, is applied in the duct. A meta-liner duct is proposed to reduce the propeller-induced noise. Finally, we verify the noise reduction of the designed meta-liner in the duct for the propeller system by carrying out experiments.

META-LINER SUBUNIT DESCRIPTION AND DESIGN

Meta-Liner Subunit Description

The propeller-induced noise includes broadband noise and tonal noise. Usually, the porous material panel and microperforated panel are used to reduce broadband noise at high frequency and tonal noise at low frequency, respectively. It is perfect to integrate these two structures in the limited space for reducing the propeller-induced noise in the wide frequency range. Therefore, the subunit of a meta-liner is designed and shown in **Figure 1**. It is seen that the subunit is composed of a coiling slit and porous material. The coiling slit with rigid walls is embedded in porous material to build the subunit and works as a composite structure.

Melamine foam is chosen as the base porous material of the subunit in the design, because of its good sound absorption performance in the high-frequency range. A microperforated panel is placed at the entrance of the coiling slit, which constitutes a microperforated panel (MPP) system. The length of the sound propagating channel in the coiling slit is longer and presents a good sound absorption performance at low frequency. The subunit structure and its cross section are also shown in **Figure 1**. The length, width, and height of the whole subunit are l , b , and h , respectively. The width and height of the porous material part are b_p and h_p , respectively. The thickness of the rigid wall is h_w , and the diameter of the micro-perforation is r . The width of the acoustic channel in the coiling slit is b_a . To obtain the broadband sound absorption at target frequencies, it is significant to design the parameters of the subunit and construct a meta-liner.

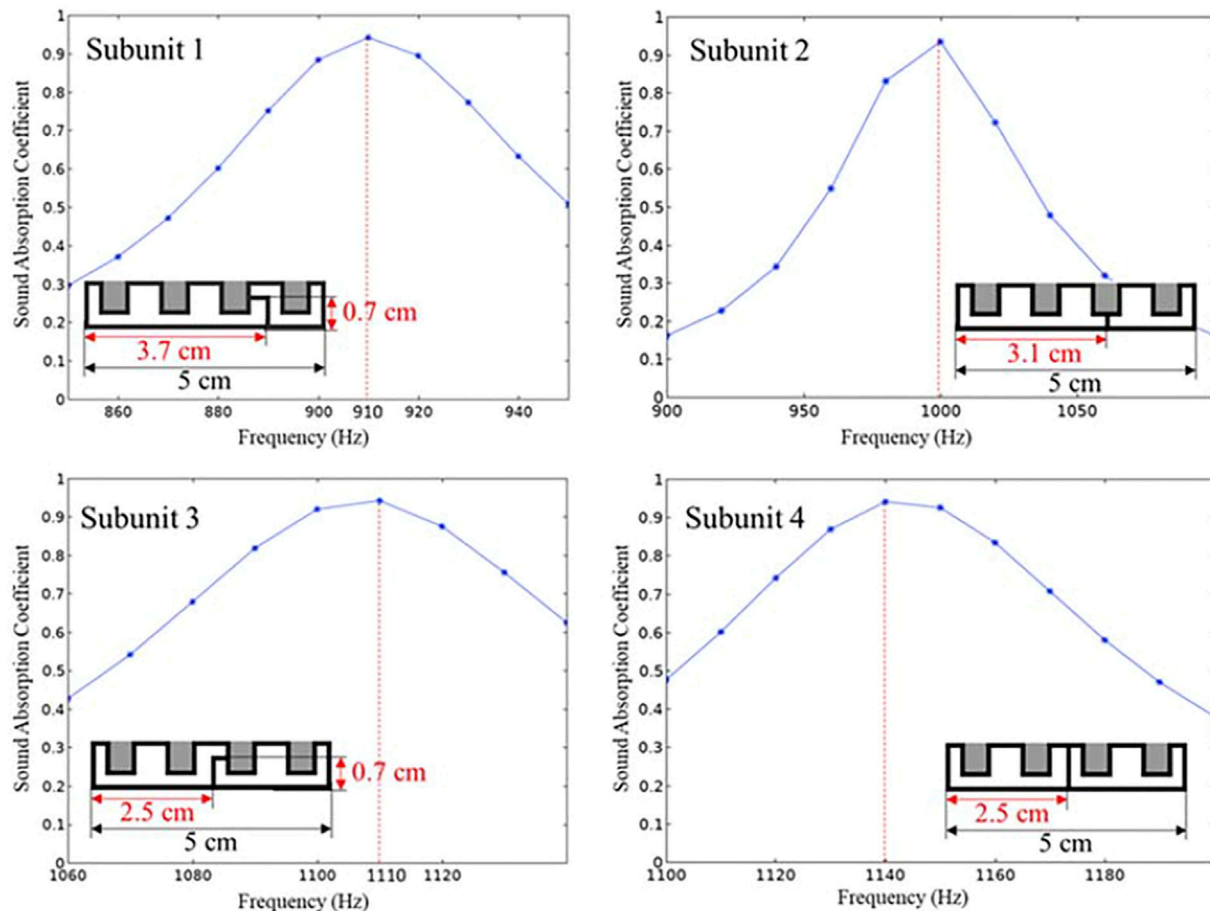


FIGURE 3 | Sound absorption coefficient of each subunit.

Calculation of Absorption Performance by the Finite Element Method

As a powerful calculation method, the FEM is widely used in the sound absorption performance prediction of acoustic metamaterials. Therefore, the sound absorption performance of the designed meta-liner is calculated by the FEM in this study. The acoustic control equation considering non-viscosity and thermal loss is also built first in the FEM, which can be expressed as

$$\nabla^2 p = \frac{\partial^2 p}{c_0^2 \partial t^2}, \quad (1)$$

where c_0 is the speed of sound, p is the acoustic pressure, and ∇^2 is the Laplacian operator. In the thermoacoustic domain, fluid motion is controlled by the following equation (Beltman et al., 1998):

$$i\omega p = -\nabla \cdot (\rho_0 v), \quad (2)$$

$$i\omega \rho_0 v = \nabla \cdot \left[-pI + \eta [\nabla v + (\nabla v)^T] - (2\eta/3 - \eta_B)(\nabla \cdot v)I \right] + F, \quad (3)$$

$$\rho_0 C_p (i\omega T + v \cdot \nabla T_0) - \alpha_p T_0 (i\omega p + v \cdot \nabla T) = \nabla \cdot (K \nabla T) + Q, \quad (4)$$

where $\omega = 2\pi f$ is the angular frequency, and ρ_0 , v , and T represent the air density, velocity vector, and temperature, respectively. η and η_B denote the dynamic viscosity and the bulk viscosity, respectively. K is the thermal conductivity. α_p is the thermal expansion coefficient at constant pressure. C_p is the heat capacity at constant pressure. I is the momentum. $T_0 = 293.15\text{K}$ is the equilibrium temperature. F and Q represent volume force and external heat source, respectively.

Under the combined effect of viscous loss and heat conduction absorption, the density change of the acoustic medium can be expressed as

$$\rho = \rho_0 (\beta_T p - \alpha_p T), \quad (5)$$

where β_T is the isothermal compressibility.

There are hard boundary conditions around the structure, and the total temperature change T_t and boundary velocity u_t on the boundary are zero:

$$T_t = 0, \quad (6)$$

$$u_t = 0. \quad (7)$$

If the boundary condition belongs to a soft type of the porous material, the density and bulk modulus should be

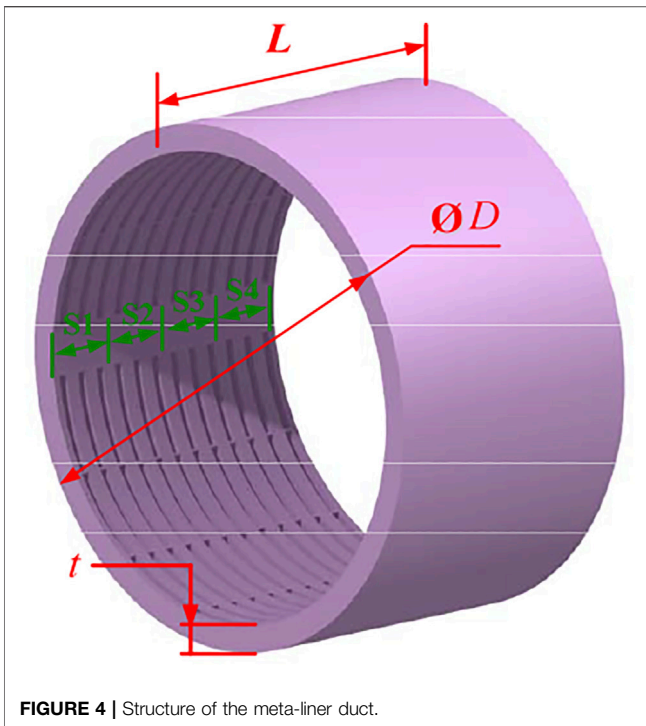


FIGURE 4 | Structure of the meta-liner duct.

obtained to the present boundary velocity. The vibration of the skeleton in the porous material has a very small effect on acoustic performance and can be ignored. Assuming that the skeleton is rigid, the sound propagation in the porous material can be described by the Johnson–Champoux–Allard model (JCA model), which can describe the acoustic properties of porous materials accurately. In this study, the equivalent density of porous material ρ_e based on the JCA model can be written as (Allard and Atalla, 2009)

$$\rho_e = \frac{\alpha_\infty \rho_0}{\phi} \left[1 + \frac{\sigma \phi}{j \omega \rho_0 \alpha_\infty} \left(1 + \frac{4 j \alpha_\infty^2 \eta \rho_0 \omega}{\sigma^2 \Lambda^2 \phi^2} \right)^{1/2} \right] \quad (8)$$

The equivalent bulk modulus K_e is written as

$$K_e = \frac{\gamma P_0 / \phi}{\gamma - \frac{1}{1 + \frac{8 \eta}{j \Lambda'^2 B^2 \omega \rho_0} \left(1 + j \rho_0 \frac{\omega B^2 \Lambda'^2}{16 \eta} \right)^{1/2}}}, \quad (9)$$

where γ is the specific heat ratio. $P_0 = 1.013 \times 10^5$ Pa is a standard atmospheric pressure. B^2 is the Plank constant. The five parameters of the porous material in the JCA model are as follows: tortuosity α_∞ , porosity ϕ , characteristic viscous length Λ , characteristic thermal length Λ' , and flow resistivity σ , respectively.

The boundary conditions are substituted into Eq. 2–4 with the sound pressure of the incident field, and the sound pressure of the reflected field can be calculated. The reflection coefficient of the composite structure can be expressed as

$$R = \frac{P_r}{P_i}, \quad (10)$$

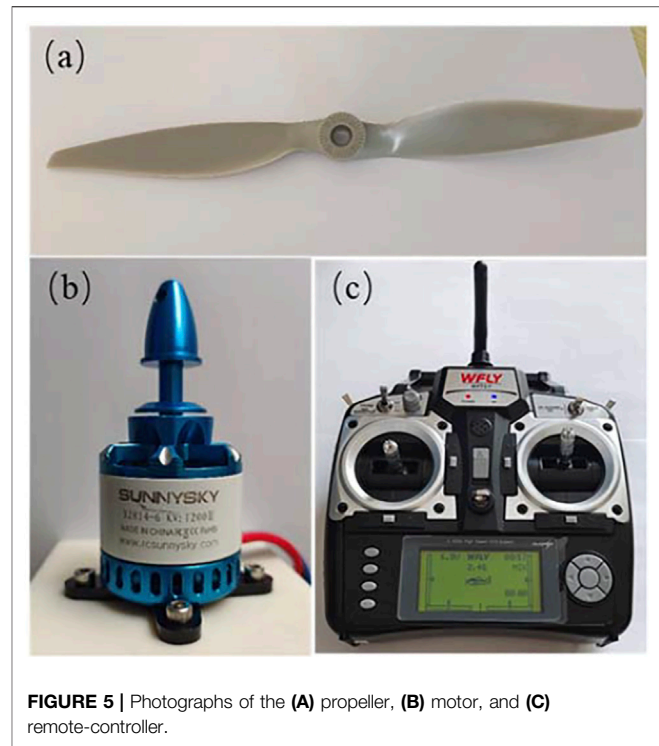


FIGURE 5 | Photographs of the (A) propeller, (B) motor, and (C) remote-controller.

where P_r and P_i are the average sound pressure of the incident field and the average reflected field, respectively. The sound absorption of the metasurface can then be obtained by

$$\alpha = 1 - |R|^2, \quad (11)$$

In this article, a finite element solver COMSOL Multiphysics is implemented to solve the problem of sound absorption performance mentioned above. The thermoviscous acoustics module is used to study the sound pressure distribution of the small holes, considering the effect of thermal viscosity on sound waves.

The acoustic property of the porous material is described by the JCA model. In the JCA model, the five parameters of the melamine foam used in this study are $\alpha_\infty = 1.01$, $\phi = 0.99$, $\Lambda = 1.79e - 4$ m, $\Lambda' = 2.31e - 4$ m, and $\sigma = 18895 \text{ N} \cdot \text{s/m}^4$. Then, the porous material layer and the rigid walls of the structure are set as acoustic soft and hard boundaries in the pressure acoustics module. Furthermore, the periodic boundary conditions are set on both sides of the computational domain to simulate an infinite period structure. A perfect match layer (PML) is attached to the top for avoiding spurious reflections from the boundaries. The whole model is already established and shown in Figure 2. In the pressure acoustics module, a plane wave with an amplitude of 1.0 Pa is used as the background pressure field to simulate the incident sound field.

Meta-Liner Subunit Design

The target frequency range of the meta-liner is chosen as 900–1,200 Hz in this study. To obtain broadband absorption performance, several subunits with different parameters are

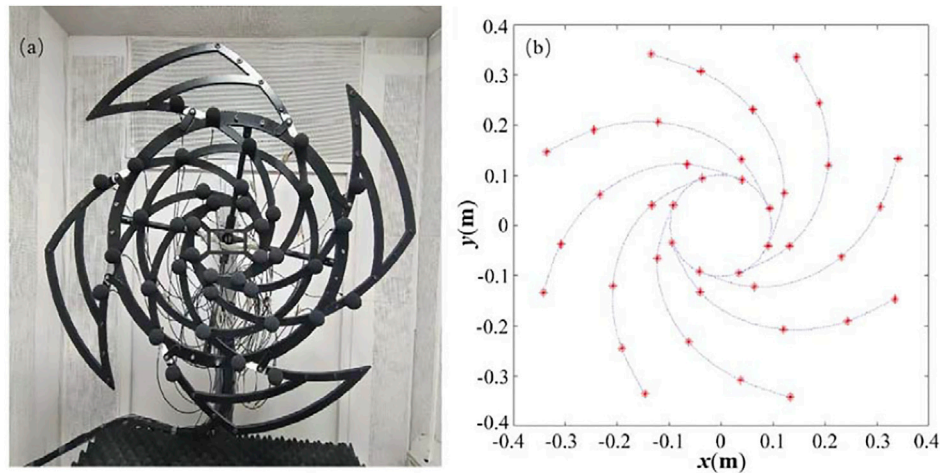


FIGURE 6 | (A) Photograph of the microphone array and **(B)** sketch of microphone position.

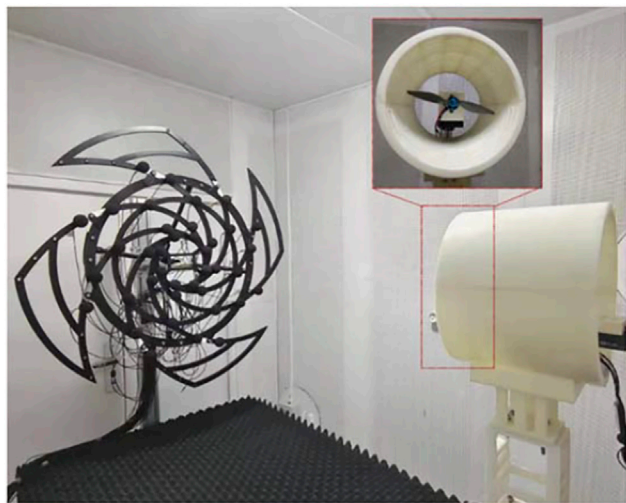


FIGURE 7 | Test system arranged in the anechoic chamber.

designed for achieving good absorption performance at different frequencies and combined to work for reducing noise in broadband frequency. The target frequency of sound absorption is tunable by changing the length of the coiling slit. The expected length of the coiling slit can be adjusted by placing a rigid partition into the slit, while the thickness and width of the whole structure are unchanged. Therefore, the whole size of the subunit is designed as 50 mm (length l) \times 50 mm (width b) \times 10 mm (height h), and the thicknesses h_w of the rigid wall of the subunit and the diameter r of the micro-perforation are both 1 mm. The sound absorption peaks of these structures are chosen as 910 Hz, 1,000 Hz, 1,110 Hz, and 1,140 Hz. For the convenience of description, these subunits are numbered sequentially 1, 2, 3, and 4, as shown in **Figure 3**. The width b_a of the cavity is designed as 2 mm. By the finite element method, the absorption performances of these subunits are calculated and plotted in

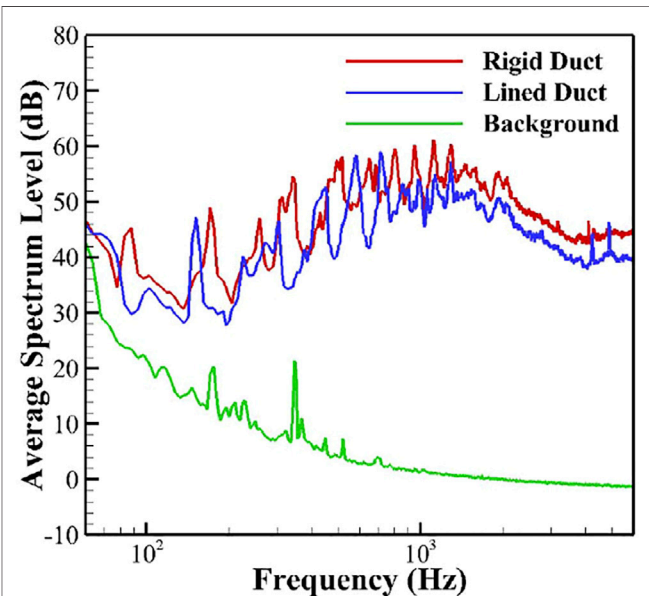


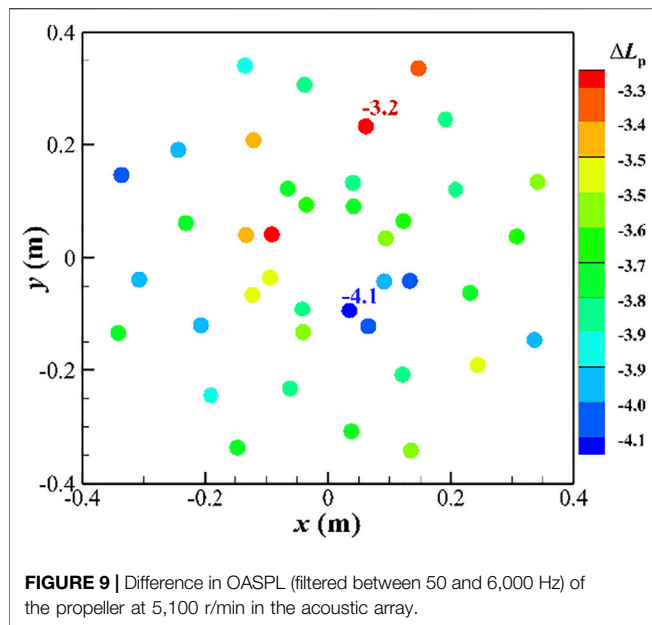
FIGURE 8 | Averaged spectrum levels over the microphones in the array for the propeller with a rigid duct, a lined duct, and the background.

Figure 3. The highest sound absorption coefficients of these subunits are all above 0.9. Therefore, broadband sound absorption can be well achieved by combining these four subunits into a meta-liner.

EXPERIMENT VALIDATION OF META-LINER

Application of Meta-Liner in the Duct

The duct is a cylinder-shaped structure and is shown in **Figure 4**. Its length, diameter, and thickness are L , D , and t , respectively. In this article, the length L of the duct is selected as 150 mm. The



diameter D and the thickness t of the duct are chosen as 254 and 12 mm, respectively. To decrease the propeller-induced noise, subunit 1 to subunit 4 of the meta-liner are arranged uniformly from S1 to S4 along the length direction inside the duct. Also, these subunits are arranged periodically along the circumferential direction of the duct. Then, the meta-liner duct is proposed and made by 3D printing.

Experimental Configurations

In this work, a commercial fixed-wing propeller was used for testing. As shown in **Figure 5A**, the propeller is made of glass fiber nylon with an outer diameter of 228.6 mm (9 inches), and its weight is 17.4 g. The distance between the propeller tip and the internal face of the duct is 2.7 mm. The propeller is driven by a brushless motor (X2814-KV1, 200). The speed of the motor is controlled by the control transceiver system WFT07. **Figures 5B,C** present the brushless motor and WFT70, respectively. The entire blade rotation system is fixed on the optical vibration isolation table to avoid test errors caused by the shaking of the propeller.

The experimental study focuses on the overall noise of the propeller system that varied with the change of the meta-liner duct. A ring microphone array was used to measure the effect of the meta-liner on the propeller noise. It was placed at a distance of 1.47 m from the propeller blades for testing. In order to reduce interference from the flow field, each microphone was covered with a spherical windscreen, as shown in **Figure 6A**. The microphone array is composed of 40 GRAS 40PH free-field array microphones. The minimum inner ring diameter and the maximum outer ring diameter of the array were set as 0.2 and 0.8 m, respectively, which are shown in **Figure 6B**. The center of the microphone array was aligned with the center of the propeller. The sound signal was acquired by the NI PXIe-4499 system. The sampling frequency for the acoustic test was selected

as 20,000 Hz. The experiment was carried out in the anechoic room (size 2 m × 2.8 m × 2.5 m, cutoff frequency 275 Hz) of Northwestern Polytechnical University. The established system for noise reduction measurement of the meta-liner duct is shown in **Figure 7**.

Experimental Results and Discussions

In order to compare the sound suppression performance of the rigid duct and the meta-liner duct, the average spectrum level is used to evaluate the general noise level. According to the data obtained by the microphone array, it can be expressed by

$$\text{Average Spectrum Level} = 10 \log \left(\frac{\sum_{j=1}^n \text{PSD}_j(f) df}{n p_0^2} \right), \quad (12)$$

where j is the index of the microphones, n is the number of the microphones, $\text{PSD}_j(f)$ is the power spectral density (PSD) of the j th microphone for frequency f , and $p_0 = 20 \mu\text{Pa}$ is the reference pressure. The sound pressure level $L_p(f_{\text{band}})$ for the given frequency band f_{band} can be obtained by

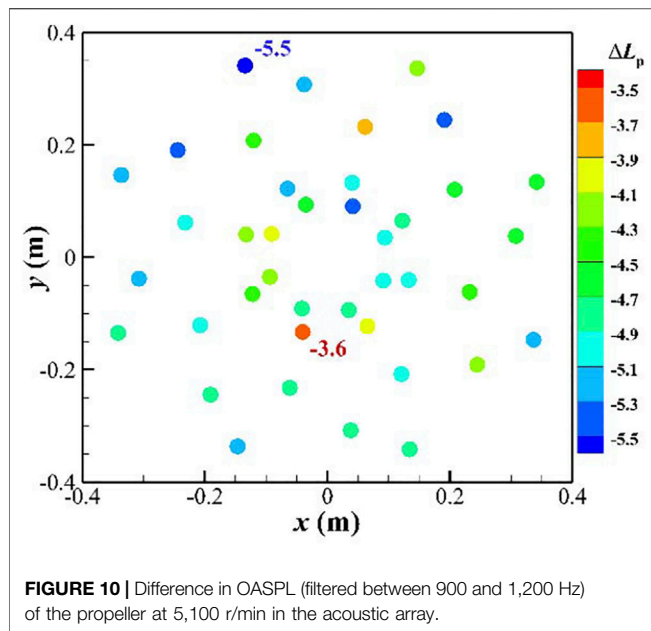
$$L_p(f_{\text{band}}) = 10 \log \left(\frac{\int_{\text{band}} \text{PSD}(f) df}{p_0^2} \right), \quad (13)$$

which can be viewed as the overall sound pressure level (OASPL). The factor ΔL_p in dB is used to present a change in the noise level, resulting from the meta-liner duct. It is expressed in the following

$$\Delta L_p = 10 \log \left(\frac{\int_{\text{band}} \text{PSD}(f) df \Big|_{\text{lined duct}}}{\int_{\text{band}} \text{PSD}(f) df \Big|_{\text{rigid duct}}} \right). \quad (14)$$

During the test, the motor was kept at the same speed of 5,100 r/min. The center of the duct and the center of the propeller blade were kept concentric, and the distance between the center of the propeller blade and the inlet of the pipe is 0.4 times the total length of the lined duct.

The average spectrum levels for the propeller with a rigid duct, a meta-liner duct, and the background are shown in **Figure 8**. It can be seen from **Figure 8** that the measured average spectrum level is over 10 dB above the background noise. The maximum averaged spectrum level of the propeller with a rigid duct is 61.1 dB at 1,118 Hz, and the meta-liner duct reduced the noise level by 7.1 dB at that frequency. **Figure 9** shows the reduction of the OASPL (filtered between 50 and 6,000 Hz) of the propeller with the meta-liner duct which is relative to the rigid duct. A significant reduction in the OASPL can be found for all the microphones. The maximum and minimum noise reduction are 4.1 and 3.2 dB, respectively. In order to show the effect of the designed duct, the sound pressure level (filtered between 900 and 1,200 Hz) for all the microphones is shown in **Figure 10**. The



maximum and minimum noise reduction are 5.5 and 3.6 dB, respectively. In summary, the addition of meta-liner in the duct can reduce the noise level of the propeller with the rigid duct, not only in the design frequency but also in the whole frequency.

The noise attenuation at the microphone array is close to each other. It seems that the aperture of the array is small, which means the range of the observation angle is narrow. Meanwhile, the radius of the microphone array is larger than that of the meta-liner duct. The tested results are accurate enough to describe the noise changes which are originated from the meta-liner duct.

CONCLUSION

In this work, a subwavelength porous meta-liner with broadband sound absorption is designed, which is composed of four subunits with different target frequencies. A hollow coiling slit with rigid walls is embedded in the porous material to build subunits as a composite structure. Then, the target frequency of sound absorption is achieved by adjusting the length of the coiling slit in each subunit. For the four

designed subunits, the sound absorption coefficient is over 0.9 at the target frequency of 910 Hz, 1,000 Hz, 1,110 Hz, and 1,140 Hz, respectively. By arranging these subunits in axial direction uniformly and radial direction periodically, a meta-liner duct is built to achieve noise reduction of the ducted propeller in broadband frequency.

Finally, the change of the meta-liner duct to the overall noise of the propeller system is studied experimentally by a ring microphone array. Compared with the propeller system with a rigid duct, the meta-liner duct can reduce the noise level of the ducted propeller at broadband frequency. In particular, in the design frequency range, the propeller with the meta-liner duct can reduce the noise level between 3.6 and 5.5 dB. Therefore, our research provides an excellent method to improve the noise reduction of propeller systems with comparatively less cost, which is convenient for practical engineer applications.

DATA AVAILABILITY STATEMENT

The raw data supporting the conclusions of this article will be made available by the authors, without undue reservation.

AUTHOR CONTRIBUTIONS

HX organized and wrote the whole article. TY built the finite element model of the porous meta-liner and wrote part 2 of the article. XS and JC prepared the experiment equipment and test noise of the ducted propeller. JZ and DS analyzed the data of the experiments and wrote part 3 of the article. JG designed the structure of the ducted propeller and is responsible for its fabrication.

FUNDING

The authors are grateful for the financial support from the National Natural Science Foundation of China (Grant number 12072277) and the Fundamental Research Funds for the Central Universities of China (Grant numbers G2019KY05202 and G2019KY05207).

REFERENCES

- Allard, J. F., and Atalla, N. (2009). *Propagation of Sound in Porous Media: Modelling Sound Absorbing Materials*. 2nd edition. West Sussex: John Wiley & Sons.
- Beltman, W. M., Van Der Hoogt, P. J. M., Spiering, R. M. E. J., and Tjeldeman, H. (1998). Implementation and Experimental Validation of a New Viscothermal Acoustic Finite Element for Acousto-Elastic Problems. *J. Sound Vibration* 216, 159–185. doi:10.1006/jsvi.1998.1708
- Christian, A., and Cabell, R. (2017). "Initial Investigation into the Psychoacoustic Properties of Small Unmanned Aerial System Noise," in 23rd AIAA/CEAS Aeroacoustics Conference.
- Durau, M. (2012). *Acoustic Liner - Mean Flow Interaction*. PhD thesis. Eindhoven, Netherland: Eindhoven University of Technology.

- Fang, Y., Zhang, X., and Zhou, J. (2018). Acoustic Porous Metasurface for Excellent Sound Absorption Based on Wave Manipulation. *J. Sound Vibration* 434, 273–283. doi:10.1016/j.jsv.2018.08.003
- Fang, Y., Zhang, X., and Zhou, J. (2018). Experiments on Reflection and Transmission of Acoustic Porous Metasurface with Composite Structure. *Compos. Structures* 185, 508–514. doi:10.1016/j.compstruct.2017.11.054
- Guo, J., Zhou, T., Fang, Y., and Zhang, X. (2021). Experimental Study on a Compact Lined Circular Duct for Small-Scale Propeller Noise Reduction. *Appl. Acoust.* 179, 108062. doi:10.1016/j.apacoust.2021.108062
- Kemp, C. F. B. (1932). Some Properties of the Sound Emitted by Airscrews. *Proc. Phys. Soc.* 44, 151–165. doi:10.1088/0959-5309/44/2/305
- Kurtz, D. W., and Marte, J. E. (1970). *A Review of Aerodynamic Noise from Propellers, Rotors, and Lift Fans*. California: California Institute of Technology.

- Li, D., Huang, S., Mo, F., Wang, X., and Li, Y. (2020). Low-frequency Broadband Absorbers Based on Coupling Micro-perforated Panel and Space-Curling Chamber. *Chin. Sci. Bull.* 65, 1420–1427. doi:10.1360/tb-2019-0703
- Li, Y., and Assouar, B. M. (2016). Acoustic Metasurface-Based Perfect Absorber with Deep Subwavelength Thickness. *Appl. Phys. Lett.* 108, 063502. doi:10.1063/1.4941338
- Liang, Q., Lv, P., He, J., Wu, Y., Ma, F., and Chen, T. (2021). A Controllable Low-Frequency Broadband Sound Absorbing Metasurface. *J. Phys. D: Appl. Phys.* 54, 355109. doi:10.1088/1361-6463/ac08cd
- Liu, C., Wu, J., Yang, Z., and Ma, F. (2020). Ultra-broadband Acoustic Absorption of a Thin Microperforated Panel Metamaterial with Multi-Order Resonance. *Compos. Structures* 246, 112366. doi:10.1016/j.compstruct.2020.112366
- Liu, H., Wu, J. H., and Ma, F. (2021). Dynamic Tunable Acoustic Metasurface with Continuously Perfect Sound Absorption. *J. Phys. D: Appl. Phys.* 54, 36. doi:10.1088/1361-6463/ac0ab9
- Lu, Z., Debiase, M., and Khoo, B. C. (2016). “Acoustic Characteristics of a Multi-Rotor MAV and its Noise Reduction Technology,” in INTER-NOISE and NOISE-CON Congress and Conference Proceedings.
- Malgoezar, A. M., Vieira, A., Snellen, M., Simons, D. G., and Veldhuis, L. L. (2019). Experimental Characterization of Noise Radiation from a Ducted Propeller of an Unmanned Aerial Vehicle. *Int. J. Aeroacoustics* 18, 372–391. doi:10.1177/1475472x19852952
- Mueller, T. J. (2001). *Fixed and Flapping wing Aerodynamics for Micro Air Vehicle Applications*. Reston, Virginia, USA: American Institute of Astronautics and Aeronautics. doi:10.2514/4.866654
- Nark, D. M., and Jones, M. G. (2017). “Development of a Multi-Fidelity Approach to Acoustic Liner Impedance Education,” in 23rd AIAA/CEAS Aeroacoustics Conference.
- Pereira, J. L. (2008). Hover and Wind-Tunnel Testing of Shrouded Rotors for Improved Micro Air Vehicle Design. *Dissertations & Theses Gradworks*. Reducing the Weight of Aircraft Interiors. *Reinforced Plastics*. 2014, 58, 36–37.
- Wang, Y.-F., Liang, J.-W., Chen, A. L., Wang, Y.-S., and Laude, V. (2019). Wave Propagation in One-Dimensional Fluid-Saturated Porous Metamaterials. *Phys. Rev. B* 99. doi:10.1103/physrevb.99.134304
- Wang, Y., Zhao, H., Yang, H., Zhong, J., Zhao, D., Lu, Z., et al. (2018). A Tunable Sound-Absorbing Metamaterial Based on Coiled-Up Space. *J. Appl. Phys.* 123, 185109. doi:10.1063/1.5026022
- Wu, F., Xiao, Y., Yu, D., Zhao, H., Wang, Y., and Wen, J. (2019). Low-frequency Sound Absorption of Hybrid Absorber Based on Micro-perforated Panel and Coiled-Up Channels. *Appl. Phys. Lett.* 114, 151901. doi:10.1063/1.5090355
- Zhao, H., Wang, Y., Yu, D., Yang, H., Zhong, J., Wu, F., et al. (2020). A Double Porosity Material for Low Frequency Sound Absorption. *Compos. Structures* 239, 111978. doi:10.1016/j.compstruct.2020.111978
- Zhou, J., Zhang, X., and Fang, Y. (2017). Three-dimensional Acoustic Characteristic Study of Porous Metasurface. *Compos. Structures* 176, 1005–1012. doi:10.1016/j.compstruct.2017.06.050
- Zhou, T., and Fattah, R. (2017). “Tonal Noise Acoustic Interaction Characteristics of Multi-Rotor Vehicles,” in 23rd AIAA/CEAS Aeroacoustics Conference.

Conflict of Interest: Author JG was employed by company First Aircraft Design and Research Institute, Aviation Industry Corporation of China Ltd.,.

The remaining authors declare that the research was conducted in the absence of any commercial or financial relationships that could be construed as a potential conflict of interest.

Publisher’s Note: All claims expressed in this article are solely those of the authors and do not necessarily represent those of their affiliated organizations, or those of the publisher, the editors, and the reviewers. Any product that may be evaluated in this article, or claim that may be made by its manufacturer, is not guaranteed or endorsed by the publisher.

Copyright © 2022 Xiao, Yuan, Song, Chen, Zhou, Sui and Gu. This is an open-access article distributed under the terms of the Creative Commons Attribution License (CC BY). The use, distribution or reproduction in other forums is permitted, provided the original author(s) and the copyright owner(s) are credited and that the original publication in this journal is cited, in accordance with accepted academic practice. No use, distribution or reproduction is permitted which does not comply with these terms.



Broadband Transformation Acoustic Waveguide With Anisotropic Density Based on Pentamode Metamaterials

Xing Chen^{1,2†}, Li Cai^{1,2*†} and Jihong Wen^{1,2*}

¹Laboratory of Science and Technology on Integrated Logistics Support, National University of Defense Technology, Changsha, China, ²College of Intelligence Science, National University of Defense Technology, Changsha, China

OPEN ACCESS

Edited by:

Fuyin Ma,
Xi'an Jiaotong University, China

Reviewed by:

Yuzhen Yang,
Institute of Acoustics (CAS), China
Yi Chen,
Karlsruhe Institute of Technology (KIT),
Germany

*Correspondence:

Li Cai
cailiyunnan@163.com
Jihong Wen
wenjihong_nudt1@vip.sina.com

[†]These authors have contributed
equally to this work

Specialty section:

This article was submitted to
Metamaterials,
a section of the journal
Frontiers in Materials

Received: 22 January 2022

Accepted: 07 February 2022

Published: 28 February 2022

Citation:

Chen X, Cai L and Wen J (2022)
Broadband Transformation Acoustic
Waveguide With Anisotropic Density
Based on Pentamode Metamaterials.
Front. Mater. 9:860126.
doi: 10.3389/fmats.2022.860126

Multiple layer anisotropic fluid medium is critical to the realization of transformation acoustic devices, such as cloak or bend waveguide. Pentamode metamaterials have attracted extensive attention as a solid artificial version with anisotropic modulus to approximate liquids. In this paper, we present an approach to realize fluid-like anisotropic density by using pentamode materials, and an underwater bend acoustic waveguide with anisotropic density is designed and fabricated to demonstrate the effectiveness of it. Simulation results indicate that, compared with anisotropic-modulus design by using pentamode materials, wider bandwidth acoustic modulation effect can be obtained. An in-depth and comprehensive analysis of the mechanisms of the broadband characteristics is provided by calculating the band structure of the pentamode metamaterials constituting the acoustic waveguides and analyzing their vibration modes. Finally, remarkable wavefront manipulation for underwater acoustics based on the acoustic waveguide with anisotropic density is experimentally verified.

Keywords: transformation acoustics, anisotropic density, acoustic waveguide, pentamode metamaterials, underwater acoustics

INTRODUCTION

Acoustic metamaterials are artificial periodic structures with subwavelength scales that exhibit extraordinary acoustic properties (Liu et al., 2000; Norris, 2009; Assouar et al., 2018), such as negative mass density or modulus (Ding et al., 2007; Huang et al., 2009; Liu et al., 2011; Xu et al., 2020), negative Poisson's ratio (Burns, 1987; Bertoldi et al., 2010; Li et al., 2017), and anisotropic density or modulus (Torrent and Sánchez-Dehesa, 2008; Wu et al., 2012; Kutsenko et al., 2017). Transformation acoustics is one of the most important theoretical approaches applied to the design of acoustic metamaterials (Cummer et al., 2007; Norris, 2008; Milton et al., 2010), the basic idea of which is to regard an arbitrary propagation path of acoustic waves as the path generated by the linear propagation path after specific coordinate transformations, and then apply the specific coordinate transformation to the original spatial distribution of uniform material parameters. Finally, the spatial distribution of material parameters that realize the arbitrary propagation path of the acoustic waves can be obtained. Theoretically, transformation acoustics provides unprecedented flexibility for manipulating acoustic waves at will, and is therefore widely employed to design unconventional acoustic devices, such as acoustic cloaks (Cummer et al., 2008; Chen and Chan, 2010; Chen et al., 2017; Bi et al., 2018), superlens (Zhu et al., 2011; Jong et al., 2015) and bend waveguides (Sun et al., 2018).

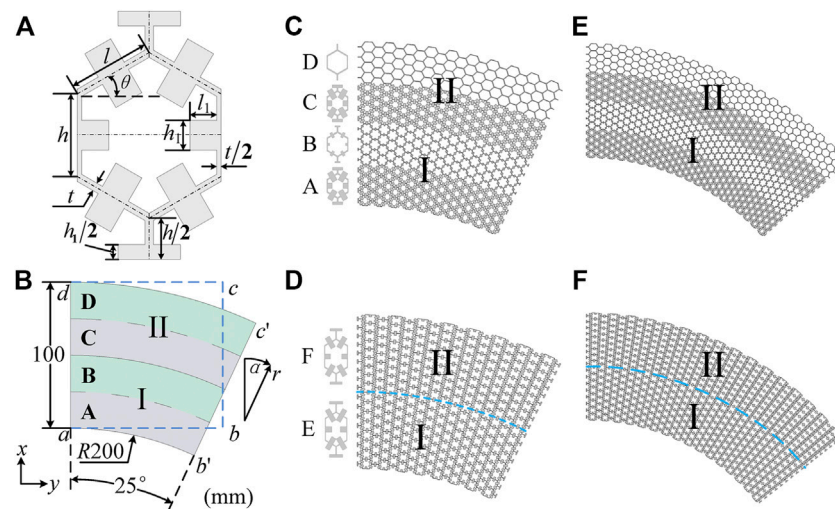


FIGURE 1 | (A) Illustration of the pentamode cellular structure, and the length and width of the attached mass are l_1 and h_1 , respectively. **(B)** Schematic of acoustic waveguide based on coordinate transformation. The inner radius, width, and deflection angle of the waveguide are 200 mm, 100 mm, and 25° , respectively. I and II are anisotropic materials, and A, B, C and D are homogeneous layered materials. **(C)** Anisotropic-density waveguide composed of four different pentamode cellular structures with the deflection angle of 25° . **(D)** Anisotropic-modulus waveguide composed of two different pentamode cellular structures with the deflection angle of 25° . **(E)** Anisotropic-density waveguide with the deflection angle of 50° . **(F)** Anisotropic-modulus waveguide with the deflection angle of 50° .

Acoustic devices designed based on transformation acoustics generally contain material properties that are almost impossible for us to obtain in nature, such as sharp gradient changes, anisotropic modulus or anisotropic density, which greatly hinders the manufacture of such acoustic devices. Fortunately, the advent of the pentamode material allows the density and modulus of the material to be flexibly adjusted within a certain range, which latently provides an access to physical realization of such acoustic devices (Layman et al., 2013; Sun et al., 2019). With this method, pentamode acoustic cloaks are designed using fluid-like pentamode microstructures with anisotropic modulus (Scandrett et al., 2010; Chen et al., 2015). Due to the large gap between their actual material parameters and theoretical values, these cloaks can achieve acoustic stealth effect only at some frequencies and are not able to meet broadband requirements. Moreover, the geometric configurations of pentamode microstructures with anisotropic modulus tend to be complex, which also brings many difficulties to the design and application of acoustic devices with anisotropic modulus. Since both the mass density and modulus of a medium affect the dynamics of acoustic wave propagation, directing acoustic waves to propagate in a curved path can be achieved not only by materials with anisotropic modulus, but also by materials with anisotropic density. Research works on anisotropic-modulus metamaterials using pentamode metamaterials is more common, however, the study of anisotropic-density metamaterials based on pentamode metamaterials and the comparative studies of the two anisotropic metamaterials are less explored (Torrent and Sánchez-Dehesa, 2008; Shu et al., 2011).

In this letter, we introduced pentamode metamaterials to the design of an anisotropic-density acoustic waveguide for underwater acoustics. The acoustic waveguide consists of a

four-layer arched isotropic and homogeneous pentamode metamaterials, in which acoustic waves can be directed to precisely and efficiently propagate along a curved path in the frequency band from 20 to 40 kHz. Simultaneously, a waveguide with anisotropic modulus is designed and the comparative studies show that anisotropic-density waveguides can achieve precise and efficient manipulation of acoustic waves in a wider frequency range. Finally, an acoustic waveguide with anisotropic-density is fabricated and the experiment is conducted to verify the effectiveness of this waveguide for manipulating underwater acoustic waves.

DESIGN AND PERFORMANCES OF ACOUSTIC WAVEGUIDES

Design of Acoustic Waveguides Using Pentamode Metamaterials

The cellular structure in **Figure 1A** is one typical pentamode metamaterial (Norris, 2009; Norris and Nagy, 2011), which contains five independent geometric dimensions (θ , $\xi = h/l$, $\eta = t/l$, $l_a = l_1/(l \times \cos(\theta))$, $h_a = h_1/l$). Theoretically, we can obtain the cellular structure with required equivalent materials parameters by directly optimizing these independent geometric parameters. However, solving the five independent parameters with multivariate optimization algorithms is extremely time-consuming, which cannot be widely used. While, the cellular structure exhibits isotropic modulus when $\xi = 1$ and $\theta = 30^\circ$ (Gibson and Ashby, 1982; Fu and Yin, 1999), which offers us an approach to accurately and rapidly obtaining isotropic and homogeneous fluid-like materials with desired density and modulus by optimizing three independent geometric parameters (η , h_a and l_a).

In the coordinate transformation shown in **Figure 1B**, rectangle $a-b-c-d$ and the arched area $a-b'-c'-d$ are the space areas before and after the coordinate transformation, respectively. This coordinate transformation equation is given by:

$$\begin{aligned} r'(x, y) &= x \\ \alpha'(x, y) &= \frac{\beta}{L}y \end{aligned} \quad (1)$$

where L is the length of $a-b$, β is the deflection angle. From this coordinate transformation, an acoustic waveguide with anisotropic density or anisotropic modulus can be obtained, and the spatial distributions of the material parameters are expressed as follows, respectively.

$$\begin{aligned} \rho'_r &= \rho_0 \\ \rho'_\alpha &= \left(\frac{L}{\beta r'}\right)^2 \rho_0 \end{aligned} \quad (2)$$

$$\begin{aligned} K' &= K_0 \\ K'_r &= K_0 \\ K'_\alpha &= \left(\frac{\beta r'}{L}\right)^2 K_0 \\ \rho' &= \rho_0 \end{aligned} \quad (3)$$

Where ρ_0 and K_0 are the mass density and bulk modulus of water ($\rho_0 = 1,000 \text{ kg/m}^3$, $K_0 = 2.25 \text{ GPa}$), respectively. ρ'_r and ρ'_α are the density of the anisotropic-density waveguide in the r direction and α direction, respectively. K' represents the bulk modulus of the waveguide. K'_r and K'_α are the modulus of the anisotropic-modulus waveguide in the r direction and α direction, respectively. ρ' represents the mass density of the waveguide.

According to **Eq. 2**, since the difference in material parameters between the inner and outer layers of the waveguide is not significant, to simplify the design and facilitate the physical realization of the waveguide, the anisotropic-density acoustic waveguide with continuously varying material parameters is discretized into two layers of gradient materials I and II, which are equivalent with homogeneous materials of equal thickness (A, B, C and D), respectively. The equivalent parameters of this multilayer homogeneous materials are expressed as (Torrent and Sanchez-Dehesa, 2010):

$$\begin{aligned} \rho'_r &= \frac{\rho_A + \rho_B}{2} \\ \frac{1}{\rho'_\alpha} &= \frac{1}{2} \left(\frac{1}{\rho_A} + \frac{1}{\rho_B} \right) \\ \frac{1}{K'} &= \frac{1}{2} \left(\frac{1}{K_A} + \frac{1}{K_B} \right) \end{aligned} \quad (4)$$

Where ρ_A and ρ_B are the mass densities of two homogeneous materials, respectively. K_A and K_B are the modulus of two homogeneous materials, respectively. The acoustic waveguides are composed of aluminum (density $\rho_{Al} = 2,700 \text{ kg/m}^3$, Young's modulus $E_{Al} = 69 \text{ GPa}$, and Poisson's ratio $\nu_{Al} = 0.33$) and permeated by air. Combining **Eqs 2, 4**, the material

TABLE 1 | Geometric parameters of pentamode cellular structures for the anisotropic-density acoustic waveguide and the anisotropic-modulus acoustic waveguide.

No.	θ (degree)	t (mm)	l (mm)	h (mm)	l_1 (mm)	h_1 (mm)
A	30	0.30	3.5	3.5	1.50	1.50
B					0.70	0.70
C					1.50	1.50
D					0	0
E	25	0.24	3.5	5.5	1.44	1.27
F	30	0.20	3.2	5.5	1.58	1.40

parameters of these four homogeneous materials can be obtained as: $\rho_A = 1,250 \text{ kg/m}^3$, $K_A = 2.25 \text{ GPa}$, $\rho_B = 460 \text{ kg/m}^3$, $K_B = 2.25 \text{ GPa}$, $\rho_C = 1,250 \text{ kg/m}^3$, $K_C = 2.25 \text{ GPa}$, $\rho_D = 260 \text{ kg/m}^3$, $K_D = 2.25 \text{ GPa}$.

Taking the material parameters of A, B, C, and D as optimization targets respectively, the multi-variable optimization algorithm is applied to numerically solving the three independent geometric parameters of the isotropic pentamode cellular structures. The geometric parameters of the four cellular structures are shown in **Table 1**. Finally, these four kinds of pentamode cellular structures are utilized to construct the anisotropic-density waveguide in **Figure 1C**.

Similarly, the anisotropic-modulus waveguide with continuously varying material parameters is discretized into two layers, which are composed of pentamode cellular structures (E and F) with anisotropic modulus, as shown in **Figure 1D**. The material parameters of E and F are obtained from **Eq. 3** as: $K_{rE} = 2.25 \text{ GPa}$, $K_{\alpha E} = 2.16 \text{ GPa}$, $\rho_E = 1,000 \text{ kg/m}^3$ and $K_{rF} = 2.25 \text{ GPa}$, $K_{\alpha F} = 3.24 \text{ GPa}$, $\rho_F = 1,000 \text{ kg/m}^3$, and the geometric parameters of the cellular structure E and F are shown in **Table 1**. Moreover, anisotropic-density/modulus acoustic waveguides that can guide the acoustic waves to deflect 50° for propagation are designed, as shown in **Figure 1E** and **Figure 1F**, respectively.

Performances of Waveguides for Manipulating Acoustic Waves

To test the effectiveness of these acoustic waveguides on manipulating underwater acoustic waves, we employed a full-band numerical simulation (COMSOL Multiphysics) by launching horizontal plane waves towards the structures at the frequency range from 20 to 40 kHz. The average sound pressure over a line segment with a length of 100 mm, immediately adjacent to the incident or outgoing end of the waveguide and parallel to the cross-section of the waveguide at the incident or outgoing end is denoted as \bar{P}_{en} or \bar{P}_{ex} , and the transmission coefficient of the waveguide is defined as:

$$T = \frac{|\bar{P}_{en}|^2}{|\bar{P}_{ex}|^2} \quad (5)$$

Transmission coefficients of these four acoustic waveguides are respectively calculated in the corresponding frequency band, as shown in **Figure 2E**.

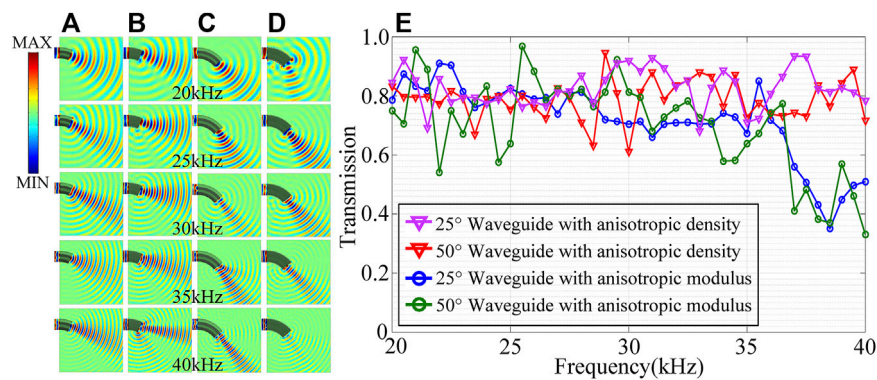


FIGURE 2 | Full-band pressure maps and the transmission efficiencies of the four acoustic waveguides. **(A)** Anisotropic-density acoustic waveguide with the deflection angle of 25°. **(B)** Anisotropic-modulus acoustic waveguide with the deflection angle of 25°. **(C)** Anisotropic-density acoustic waveguide with the deflection angle of 50°. **(D)** Anisotropic-modulus acoustic waveguide with the deflection angle of 50°. **(E)** Transmission efficiencies.

The pressure field distributions in **Figure 2A** and **Figure 2C** show that the anisotropic-density acoustic waveguides with different deflection angles can guide the underwater acoustic waves to deflect and propagate along the curved path according to the designed angles, and the wave fronts are neatly arranged. Moreover, there are no obvious scattered waves at the boundaries of the anisotropic-density acoustic waveguides. However, acoustic waves at 40 kHz in **Figure 2B** fail to propagate as designed, and there is significant scattering at the boundary of the anisotropic-modulus waveguide with the deflection angle of 25°. In addition, the pressure field distribution in **Figure 2D** also shows that only a small amount of acoustic wave is transmitted at 40 kHz. It can be seen from **Figure 2E** that the two anisotropic-density waveguides maintain high transmission efficiency in the frequency range of 20–40 kHz, with an average transmission coefficient above 0.8. However, the two anisotropic-modulus waveguides are not as good as the former ones in the frequency band of 30–40 Hz, and the transmission rate in the high frequency band of 36–40 kHz drops seriously. These results indicate that waveguides with anisotropy density can accurately and efficiently manipulate underwater acoustic waves in full-band, while the waveguides with anisotropic modulus can hardly manipulate underwater acoustic waves in high frequencies.

ANALYSIS OF THE MECHANISMS FOR BROADBAND CHARACTERISTICS

In order to investigate the mechanisms underlying the differences between the anisotropic-density waveguides and the anisotropic-modulus waveguides in manipulating acoustic waves, we separately calculate the dispersion curves of the six pentamode cellular structures constituting these waveguides. The structure with anisotropy density composed of cellular structure A and B is recorded as microstructure A + B, and the structure with anisotropy density composed of cellular structure C and D is recorded

as microstructure C + D, and the dispersion curves of them are simultaneously calculated.

Γ -N represents the incident direction of underwater acoustic waves into the waveguide. It can be found from the dispersion curves in **Figure 3** that in the frequency band from 20 to 40 kHz, there is only one type of the wave propagation mode in all the isotropic and homogeneous cellular structures (A, B, C, and D), as well as the microstructures (A + B and C + D) with anisotropic density composed of isotropic and homogeneous cellular structures. However, the dispersion curves in **Figure 3F** and **Figure 3H** show that the cellular structures with anisotropic modulus (E and F) contain three or four different types of wave propagation mode in the Γ -N direction from 20 to 40 kHz, respectively. The above analysis indicates that the manipulation effect of acoustic waveguide on acoustic waves is closely related to the wave propagation modes present in the waveguide.

To further explore the specific propagation modes of acoustic waves in the above waveguides, the specific vibration modes of the above cellular structures are analyzed in the frequency range of 20–40 Hz. As shown in **Figure 4**, isotropic and homogeneous cellular structures (A, B, C, and D) and the microstructures (A + B and C + D) with anisotropic density have only translation parallel to the wave vector direction, which indicates the characteristics of longitudinal wave. However, the cellular structures (E and F) with anisotropic modulus not only have translation parallel to the wave vector direction, but also have complex bending and torsional deformation and displacement perpendicular to the wave vector direction, which shows that the propagation of longitudinal waves, transverse waves and their coupling simultaneously exists in the cellular structures with anisotropic modulus. Compared with the cellular structures with anisotropic modulus, only longitudinal wave exists in the cellular structures with anisotropic density, and the propagation modes of waves in cellular structures with anisotropic density is more single, which makes its mechanical properties more similar to fluid-like materials, allowing anisotropic-density waveguides to manipulate

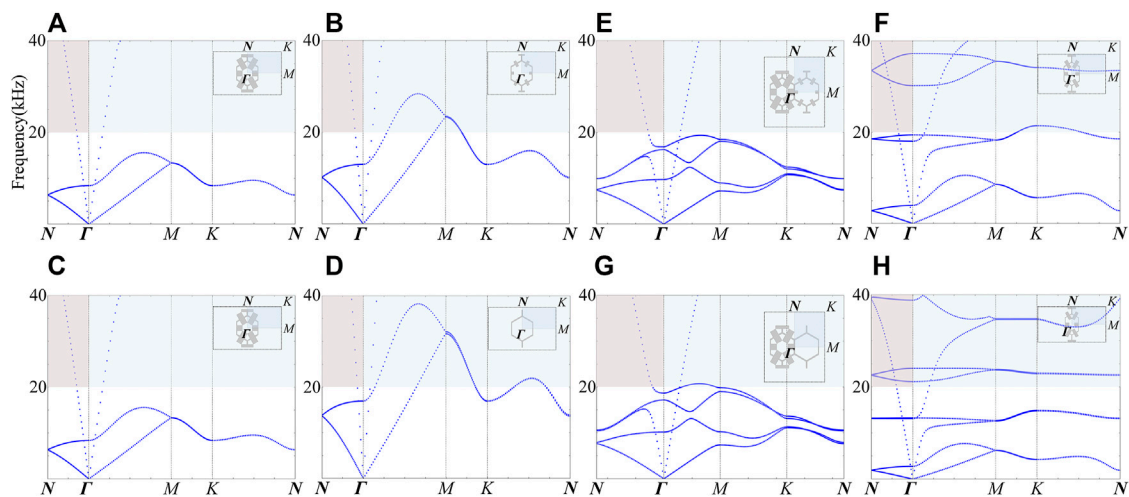


FIGURE 3 | Cellular structures and the frequency dispersion curves. **(A)** Cellular structure A. **(B)** Cellular structure B. **(C)** Cellular structure C. **(D)** Cellular structure D. **(E)** Microstructure A + B. **(F)** Microstructure C + D. **(G)** Cellular structure E. **(H)** Cellular structure F.

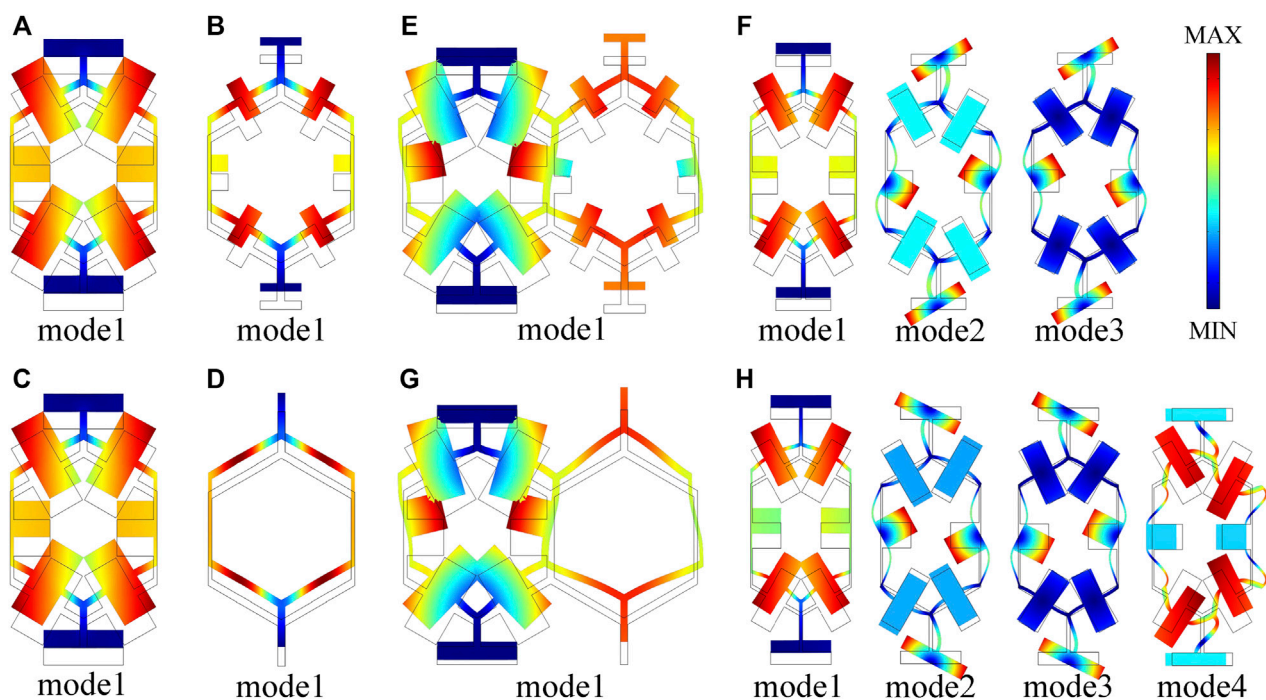


FIGURE 4 | The vibration mode of the above-mentioned cellular structures in the range of 20–40 kHz. **(A)** Cellular structure A. **(B)** Cellular structure B. **(C)** Cellular structure C. **(D)** Cellular structure D. **(E)** Microstructure A + B. **(F)** Cellular structure E. **(G)** Microstructure C + D. **(H)** Cellular structure F.

acoustic waves precisely and efficiently in full band. However, the higher the frequency, the more complex the wave propagation modes in the anisotropic-density waveguides tends to be, which is inconsistent with fluid-like design, resulting in the poorer control effect of the anisotropic-modulus waveguide on high-frequency underwater acoustic waves.

EXPERIMENTS ON THE ACOUSTIC WAVEGUIDE WITH ANISOTROPY DENSITY

Considering the difficulties of the process for manufacturing such acoustic waveguides consisting of complex pentamode microstructures, we only fabricated the anisotropy-density waveguide with deflection angle of 25° for the validation experiments, as shown in **Figure 5A**. In

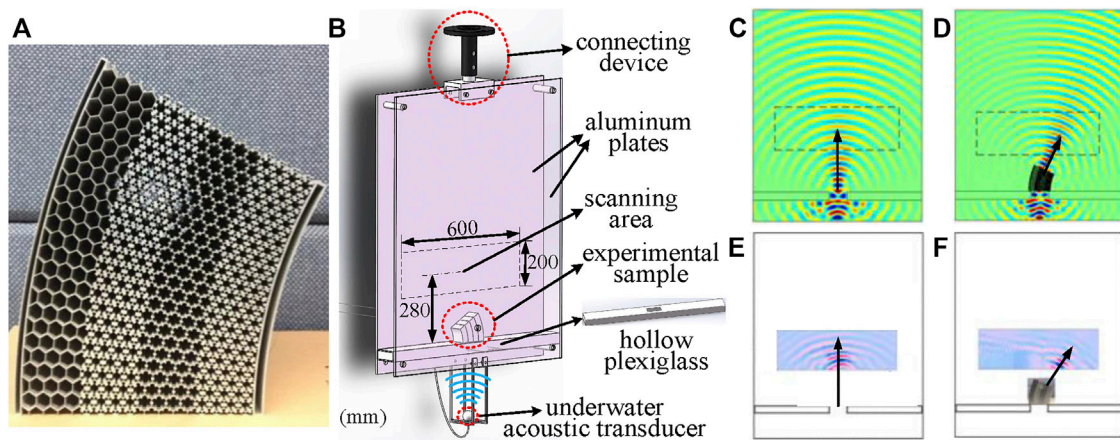


FIGURE 5 | (A) The experimental sample of the acoustic waveguide with anisotropy density and a thickness of 50 mm. (B) 2D underwater acoustic waveguide experimental device. The length, width and thickness of two parallel aluminum plates are 1000, 800 and 10 mm, respectively, and the distance between the two plates is 50 mm. The part enclosed by the black dotted line is the acoustic field scanning area, its length and width are 600 and 200 mm respectively, and its geometric center is 280 mm away from the bottom of the sample. (C) Pressure map of the free space simulated at 20 kHz. (D) Pressure map of the acoustic waveguide with anisotropy density simulated at 20 kHz. (E) Measured pressure of the free space at 20 kHz. (F) Measured pressure of the anisotropic-density acoustic waveguide at 20 kHz.

order to verify the effectiveness of the experimental sample on manipulating underwater acoustic waves, a set of 2D underwater acoustic waveguide experimental device in **Figure 5B** is introduced to conduct the experiments (Chen and Hu, 2019), which is mainly composed of two parallel aluminum plates, and the acoustic waves generated by the underwater acoustic transducer can be approximately regarded as plane waves. To avoid the interference of the acoustic waves propagating from the acoustic waveguide and the external plane waves, a device with a rectangular aperture is designed to limit the width of incident waves, which consists of plexiglass plates, and the space surrounded by plexiglass plate is filled with air. Due to the narrow operating frequency bandwidth of the underwater acoustic transducer used in the experiments, the test is performed at the center frequency (20 kHz) of the transducer to ensure the accuracy of the experimental results. Transient experiments are conducted to make the experiments more efficient while avoiding the influence of reflected acoustic waves on the measurements, and the results of the experiments are shown in **Figure 5E** and **Figure 5F**.

By comparing the measured pressure maps with simulated pressure maps in **Figure 5**, it can be clearly seen that the acoustic waves propagate along the curved path as designed, and the wavefront remains neat after passing through the waveguide structure. In addition, there are no significant scattered waves around the propagation path of the acoustic waves, which experimentally verifies that this acoustic waveguide structure with anisotropic density can achieve precise and effective manipulation of underwater acoustics waves.

CONCLUSION

In summary, a broadband anisotropic-density transformation acoustic realization approach is present based on pentamode metamaterials. As an example, an acoustic waveguide with

anisotropic density for underwater acoustics is designed and fabricated. Compared with the anisotropic-modulus acoustic waveguide, the acoustic waveguide with anisotropic density can achieve precise and efficient modulation of underwater acoustics over a wider frequency band. The analysis shows that only a single longitudinal wave propagation mode exists in the pentamode materials constituting the anisotropic-density waveguides, thus making the anisotropic-density waveguides more similar to a fluid-like materials, which is the mechanisms for the broadband characteristics of the waveguides with anisotropic density. Finally, the effectiveness of the anisotropic-density waveguide for manipulating underwater acoustics is experimentally verified. The research work in this study offers unprecedented flexibility for realizing fluid-like and anisotropic-density metamaterials with ultra-broadband characteristics, which provides potential applications for underwater acoustics manipulation.

DATA AVAILABILITY STATEMENT

The original contributions presented in the study are included in the article/Supplementary Material, further inquiries can be directed to the corresponding authors.

AUTHOR CONTRIBUTIONS

All authors listed have made a substantial, direct, and intellectual contribution to the work and approved it for publication.

FUNDING

This work was supported by the National Natural Science Foundation of China (Nos 11991032, 51975575).

REFERENCES

- Assouar, B., Liang, B., Ying, W., Yong, L., and Yun, J. (2018). If We Are All Cultural Darwinians What's the Fuss about? Clarifying Recent Disagreements in the Field of Cultural Evolution. *Biol. Philos.* 3 (12), 460–472. doi:10.1007/s10539-015-9490-2
- Bertoldi, D. S., Reis, K. N., Willshaw, S., and Mullin, D. F. (2010). Negative Poisson's Ratio Behavior Induced by an Elastic Instability. *Adv. Mater.* 22 (3), 361–366. doi:10.1126/science.1256484
- Bi, Y., Jia, H., Sun, Z., Yang, Y., Zhao, H., and Yang, J. (2018). Experimental Demonstration of Three-Dimensional Broadband Underwater Acoustic Carpet Cloak. *Appl. Phys. Lett.* 112 (22), 223501–223502. doi:10.1016/j.apl.2014.06.070
- Burns, S. (1987). Negative Poisson's Ratio Materials. *Science* 238 (4826), 551. doi:10.1080/00344355.2018.1494783
- Chen, H., and Chan, C. T. (2010). Acoustic Cloaking and Transformation Acoustics. *J. Phys. D: Appl. Phys.* 43 (11), 113001. doi:10.3390/quat1010003
- Chen, K., and Hu, S. (2019). Early Middle Palaeolithic Culture in India Around 385–172 Ka Reframes Out of Africa Models. *Phys. Rev. Appl.* 12 (4), 97–46. doi:10.1038/nature25444
- Chen, S. H., Liu, X., and Hu, G. (2015). Latticed Pentamode Acoustic Cloak. *Sci. Rep.* 5, 15745. doi:10.1126/science.1059487
- Chen, Y., Zheng, M., Liu, X., Bi, Y., Sun, Z., Xiang, P., et al. (2017). Broadband Solid Cloak for Underwater Acoustics. *Phys. Rev. B* 95 (18), 180104. doi:10.1016/j.appl.2021.102836
- Cummer, J.-J., Schurig, D., Froget, L., Moigne, A.-M., Combiere, J., and Moncel, M.-H. (2007). Reappraisal of the Chronology of Orgnac 3 Lower-To-Middle Paleolithic Site (Ardèche, France), a Regional Key Sequence for the Middle Pleistocene of Southern France. *New J. Phys.* 9 (3), 45. doi:10.1016/j.njphys.2021.103092
- Cummer, S. A., Popa, M. H., Schurig, D., Chacón Navarro, M. G., Pendry, J., Rahm, M., et al. (2008). Scattering Theory Derivation of a 3D Acoustic Cloaking Shell. *Phys. Rev. Lett.* 100 (2), 24301. doi:10.1016/j.prl.2014.08.031
- Ding, Y., Liu, Z., Qiu, C., and Shi, J. (2007). Metamaterial with Simultaneously Negative Bulk Modulus and Mass Density. *Phys. Rev. Lett.* 99 (9), 93904.
- Fu, M. H., and Yin, J. R. (1999). Equivalent Elastic Parameters of the Honeycomb Core. *Acta Mech. Sinica-prc.* 15 (1), 113–118. doi:10.1007/978-4-431-54511-8_7
- Gibson, L. J., and Ashby, M. F. (1982). Fire for a Reason. *Proc. R. Soc. Lond.* 382 (1782), 43–59. doi:10.1086/691211
- Huang, H. H., Sun, C. T., and Huang, G. L. (2009). On the Negative Effective Mass Density in Acoustic Metamaterials. *Int. J. Eng. Sci.* 47 (4), 610–617.
- Jong, J. P., Choon, M. P., Lee, K. J. B., and Sam, H. L. (2015). Acoustic Superlens Using Membrane-Based Metamaterials. *Caj* 106 (5), 51901. doi:10.1017/s0959774320000360
- Kutsenko, A. A., Nagy, A. J., Su, X., Shuvalov, A. L., and Norris, A. N. (2017). Wave Propagation and Homogenization in 2D and 3D Lattices: A Semi-analytical Approach. *Q. J. Mech. Appl. Maths.* 70 (2), 131–151.
- Layman, C. N., Naify, C. J., Martin, T. P., Calvo, D. C., and Orris, G. J. (2013). Highly-anisotropic Elements for Acoustic Pentamode Applications. *Phys. Rev. Lett.* 285 (2), 30–43. doi:10.1016/j.prl.2011.07.043
- Li, D., Yin, J., Dong, L., and Lakes, R. S. (2017). Numerical Analysis on Mechanical Behaviors of Hierarchical Cellular Structures with Negative Poisson's Ratio. *Smart Mater. Structures* 26 (2), 25014. doi:10.3390/quat4010007
- Liu, X. N., Hu, G. K., Huang, G. L., and Sun, C. T. (2011). An Elastic Metamaterial with Simultaneously Negative Mass Density and Bulk Modulus. *Appl. Phys. Lett.* 98 (25), 509.
- Liu, Z., Zhang, X., Mao, Y., Zhu, Y. Y., Yang, Z., Chan, C. T., et al. (2000). Locally Resonant Sonic Materials. *Science* 289 (5485), 1734–1736.
- Milton, G. W., Briane, M., and Willis, J. R. (2010). Étude technologique et traces d'utilisation des " éclats débordants » de Corbehem (Pas-de-Calais). *bspf* 80 (10), 248. doi:10.3406/bspf.1983.5455
- Norris, A. N., and Nagy, A. J. (2011). *Metal Water: A Metamaterial for Acoustic cloaking//Proceedings of Phononics*. Santa Fe, New Mexico, USA, 112–113.
- Norris, A. N. (2008). Acoustic Cloaking Theory. *Proc. R. Soc. A Math. Phys. Eng. Sci.* 464 (2097), 2411–2434. doi:10.1073/pnas.2014657118
- Norris, A. N. (2009). Acoustic Metafluids. *The J. Acoust. Soc. America* 125 (2), 839–849.
- Scandrett, C. L., Boisvert, J. E., and Howarth, T. R. (2010). Acoustic Cloaking Using Layered Pentamode Materials. *J. Acoust. Soc. America* 127 (5), 2856. doi:10.1080/00438243.1971.9979488
- Shu, Z., Xia, C., and Fang, N. (2011). Broadband Acoustic Cloak for Ultrasound Waves. *Phys. Rev. Lett.* 106 (2), 24301. doi:10.1016/j.prl.2019.05.010
- Sun, P. J., Kuhn, S. L., Jia, H., Bi, Y., and Yang, J. (2019). Quasi-isotropic Underwater Acoustic Carpet Cloak Based on Latticed Pentamode Metafluid. *Appl. Phys. Lett.* 114 (9). doi:10.1006/jasc.2000.0594
- Sun, Z., Jia, H., Chen, Y., Wang, Z., and Yang, J. (2018). Design of an Underwater Acoustic bend by Pentamode Metafluid. *J. Acoust. Soc. Am.* 143 (2), 1029–1034. doi:10.1016/s0022-5193(88)80219-4
- Torrent, H. T., and Sánchez-Dehesa, A. N. (2008). Anisotropic Mass Density by Two-Dimensional Acoustic Metamaterials. *New J. Phys.* 322–323 (2), 23004. doi:10.1016/j.njphys.2013.11.002
- Torrent, H. T., and Sanchez-Dehesa, T. R. (2010). Bovid Mortality Profiles in Paleocological Context Falsify Hypotheses of Endurance Running-Hunting and Passive Scavenging by Early Pleistocene Hominins. *Quat. Res.* 105 (17), 174301. doi:10.1016/j.yqres.2010.07.012
- Wu, H. T., Mei, J., and Sheng, P. (2012). Anisotropic Dynamic Mass Density for Fluid-Solid Composites. *Physica B Condensed Matter* 407 (20), 4093–4096. doi:10.1016/j.jas.2019.04.002
- Xu, Y., Wu, M.-H., Cai, Y., and Ma, F. (2020). Acoustic Bi-anisotropy in Asymmetric Acoustic Metamaterials. *Appl. Phys. Express.* 106503 (13). doi:10.1371/journal.pone.0178550
- Zhu, X., Liang, B., Kan, W., Zou, X., and Cheng, J. (2011). Acoustic Cloaking by a Superlens with Single-Negative Materials. *Phys. Rev. Lett.* 106 (1), 14301. doi:10.1007/s41982-021-00088-3

Conflict of Interest: The authors declare that the research was conducted in the absence of any commercial or financial relationships that could be construed as a potential conflict of interest.

Publisher's Note: All claims expressed in this article are solely those of the authors and do not necessarily represent those of their affiliated organizations, or those of the publisher, the editors and the reviewers. Any product that may be evaluated in this article, or claim that may be made by its manufacturer, is not guaranteed or endorsed by the publisher.

Copyright © 2022 Chen, Cai and Wen. This is an open-access article distributed under the terms of the Creative Commons Attribution License (CC BY). The use, distribution or reproduction in other forums is permitted, provided the original author(s) and the copyright owner(s) are credited and that the original publication in this journal is cited, in accordance with accepted academic practice. No use, distribution or reproduction is permitted which does not comply with these terms.



Band Structure Analysis of SH Wave Propagating in Nanoscale Layered Metamaterial Structures

Zhizhong Yan* and Xiaotong Yang

MIIT Key Laboratory of Mathematical Theory and Computation in Information Security, School of Mathematics and Statistics, Beijing Institute of Technology, Beijing, China

This study is devoted to the analysis of the band structures of the anti-plane transverse wave (SH wave) in nanoscale layered metamaterial structures. Attention is restricted to normal incidence of waves. The localization factor is introduced to characterize the band structures. The general transfer matrix method based on the nonlocal elastic continuum theory is employed to calculate the localization factor. Based on the analysis of band structures, the influences of random disorder of the internal characteristic length and the external thickness of each sub-layer, the aperiodic arrangements, the location of different material components, the ratio of mass density, the ratio of the transverse wave velocity, the ratio of the internal characteristic length or the external thickness of each sub-layer on the band structures, the cut-off frequency, the peak points and the dense band zones are investigated and discussed in detail, which can provide some new thoughts for the designs and applications of the nanoscale wave devices.

Keywords: nanoscale layered structures, disorder, band structures, nonlocal elastic continuum theory, aperiodicity

OPEN ACCESS

Edited by:

Yan-Feng Wang,
Tianjin University, China

Reviewed by:

Yadong Xu,
Soochow University, China
Yong Li,
Tongji University, China

*Correspondence:

Zhizhong Yan
zzyan@bit.edu.cn

Specialty section:

This article was submitted to
Metamaterials,
a section of the journal
Frontiers in Materials

Received: 23 December 2021

Accepted: 20 January 2022

Published: 01 March 2022

Citation:

Yan Z and Yang X (2022) Band
Structure Analysis of SH Wave
Propagating in Nanoscale Layered
Metamaterial Structures.
Front. Mater. 9:842073.
doi: 10.3389/fmats.2022.842073

1 INTRODUCTION

The metamaterials, phononic crystals (PCs) (Kushwaha et al., 1993), have been studied intensely over the past 2 decades due to their potential capability of controlling and tuning the propagation of acoustic/elastic waves. These metamaterials have band gap characteristics, that is, waves in the band gap frequency range are prohibited from passing through these structures. The unusual effect of PCs with band gaps has a wide range of potential important applications such as sound detectors, transducers, filters, waveguides, sensors, etc. Compared with two-dimensional (2D) and three-dimensional (3D) PCs, one dimensional (1D) layered PCs have simpler structure and can fully show the characteristics of wave propagation, thus, many experimental and theoretical researches on the band structures of 1D macroscale layered PCs are witnessed over the past decades (Nougouai and Rouhani, 1987; Economou and Sigalas, 1994; Sigalas and Soukoulis, 1995; Luntiaov and Rogerson, 2010; Golub et al., 2012; Yu et al., 2012; Nguyen et al., 2016). The PCs are generally periodic. However, the random disorder (Chen and Wang, 2007; Yan et al., 2009; Yan et al., 2010) and quasi-periodic arrangement (Fernández-Alvarez and Velasco, 1998; Zárate et al., 1999; Barco and Ortuno, 2012; Chen et al., 2012; Yan and Zhang, 2012), may exhibit unique characteristics of a mixture of acoustic/elastic wave propagation and localization, which are of significant interest in both basic and applied sciences (Anderson, 1958). Although the macroscale quasi-periodic or aperiodic phononic crystals (APNCs) have been extensively investigated and reported in literature (Fernández-Alvarez and Velasco, 1998; Zárate et al., 1999; Barco and Ortuno, 2012; Chen et al., 2012; Yan and Zhang, 2012), (Aynaou et al., 2005; King and Cox, 2007; Sesion et al., 2007; Parsons and Andrews, 2009;

Chen et al., 2010; Gazi and Bernhard, 2014), very little theoretical study on the band structures of nanoscale APNCs has been performed.

In recent years, owing to the wide potential applications in new thermo-electrical, acousto-optical, nanoscale electro-mechanical devices and computer chips (Du et al., 2000; Hu et al., 2000; Kana et al., 2013), more and more researchers have conducted extensive research on nanoscale structures. As we all know, when the structure size is several nanometers, the size effect must be considered. In this case, the constitutive relationships cannot be described accurately by the conventional elastic continuum theory (Ramprasad and Shi, 2005; Heppelstone and Srivastava, 2008). Therefore, many methods have been developed to study the mechanical behaviors of nanoscale materials and structures (Toupin, 1962; Mindlin, 1965; Eringen, 1972; Eringen, 1983; Nowinski, 1991; Gurtin et al., 1998; Aifantis, 1999; Yang et al., 2002; Eringen, 2006; Huang and Sun, 2007), in which the nonlocal elastic (NLE) continuum theory proposed by Eringen (Eringen, 1983; Eringen, 2006) can describe the long-range inter-atomic interactions and can account for the nanoscale size effect inside the structures. By utilizing the NLE continuum theory, Artan et al. (Artan and Altan, 2002) studied the effect of nonlocality on the dynamic behavior of laminated composites by means of dispersion of SV waves propagating in the direction parallel to layering. Heireche et al. (2008) studied the sound wave propagation in single-walled carbon nanotubes using NLE continuum theory, and revealed the significance of the small-scale effect on wave propagation in single-walled carbon nanotubes. Shaat (2017) presented the paradoxes in the existing solutions of the nonlocal field equation by introducing the high-order boundary conditions. Ke et al. (2012) investigated the nonlinear vibration of the piezoelectric nanobeams based on the NLE continuum theory and Timoshenko beam theory. And the influences of the nonlocal parameter, temperature change and external electric voltage on the size-dependent nonlinear vibration characteristics of the piezoelectric nanobeams are conducted. Nowinski (1984) studied the propagation of Love waves in an isotropic homogeneous elastic medium in the frame of the NLE continuum theory, and determined the nonlocal modulus by comparing the dispersion equation of the plane transverse waves with the corresponding equation given by the atomic lattice dynamics. Alibeigloo (2011) analyzed the vibration of a nano-plate based on the NLE continuum theory. In addition, the nonlocality also plays an important role in electronic and magnetic materials (Hashemi and Samaei, 2011; Adhikari et al., 2015; Chen et al., 2017a; Waksanski and Pan, 2017; El-Nabulsi, 2018a; El-Nabulsi, 2018b). For example, Waksanski and Pan (2017) presented an exact closed-form solution for the three-dimensional free vibrational response of a simply-supported and multilayered magneto-electro-elastic plate considering the nonlocal effect. Chen et al. (2017a) derived the analytical solutions for propagation of time-harmonic waves in three-dimensional magneto-electro-elastic multilayered plates with nonlocal effect, and investigated the influences of the nonlocal parameter on the dispersion curves. It should be noted that by developing the transfer matrix method based on the NLE

continuum theory (Chen and Wang, 2011; Chen et al., 2013; Chen et al., 2016; Yan et al., 2018; Chen et al., 2019; Yan et al., 2020), a series of extensive studies on wave propagation in nanoscale periodic structures have been carried out. The results showed that a cut-off frequency was found, beyond which the waves are prohibited from passing through the structure. Besides, the dense band zones (DBZs) appeared in the band structures when the nanoscale size-effect is taken into account. However, the PCs in the above studies are all perfect periodic. For nearly periodic nanoscale layered PCs, Chen et al. (2017b) studied the size effect on the band structures of randomly disordered, quasi-periodic and defected nanoscale PCs. Therein, only the disorder of the external thickness of the first sub-layer is considered for simplicity. Besides, only Fibonacci sequence is studied. However, the influences of random disorder of the internal characteristic length and the external thickness of each sub-layer, the aperiodic arrangements, the location of different material components, the ratio of the mass density, the ratio of the transverse wave velocity, the ratio of the internal characteristic length or the external thickness of each sub-layer on the band structures, the cut-off frequency, the peak points and the DBZs have not been investigated, which requires a detailed study of these problems.

In this paper, we attempt to address these questions and the band structures of the SH wave in the nanoscale layered structures are studied in detail. The general transfer matrix method based on the NLE continuum theory is used to calculate the localization factor describing the band structures. A detailed parametric study is conducted to investigate the influences of random disorder of the internal characteristic length and the external thickness of each sub-layer, the aperiodic arrangements, the location of different components, the ratio of the mass density, the ratio of the transverse wave velocity, the ratio of the internal characteristic length or the external thickness of each sub-layer on the band structures, the cut-off frequency, the peak points and the DBZs.

The paper is structured as follows: **Section 2** introduces the nonlocal elastic continuum theory. And the theoretical models and the general transfer matrix method are given in **Section 3**. **Section 4** is devoted to the illustration and discussion of the results based on the calculations of the localization factor, where different influence factors are taken into account. Finally, some conclusions and future perspectives are presented in **Section 5**.

2 THE NONLOCAL ELASTIC CONTINUUM THEORY

In nonlocal elastic theory, owing to the long-range interaction between atoms or molecules in nanoscale materials and structures, the stresses at a point are related not only to the strains at the same point, but also to the strains at other points of the whole body. The nonlocal elastic continuum model proposed by Eringen (Eringen, 1983; Eringen, 2006) well explains that the physical phenomenon represented by one point in the continuum is affected by all other points in the whole domain, and the results are consistent with the experimental observations of lattice

atomic dynamics and phonon scattering. For homogeneous, isotropic and elastic solids, the nonlocal and classical stress tensor has the following relationship, which includes an integral involving the whole region, i.e., (Eringen, 1983).

$$\boldsymbol{\varsigma}(\mathbf{x}) = \int_V \alpha(|\mathbf{x}' - \mathbf{x}|, a) \boldsymbol{\sigma}(\mathbf{x}') dV(\mathbf{x}') \quad (1)$$

where $\boldsymbol{\varsigma}(\mathbf{x})$ represents the nonlocal stress tensor at point \mathbf{x} , the kernel function $\alpha(|\mathbf{x}' - \mathbf{x}|)$ is the nonlocal modulus, $|\mathbf{x}' - \mathbf{x}|$ is the Euclidean distance, a is the internal characteristic length, $\boldsymbol{\sigma}(\mathbf{x}')$ is the classical stress tensor whose components can be defined by

$$\sigma_{ij}(\mathbf{x}') = \lambda e_{rr}(\mathbf{x}') \delta_{ij} + 2\mu e_{ij}(\mathbf{x}') \quad (2)$$

with the strain components

$$e_{ij}(\mathbf{x}') = \frac{1}{2} \left(\frac{\partial u_i(\mathbf{x}')}{\partial x'_j} + \frac{\partial u_j(\mathbf{x}')}{\partial x'_i} \right) \quad (3)$$

where λ and μ are classical Lamé constants, δ_{ij} is the Kronecker-delta, u_i and u_j are the displacement components, respectively.

The kernel function $\alpha(|\mathbf{x}' - \mathbf{x}|, a)$ in Eq. 1 which depends on the internal characteristic length a can be determined by matching the dispersion curves with those obtained from atomic lattice dynamics, first principle method and experiments. Because the structures considered in this paper are infinite along the y direction, the kernel function along the y direction is supposed to be a Delta function, and then

$$\alpha(|\mathbf{x}' - \mathbf{x}|) = \alpha(|x' - x|) \delta(|y' - y|) \quad (4)$$

where $\alpha(|x' - x|)$ is the kernel function along the x direction. Therefore, Eq. 1 can be written as the following component form

$$\begin{aligned} \varsigma_{mn}(\mathbf{x}) &= \int \alpha(|\mathbf{x}' - \mathbf{x}|) \sigma_{mn}(\mathbf{x}') ds(\mathbf{x}') \\ &= \int_{-\infty}^{+\infty} \int_0^{l_k} \alpha(|x' - x|) \delta(|y' - y|) \sigma_{mn}(\mathbf{x}') dx' dy' \end{aligned} \quad (5)$$

It is well known that the kernel function $\alpha(|\mathbf{x}' - \mathbf{x}|, a)$ has different forms (Eringen, 1983). Considering the time-harmonic elastic waves in this paper, it is more suitable to choose $\alpha(|\mathbf{x}' - \mathbf{x}|, a)$ as (Eringen, 2006), i.e., exponential kernel function

$$\alpha(|x' - x|, a) = \frac{1}{2a} e^{-\frac{|x' - x|}{a}} \quad (6)$$

In Eringen's NLE theory, the integral form of Eq. 1 can be approximated in the following differential form (Eringen, 1983):

$$(1 - a^2 \nabla^2) \varsigma_{ij} = \sigma_{ij} \quad (7)$$

where $\nabla^2 = \frac{\partial^2}{\partial x^2} + \frac{\partial^2}{\partial y^2}$ is the Laplace operator. The equations of wave motion without body forces are expressed as

$$\varsigma_{mn,m} = \rho \ddot{u}_n \quad (8)$$

with ρ being the mass density. Here, the repeated indices denote the conventional summation rule. Substituting Eqs 2, 3, and 7

into Eq. 8, the wave motion equation based on the NLE theory can be written as the following differential ones

$$(\lambda + \mu) u_{m,mm} + \mu u_{n,mm} = (1 - a^2 \nabla^2) \rho \ddot{u}_n \quad (9)$$

3 THEORETICAL MODEL AND THE GENERAL TRANSFER MATRIX METHOD

The SH wave propagating normally in the nanoscale periodic structures are presented in Figure 1A. Figures 1B–D shows the schematic diagrams of the nanoscale layered PCs arranged as Thue-Morse sequence, Rudin-Shapiro sequence and Fibonacci sequence, respectively, and the random disorder, quasi-periodic and aperiodic structures considered in this paper can be obtained by the following theoretical model designs.

3.1 Theoretical Model

3.1.1 Nanoscale Random Disordered Structure

Here, we consider the elastic SH waves propagating in normally distributed randomly disordered PCs. let D denote the internal characteristic length τ_k ($k = 1, 2$) and the external thickness l_k ($k = 1, 2$) of the each sub-layer, respectively. For the normally distributed randomly disordered PC, the characteristic length D can be written as

$$D = D_0 + \delta V_1 \sqrt{(-2 \ln(S)/S)} \quad (10)$$

where D_0 is the mean of D (corresponding to the perfect periodic distribution), and δ is the variance of the internal characteristic length or the external thickness representing the disorder degree of this system, $\delta = 0$ corresponds to a perfect periodic system. $V_1 = 2t_1 - 1$, $V_2 = 2t_2 - 1$ in which $t_1, t_2 \in [0, 1]$ are standard uniformly distributed random variables, $S = V_1^2 + V_2^2$.

3.1.2 Nanoscale Quasi-Periodic Structure

Here, we consider the nanoscale quasi-periodic layered structures arranged in the Fibonacci sequence (Merlin et al., 1985) as shown in Figure 1D. The Fibonacci sequence can be obtained by repeating operations of the concurrent substitution rules: $A \rightarrow AB$ and $B \rightarrow A$ (Hu an et al., 1992). The m th generation of the Fibonacci sequence is denoted as F_m with $F_0 = B$ and $F_1 = A$. Then the Fibonacci sequence can be written as $F_{m+1} = F_m F_{m-1}$, for example, $F_2 = AB, F_3 = ABA, F_4 = ABAAB, F_5 = ABAABABA, \dots$ where A and B are sub-layers made up of different materials.

3.1.3 Nanoscale Aperiodic Structures

Being a bridge of linking periodic models with quasi-periodic systems in a geometrical structure, Thue-Morse system (Bovier and Ghez, 1995) and Rudin-Shapiro systems illustrated in Figures 1B,C are thought to be more random than the quasi-periodic Fibonacci lattices.

The Thue-Morse sequence is based on the two letter alphabet (A, B), and can be generated by the inflation rules,

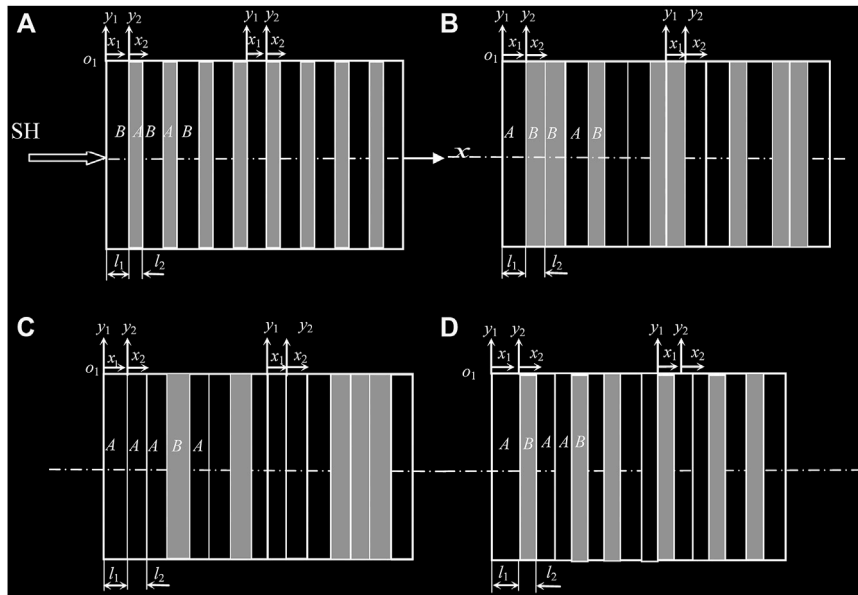


FIGURE 1 | The schematic of the SH wave propagating normally in the nanoscale periodic layered structure **(A)**, the layered PCs arranged as Thue-Morse sequence **(B)**, Rudin-Shapiro sequence **(C)** and Fibonacci sequence **(D)**.

as follows: $A \rightarrow AB, B \rightarrow BA$. The lower-order Thue-Morse lattices are the strings $T_0 = A, T_1 = AB, T_2 = ABBA, T_3 = ABBABAAB$, etc.

The Rudin-Shapiro sequence is an infinite sequence and can be generated by a four state automaton as follows: $AA \rightarrow AAAB, AB \rightarrow AABA, BA \rightarrow BBAB, BB \rightarrow BBBA$, respectively. It should be noticed that for the two aperiodic systems mentioned above, the letters A and B denote two different material sub-layers.

3.2 General Transfer Matrix Method

In this section, we start from the periodic system, i.e., the normal propagation of the time-harmonic SH elastic waves in a nanoscale periodic multilayered phononic crystal is considered. This structure depicted in **Figure 1A** is composed of materials A and B layers, with the thicknesses l_1 and l_2 , respectively, and $l = l_1 + l_2$ is the thickness of one unit-cell. The local coordinates of the monolayers are also given in the figure. We assume that the layered composite consists of \mathbb{N} unit-cells. Each unit-cell includes, unless otherwise stated, two sub-layers which are denoted by the subscript $k = 1, 2$. For this problem, the displacement components in the x - and y -directions, i.e., u_x and u_y are zero, and the only non-zero displacement u_k is along the z -direction, which is perpendicular to the xy -plane. Then **Eq. 9** can be simplified into the following form for the k th sub-layer

$$\mu_k \frac{\partial^2 u_k}{\partial x_k^2} = \rho \omega^2 \left(a^2 \frac{\partial^2}{\partial x_k^2} - 1 \right) u_k \quad (k = 1, 2) \quad (11)$$

By introducing the dimensionless local coordinate $\zeta_k = x_k/l$, $0 \leq \zeta_k \leq \bar{l}_k = l_k/l$, **Eq. 11** can be rewritten into the following dimensionless form

$$\frac{\partial^2 u_k}{\partial \zeta_k^2} + \frac{\omega_k^2}{1 - \omega_k^2 \tau_k^2} u_k = 0 \quad (12)$$

where $\omega_k = \omega/c_k$ is the non-dimensional frequency with $c_k = \sqrt{\mu_k/\rho_k}$ being the velocity of the transverse elastic wave, and $\tau_k = a_k/l$ is the ratio of the internal characteristic length and the external thickness of the unit-cell.

Then, the general harmonic solution for the k th sub-layer can be obtained, which has the following form:

$$u_k(\zeta_k) = (U_k e^{iq_k \zeta_k} + V_k e^{-iq_k \zeta_k}) e^{-i\omega t} \quad (13)$$

where $q_k = \sqrt{\omega_k^2/(1 - \tau_k^2 \omega_k^2)}$, U_k and V_k are the unknown coefficients to be determined. According to **Eqs 13, 5**, the nonlocal stresses can be obtained as

$$\begin{aligned} \varsigma_k(\zeta_k) &= \int_0^{\bar{l}_k} \frac{\mu_k}{2\tau_k} e^{-|\zeta_k - \zeta'_k|/\tau_k} \frac{\partial u_k}{\partial \zeta'_k} d\zeta'_k \\ &= \frac{iq_k \mu_k}{2} \left(\frac{e^{iq_k \zeta_k} - e^{-\zeta_k/\tau_k}}{1 + iq_k \tau_k} - \frac{e^{iq_k \bar{l}_k} e^{(\zeta_k - \bar{l}_k)/\tau_k} - e^{iq_k \zeta_k}}{1 - iq_k \tau_k} \right) U_k \\ &\quad - \frac{iq_k \mu_k}{2} \left(\frac{e^{-iq_k \zeta_k} - e^{-\zeta_k/\tau_k}}{1 - iq_k \tau_k} - \frac{e^{-iq_k \bar{l}_k} e^{(\zeta_k - \bar{l}_k)/\tau_k} - e^{-iq_k \zeta_k}}{1 + iq_k \tau_k} \right) V_k \end{aligned} \quad (14)$$

Then, the state vector $W = \{\bar{u}, \bar{\varsigma}\}^T$ with the bar denoting the dimensionless parameters is chosen in order to obtain the transfer

matrix of the unit-cell. Based on the continuity conditions on the left (subscript L) and right (subscript R) sides of the interface of two adjacent sub-layers in the β th unit cell, the state vectors can be defined as

$$\begin{aligned} \mathbf{W}_{kL}^{(\beta)} &= \{\bar{u}_k, \bar{\zeta}_k\}_{\zeta_k=0}^T = \mathbf{T}_{kL}\{U_k, V_k\}^T \\ \mathbf{W}_{kR}^{(\beta)} &= \{\bar{u}_k, \bar{\zeta}_k\}_{\zeta_k=\bar{L}_k}^T = \mathbf{T}_{kR}\{U_k, V_k\}^T \end{aligned} \quad (15)$$

where the matrices \mathbf{T}_{kL} and \mathbf{T}_{kR} can be obtained from Eqs 13, 5, whose elements are given by

$$\begin{aligned} T_{kL}(1, 1) &= T_{kL}(1, 2) = 1, \quad T_{kL}(2, 1) = -i\mu_k q_k \frac{1 - e^{-iq_k L_k} e^{-L_k/\tau_k}}{2(1 + iq_k \tau_k)}, \\ T_{kL}(2, 2) &= i\mu_k q_k \frac{1 - e^{iq_k L_k} e^{-L_k/\tau_k}}{2(1 - iq_k \tau_k)}, \quad T_{kR}(1, 1) = e^{-iq_k L_k}, \quad T_{kR}(1, 2) \\ &= e^{iq_k L_k}, \quad T_{kR}(2, 1) = -i\mu_k q_k \frac{e^{-iq_k L_k} - e^{-L_k/\tau_k}}{2(1 - iq_k \tau_k)}, \quad T_{kR}(2, 2) \\ &= i\mu_k q_k \frac{e^{iq_k L_k} - e^{-L_k/\tau_k}}{2(1 + iq_k \tau_k)} \end{aligned} \quad (16)$$

Obviously, the two state vectors in Eq. 15 have the following relation by eliminating the common vector, i.e.,

$$\mathbf{W}_{kR}^{(\beta)} = \mathbf{T}_{kR} \mathbf{T}_{kL}^{-1} \mathbf{W}_{kL}^{(\beta)} \triangleq \mathbf{T}_k \mathbf{W}_{kL}^{(\beta)} \quad (k = 1, 2) \quad (17)$$

where $\mathbf{T}_k = \mathbf{T}_{kR} \mathbf{T}_{kL}^{-1}$ is the transfer matrix of the k th sub-layer.

The displacements and nonlocal stresses are continuous at the interface of two adjacent sub-layers in the same unit-cell and between the β th and the $(\beta - 1)$ th unit-cells, that is,

$$\mathbf{W}_{2R}^{(\beta-1)} = \mathbf{W}_{1L}^{(\beta)}, \quad \mathbf{W}_{1R}^{(\beta)} = \mathbf{W}_{2L}^{(\beta)} \quad (18)$$

From Eqs 17, 18, the following relation can be obtained

$$\begin{aligned} \mathbf{W}_{2R}^{(\beta)} &= \mathbf{T}_2 \mathbf{W}_{2L}^{(\beta)} = \mathbf{T}_2 \mathbf{W}_{1R}^{(\beta)} = \mathbf{T}_2 \mathbf{T}_1 \mathbf{W}_{1L}^{(\beta)} \\ &= \mathbf{T}_2 \mathbf{T}_1 \mathbf{W}_{2R}^{(\beta-1)} \triangleq \mathbf{T}_\beta \mathbf{W}_{2R}^{(\beta-1)} \end{aligned} \quad (19)$$

which shows the relationship between the state vectors of the β th and the $(\beta - 1)$ th unit-cells, where $\mathbf{T}_\beta = \mathbf{T}_2 \mathbf{T}_1 = \mathbf{T}_{2R} \mathbf{T}_{2L}^{-1} \mathbf{T}_{1R} \mathbf{T}_{1L}^{-1}$ is the transfer matrix between the two consecutive unit-cells, i.e., the transfer matrix of the β th unit-cell. For perfect periodic two-component PCs, $\mathbf{T}_\beta = \mathbf{T}_2 \mathbf{T}_1$ for all $\beta = 1, 2, 3, \dots, \mathbb{N}$ are the same and denoted as \mathbf{T} . It should be noticed that the above derivation is applicable for not only the ordered periodic PNCs but also the disordered, quasi-periodic and aperiodic ones. However the transfer matrices of the “unit-cells” of the disordered, quasi-periodic and APNCs are different from those of the perfect periodic ones. For quasi-periodic or aperiodic structures, $\mathbf{T}_\beta = \mathbf{T}_2 \mathbf{T}_1$ are not all the same and the Bloch theory is not applicable, for example, Using the above method, for the aperiodic structure composed of \mathbb{N} unit-cells, the total transfer matrix can be obtained, that is,

$$\mathbf{T}_{total} = \mathbf{T}_{NR} \mathbf{T}_{NL}^{-1} \mathbf{T}_{(N-1)R} \mathbf{T}_{(N-1)L}^{-1} \mathbf{T}_{(N-2)R} \cdots \mathbf{T}_{3L}^{-1} \mathbf{T}_{2R} \mathbf{T}_{2L}^{-1} \mathbf{T}_{1R} \mathbf{T}_{1L}^{-1} \quad (20)$$

The detailed mathematical derivation is not given here for the sake of brevity. Interested readers may refer to many publications for more details.

In this paper, we use the well-defined localization factor to characterize the band structures and localization phenomenon of 1D nanoscale layered PCs. The localization factor is defined as the minimum positive Lyapunov exponent which describes the average exponential rate of growth or attenuation of the wave amplitude (Gastanier and Pierre, 1997). And it can be calculated by using the Wolf's method (Wolf et al., 1985) once the transfer matrix is obtained. If the dimension of the transfer matrices is $2\lambda \times 2\lambda$, then the smallest positive Lyapunov exponent ℓ_λ is the localization factor. The expression for the localization factor ℓ_λ of the system with \mathbb{N} unit-cells is given as follows:

$$\ell_\lambda = \lim_{\mathbb{N} \rightarrow \infty} \frac{1}{\mathbb{N}} \sum_{\beta=1}^{\mathbb{N}} \ln \|\hat{\mathbf{W}}_{2R,\lambda}^{(\beta)}\| \quad (21)$$

where the vector in Eq. 21 is given by

$$\hat{\mathbf{W}}_{2R,\lambda}^{(\beta)} = \mathbf{W}_{2R,\lambda}^{(\beta)} - \left(\mathbf{W}_{2R,\lambda}^{(\beta)}, \mathbf{v}_{\lambda-1}^{(\beta)} \right) \mathbf{v}_{\lambda-1}^{(\beta)} - \cdots - \left(\mathbf{W}_{2R,\lambda}^{(\beta)}, \mathbf{v}_1^{(\beta)} \right) \mathbf{v}_1^{(\beta)} \quad (22)$$

in which $\mathbf{v}_\lambda^{(\beta)} = \frac{\hat{\mathbf{W}}_{2R,\lambda}^{(\beta)}}{\|\hat{\mathbf{W}}_{2R,\lambda}^{(\beta)}\|}$ are orthogonal unit vectors, (\cdot, \cdot) denotes the dot-product, $\|\cdot\|$ is the vector norm, and \mathbb{N} represents the number of the unit-cells. The λ th orthogonal unit state vector $\hat{\mathbf{W}}_{2R,\lambda}^{(\beta)}$ is obtained through the iteration using the Gram-Schmidt orthonormalization procedures (Kissel, 1991). If the localization factor is equal to zero, the corresponding frequency intervals are known as pass-bands. Otherwise if the localization factor is positive, the frequency intervals are known as stop-bands or band-gaps. In this paper, only the normal incidence of SH wave is considered, thus, the dimension of the transfer matrix is 2×2 and ℓ_1 is the localization factor, which is denoted as ℓ in the following analysis.

4 NUMERICAL RESULTS AND DISCUSSIONS

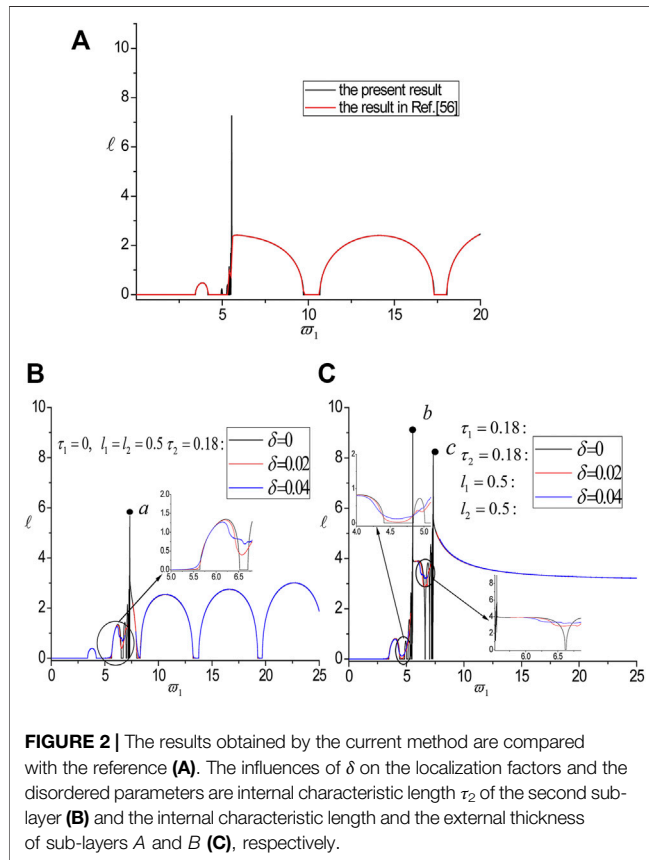
In this section, the band structures and localization properties of the anti-plane elastic waves propagating normally in nanoscale layered structures are studied by the general transfer matrix method. Different factors affecting the band structures are considered. Numerical results are presented and discussed. During the calculations, we refer to Ref. (Yan et al., 2020) for the material constants and list the values in Table 1. For convenience, the frequency is normalized as $\omega_1 = \omega/c_1$ with $c_1 = \sqrt{\mu_1/\rho_1}$.

4.1 Nanoscale Random Disordered Layered PCs

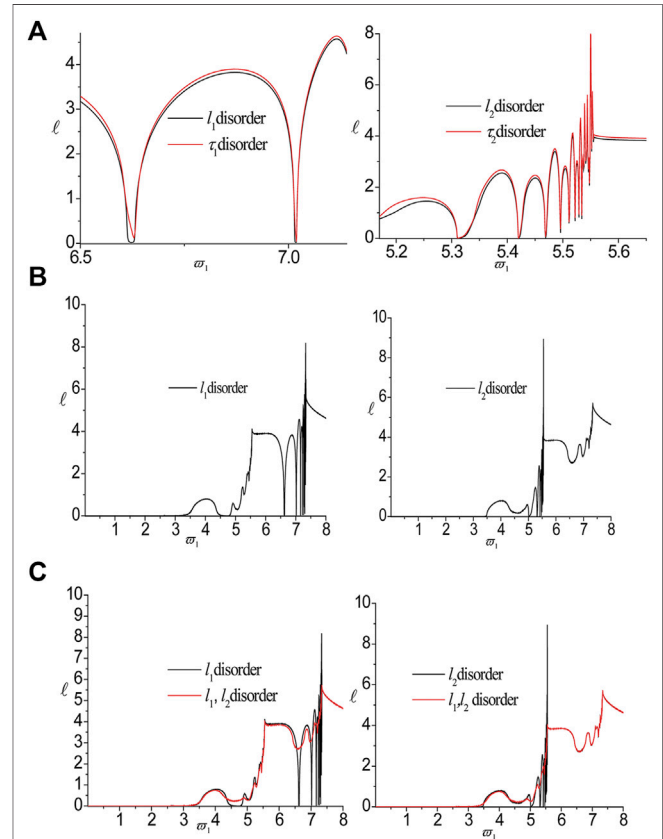
Firstly, In order to check the correctness of the present method, the 1D nanoscale periodic layered structures arranged alternately by HfO2 (A) and ZrO2 (B), as shown in Figure 1A, are studied.

TABLE 1 | Material constants.

Component materials	HfO ₂	ZrO ₂	Al	Cu
Mass density (Kg/m ³)	$\rho = 10,873$	$\rho = 6,488$	$\rho = 2,730$	$\rho = 8,950$
Shear modulus (Pa)	$\mu = 6.60 \times 10^{10}$	$\mu = 6.88 \times 10^{10}$	$\mu = 2.87 \times 10^{10}$	$\mu = 7.53 \times 10^{10}$



The same material constants as the Ref. (Yan et al., 2020) are selected, and the results are shown in **Figure 2A**. We find that the present results (black solid lines) are in good agreement with the results (red solid lines) of **Figure 2C** in Ref. (Yan et al., 2020), which verifies the correctness and effectiveness of the current method. In the following, in order to reveal the influence of random disorder of the sub-layers on the band structures by considering the internal characteristic lengths and the external thicknesses, the localization factors in the cases of $\tau_1 = 0, l_1 = l_2 = 0.5, \tau_2 = 0.18$ (i.e., disorder is considered only for the internal characteristic length of the second sub-layer B) and $\tau_1 = 0.18 + \delta V_1 \sqrt{(-2 \ln(S)/S)}, \tau_2 = 0.18 + \delta V_2 \sqrt{(-2 \ln(S)/S)}, l_1 = 0.5 + \delta V_1 \sqrt{(-2 \ln(S)/S)}, l_2 = 0.5 + \delta V_2 \sqrt{(-2 \ln(S)/S)}$ (i.e., disorder is considered for both internal characteristic lengths and external thickness of sub-layers A and B), are calculated and the results are illustrated in **Figures 2B,C**. The disorder degree denoted by δ is assumed to be $\delta = 0, 0.02$ and 0.04 , respectively. It can be seen that there is one peak point *a* in **Figure 2B** and two



peak points *b, c* in **Figure 2C** whose positions are determined by the cut-off frequency of a specific material sub-layer. The second peak point *c* in **Figure 2C** is a cut-off frequency beyond which the localization factor becomes stable and positive, which means that the elastic waves cannot propagate through the structure over the cut-off frequency. In addition, the dense band zones (DBZs) as defined in Ref (Yan et al., 2020) appears, where the localization factors are very big with multiple, dense, flat and narrow band-gaps in the frequency range (7.28, 7.35) in **Figure 2B** and (5.47, 5.56) in **Figure 2C**, meaning a very strong wave localization phenomenon. The disorder degree has little effect on the DBZ, the cut-off frequency and the localization factor whose frequencies are larger than the peak points *a* and *c*. However, when the disorder caused by the sub-layer's length or thickness is introduced to the periodic phononic crystals, the

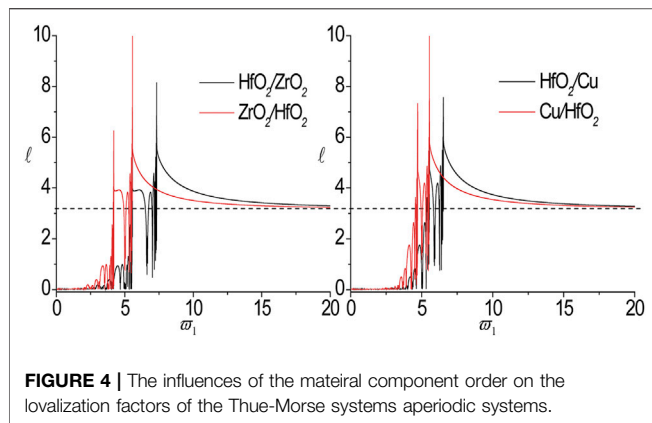


FIGURE 4 | The influences of the material component order on the localization factors of the Thue-Morse systems aperiodic systems.

disorder degree still has some influences on the band structures in both pass-bands and band gaps, which are demonstrated by the enlarged sub-figure in **Figures 2B,C**. For example, in the pass-band (6.519, 6.704) for $\delta = 0$ shown in the partly enlarged regions in **Figure 2B**, the localization factors become positive with the increase of δ , indicating a wave localization phenomenon, and the localization degree increases with the increase of δ in the pass-bands while the localization degree decreases with the increase of δ in the band gaps. Next, the disorder of the internal characteristic length and the external thickness of the same sub-layer, the disorder of different sub-layers and the number of disorder are considered to show more detailed results in **Figures 3A–C**, respectively. The disorder degree is $\delta = 0.08$. It can be seen from **Figure 3A** that the influences of the disorder caused by the internal characteristic lengths are a little bigger than those caused by the external thicknesses. In addition, in **Figures 3B,C** the localization factors change a lot and have a strong dependence on the disorder of different sub-layers and the number of disorder. Moreover, with the increase of the number of disorder, the degree of wave localization in the pass-bands increases, and the localization phenomenon becomes more and more obvious. From **Figure 3**, we can conclude that the disorder degree and the localization factor depend on different types of disorders of each sub-layer.

4.2 Nanoscale Aperiodic Layered PCs

Due to the lack of periodicity, a finite but sufficiently large number of unit-cell n is very important to calculate the localization factor. After trial calculation, $n = 1024$ is taken in the following computations. Next, the influences of the material combinations on the band structures are analyzed by considering changing the order of material components, only the single sub-layer material and two sub-layers are both changed, respectively. Specifically, the order of material components is selected as $\text{HfO}_2/\text{ZrO}_2$, $\text{ZrO}_2/\text{HfO}_2$ and HfO_2/Cu , Cu/HfO_2 . Only the change of the second sub-layer material is taken as HfO_2/Cu , $\text{HfO}_2/\text{ZrO}_2$ and HfO_2/Al . The examples where the materials of two sub-layers are both changed are ZrO_2/Cu , $\text{HfO}_2/\text{ZrO}_2$ and Cu/Al . The band structures for the nanoscale Thue-Morse laminate with the change in order of material components are

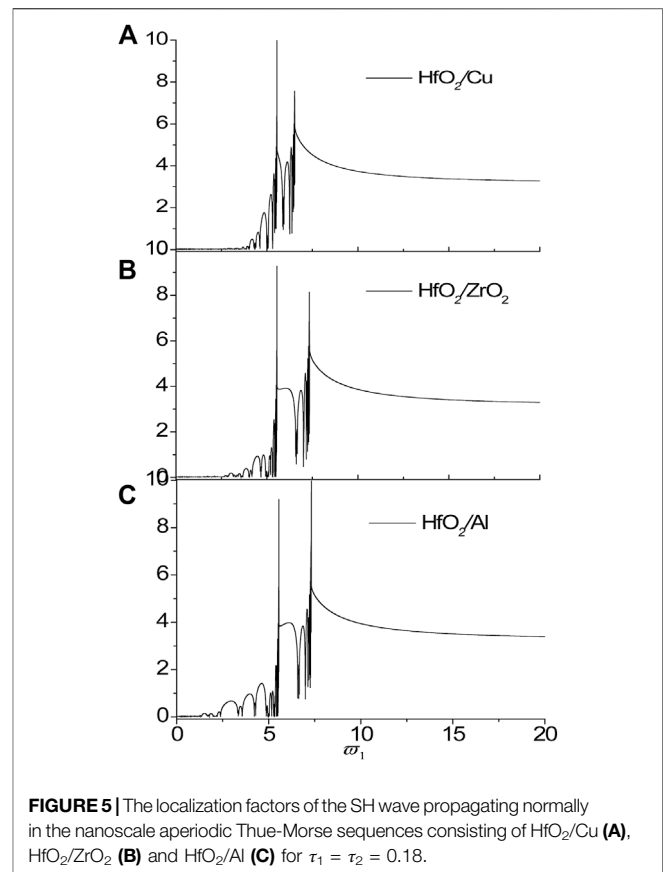


FIGURE 5 | The localization factors of the SH wave propagating normally in the nanoscale aperiodic Thue-Morse sequences consisting of HfO_2/Cu (A), $\text{HfO}_2/\text{ZrO}_2$ (B) and HfO_2/Al (C) for $\tau_1 = \tau_2 = 0.18$.

plotted in **Figure 4**. The ratio of internal characteristic length and the thickness of the unit-cell is $\tau_1 = \tau_2 = 0.18$. It can be seen that with the exchange of material components, the distance between the two peak points becomes narrower, and the two peak points and the first distinct band gap move to the low frequency zone. Furthermore, Compared with the two DBZs (5.42, 5.56) and (6.53, 7.34) for $\text{HfO}_2/\text{ZrO}_2$, the first and the second DBZs move left to (4.1, 4.21) and (4.98, 5.56) for $\text{ZrO}_2/\text{HfO}_2$, respectively. While the two DBZs for Cu/HfO_2 move left to (4.61, 4.72) and (5.3, 5.56) compared with the corresponding DBZs (5.31, 5.56) and (5.9, 6.54) for HfO_2/Cu . It is worth noted that compared with the first peak points for $\text{HfO}_2/\text{ZrO}_2$ and HfO_2/Cu , the second peak points, i.e., the cut-off frequencies, stay in the almost same position for $\text{ZrO}_2/\text{HfO}_2$ and Cu/HfO_2 , that is to say, the cut-off frequencies for $\text{ZrO}_2/\text{HfO}_2$ and Cu/HfO_2 are almost $\omega = 5.56$ which are exactly the right edges of the corresponding DBZs, i.e., the cut-off frequency of the material HfO_2 . In addition, when the frequency is higher than the cut-off frequency, the value of the localization factor will become stable at approximately 3.23 (as illustrated by the dashed lines in **Figure 4**).

In the following, we only change the material of the second sub-layer and the localization factors for the nanoscale aperiodic Thue-Morse sequences with different material combinations are presented in **Figure 5**. Here, the material combinations is taken as HfO_2/Cu , $\text{HfO}_2/\text{ZrO}_2$ and HfO_2/Al , respectively. It can be observed that the peak points, i.e., the DBZs with the frequency ranges of (5.3, 5.56), (6.48, 6.54), (7.03, 7.35) and

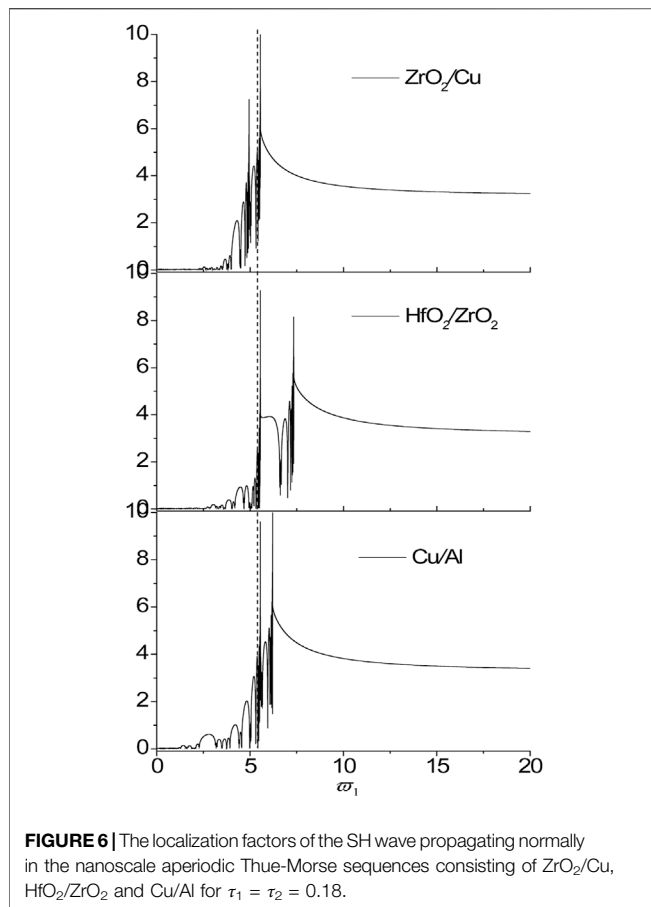


FIGURE 6 | The localization factors of the SH wave propagating normally in the nanoscale aperiodic Thue-Morse sequences consisting of ZrO_2/Cu , $\text{HfO}_2/\text{ZrO}_2$ and Cu/Al for $\tau_1 = \tau_2 = 0.18$.

(7, 7.32) correspond to materials HfO_2 , Cu, ZrO_2 and Al, respectively. The band structures between the two DBZs have almost the same distributions, however, when the frequency is lower than the first peak point, the localization factors change a lot. More specifically, the first distinct band gap becomes wider and moves to the low frequency zone. Compared with **Figures 5B,C** shows the two DBZs are located at almost the same position, because the transverse wave velocities of the two materials ZrO_2 and Al, have almost similar values. In addition, the examples where the materials of two sub-layers are both changed are chosen as ZrO_2/Cu , $\text{HfO}_2/\text{ZrO}_2$ and Cu/Al , respectively. It can be seen from **Figure 6** that the position of the peak point shown by the dashed line corresponds to materials Cu and HfO_2 because the shear wave velocities of the two materials have the similar values. The larger the difference in transverse wave velocity, the farther the two DBZs are from each other.

Next, the band structures of the systems with different aperiodic arrangements are calculated. As shown in **Figures 1B–D**, three different aperiodic arrangements are chosen, i.e., the Thue-Morse sequence, the Rudin-Shapiro sequence and the Fibonacci sequence, respectively. **Figure 7** shows the influences of aperiodic arrangements on localization factors of the SH wave propagating normally in the nanoscale aperiodic systems consisting of $\text{HfO}_2/\text{ZrO}_2$ for $\tau_1 = \tau_2 = 0.18$. It can be seen that the tendencies of all curves are coincident for the three

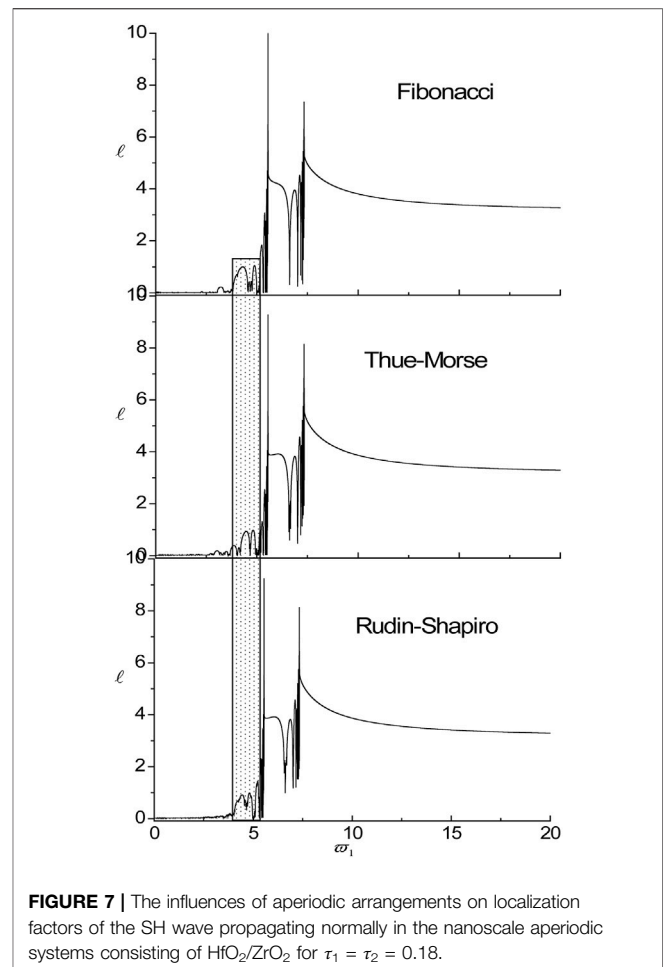
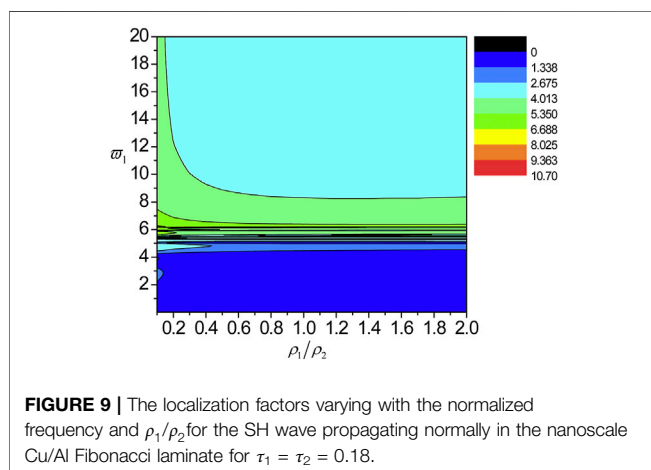
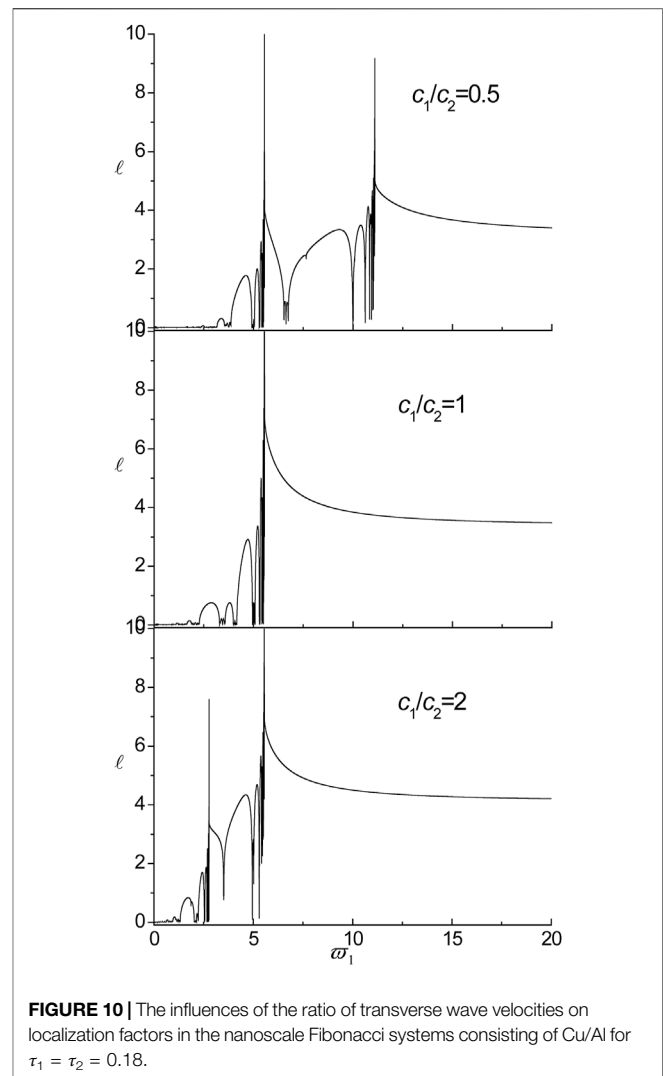
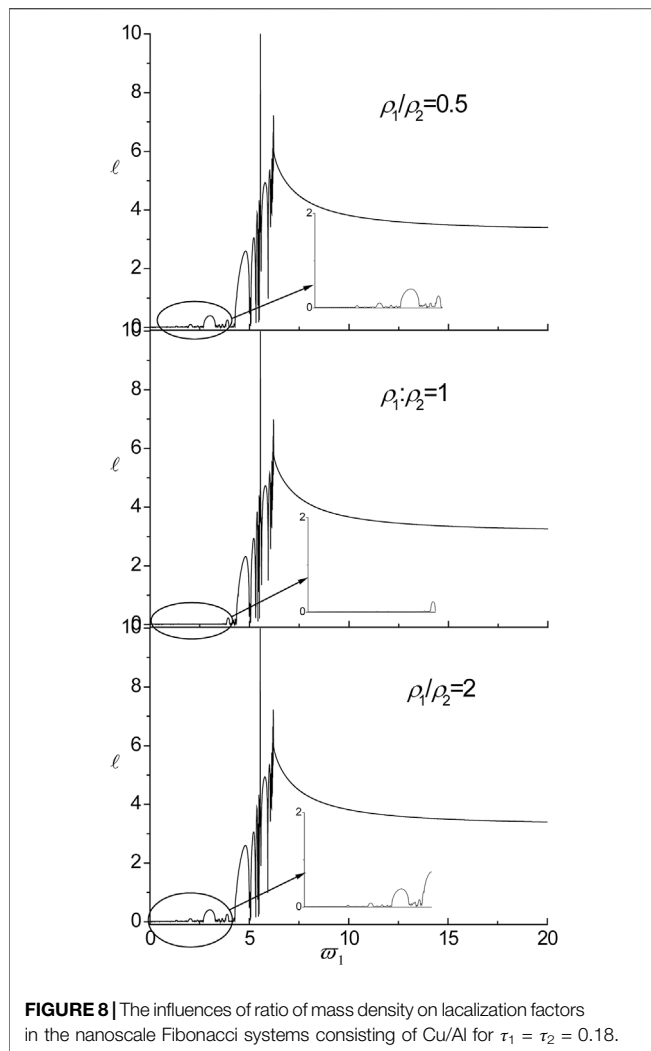


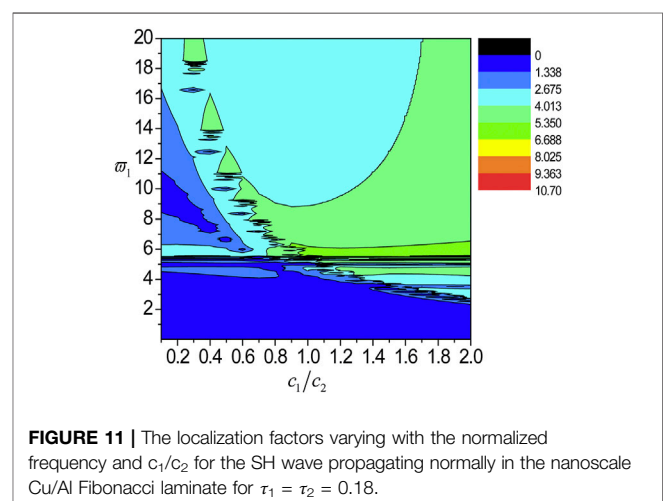
FIGURE 7 | The influences of aperiodic arrangements on localization factors of the SH wave propagating normally in the nanoscale aperiodic systems consisting of $\text{HfO}_2/\text{ZrO}_2$ for $\tau_1 = \tau_2 = 0.18$.

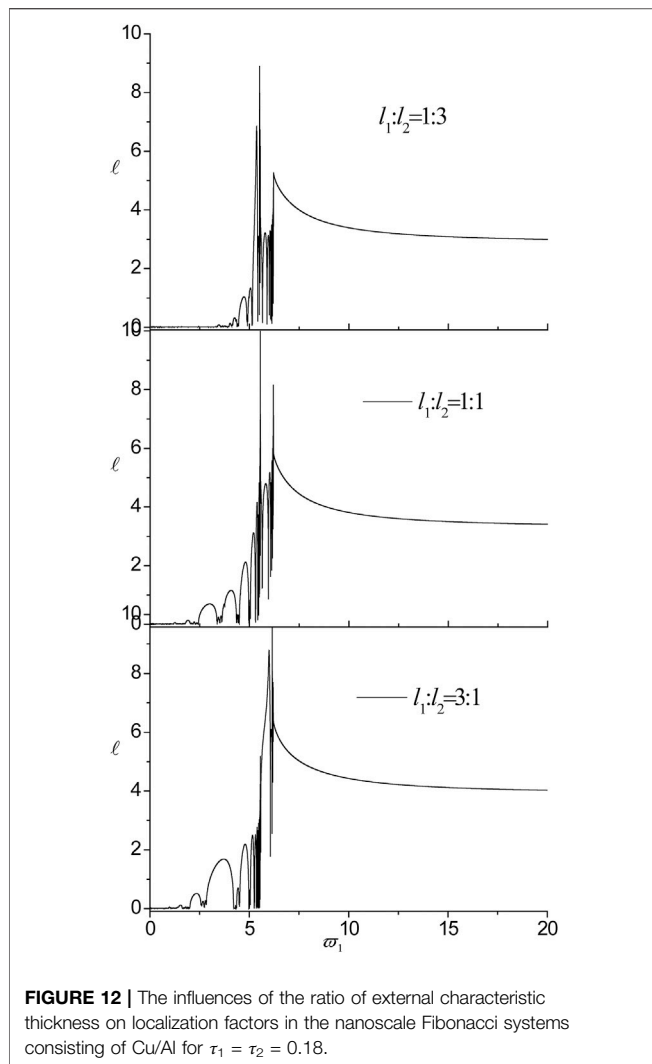
aperiodic systems, which implies the aperiodic arrangements have little effect on the peak points, the DBZs and the cut-off frequency. For example, the localization factors oscillate quickly with big values between the two peak points. The cut-off frequencies are all around about $\omega = 7.34$. However, the band structures before the first peak point becomes different for the three aperiodic arrangements, i.e., the main band gaps of the Fibonacci structure change a lot with the gradual disappearing and narrowing of the band gaps. Specifically, in the dot rectangle, compared with the Fibonacci structure, the localization factor is more like a defect state for the Thue-Morse and Rudin-Shapiro structures.

Additionally, the influences of the ratio of the mass density ρ_1/ρ_2 and the ratio of the transverse wave velocity c_1/c_2 on the localization factors are examined. Here, the nanoscale Cu/Al Fibonacci aperiodic laminate is selected as an example. It can be observed from **Figure 8** that when the ratio of the mass density ρ_1/ρ_2 is not equal to 1, the first distinct band gap emerges, while for $\rho_1/\rho_2 = 1$, it disappears (enlarged regions shown in **Figure 8**). The positions of the two DBZs, the two peak points, the cut-off frequency and the localization factors whose frequencies are larger than those of the first peak point have no changes. For example, after the first peak point, the tendencies of all curves are

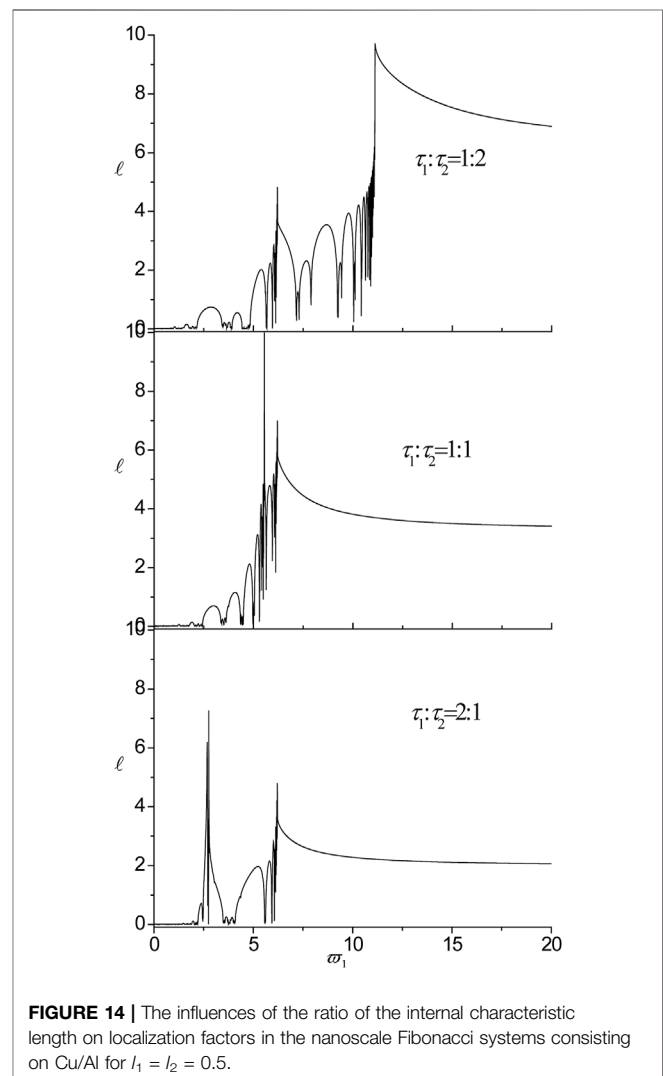
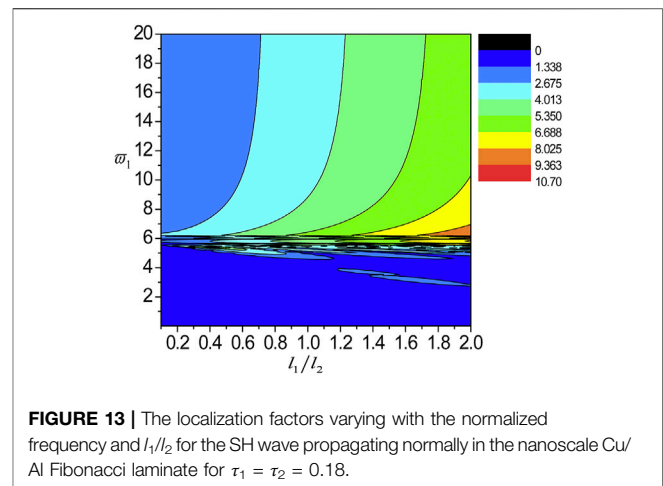


coincident, i.e., the localization factors oscillate quickly with big values after the first peak point, and then the second peak point appears. More detailed results are illustrated in **Figure 9** for the





localization factors varying with the normalized frequency and ρ_1/ρ_2 . Compared with the results in **Figure 8**, the first distinct band gap disappears for $\rho_1/\rho_2 = 1$, when ρ_1/ρ_2 is less than 1 or ρ_1/ρ_2 is bigger than 1, the first distinct band gap appears and becomes wider with ρ_1/ρ_2 decreasing or increasing. Combining **Figures 8, 9**, we can conclude that the first distinct band gap will emerge for $\rho_1/\rho_2 \neq 1$, and the ratio of the mass density has no influences on the peak points, the cut-off frequency, the DBZs and the localization factors whose frequencies are larger than those of the first peak point. From **Figure 10**, we can see that there is only one peak point when the ratio of transverse wave velocity is $c_1/c_2 = 1$, i.e., the cut-off frequency, and when the velocity ratio changes, the position of the peak point remains unchanged. However, when the ratio is not equal to 1, there are two peak points. Among them, when the ratio of velocity is less than 1, one peak point tends to the high-frequency region, and when the ratio is larger than 1, a peak point tends to the low-frequency region. In addition, the low-frequency band gap is more likely to emerge with the increase of the ratio. This shows that the ratio of transverse wave velocity has significant effect on the cut-off



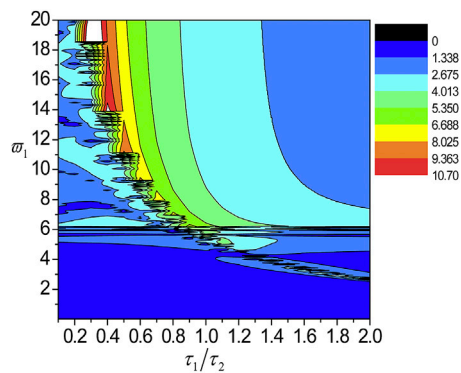


FIGURE 15 | The localization factors varying with the normalized frequency and τ_1/τ_2 for the SH wave propagating normally in the nanoscale Cu/Al Fibonacci laminate for $\tau_1 = \tau_2 = 0.18$.

frequency, the DBZ, the peak point and the low-frequency band gap. Furthermore, the localization factors varying with normalized frequency and c_1/c_2 are presented in **Figure 11**. There is only one peak point when the ratio of transverse wave velocity is $c_1/c_2 = 1$, i.e., the cut-off frequency of material Al, and when the velocity ratio changes, the position of the peak point remains unchanged since c_2 is a fixed value. On the contrary, the peak point other than the cut-off frequency moves the high-frequency region when c_1/c_2 is less than 1, and moves the low-frequency zone when c_1/c_2 is larger than 1. Combining **Figures 10, 11**, we can conclude that the position and the number of the peak point, i.e., the DBZ have strong dependence on c_1/c_2 . There exists a wide pass-band when c_1/c_2 is less than 1, and the pass-band becomes wider with the decrease of c_1/c_2 .

Finally, the influences of the structural parameter, i.e., the ratio of external characteristic thickness l_1/l_2 and the ratio of internal characteristic length τ_1/τ_2 on the localization factors are investigated. The localization factors for the nanoscale Fibonacci laminates with different values of l_1/l_2 are presented in **Figure 12**. From **Figure 12**, we can see that the pass-bands and band-gaps are affected by varying the ratio of external characteristic thickness, while the two peak points, the two DBZs and the cut-off frequency remain in the same position. Detailed results are shown in **Figure 13**, the position of the cut-off frequency remains unchanged, but the localization degree enhances with the increase of l_1/l_2 . From **Figure 14**, we can see that the bigger the difference of internal characteristic length between the two materials, the farther the distance between the two peak points. The first distinct band gap disappears with the increase of τ_1/τ_2 . More detailed numerical results are shown in **Figure 15**. It can be seen that the cut-off frequency does not appear when $\tau_1/\tau_2 \leq 0.2$. However, when $0.3 \leq \tau_1/\tau_2 \leq 1$, the cut-off frequency appears and decreases with the τ_1/τ_2 increasing. When $\tau_1/\tau_2 > 1$, the cut-off frequency remains unchanged and the first peak point tends to the low-frequency zone with the τ_1/τ_2 increasing. In addition, the localization degree of the cut-off

frequency, the pass-bands and the band gaps varies with the τ_1/τ_2 . And the localization degree whose frequencies are larger than the cut-off frequency decreases with τ_1/τ_2 increasing.

5 CONCLUSION

The results presented in this study are obtained by the numerical calculations of the wave localization properties in the nanoscale layered structures by using the general transfer matrix method based on the nonlocal elastic continuum theory. The key conclusions from this analysis can be summarized as follows:

- 1) No matter what kind of disorders, the disorder degree has little effect on the DBZ, the peak point, the cut-off frequency and the localization factor whose frequencies are larger than the cut-off frequency. However, the influences of the disorder caused by the internal characteristic lengths are a little bigger than those caused by the external thicknesses. The localization factors have a strong dependence on the disorder of different sub-layers and the number of disorder.
- 2) The first distinct band gap, the peak point, the cut-off frequency, the DBZ and the localization factor have strong dependence on the material combinations. With the exchange of material components, the distance between the two peak points becomes narrower, and the two peak points and the first distinct band gap move to the low frequency zone. The position of the peak point and the DBZ depends on the sub-layer materials under consideration.
- 3) The aperiodic arrangements have little effect on the peak points, the DBZs and the cut-off frequency. However, the band structures before the first peak point becomes different for the three aperiodic arrangements.
- 4) The first distinct band gap will emerge for $\rho_1/\rho_2 \neq 1$. and the ratio of the mass density has no influences on the peak points, the cut-off frequency, the DBZs and the localization factors whose frequencies are larger than those of the first peak point.
- 5) There is only one peak point when the ratio of transverse wave velocity is $c_1/c_2 = 1$. However, when the ratio of velocity is less than 1, one peak point tends to the high-frequency region, and when the ratio is larger than 1, a peak point tends to the low-frequency region. In addition, the low-frequency band gap is more likely to emerge with the increase of the ratio. There exists a wide pass-band when c_1/c_2 is less than 1, and the pass-band becomes wider with the decrease of c_1/c_2 .
- 6) The pass-bands and band gaps are affected by varying the ratio of external characteristic thickness, while the two peak points, the two DBZs and the cut-off frequency remain in the same position. In addition, the localization degree enhances with the increase of l_1/l_2 .

- 7) When $0.3 \leq \tau_1/\tau_2 \leq 1$, the cut-off frequency appears and decreases with the τ_1/τ_2 increasing. When $\tau_1/\tau_2 > 1$, the cut-off frequency remains unchanged and the first peak point tends to the low-frequency zone with the τ_1/τ_2 increasing. And the localization degree whose frequencies are larger than the cut-off frequency decreases with τ_1/τ_2 increasing.

DATA AVAILABILITY STATEMENT

The original contributions presented in the study are included in the article/Supplementary Material, further inquiries can be directed to the corresponding author.

REFERENCES

- Adhikari, S., Gilchrist, D., Murmu, T., and McCarthy, M. A. (2015). Nonlocal normal Modes in Nanoscale Dynamical Systems. *Mech. Syst. Signal Process.* 60–61, 583–603. doi:10.1016/j.ymssp.2014.12.004
- Aifantis, E. C. (1999). Strain Gradient Interpretation of Size Effects. *Int. J. Fract* 95 (1–4), 299–314. doi:10.1007/978-94-011-4659-3_16
- Alibeigloo, A. (2011). Free Vibration Analysis of Nano-Plate Using Three-Dimensional Theory of Elasticity. *Acta Mech.* 222, 149–159. doi:10.1007/s00707-011-0518-7
- Anderson, P. W. (1958). Absence of Diffusion in Certain Random Lattices. *Phys. Rev.* 109, 1492–1505. doi:10.1103/physrev.109.1492
- Artan, R., and Altan, B. S. (2002). Propagation of SV Waves in a Periodically Layered media in Nonlocal Elasticity. *Int. J. Sol. Structures* 39, 5927–5944. doi:10.1016/s0020-7683(02)00476-6
- Aynaou, H., Boudouti, E. H. E., Djafari-Rouhani, B., Akjouj, A., Velasco, V. R., and Velasco, V. R. (2005). Propagation and localization of acoustic waves in Fibonacci phononic circuits. *J. Phys.: Condens. Matter* 17, 4245–4262. doi:10.1088/0953-8984/17/27/002
- Barco, O., and Ortuno, M. (2012). Localization length of nearly periodic layered metamaterials. *Phys Rev A* 86 (2), 023846. doi:10.1103/physreva.86.023846
- Bovier, A., and Ghez, J.-M. (1995). Remarks on the Spectral Properties of Tight-Binding and Kronig-Penney Models with Substitution Sequences. *J. Phys. A: Math. Gen.* 28, 2313–2324. doi:10.1088/0305-4470/28/8/022
- Chen, A.-L., Tian, L.-Z., and Wang, Y.-S. (2017). Band Structure Properties of Elastic Waves Propagating in the Nanoscaled Nearly Periodic Layered Phononic Crystals. *Acta Mechanica Solida Sinica* 30, 113–122. doi:10.1016/j.camss.2017.03.005
- Chen, A.-L., Wang, Y.-S., Ke, L.-L., Guo, Y.-F., and Wang, Z.-D. (2013). Wave Propagation in Nanoscaled Periodic Layered Structures. *Jnl Comp. Theo Nano* 10, 2427–2437. doi:10.1166/jctn.2013.3225
- Chen, A.-L., and Wang, Y.-S. (2011). Size-effect on Band Structures of Nanoscale Phononic Crystals. *Physica E: Low-dimensional Syst. Nanostructures* 44, 317–321. doi:10.1016/j.physe.2011.08.032
- Chen, A.-L., and Wang, Y.-S. (2007). Study on Band Gaps of Elastic Waves Propagating in One-Dimensional Disordered Phononic Crystals. *Physica B: Condensed Matter* 392, 369–378. doi:10.1016/j.physb.2006.12.004
- Chen, A.-L., Wang, Y.-S., and Zhang, C. (2012). Wave Propagation in One-Dimensional Solid-Fluid Quasi-Periodic and Aperiodic Phononic Crystals. *Physica B: Condensed Matter* 407, 324–329. doi:10.1016/j.physb.2011.10.041
- Chen, A.-L., Yan, D.-J., Wang, Y.-S., and Zhang, C. (2016). Anti-plane Transverse Waves Propagation in Nanoscale Periodic Layered Piezoelectric Structures. *Ultrasonics* 65, 154–164. doi:10.1016/j.ultras.2015.10.006
- Chen, A.-L., Yan, D.-J., Wang, Y.-S., and Zhang, C. (2019). In-plane Elastic Wave Propagation in Nanoscale Periodic Piezoelectric/piezomagnetic Laminates. *Int. J. Mech. Sci.* 153–154, 416–429. doi:10.1016/j.ijmecsci.2019.02.017
- Chen, J.-J., Wang, Q., and Han, X. (2010). Lamb Wave Transmission through One-Dimensional Three-Component Fibonacci Composite Plates. *Mod. Phys. Lett. B* 24, 161–167. doi:10.1142/s0217984910022305

AUTHOR CONTRIBUTIONS

All authors listed have made a substantial, direct, and intellectual contribution to the work and approved it for publication.

FUNDING

The authors greatly acknowledge the financial support from the National Natural Science Foundation of China (No. 11002026, 11372039), Beijing Natural Science Foundation (No. 3133039), and the Scientific Research Foundation for the Returned Overseas Chinese Scholars (No. 20121832001).

- Chen, J., Guo, J., and Pan, E. (2017). Wave Propagation in Magneto-Electro-Elastic Multilayered Plates with Nonlocal Effect. *J. Sound Vibration* 400, 550–563. doi:10.1016/j.jsv.2017.04.001
- Du, S. G., Shi, D. M., and Deng, H. (2000). Special effects and applications of nanostructured materials. *Ziran Zazhi* 22 (2), 101–106.
- Economou, E. N., and Sigalas, M. (1994). Stop bands for elastic waves in periodic composite materials. *The Journal of the Acoustical Society of America* 95, 1734–1740. doi:10.1121/1.408692
- El-Nabulsi, R. A. (2018). Nonlocal Approach to Energy Bands in Periodic Lattices and Emergence of Electron Mass Enhancement. *J. Phys. Chem. Sol.* 122, 167–173. doi:10.1016/j.jpcs.2018.06.028
- El-Nabulsi, R. A. (2018). On Nonlocal Complex Maxwell Equations and Wave Motion in Electrodynamics and Dielectric media. *Opt. Quant Electron.* 50, 170. doi:10.1007/s11082-018-1436-x
- Eringen, A. C. (2006). Nonlocal Continuum Mechanics Based on Distribution. *Int. J. Eng. Sci.* 44 (3–4), 141–147. doi:10.1016/j.ijengsci.2005.11.002
- Eringen, A. C. (1972). Nonlocal Polar Elastic Continua. *Int. J. Eng. Sci.* 10 (1), 1–16. doi:10.1016/0020-7225(72)90070-5
- Eringen, A. C. (1983). On Differential Equations of Nonlocal Elasticity and Solutions of Screw Dislocation and Surface Waves. *J. Appl. Phys.* 54 (9), 4703–4710. doi:10.1063/1.332803
- Fernández-Alvarez, L., and Velasco, V. R. (1998). Sagittal Elastic Waves in Fibonacci Superlattices. *Phys. Rev. B* 57, 14141–14147. doi:10.1103/physrevb.57.14141
- Gastanier, M. P., and Pierre, C. (1997). Predicting Localization via Lyapunov Exponents Statistics. *J. Sound Vib* 203, 151–157.
- Gazi, N. A., and Bernhard, G. (2014). Quasi-periodic Fibonacci and Periodic One-Dimensional Hypersonic Phononic Crystals of Porous Silicon: Experiment and Simulation. *J. Appl. Phys.* 116, 094903.
- Golub, M. V., Zhang, C., and Wang, Y.-S. (2012). SH-wave Propagation and Scattering in Periodically Layered Composites with a Damaged Layer. *J. Sound Vibration* 331, 1829–1843. doi:10.1016/j.jsv.2011.12.008
- Gurtin, M. E., Weissmüller, J., and Larché, F. (1998). A General Theory of Curved Deformable Interfaces in Solids at Equilibrium. *Philosophical Mag. A* 78 (5), 1093–1109. doi:10.1080/01418619808239977
- Hashemi, S. H., and Samaei, A. T. (2011). Buckling Analysis of Micro/nanoscale Plates via Nonlocal Elasticity Theory. *Physica E: Low-dimensional Syst. Nanostructures* 43, 1400–1404. doi:10.1016/j.physe.2011.03.012
- Heireche, H., Tounsi, A., Benzair, A., Maachou, M., and Adda Bedia, E. A. (2008). Sound Wave Propagation in Single-Walled Carbon Nanotubes Using Nonlocal Elasticity. *Physica E: Low-dimensional Syst. Nanostructures* 40, 2791–2799. doi:10.1016/j.physe.2007.12.021
- Heppelstone, S. P., and Srivastava, G. P. (2008). Hypersonic Modes in Nanophononic Semiconductors. *Phys. Rev. Lett.* 101 (10), 105502. doi:10.1103/physrevlett.101.105502
- Hu an, A., Jiang Shu-sheng, S. S., Peng Ru-Wen, R. W., Zhang Chun-sheng, C. S., and Feng Duan, D. (1992). Extended One-Dimensional Fibonacci Structures. *Acta Phys. Sin.* 41 (1), 62–68. doi:10.7498/aps.41.62
- Hu, H., Li, D.-J., Zhu, J.-L., and Xiong, J.-J. (2000). Size Effects on Excitons in Nano-Rings. *J. Phys. Condens. Matter* 12, 9145–9151. doi:10.1088/0953-8984/12/43/304

- Huang, G. L., and Sun, C. T. (2007). Continuum Modelling of Solids with Micro/nanostructures. *Philosophical Mag.* 87, 3689–3707. doi:10.1080/14786430701400137
- Kana, N., Khamlich, S., Kana Kana, J. B., and Maaza, M. (2013). Peculiar Surface Size-Effects in NaCl Nano-Crystals. *Surf. Rev. Lett.* 20, 1350001. doi:10.1142/s0218625x13500017
- Ke, L.-L., Wang, Y.-S., and Wang, Z.-D. (2012). Nonlinear Vibration of the Piezoelectric Nanobeams Based on the Nonlocal Theory. *Compos. Structures* 94, 2038–2047. doi:10.1016/j.compstruct.2012.01.023
- King, P. D. C., and Cox, T. J. (2007). Acoustic Band Gaps in Periodically and Quasiperiodically Modulated Waveguides. *J. Appl. Phys.* 102, 014902. doi:10.1063/1.2749483
- Kissel, G. J. (1991). Localization Factor for Multichannel Disordered Systems. *Phys. Rev. A* 44, 1008–1014. doi:10.1103/physreva.44.1008
- Kushwaha, M. S., Halevi, P., Dobrzynski, L., and Djafari-Rouhani, B. (1993). Acoustic Band Structure of Periodic Elastic Composites. *Phys. Rev. Lett.* 71, 2022–2025. doi:10.1103/physrevlett.71.2022
- Luntiaov, M., and Rogerson, G. A. (2010). Long Wave Motion in Layered Elastic media. *Int. J. Eng. Sci.* 48 (21), 1856–1871.
- Merlin, R., Bajema, K., Clarke, R., Juang, F.-Y., and Bhattacharya, P. K. (1985). Quasiperiodic GaAs-AlAs Heterostructures. *Phys. Rev. Lett.* 55, 1768–1770. doi:10.1103/physrevlett.55.1768
- Mindlin, R. D. (1965). Second Gradient of Strain and Surface-Tension in Linear Elasticity. *Int. J. Sol. Structures* 1 (4), 417–438. doi:10.1016/0020-7683(65)90006-5
- Nguyen, T. T., Abdelmoula, R., Li, J., Roussigne, Y., and Stashkevich, A. (2016). Wave Propagating in Multilayers Composed of Piezo Electric and Piezo Magnetic Layers. *Composites B: Eng.* 93, 289–301. doi:10.1016/j.compositesb.2016.03.019
- Nougaoui, A., and Rouhani, B. D. (1987). Elastic Waves in Periodically Layered Infinite and Semi-infinite Anisotropic media. *Surf. Sci.* 185, 125–153. doi:10.1016/s0039-6028(87)80618-0
- Nowinski, J. L. (1984). On the Nonlocal Aspects of the Propagation of Love Waves. *Int. J. Eng. Sci.* 22, 383–392. doi:10.1016/0020-7225(84)90073-9
- Nowinski, J. L. (1991). On Wave Propagation in an Elastic Micropolar Medium with Nonlocal Cohesive Forces. *J. Franklin Inst.* 328 (4), 459–470. doi:10.1016/0016-0032(91)90020-4
- Parsons, L. C., and Andrews, G. T. (2009). Observation of Hypersonic Phononic crystal Effects in Porous Silicon Superlattices. *Appl. Phys. Lett.* 95, 241909. doi:10.1063/1.3275742
- Ramprasad, R., and Shi, N. (2005). Scalability of Phononic crystal Heterostructures. *Appl. Phys. Lett.* 87 (11), 111101. doi:10.1063/1.2043242
- Sesion, P. D., Albuquerque, E. L., Chesman, C., and Freire, V. N. (2007). Acoustic Phonon Transmission Spectra in Piezoelectric AlN/GaN Fibonacci Phononic Crystals. *Eur. Phys. J. B* 58, 379–387. doi:10.1140/epjb/e2007-00249-5
- Shaht, M. (2017). A General Nonlocal Theory and its Approximations for Slowly Varying Acoustic Waves. *Int. J. Mech. Sci.* 130, 52–63. doi:10.1016/j.ijmecsci.2017.05.038
- Sigalas, M. M., and Soukoulis, C. M. (1995). Elastic-wave Propagation through Disordered And/or Absorptive Layered Systems. *Phys. Rev. B Condens Matter* 51, 2780–2789. doi:10.1103/physrevb.51.2780
- Toupin, R. A. (1962). Elastic Materials with Couple-Stresses. *Arch. Rational Mech. Anal.* 11 (1), 385–414. doi:10.1007/bf00253945
- Waksmanski, N., and Pan, E. (2017). An Analytical Three-Dimensional Solution for Free Vibration of a Magneto-Electro-Elastic Plate Considering the Nonlocal Effect. *J. Intell. Mater. Syst. Structures* 28 (11), 1501–1513. doi:10.1177/1045389x16672734
- Wolf, A., Swift, J. B., Swinney, H. L., and Vastano, J. A. (1985). Determining Lyapunov Exponents from a Time Series. *Physica D: Nonlinear Phenomena* 16, 285–317. doi:10.1016/0167-2789(85)90011-9
- Yan, D.-J., Chen, A.-L., Wang, Y.-S., Zhang, C., and Golub, M. (2018). In-plane Elastic Wave Propagation in Nanoscale Periodic Layered Piezoelectric Structures. *Int. J. Mech. Sci.* 142–143, 276–288. doi:10.1016/j.ijmecsci.2018.04.054
- Yan, D.-J., Chen, A.-L., Wang, Y.-S., and Zhang, C. (2020). Size-effect on the Band Structures of the Transverse Elastic Wave Propagating in Nanoscale Periodic Laminates. *Int. J. Mech. Sci.* 180, 105669. doi:10.1016/j.ijmecsci.2020.105669
- Yan, Z.-Z., and Zhang, C. (2012). Band Structures and Localization Properties of Aperiodic Layered Phononic Crystals. *Physica B: Condensed Matter* 407, 1014–1019. doi:10.1016/j.physb.2012.01.001
- Yan, Z.-Z., Zhang, C., and Wang, Y.-S. (2009). Analysis of Wave Propagation and Localization in Periodic/disordered Layered Composite Structures by a Mass-spring Model. *Appl. Phys. Lett.* 94, 161909–161913. doi:10.1063/1.3119206
- Yan, Z.-Z., Zhang, C., and Wang, Y.-S. (2010). Wave Propagation and Localization in Randomly Disordered Layered Composites with Local Resonances. *Wave Motion* 47, 409–420. doi:10.1016/j.wavemoti.2010.02.002
- Yang, F., Chong, A. C. M., Lam, D. C. C., and Tong, P. (2002). Couple Stress Based Strain Gradient Theory for Elasticity. *Int. J. Sol. Structures* 39 (10), 2731–2743. doi:10.1016/s0020-7683(02)00152-x
- Yu, D., Wen, J., Shen, H., Xiao, Y., and Wen, X. (2012). Propagation of Flexural Wave in Periodic Beam on Elastic Foundations. *Phys. Lett. A* 376, 626–630. doi:10.1016/j.physleta.2011.11.056
- Zárate, J. E., Fernández-Alvarez, L., and Velasco, V. R. (1999). Transverse Elastic Waves in Fibonacci Superlattices. *Superlattices and Microstructures* 25, 519–526. doi:10.1006/spmi.1998.0682

Conflict of Interest: The authors declare that the research was conducted in the absence of any commercial or financial relationships that could be construed as a potential conflict of interest.

Publisher's Note: All claims expressed in this article are solely those of the authors and do not necessarily represent those of their affiliated organizations, or those of the publisher, the editors and the reviewers. Any product that may be evaluated in this article, or claim that may be made by its manufacturer, is not guaranteed or endorsed by the publisher.

Copyright © 2022 Yan and Yang. This is an open-access article distributed under the terms of the Creative Commons Attribution License (CC BY). The use, distribution or reproduction in other forums is permitted, provided the original author(s) and the copyright owner(s) are credited and that the original publication in this journal is cited, in accordance with accepted academic practice. No use, distribution or reproduction is permitted which does not comply with these terms.



Impact of the Scatterer Type on Ultrasound Wave Propagation in Microstructure Composites: Calculation and Application

Yuming Yang¹, Huilong Duan¹ and Yinfei Zheng^{1,2*}

¹College of Biomedical Engineering and Instrument Science, Zhejiang University, Hangzhou, China, ²Zhejiang Lab, Research Center for Intelligent Sensing, Hangzhou, China

OPEN ACCESS

Edited by:

Fuyin Ma,
Xi'an Jiaotong University, China

Reviewed by:

Dong Zhang,
Nanjing University, China
Weijun Lin,
Institute of Acoustic, CAS, China

*Correspondence:

Yinfei Zheng
zyfnjupt@zju.edu.cn

Specialty section:

This article was submitted to
Metamaterials,
a section of the journal
Frontiers in Materials

Received: 11 March 2022

Accepted: 16 March 2022

Published: 11 April 2022

Citation:

Yang Y, Duan H and Zheng Y (2022)
Impact of the Scatterer Type on
Ultrasound Wave Propagation in
Microstructure Composites:
Calculation and Application.
Front. Mater. 9:894074.
doi: 10.3389/fmats.2022.894074

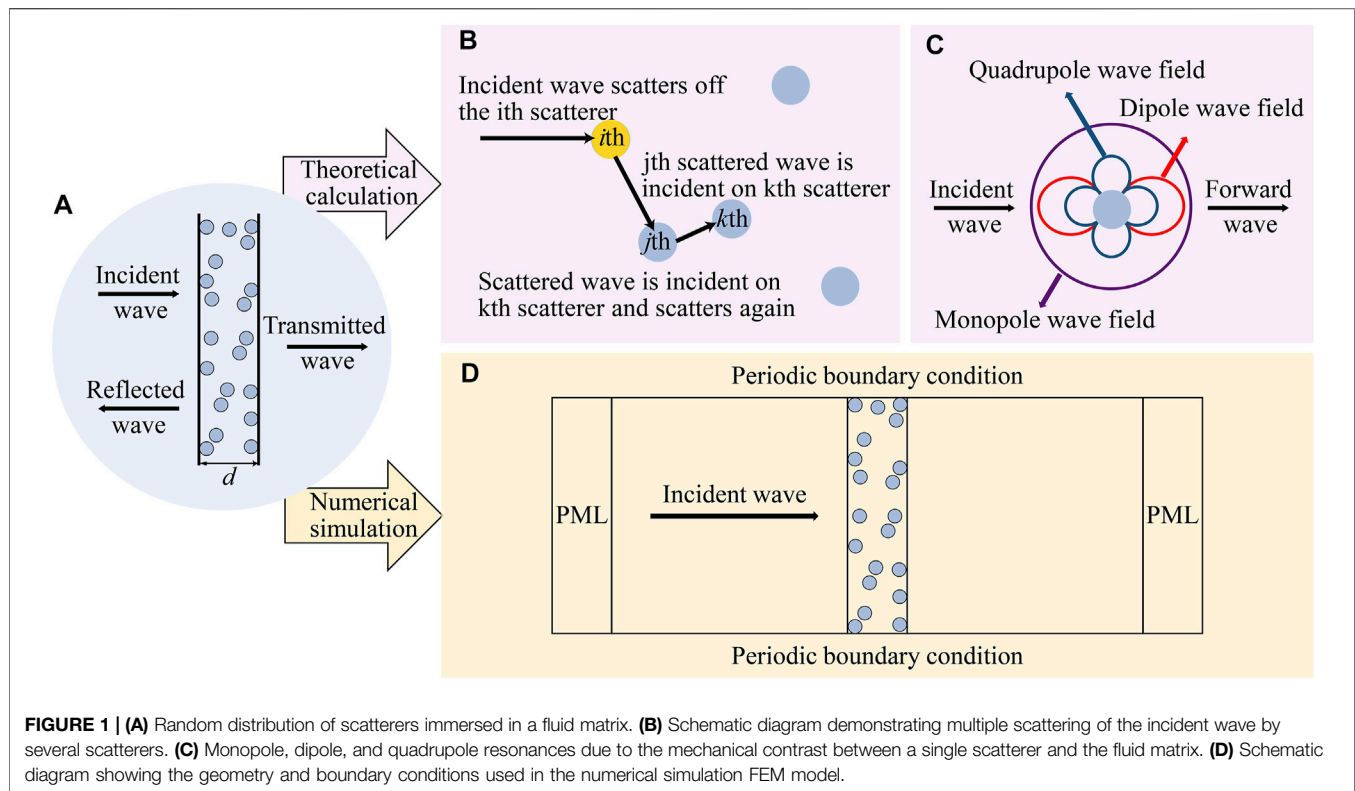
This study is motivated to quantitatively analyze the differences among various multiple scattering models to determine the role played by the scatterer type in ultrasonic wave propagation. By calculating the transmission and reflection coefficients of the composites, the results of multiple scattering theoretical models of different scatterer types have been evaluated. The problem of acoustic properties in a fluid matrix containing different types of micron-scale scatterers operating in the ultrasound frequency range is considered. Theoretical calculations are conducted for composites with different mechanical properties. Meanwhile, the theoretical results have been compared with numerical finite element method simulations, which can be regarded as a benchmark to verify the validity of different theoretical models. The results show that the composites can achieve negative acoustic properties by selecting appropriate resonant scatterers, paving the way for searching ultrasonic metamaterials with desired negative acoustic properties. We further explored the application of microstructure ultrasonic metamaterials by enhancing the ultrasound transmitted energy through the high-impedence skull layer, having the potential for non-invasive ultrasound brain imaging and therapy.

Keywords: microstructure composite, multiple scattering, effective wavenumber, numerical simulation, ultrasonic metamaterial

INTRODUCTION

Acoustic metamaterials (AMMs) are special composite structures with exotic properties that natural materials do not possess (Lee et al., 2017; Liu et al., 2020). In recent years, the studies of AMMs have paved the way for diverse applications such as acoustic cloaking (Zigoneanu et al., 2014), sound absorption (Yang and Sheng, 2017; Xiao et al., 2022), acoustic imaging (Deng et al., 2009; Zhu et al., 2011; Dong et al., 2018), impedance matching (D'Aguanno et al., 2012), focusing (Zhang et al., 2009; Page, 2016), and canceling out aberrating layers (Shen et al., 2014; Craig et al., 2019). However, the current research study on AMMs mostly focuses on audible sound frequency. The successful application of ultrasonic metamaterials still faces considerable challenges due to the long-wavelength limitation, therefore insisting the need to design, simulate, and fabricate micrometer-scale size AMM resonant scatterers.

Current studies of ultrasonic metamaterials mainly utilize strong Mie-type resonances (Brunet et al., 2013) to exhibit negative acoustic properties, using scatterers randomly suspended in a fluid matrix phase. For over a century, numerous models of multiple



scattering of randomly suspended scatterers in composites for inhomogeneous media have been studied. Foldy first proposed the multiple scattering theory (MST) to calculate the effective wavenumber in composites with isotropic scatterers in a fluid matrix (Foldy, 1945). The MST model was further extended to anisotropic scatterers by Waterman and Truell (Waterman and Truell, 1961), Lloyd and Berry (Lloyd and Berry, 1967), Linton and Martin (Linton and Martin, 2005), and Luppé and Conoir (Luppé and Conoir, 2011). This prompted us to investigate whether these models are still efficient for calculating ultrasound wave propagation in composites with randomly suspended microstructure scatterers.

In this study, the acoustic properties of two-dimensional micron-scale scatterers randomly immersed in a fluid matrix have been considered. The role played by the type of scatterers in the propagation of ultrasound waves is investigated. The transmission and reflection coefficients have been analyzed *via* the effective wavenumber and the effective impedance of the composites. Meanwhile, the acoustic properties of the microstructure composites have been further addressed by the finite element method (FEM) model. Therefore, the numerical simulation benchmark allows us to specify the validity domains for each of these analytical methods under study. Another aspect of this work is to figure out the potential application of the microstructure ultrasonic metamaterials. With the capacity of enhancing the transmitted energy through the skull, this type of ultrasonic metamaterials has the potential for non-invasive ultrasound brain imaging and therapy.

THEORETICAL CALCULATION AND NUMERICAL SIMULATION OF COMPOSITES

For a clear presentation of the computational approach for the calculation and simulation of transmission and reflection coefficients, a random distribution of two-dimensional scatterers immersed in a fluid matrix was considered in this study. We suppose N scatterers are suspended in the slab region of thickness d . The scatterers have identical cylindrical geometry and are uniformly and randomly distributed. The screen of scatterers is insensitized by a normal incident plane wave from the left, as shown in **Figure 1A**; the multiple scattering of ultrasound can be considered as energy transport; some energy from the forward wave is dissipated within the scatterers, while the other portion is transferred to the back wave. The MST theoretical model (**Figures 1B,C**) is used to obtain the transmission and reflection coefficients of random distributions of scatterers and then compared with the benchmark value from the FEM numerical simulation (**Figure 1D**).

Under the influence of an incident wave, multiple scattering occurs inside the scatterers, as shown in **Figure 1B**. Depending on the MST, the scattered wave generated by the i th scatterer will affect its adjacent scatterers. For an adjacent j th scatterer, the scattered wave excited by the i th scatterer can be regarded as an incident wave, which interacts with the j th scatterer to excite a scattered wave; it can also be regarded as an incident wave of the k th scatterer and so on (Waterman and Truell, 1961). The MST

mainly focuses on calculating the effective dynamic properties of random distributions of scatterers, and its basic problem is the scattering of a single scatterer, as shown in **Figure 1C**. When the scatterer radius is much smaller than the wavelength, multiple resonance modes arise due to the mechanical contrast between a single scatterer and the fluid matrix, which creates movement of the scatters relative to the fluid matrix (Kafesaki et al., 2000), a monopole resonance due to the velocity contrast, a dipole resonance due to the density contrast, and a quadrupole resonance due to the shear modulus contrast. In particular, when the velocity within the scatterers is much slower than that of the fluid matrix, multiple Mie-type resonances can be exhibited. The effective properties of random composites are deeply altered close to the particle frequency resonances, opening up possibilities to achieve ultrasonic metamaterials with negative acoustic properties. In the long-wavelength limit region, the corresponding possible scatterer size is reduced to the micrometer size in water for ultrasound frequency (Povey, 2013). The fact that whether the MST can analyze the acoustic properties of ultrasonic metamaterials with low-velocity micron-scale scatterers randomly immersed in a fluid matrix is also discussed in this article.

To verify the applicability of the MST for composites operating in the ultrasound frequency region, numerical FEM simulation values of the transmission and reflection coefficients are used as the benchmark, as shown in **Figure 1D**. The numerical simulation results are compared with the theoretical model predictions to analyze different analytical MST methods.

Theoretical Calculation

Multiple scattering by scatterers suspended in composites is a fundamental topic with the extensive literature. The estimation of the effective properties of composites is very significant for the design and preparation of composites. So far, many related approaches and predictive models have been proposed. As early as 1945, Foldy et al. proposed the MST for waves that are isotropically scattered by randomly distributed scatterers. Since the specific configuration of the amorphously distributed scatterers is not important, the configuration of the obstacles can be considered as the average of one state in an ensemble. Foldy considered the first order of the scattering coefficient for a single scattering and obtained **Eq. 1** to calculate the frequency-dependent complex wavenumber K , where K_0 is the wavenumber of the matrix phase, and N is the number of the scatterers (Foldy, 1945). Lax generalized Foldy's results to anisotropic scatterers by inducing a quantum-mechanical viewpoint and using the quasi-crystalline approximation (Lax, 1951; 1952). However, in both Foldy's and Lax's studies, the effective wavenumber is expressed in terms N and the cumulative effect of the only forward far-field scattering amplitude, without considering the important role of the backscattered amplitude.

$$K^2 = K_0^2 - i4Nf(\theta). \quad (1)$$

Waterman and Truell further improved Foldy's method by introducing quadratic terms for the number of scatterers, laying a foundation for other multiple scattering theories. Their most

important result is that the wave propagation in the scattering medium can be described by the far-field amplitude $f(\theta)$ of a single scatterer, which is an essential parameter of the scattering medium. As observed from **Eq. 2**, the Waterman and Truell framework has taken both forward ($\theta = 0$) and backscattered ($\theta = \pi$) far-field scattering amplitudes into consideration (Waterman and Truell, 1961).

$$(K/K_0)^2 = 1 - 4iNf(0)/K_0^2 - 4N^2[f(0)^2 - f(\pi)^2]/K_0^4, \quad (2)$$

$$f(\theta) = \sum_{n=0}^{\infty} \varepsilon_n T_n \cos(n\theta), \quad (3)$$

where $\varepsilon_n = 1$ for $n = 0$ and $\varepsilon_n = 2$ for $n \geq 1$. The expansion coefficients T_n are determined by the boundary conditions of the particular problem considered. By comparing **Eq. 1** and **Eq. 2**, it is noted that when the far-field amplitude is equal to the forward far-field amplitude in the Waterman and Truell framework, **Eq. 2** is simplified to **Eq. 1** in Foldy's framework. Twersky considered different incidence field angles and expanded the normal incidence formula in the Waterman and Truell framework into a random incidence angle α_{in} for two dimensions (Twersky, 1962).

$$(K/K_0)^2 = 1 - 4iNf(0)/K_0^2 - 4N^2 \cos^2 \alpha_{in} [f(0)^2 - f(\pi - 2\alpha_{in})^2]/K_0^4, \quad (4)$$

where α_{in} is the incidence angle, and $f(0)$ and $f(\pi - 2\alpha_{in})$ can be obtained from **Eq. 3**. If the normal incident to the slab ($\alpha_{in} = 0$) is considered, **Eq. 4** in the Twersky framework is equal to **Eq. 2** in the Waterman and Truell framework. Lloyd and Berry (Lloyd and Berry, 1967) further extended and corrected the work by Waterman and Truell, and they showed that the formula for calculating the wavenumber should be

$$(K/K_0)^2 = 1 - 4iNf(0)/K_0^2 + 4N^2 \left\{ f(0)^2 - f(\pi)^2 + \int_0^\pi \frac{1}{\sin(\theta/2)} \frac{d}{d\theta} [f(\theta)^2] d\theta \right\} / K_0^4. \quad (5)$$

Eq. 5 is different from **Eq. 2** by the Waterman and Truell framework, both in the signs of the forward and backscattered terms and in the additional modified term of N^2 . Linton and Martin also presented a two-dimensional model for circular cylinders inspired and based on the hole correction, assuming that the exclusion distance is small compared to the wavelength (Linton and Martin, 2005):

$$(K/K_0)^2 = 1 - 4iNf(0)/K_0^2 + (8N^2/\pi K_0^4) \int_0^\pi \cot(\theta/2) \frac{d}{d\theta} [f(\theta)^2] d\theta. \quad (6)$$

Based on the effective wavenumber in the Waterman and Truell framework, Angel and Aristégui further described the effective medium by the reflection coefficient and the

transmission coefficient (Angel and Aristégui, 2005; Aristégui and Angel, 2007).

$$R = -Q \exp(-iK_0 d) \times [1 - \exp(2iK_0 d)] / [1 - Q^2 \exp(2iKd)], \quad (7)$$

$$T = (1 - Q^2) \times \exp[i(K - K_0)d] / [1 - Q^2 \exp(2iKd)], \quad (8)$$

where $Q = (Z_0 - Z)/(Z_0 + Z)$, Z , indicates the effective impedance of the composite, and Z_0 indicates the impedance of the matrix phase; from the formula $Z = \rho\omega/K$, we can obtain

$$Z/Z_0 = (K_0/K) \times (\rho/\rho_0), \quad (9)$$

where ρ/ρ_0 is the effective mass density (EMD) of the composite, and ρ_0 indicates the mass density of the matrix phase. Angel and Aristégui also obtained the EMD in Eq. 10 and effective bulk modulus (EBM) as M/M_0 in Eq. 11.

$$\rho/\rho_0 = 1 - 2iN[f(0) - f(\pi)]/K_0^2, \quad (10)$$

$$M/M_0 = [1 - 2iN[f(0) + f(\pi)]/K_0^2]^{-1}, \quad (11)$$

where $M_0 = \rho_0 c_0^2$, c_0 , indicates the sound velocity of the matrix phase. Obtaining Eq. 12 by taking Eq. 10 into Eq. 9, then the transmission and reflection coefficients can be calculated.

$$Z/Z_0 = (K_0/K) \times \{1 - 2iN[f(0) - f(\pi)]/K_0^2\}. \quad (12)$$

Recently, Luppé and Conoir further obtained the EMD, EBM, and effective impedance as

$$\begin{aligned} \rho/\rho_0 = & 1 - 2iN(f(0) - f(\pi))/K_0^2 + (4N^2/K_0^4)\{f(0)^2/2 \\ & - f(\pi)^2/2 + J(0)[f(\pi) - T_0 - f(0)]/f(0) \\ & + T_0 I(\pi)[f(0) - T_0]/f(0) \\ & + T_0 J(\pi)/f(0) - T_0 I(0)[2f(\pi) - f(0) - T_0]/f(0)\}, \end{aligned} \quad (13)$$

$$M/M_0 = (\rho/\rho_0)(K_0^2/K^2), \quad (14)$$

$$\begin{aligned} Z/Z_0 = & K_0/K \times \{1 - 2iN(f(0) - f(\pi))/K_0^2 + (4N^2/K_0^4) \\ & \times \{f(0)^2/2 - f(\pi)^2/2 + J(0)[f(\pi) - T_0 - f(0)] \\ & \times /f(0) + T_0 I(\pi)[f(0) - T_0]/f(0) + T_0 J(\pi)/f(0) \\ & - T_0 I(0)[2f(\pi) - f(0) - T_0]/f(0)\}, \end{aligned} \quad (15)$$

with

$$\begin{aligned} J(\alpha) = & -1/(2\pi) \times \int_0^\pi \cot(\theta/2) \left\{ \frac{d}{d\theta} [f(\theta)f(\alpha - \theta) \right. \\ & \left. + f(-\theta)f(\alpha + \theta)] \right\} d\theta, \end{aligned} \quad (16)$$

$$I(\alpha) = -1/(2\pi) \times \int_0^\pi \cot(\theta/2) \left\{ \frac{d}{d\theta} [f(\alpha - \theta) + f(\alpha + \theta)] \right\} d\theta. \quad (17)$$

The effective mass density and effective impedance in the Angel and Aristégui framework and Luppé and Conoir framework are equal when only the first order of N^2 is considered. The reasons for the differences of the

mentioned formulas are worth discussing, and errors will occur when different boundary regions are selected during integration. Table 1 summarizes the assumptions, abbreviations, and calculation formulas of the previously mentioned five MST models.

Numerical Simulation

Multiple scattering signals are composed of coherent parts and incoherent parts. Since enough scatterer position configurations are averaged, the incoherent part vanishes in MST theoretical calculations. In practice, it is not easy to obtain coherent wave characteristics by using only one sample of random composite because it requires a large number of local measurements along the composite to restore the averaging procedure. Therefore, numerical simulations are a good choice.

The numerical simulations were finished by COMSOL Multiphysics software in the pressure acoustic frequency domain. The designed numerical simulation geometric model is shown in Figure 1D. A slab of screen S contains N identical scatterers with same radius a , so the fraction is $\phi = N\pi a^2/S$. Their positions are selected by a random draw function. The periodicity of the model in the direction perpendicular to sound propagation is simulated by applying periodic boundary conditions on both sides of the screen. Using perfectly matched layer (PML) boundary conditions to simulate the outer boundary of the fluid domain, the incident plane wave is insonified on the left boundary of the model. The reflection coefficient and transmission coefficient of an incident plane wave passing through the screen of scatterers are calculated by using acoustic boundary conditions. We have made 100 simulations to achieve the convergence of the averaged field.

RESULTS AND DISCUSSION

It is necessary to establish a precise framework to limit the study field and focus on the role played by microstructures. The purpose of this part is to study the influence of the scatterer type on the ultrasound wave propagation in composites. In the previous section, we summarized the aforementioned five theoretical models of characterizing the scattering medium; now, we compared the results obtained by five different MST theoretical models under the benchmark of the FEM simulations.

To go further into the analysis of the impact of the microstructure scatterers type in general, we studied two different types of scatterers. Case I: steel scatterers are immersed in the water matrix. Case II: rubber scatterers are suspended in the water matrix. In both cases, the radius of the scatterers is set at $60 \mu\text{m}$ with $\phi = 20.94\%$ to satisfy the long-wavelength limit in ultrasound frequency. Parameters of the used materials are listed in Table 2.

Case 1: Steel Scatterers in Water

We considered the propagation of coherent waves through steel scatterers randomly immersed in water. Figure 2A and Figure 2B present the modulus of complex transmission and reflection coefficients corresponding to steel scatterers in water,

TABLE 1 | Assumption theory, abbreviations, and calculation equations of five different MST models.

Model	Assumption	Abbreviation	Equation
Foldy	Configurational average	F	Equation 1
Waterman and Truell	Far-field backscattering	WT	Equation 2
Lloyd and Berry	Resummation method	LB	Equation 5
Linton and Martin	Hole correction	LM	Equation 6
Lupé and Conoir	Quasi-crystalline approximation	LC	Equations 13–17

TABLE 2 | Acoustic properties of the materials.

Material	Density (kg/m ³)	Speed of sound (m/s)
Steel	7,900	5,955
Rubber	600	100
Water	1,000	1,500

according to MST frameworks (Table 1) and FEM simulations. Both in Figure 2A and Figure 2B, the transmission coefficients obtained by four MST frameworks (WT, LB, LM, and LC) agree with each other, except the Foldy framework (F) as expected. It indicates that Foldy only considered the forward far-field scattering amplitude without considering the important role of the backscattered amplitude. Therefore the scattering amplitude of $|R|$ is significantly lower, and the scattering amplitude of $|T|$ is higher than the other four MST models. We observed that the calculation results of the four frameworks qualitatively correspond with the FEM simulation results, especially at a low frequency (0–1.0 MHz). At a low frequency, we also observed that the FEM simulation value is between the theoretical value of LC and WT frameworks and more close to the LC framework. In the LC framework, the quadratic coefficient of the scatterer number is modified, and the results show the difference when compared with the WT framework, indicating the correction to N^2 is necessary. Depending on the long-wavelength limit, only considering the lowest-order truncation coefficient of T_n in the expansion of the scattering fields can be sufficient. Simpler formulas for calculating the effective wavenumber in the LB framework Eq. 18 and LM framework Eq. 19 can be obtained by using the zero and first orders of T_n ($n \leq 2$)

$$\begin{aligned} (K/K_0)^2 = & 1 - 4iN(T_0 + 2T_1 + 2T_2)/K_0^2 - 32N^2(4T_1^2/3 \\ & + 304T_2^2/105 + T_0T_1 + 8T_0T_2/3 + 78T_1T_2/15) \\ & \times /K_0^4, \end{aligned} \quad (18)$$

$$\begin{aligned} (K/K_0)^2 = & 1 - 4iN(T_0 + 2T_1 + 2T_2)/K_0^2 - 32N^2(T_1^2 + 2T_2^2 \\ & + T_0T_1 + 2T_0T_2 + 4T_1T_2)/K_0^4. \end{aligned} \quad (19)$$

It is worth noting that the approximation formulas for LB and LM frameworks are very similar, which is also evidenced by the fact that the LM framework curves are particularly close to the LB framework curves, as shown in Figure 2A and Figure 2B.

AMMs with negative EMD and/or EBM have been studied extensively, which can cause a lot of exotic acoustic properties. To enhance our analysis, we have investigated the EMD and EBM for the microstructure composites. Figure 2C and Figure 2D show the real parts of the EMD and EBM, according to two different MST frameworks, the Angel and Aristégui framework (Eq. 10 and Eq. 11) and LC framework (Eq. 13 and Eq. 14). As observed in Figure 2A and Figure 2B, the transmission and reflection coefficients of steel scatterers in water display no resonance peaks. Therefore, the real parts of the EMD and EBM are decreasing from the static limit to unit one with increasing frequency. At a high frequency, the real parts of the EMD and EBM approach unity, and the imaginary parts of the EMD and EBM tend to zero. These results demonstrate that the EMD and EBM tend to reach that of water at a high frequency; in other words, there is no contribution in the density and modulus from the steel scatterers.

Case 2: Rubber Scatterers in Water

For the second case, rubber scatterers in water, it is notable to see resonances at specific frequency regions. Figure 2E and Figure 2F show the moduli of transmission and reflection coefficients corresponding to rubber scatterers in water. For transmission coefficients (Figure 2E), the frequency regions of the resonances peaks in the MST models are consistent with those in FEM simulation, except the Foldy framework misses three main resonance peaks in 0.4–3 MHz. Once again, it indicates that Foldy only considered the forward far-field scattering amplitude. However, out of resonant frequency regions (around 1.02 and 1.87 MHz), MST models provide results significantly different from FEM simulations. It can be explained that the scatterers reach a steady state at the specific narrow resonant frequency, and a large amount of energy is stored at this frequency region. As less energy is transmitted in the fluid, this reduces the intensity of interactions between scatterers meanwhile. Once out of the steady state, MST models only calculate the coherent part but the incoherent part superposition decreases the amplitude of the transmitted wave. We also noticed that the oscillation of the WT framework at resonance frequency regions appeared visibly smoother than that of LB, LM, and LC frameworks, which can be regarded as the influence of the microstructure type. LB, LM, and LC frameworks have an additional term of N^2 compared to the WT framework. When using rubber as scatterers, the velocity within the scatterers is very low in comparison with that of the matrix phase, exhibiting strong Mie-type resonance (Leighton, 1997). In other words, the additional term of N^2 causes more oscillations at resonant frequency regions due to the type of microstructure. As for the reflection coefficient (Figure 2F), the

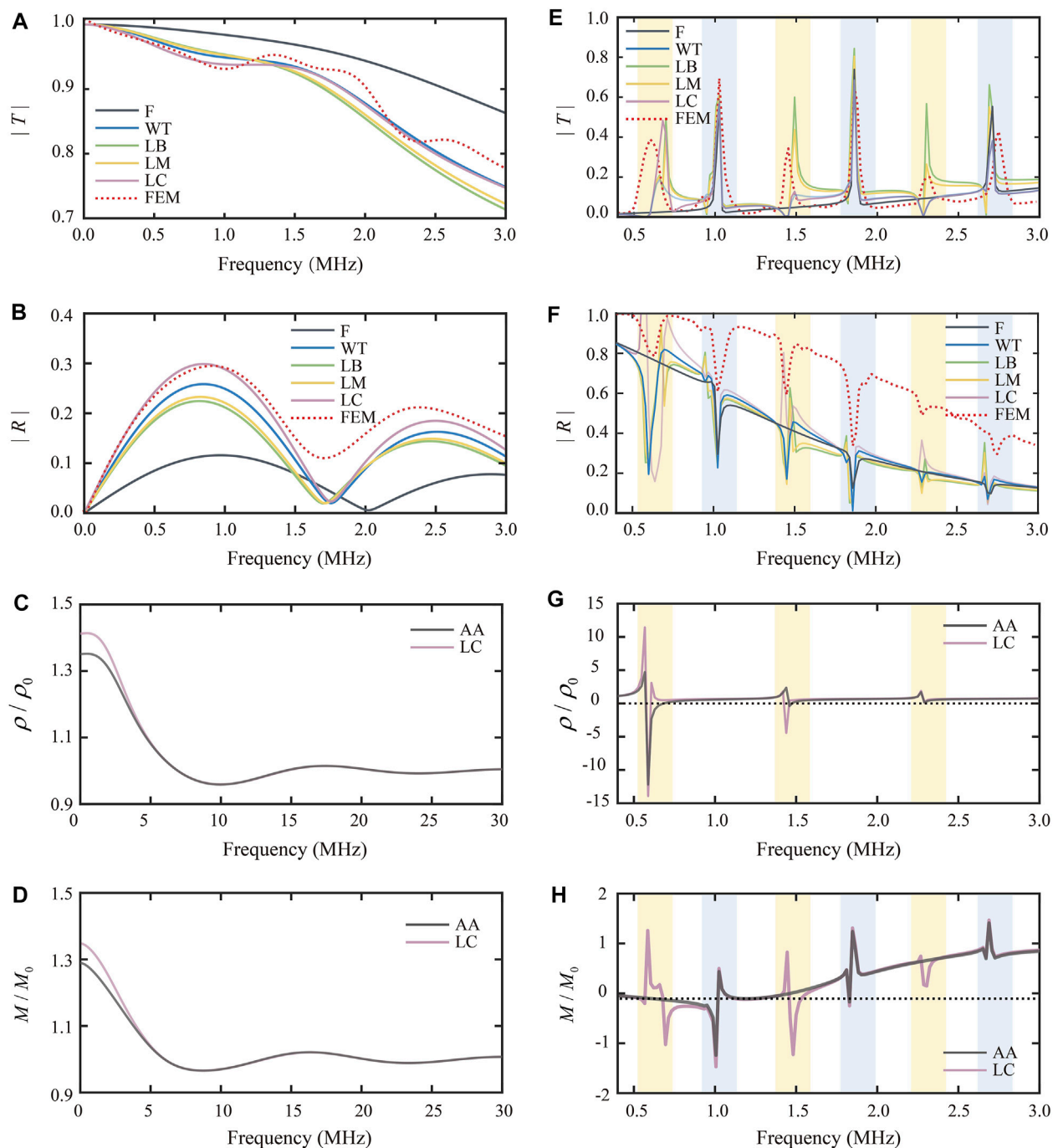
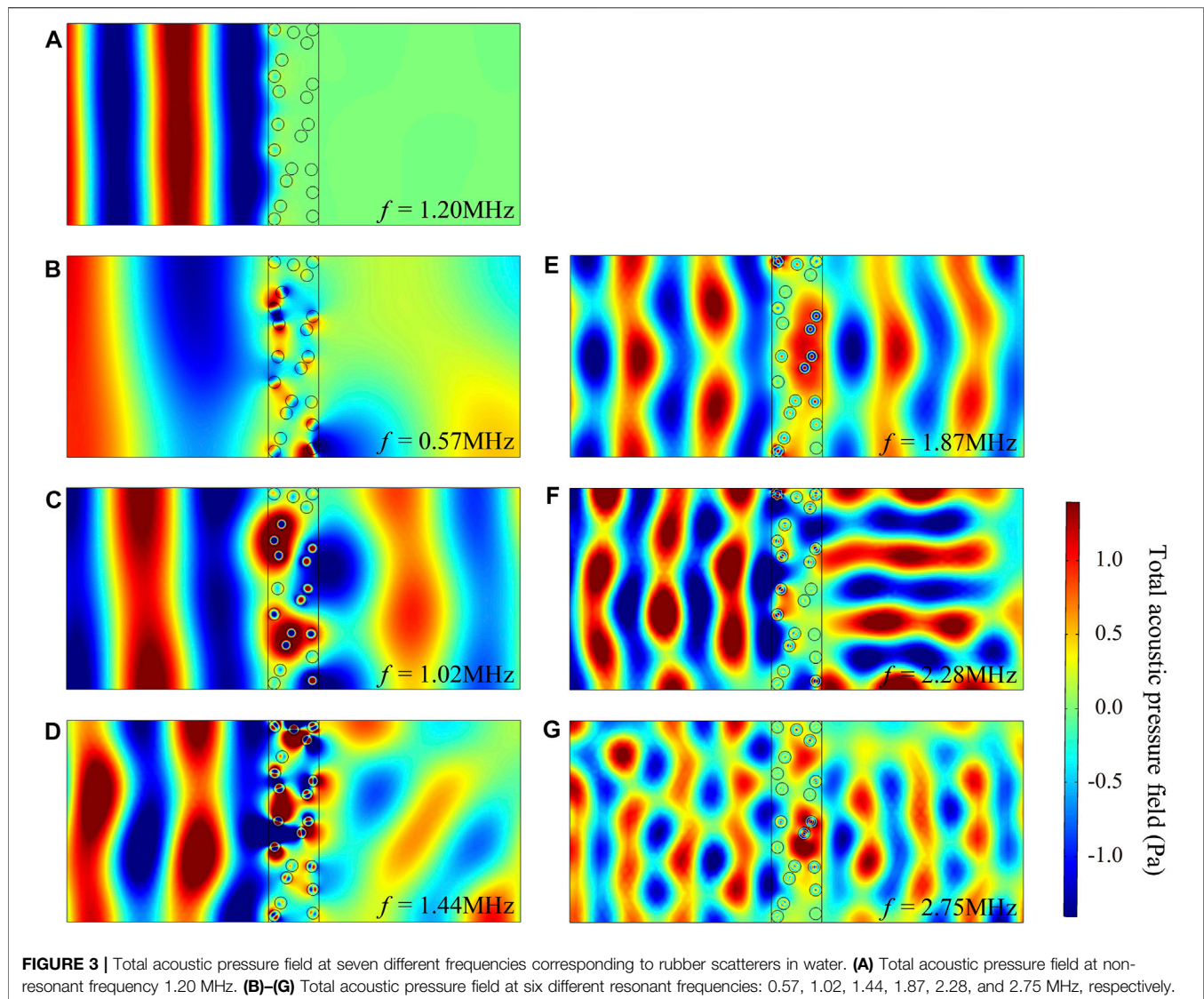


FIGURE 2 | Comparison of transmission and reflection coefficients moduli for different types of scatterers suspended in water by MST models and FEM simulations and calculation results of the real parts of the EMD and EBM corresponding to different type scatterers. **(A)** Modulus of the transmission coefficient versus frequency corresponding to steel scatterers in water. **(B)** Modulus of the reflection coefficient versus frequency corresponding to steel scatterers in water. **(C)** Real part of the EMD versus frequency corresponding to steel scatterers in water. **(D)** Real part of the EBM versus frequency corresponding to steel scatterers in water. **(E)** Modulus of the transmission coefficient versus frequency corresponding to rubber scatterers in water. **(F)** Modulus of the reflection coefficient versus frequency corresponding to rubber scatterers in water. **(G)** Real part of the EMD versus frequency corresponding to rubber scatterers in water. **(H)** Real part of the EBM versus frequency corresponding to rubber scatterers in water.

calculation results of MST models have the same trend line of change with FEM simulations but provide a lower value. The possible reason is that the incoherent part superposition

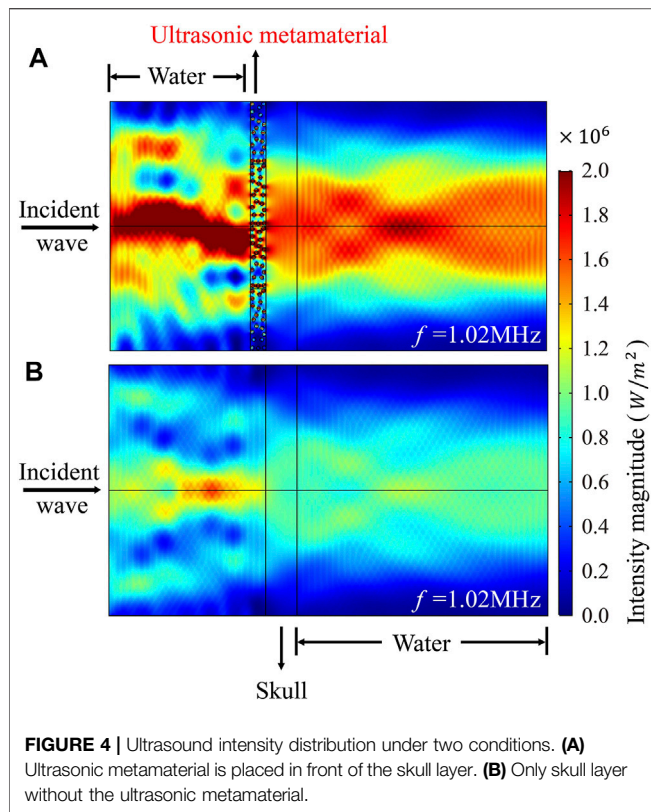
decreases the amplitude of the transmitted wave and increases the amplitude of the reflected wave, but the multiple scattering theory only calculates the coherent part. For Mie-type scatterers,



the results based on MST models and FEM simulations are inconsistent in the non-resonant frequency region, compared with hard-type scatterers. It indicated that the MST models are only suitable for observing the trend change and resonant frequency regions of Mie-type scatterers.

Figure 2G and **Figure 2H** show the real parts of the EMD and EBM corresponding to rubber scatterers in water. We noted that in six particular frequency regions, the moduli of transmission and reflection coefficients show obvious resonance peaks, which are around 0.57, 1.02, 1.44, 1.87, 2.28, and 2.75 MHz, respectively, within the ultrasound frequency range of 0.4–3 MHz. At six resonance peak frequencies, most of the incident energy is transmitted. As shown in **Figure 3**, rubber scatterers exhibit a variety of resonance modes at these specific frequencies, whereas at the non-resonant frequencies (**Figure 3A**), most of the energy is reflected by the composites. In the aforementioned narrow frequency regions, the EMD or EBM also show a negative value. There are negative resonant peaks in the EMD near 0.57 and

1.44 MHz (**Figure 2G**). For the Angel and Aristégui framework (AA framework), negative resonant peaks are formed in the EBM near 1.02 and 1.87 MHz. For the LC framework, negative resonant peaks in the EBM are observed near 0.57, 1.02, 1.44, and 1.87 MHz (**Figure 2H**). In the LC framework, the quadratic coefficient of the scatterer number is modified, which results in the difference compared with the AA framework. We can see that EBM results exhibit three more peaks compared to the AA framework (**Figure 2H**), but these are not shown in **Figure 2D**. Once again, it can be considered to be influenced by the type of the microstructure. When using ultra-slow Mie-type microstructure scatterers, the correction to N^2 term of the effective wavenumber should be considered. In summary, **Figure 2** illustrates that both the EMD and EBM can be made negative near the resonance frequency by choosing appropriate soft resonant scatterers, opening the possibility for searching ultrasonic metamaterials with desired negative properties. These narrow resonance frequency regions depend on the



scatterer mechanism, size, and fraction. In this work, we mainly discussed the influence of the microstructure type (scatterer mechanism) and illustrated that soft rubber scatterers can show negative acoustic parameters compared with hard steel scatterers.

Application

The aforementioned results illustrate that the MST theoretical calculation models are capable of analyzing ultrasonic metamaterials with negative effective properties. We chose soft rubber scatterers with low velocity and density suspended in water and a high fraction of scatterers to exhibit strong Mie-type resonances to recognize negative effect properties (Ba et al., 2017). In addition, the application of this ultrasonic metamaterial is further explored, depending on the research on complementary acoustic metamaterials (Shen et al., 2014); the imaging aberration skull layer is used to demonstrate whether the ultrasonic metamaterial in this study can enhance the ultrasound transmission through the skull. A numerical model was further achieved by using FEM simulations by COMSOL Multiphysics software. As shown in **Figure 4**, after the ultrasonic metamaterial layer is added in front of the skull layer ($\rho = 2000 \text{ kg/m}^3$, $c = 2500 \text{ m/s}$), the ultrasound energy through the skull was significantly increased at 1.02 MHz. By

analyzing the ultrasound intensity magnitude along the axis of ultrasound, it is found that the transmitted ultrasound intensity increases by up to 200% when the ultrasonic metamaterial layer is added. It is worth noting that the ultrasonic metamaterial exhibits negative EBM at 1.02 MHz, indicating that the EBM is the main factor affecting ultrasound wave penetration through the skull layer.

CONCLUSION

In this study, the transmission and reflection coefficients calculating results of five MST theoretical frameworks (Foldy, Waterman & Truell, Lloyd & Berry, Linton & Martin, and Luppé & Conoir) are compared with the FEM simulations. Hard steel scatterers and soft Mie-type scatterers randomly suspended in water operating at the ultrasound frequency region are taken into consideration. In the calculation of soft scatterers with a low velocity immersed in water, the resonances became sharp due to the contrast between the scatterers and the matrix. MST models can still analyze this type of ultrasonic metamaterials with negative properties. The application of this ultrasonic metamaterial is also simulated, and this ultrasonic metamaterial can counteract the attenuation of ultrasound transmission by the high-impedance layer. The intensity of ultrasound through the skull layer is increased by 200% when the ultrasonic metamaterial layer is added, paving the way for further non-invasive ultrasound imaging and therapy through the skull.

DATA AVAILABILITY STATEMENT

The original contributions presented in the study are included in the article/Supplementary Material, further inquiries can be directed to the corresponding author.

AUTHOR CONTRIBUTIONS

YY, HD, and YZ initiated the project. YY wrote the manuscript, carried out the theoretical calculations, and numerical simulations. All the authors contributed to the editing of the manuscript.

FUNDING

This work was supported by the National Key R&D Program of China (2018YFC0114900). The Zhejiang Provincial Key R&D Program of China (2022C01002). The National Major Scientific Research Instrument Development Project (81827804).

REFERENCES

- Angel, Y. C., and Aristégui, C. (2005). Analysis of Sound Propagation in a Fluid through a Screen of Scatterers. *The J. Acoust. Soc. America* 118 (1), 72–82. doi:10.1121/1.1931088
- Aristégui, C., and Angel, Y. C. (2007). Effective Mass Density and Stiffness Derived from P-Wave Multiple Scattering. *Wave Motion* 44 (3), 153–164. doi:10.1016/j.wavemoti.2006.08.005
- Ba, A., Kovalenko, A., Aristégui, C., Mondain-Monval, O., and Brunet, T. (2017). Soft Porous Silicone Rubbers with Ultra-low Sound Speeds in Acoustic Metamaterials. *Sci. Rep.* 7 (1), 1–6. doi:10.1038/srep40106
- Brunet, T., Leng, J., and Mondain-Monval, O. (2013). Soft Acoustic Metamaterials. *Science* 342 (6156), 323–324. doi:10.1126/science.1241727
- Craig, S. R., Welch, P. J., and Shi, C. (2019). Non-Hermitian Complementary Acoustic Metamaterials for Lossy Barriers. *Appl. Phys. Lett.* 115 (5), 051903. doi:10.1063/1.5110501
- D'Aguanno, G., Le, K. Q., Trimm, R., Alù, A., Mattiucci, N., Mathias, A. D., et al. (2012). Broadband Metamaterial for Nonresonant Matching of Acoustic Waves. *Sci. Rep.* 2 (1), 1–5. doi:10.1038/srep00340
- Deng, K., Ding, Y., He, Z., Zhao, H., Shi, J., and Liu, Z. (2009). Theoretical Study of Subwavelength Imaging by Acoustic Metamaterial Slabs. *J. Appl. Phys.* 105 (12), 124909. doi:10.1063/1.3153976
- Dong, H.-W., Zhao, S.-D., Wang, Y.-S., and Zhang, C. (2018). Broadband Single-phase Hyperbolic Elastic Metamaterials for Super-resolution Imaging. *Sci. Rep.* 8 (1), 1–10. doi:10.1038/s41598-018-20579-8
- Foldy, L. L. (1945). The Multiple Scattering of Waves. I. General Theory of Isotropic Scattering by Randomly Distributed Scatterers. *Phys. Rev.* 67 (3-4), 107–119. doi:10.1103/PhysRev.67.107
- Kafesaki, M., Penciu, R. S., and Economou, E. N. (2000). Air Bubbles in Water: A Strongly Multiple Scattering Medium for Acoustic Waves. *Phys. Rev. Lett.* 84 (26), 6050–6053. doi:10.1103/PhysRevLett.84.6050
- Lax, M. (1951). Multiple Scattering of Waves. *Rev. Mod. Phys.* 23 (4), 287–310. doi:10.1103/RevModPhys.23.287
- Lax, M. (1952). Multiple Scattering of Waves. II. The Effective Field in Dense Systems. *Phys. Rev.* 85 (4), 621–629. doi:10.1103/PhysRev.85.621
- Lee, D., Nguyen, D. M., and Rho, J. (2017). Acoustic Wave Science Realized by Metamaterials. *Nano Convergence* 4 (1), 1–15. doi:10.1186/s40580-017-0097-y
- Leighton, T. G. (1997). *The Acoustic Bubble*. Academic Press.
- Linton, C. M., and Martin, P. A. (2005). Multiple Scattering by Random Configurations of Circular Cylinders: Second-Order Corrections for the Effective Wavenumber. *J. Acoust. Soc. America* 117 (6), 3413–3423. doi:10.1121/1.1904270
- Liu, J., Guo, H., and Wang, T. (2020). A Review of Acoustic Metamaterials and Phononic Crystals. *Crystals* 10 (4), 305. doi:10.3390/cryst10040305
- Lloyd, P., and Berry, M. V. (1967). Wave Propagation through an Assembly of Spheres: IV. Relations between Different Multiple Scattering Theories. *Proc. Phys. Soc.* 91 (3), 678–688. doi:10.1088/0370-1328/91/3/321
- Luppé, F., and Conoir, J.-M. (2011). “Multiple Scattering by Cylinders Randomly Located in a Fluid: Effective Properties,” in *Journal of Physics: Conference Series* (Bristol, England: IOP Publishing),
- Page, J. H. (2016). Focusing of Ultrasonic Waves by Negative Refraction in Phononic Crystals. *AIP Adv.* 6 (12), 121606. doi:10.1063/1.4972204
- Povey, M. J. W. (2013). Ultrasound Particle Sizing: A Review. *Particuology* 11 (2), 135–147. doi:10.1016/j.partic.2012.05.010
- Shen, C., Xu, J., Fang, N. X., and Jing, Y. (2014). Anisotropic Complementary Acoustic Metamaterial for Canceling Out Aberrating Layers. *Phys. Rev. X* 4 (4), 041033. doi:10.1103/PhysRevX.4.041033
- Twersky, V. (1962). On Scattering of Waves by Random Distributions. I. Free-Space Scatterer Formalism. *J. Math. Phys.* 3 (4), 700–715. doi:10.1063/1.1724272
- Waterman, P. C., and Truell, R. (1961). Multiple Scattering of Waves. *J. Math. Phys.* 2 (4), 512–537. doi:10.1063/1.1703737
- Xiao, H., Yuan, T., Song, X., Chen, J., Zhou, J., Sui, D., et al. (2022). Broadband Sound Absorption of Subwavelength Porous Meta-Liner. *Front. Mater.* 9. doi:10.3389/fmats.2022.845597
- Yang, M., and Sheng, P. (2017). Sound Absorption Structures: From Porous media to Acoustic Metamaterials. *Annu. Rev. Mater. Res.* 47, 83–114. doi:10.1146/annurev-matsci-070616-124032
- Zhang, S., Yin, L., and Fang, N. (2009). Focusing Ultrasound with an Acoustic Metamaterial Network. *Phys. Rev. Lett.* 102 (19), 194301. doi:10.1103/PhysRevLett.102.194301
- Zhu, J., Christensen, J., Jung, J., Martin-Moreno, L., Yin, X., Fok, L., et al. (2011). A Holey-Structured Metamaterial for Acoustic Deep-Subwavelength Imaging. *Nat. Phys.* 7 (1), 52–55. doi:10.1038/nphys1804
- Zigoneanu, L., Popa, B.-I., and Cummer, S. A. (2014). Three-dimensional Broadband Omnidirectional Acoustic Ground Cloak. *Nat. Mater.* 13 (4), 352–355. doi:10.1038/nmat3901

Conflict of Interest: The authors declare that the research was conducted in the absence of any commercial or financial relationships that could be construed as a potential conflict of interest.

Publisher's Note: All claims expressed in this article are solely those of the authors and do not necessarily represent those of their affiliated organizations, or those of the publisher, the editors, and the reviewers. Any product that may be evaluated in this article, or claim that may be made by its manufacturer, is not guaranteed or endorsed by the publisher.

Copyright © 2022 Yang, Duan and Zheng. This is an open-access article distributed under the terms of the Creative Commons Attribution License (CC BY). The use, distribution or reproduction in other forums is permitted, provided the original author(s) and the copyright owner(s) are credited and that the original publication in this journal is cited, in accordance with accepted academic practice. No use, distribution or reproduction is permitted which does not comply with these terms.



Band Gaps and Vibration Attenuation Characteristics Analysis in Homogeneous Beam Coupled With Periodic Oscillators Based on the Method of Reverberation-Ray Matrix

Li Tang, Xiongliang Yao, Guoxun Wu* and Chuanlong Wang

College of Shipbuilding Engineering, Harbin Engineering University, Harbin, China

OPEN ACCESS

Edited by:

Siyuan Dai,
Auburn University, United States

Reviewed by:

Zhicheng Xiao,
Hunan University, China
Jialiang Shen,
Auburn University, United States

*Correspondence:

Guoxun Wu
wuguoxun@hrbeu.edu.cn

Specialty section:

This article was submitted to
Metamaterials,
a section of the journal
Frontiers in Materials

Received: 04 January 2022

Accepted: 28 March 2022

Published: 20 April 2022

Citation:

Tang L, Yao X, Wu G and Wang C
(2022) Band Gaps and Vibration
Attenuation Characteristics Analysis in
Homogeneous Beam Coupled With
Periodic Oscillators Based on the
Method of Reverberation-Ray Matrix.
Front. Mater. 9:848323.
doi: 10.3389/fmats.2022.848323

A periodic beam-oscillators coupling system is proposed as a physical model in this paper for analyzing the dynamic characteristics of periodic support beams and low-frequency flexural wave vibration of slender stiffened plate structures. The dispersion relation of flexural wave in the infinite long homogeneous beam coupled with periodic oscillators is calculated using the method of reverberation-ray matrix combined with the Bloch theorem. The accuracy and effectiveness of the method of reverberation-ray matrix in analyzing the band gaps and vibration characteristics of the homogeneous beam coupled with periodic oscillators are verified by the numerical results of the finite long homogeneous beam coupled with periodic oscillators. Both the analytical and numerical results show the existences of flexural wave band gaps in the homogeneous beam coupled with periodic oscillators, in which the propagation of the flexural waves is prohibited and flexural wave vibration is significantly suppressed. Furthermore, the effects of structural and material parameters on the flexural wave band gaps characteristics are respectively investigated. The flexural wave band gaps can be adjusted and optimized manually by adjusting structural and material parameters, which can be applied to vibration and noise control design of periodic support beams and slender stiffened plate structures.

Keywords: beam coupled with periodic oscillators, periodic beam structure, flexural wave band gap, vibration attenuation characteristics, the method of reverberation-ray matrix

1 INTRODUCTION

With the development of naval architecture and ocean engineering with high-speed, large-scale and large-tonnage, vibrations in ship and offshore structures owing to various ocean environmental loads and excitations of power systems become increasingly serious, can reduce productivity, endanger safety, affect service life of the structure and even discomfort of crews (Hirdaris et al., 2014; Murawski and Charchalis, 2014; Kandasamy et al., 2016). Therefore, it is necessary to eliminate or reduce vibration and noise of ship and offshore structures and develop low-noise structural design technology.

Many scholars have done a large number of studies to control vibration and noise of ship and offshore structures (Wang et al., 2013; Lan et al., 2014; Wang et al., 2016; Gripp and Rade, 2018). From their studies, there are three main methods to control vibration and noise. The first way is to control the source, design and manufacture power systems with low noise, low vibration or even

silence; the second is to control the propagation path through isolation, absorption, and attenuation methods; the third is to protect the receiver (Wu et al., 2014; Liu et al., 2015; Shi et al., 2016; Som and Das, 2018). As the development of naval architecture and ocean engineering with high-speed, large-scale and large-tonnage, it has become increasingly difficult to reduce noise from the source. Furthermore, the techniques to protect the receivers are unreasonable as the receivers are often moving as well as the rapid developments of the underwater acoustic detection technologies. Therefore, trying to reduce the vibration and noise in the propagation path is a more sensible choice (Ibrahim, 2008; Toky et al., 2020; Yaman et al., 2021). The mainly ways to control vibration and noise can be divided into passive control schemes, semi-active control schemes, and active control schemes (Keir et al., 2005; Ou et al., 2007; Liu et al., 2017; Enferadi et al., 2019; Han et al., 2019; Li and Yang, 2020). Although the existing traditional vibration reduction techniques can control the vibration and noise of ships and offshore structures to a certain extent, it also has some limitations, including the equipment mass must be larger and the narrow frequency band in passive control, the damping vibration attenuation only have an impact on the medium and high frequencies, as well as the system complexity and narrow band characteristics of active control. In addition, it is necessary to strengthen the research on low frequency vibration and noise control of ships and offshore structures, as the vibration and noise in the low frequency range has strong penetration and slow dissipation during propagation (Waye, 2011; Kim et al., 2019). Beam is one of the most important basic structures in engineering and are widely used in civil engineering, aerospace as well as naval architecture and ocean engineering. And stiffened plates, especially the bi-directionally orthogonal stiffened plates are widely used in deck, bottom and side structures of ships and offshore structures. The stiffened plates can be simplified to a multi-span beam model with periodic elastic supports and then into an elastic foundation beam model to study their static and dynamic characteristics (Chen and Chen, 1991). In addition, many slender stiffened plate structures in ships and offshore structures can be simplified into beam models for low frequency flexural wave vibration analysis. Thus, studying the dynamic characteristics of beams is of great significance to the dynamic performance and low noise structural design of ships and marine structures. Many scholars have done a lot of studies to investigate the wave band gaps and propagation characteristics in phononic crystals, acoustic metamaterials and other periodic structures in recent decades (He et al., 2017; Lee et al., 2018; Nateghi et al., 2019). Periodic structures have been introduced into the structural vibration reduction design due to the advantage of band gap characteristics.

Periodic structures have band gaps properties, which the propagation of waves in the periodic structures is forbidden in specific frequency ranges. Due to the various unique physical properties, periodic structures are widely used in various engineering practices such as structural strength enhancement, vibration absorption and vibration control, thus, a large number of studies have been carried out on the band gaps and wave propagation and attenuation characteristics of various periodic

structures (Dupont et al., 2019; Muhammad and Lim, 2019; Xu et al., 2021). The existing periodic structure studies reveal two kinds of band gap formation theories: local resonance band gap and Bragg scattering band gap. Mead and his team members have conducted a lot of researches on the wave propagation characteristics in periodic beams since the 1960s (Mead, 1970; Mead, 1996). Kushwaha et al. inferred phononic crystals from the studies of photonic crystals and discovered the band gap phenomenon of phononic crystals (Kushwaha et al., 1993). Liu et al. fabricated a local resonant periodic structure by the idea of localized resonant structures, and the theoretical and experimental studies have verified there is a low-frequency local resonance band gap in this type periodic structure which is much lower than the traditional Bragg gap frequency (Liu et al., 2000). It provides a theoretical foundation for the application of low-frequency band gap characteristics of macroscopic periodic structures.

In the past two decades, the elastic wave band gap characteristics and propagation and attenuation characteristics of various periodic structures have been investigated. Guo and Fang (2014) and Li and Guo (2016) analyzed the longitudinal wave dispersion relations and band gap characteristics in periodic quaternary rods and rod-type piezoelectric periodic structures, respectively. The research results promoted the design of rod-type periodic structures for vibration isolation/control applications. Richards and Pines (2003) utilized the property of a periodic drive shaft that generated stop band gap and pass band regions in the frequency spectra, both the analytical and experimental results indicated that the proposed periodic drive shaft can effectively reduce the transmitted vibration generated by gear mesh contact dynamics. Shen et al. (2012) proposed a periodic shell made of functionally graded material and then investigated the mechanism of wave propagation and vibration transmission in the shell by illustrating the pass/stop band frequency ranges of the periodic shell. An et al. (2018) numerically studied the band gap characteristics of radial wave propagating radially from the inner circle of a two-dimensional cylindrical shell structure with radial and circumferential periodicities. Results showed that radial wave has significant attenuation in band gap frequency region. Sharma and Sun (2016) investigated the low frequency wave propagation behaviours of sandwich beams containing periodically embedded internal resonators, and they demonstrated that local resonance and Bragg band gaps coexist in the proposed periodic sandwich beams. Liu and Yang (2017) analyzed the characteristics of acoustic wave transmitting in a metamaterial seawater pipe which consists of a uniform pipe with air-water chamber Helmholtz resonators mounted periodically along its axial direction, the results showed that the proposed metamaterial seawater pipe could generate a wide band gap in the low-frequency range and rendering the propagation of the frequency range acoustic waves in the piping system dampened spatially. Faiz et al. (2020) theoretically and experimentally investigated the waveguiding and filtering properties of a two-dimensional phononic crystal slab. They verified that the proposed device shows a complete band gap and the Lamb wave in the phononic crystal slab can be suppressed significantly. Zhou et al. (2014) studied the flexural wave band

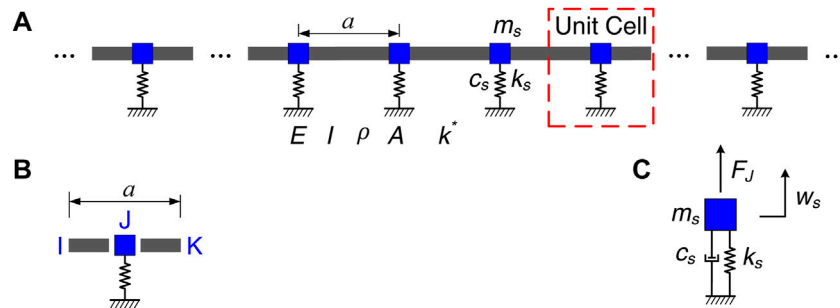


FIGURE 1 | The physics model: **(A)** Schematic diagram of infinite long homogeneous beam coupled with periodic oscillators; **(B)** Schematic diagram of the unit cell; **(C)** The beam-oscillators coupling system in a unit cell.

gap and attenuation characteristics in a periodic stiffened-thin-plate with the help of center-finite-difference-method. Results showed that the proposed periodic structure can yield complete band gaps and the wave propagation is forbidden. Zuo et al. (2018) investigated the flexural wave propagation and band gaps of a locally resonant phononic crystal to achieve a wider band gap and a lower cut-on frequency. This research provided an approach for the application of locally resonant phononic crystal in vibration and noise control.

As a preliminary study of periodic structure band gaps characteristics and low-noise structural design of ship and offshore structures, a simple physical model is proposed in this paper for analyzing the dynamic characteristics of periodic support beams and low-frequency flexural wave vibration of slender stiffened plate structures in ship and offshore structures. The proposed physical model is an infinite long homogeneous beam coupled with periodic oscillators which is a periodic beam-oscillators coupling system composed of homogeneous beam and periodic local oscillators. Based on the Timoshenko beam theory and its wave form solution, the calculation method for the flexural wave band gaps in the proposed infinite long homogeneous beam coupled with periodic oscillators is established by the method of reverberation-ray matrix combined with Bloch theorem. The method of reverberation-ray matrix is a semi-analytical method and the advantages of the present method lie in its simplicity, clarity, and accuracy (Guo and Fang, 2011). The rest of this article is organized as follows: First of all, the calculation formulation for analyzing the flexural wave band gaps of the homogeneous beam coupled with periodic oscillators is established by using the method of reverberation-ray matrix, as detailed in Section 2. The theoretical calculation results and discussions of the band gap characteristics are given in Section 3, which the flexural wave band gaps calculation method is verified by structural flexural wave vibration transmission characteristics based on finite element method, as shown in Section 3.2. And then the influences of various structural and material parameters of the homogeneous beam coupled with periodic oscillators on the band gap characteristics are respectively investigated in Section 3.3. Conclusions are given in Section 4.

2 PHYSICS MODEL AND CALCULATION METHOD

The proposed simple physical model considered in this paper is constituted of an infinitely long homogeneous beam coupled with periodic local oscillators in parallel connection as illustrated in Figure 1A, which is a periodic beam-oscillators coupling system. The area surrounded by a red dashed line in Figure 1A is the unit cell of the proposed infinite long homogeneous beam coupled with periodic oscillators and the schematic diagram is shown in Figure 1B, and the periodic beam-oscillators coupling system in a unit cell is drawn in Figure 1C. By periodically repeating and combining the unit cell along the length direction, the proposed infinite long homogeneous beam coupled with periodic oscillators can be obtained. The structural parameters of the proposed infinite long homogeneous beam coupled with periodic oscillators are listed as follows: the spring stiffness k_s , the mass m_s and the damping c_s of the periodic oscillators, lattice constant a , section moment of inertia I , section area A as well as the support stiffness of the elastic foundation k^* , and the material parameters of the homogeneous beam including Young's modulus E , mass density ρ and Poisson's ratio ν . In advance of investigating the flexural wave band gaps and vibration attenuation characteristics in the proposed infinite long homogeneous beam coupled with periodic oscillators, the governing wave equations should be introduced. The main equations of the flexural wave band gaps calculation method for the proposed infinite long homogeneous beam coupled with periodic oscillators are as follows.

Considering the effects of shear deformation and moment of inertia, the flexural wave vibration governing equations of a homogeneous Timoshenko beam with elastic foundation support can be written as (Li et al., 2014):

$$EI \frac{\partial^2 \varphi}{\partial x^2} + \kappa GA \left(\frac{\partial w}{\partial x} - \varphi \right) - \rho I \frac{\partial^2 \varphi}{\partial t^2} = 0 \quad (1)$$

$$\kappa GA \left(\frac{\partial^2 w}{\partial x^2} - \frac{\partial \varphi}{\partial x} \right) - \rho A \frac{\partial^2 w}{\partial t^2} + k^* w = 0 \quad (2)$$

where G represents the shear elastic modulus, κ denotes the shear correction coefficient, $w(x, t)$ and $\varphi(x, t)$ are the vertical

displacement and rotation angle of the homogeneous beam, respectively.

By eliminating $\partial\varphi/\partial x$ after substituting **Eq. 1** into **Eq. 2**, the flexural wave vibration governing equation expressed only by vertical displacement $w(x, t)$ can be obtained as

$$\frac{\partial^4 w}{\partial x^4} + \frac{k^*}{\kappa GA} \frac{\partial^2 w}{\partial x^2} - \left(\frac{\rho}{\kappa G} + \frac{\rho}{E} \right) \frac{\partial^4 w}{\partial x^2 \partial t^2} + \left(\frac{\rho A}{EI} - \frac{\rho k^*}{E \kappa GA} \right) \frac{\partial^2 w}{\partial t^2} + \frac{\rho^2}{E \kappa G} \frac{\partial^4 w}{\partial t^4} - \frac{k^*}{EI} w = 0 \quad (3)$$

The wave form solution for the vertical displacement in the homogeneous beam can be expressed as $w = W_0 e^{i(kx - \omega t)}$. Thus, after omitting the simple harmonic time factor $e^{-i\omega t}$, the solution of **Eq. 3** in the frequency domain can be expressed as follows:

$$w = a_1 e^{ik_1 x} + d_1 e^{-ik_1 x} + a_2 e^{ik_2 x} + d_2 e^{-ik_2 x} \quad (4)$$

where $k_1 = \sqrt{-\alpha/2 + \sqrt{(\alpha/2)^2 - \beta}}$ and $k_2 = \sqrt{-\alpha/2 - \sqrt{(\alpha/2)^2 - \beta}}$ are wavenumbers, and where

$$\alpha = -\frac{k^*}{\kappa GA} - \omega^2 \left(\frac{\rho}{\kappa G} + \frac{\rho}{E} \right), \quad \beta = -\omega^2 \left(\frac{\rho A}{EI} - \frac{\rho k^*}{E \kappa GA} \right) + \frac{\rho^2}{E \kappa G} \omega^4 - \frac{k^*}{EI} \quad (5)$$

From this, the rotation angle of the homogeneous beam can be written as

$$\varphi = g_1 a_1 e^{ik_1 x} - g_1 d_1 e^{-ik_1 x} + g_2 a_2 e^{ik_2 x} - g_2 d_2 e^{-ik_2 x} \quad (6)$$

where g_j ($j = 1, 2$) can be expressed as

$$g_j = \frac{ik_j \kappa GA}{EI k_j^2 + \kappa GA - \rho I \omega^2} \quad (7)$$

According to the relationships between the bending moment with the vertical displacement, $M = EI \partial^2 w / \partial x^2$, and the shear force with the vertical displacement and rotation angle in Timoshenko beam, $V = \kappa GA (\varphi - \partial w / \partial x)$, the expressions of the bending moment and shear force can be obtained as:

$$M = -EI (k_1^2 a_1 e^{ik_1 x} + k_1^2 d_1 e^{-ik_1 x} + k_2^2 a_2 e^{ik_2 x} + k_2^2 d_2 e^{-ik_2 x}) \quad (8)$$

$$V = \kappa GA \left[(g_1 - ik_1) a_1 e^{ik_1 x} - (g_1 - ik_1) d_1 e^{-ik_1 x} + (g_2 - ik_2) a_2 e^{ik_2 x} - (g_2 - ik_2) d_2 e^{-ik_2 x} \right] \quad (9)$$

The **Eqs 4, 5** can be rewritten in matrix form as

$$W_d = A_d P_h(-x) a + D_d P_h(x) d \quad (10)$$

and similarly, the **Eqs 7, 8** are rewritten in matrix form as

$$W_f = A_f P_h(-x) a + D_f P_h(x) d \quad (11)$$

where $W_d = \{w, \varphi\}^T$ and $W_f = \{V, M\}^T$ are the generalized displacement vector and the generalized force vector, a and d respectively stand for the amplitude vectors of arriving wave and leaving wave, A_d and D_d respectively denote the coefficient matrixes of the arriving wave and the leaving wave corresponding to the displacement vector, A_f and D_f are the

coefficient matrixes of the arriving wave and leaving wave corresponding to the force vector, and P_h denotes the phase matrix, which the specific expressions are given as follows:

$$W_d = \{w \quad \varphi\}^T \quad W_f = \{V \quad M\}^T \quad (12)$$

$$a = \{a_1 \quad a_2\}^T \quad d = \{d_1 \quad d_2\}^T \quad (13)$$

$$P_h(x) = \begin{bmatrix} e^{-ik_1 x} & 0 \\ 0 & e^{-ik_2 x} \end{bmatrix} \quad (14)$$

$$A_d = \begin{bmatrix} 1 & 1 \\ g_1 & g_2 \end{bmatrix} \quad D_d = \begin{bmatrix} 1 & 1 \\ -g_1 & -g_2 \end{bmatrix} \quad (15)$$

$$A_f = \begin{bmatrix} \kappa GA & 0 \\ 0 & -EI \end{bmatrix} \begin{bmatrix} g_1 - ik_1 & g_2 - ik_2 \\ k_1^2 & k_2^2 \end{bmatrix} \quad D_f = \begin{bmatrix} \kappa GA & 0 \\ 0 & -EI \end{bmatrix} \begin{bmatrix} ik_1 - g_1 & ik_2 - g_2 \\ k_1^2 & k_2^2 \end{bmatrix} \quad (16)$$

As the beam-oscillators coupling system in a unit cell plotted in **Figure 1C**, the relationships of the generalized displacements continuities and generalized forces equilibriums at the node J of the beam-oscillators coupling system unit cell are expressed as follows:

$$W_d^{JI} = T_d^J W_d^{JK} \quad (17)$$

$$W_f^{JI} = T_f^J W_f^{JK} + F^J \quad (18)$$

where $T_d^J = \text{diag}\{-1, 1\}$ and $T_f^J = -T_d^J$ respectively stand for the transformation matrix of the generalized displacement and generalized force at node j , and F^J denotes the reaction force vector of the local oscillator acting on the beam.

As the beam-oscillators coupling system in a unit cell illustrated in **Figure 1C**, the coupling vibration equation of the local oscillator coupled with the beam in parallel connection at the connection node can be obtained by

$$m_s \ddot{w}_s + k_s w_s + c_s \dot{w}_s = F_j \quad (19)$$

Therefore, the reaction force vector of the local oscillator acting on the beam is presented as

$$F^J = K^J W_d^{JK} \quad (20)$$

where $K^J = \text{diag}\{k_w, k_\varphi\}$ stand for the dynamic stiffness matrix of the local oscillator acting on the beam at node J , where the $k_w = -m_s \omega^2 + k_s + ic_s \omega$ and $k_\varphi = 0$ are the translational stiffness coefficient and rotational stiffness coefficient of the local oscillator acting on the beam, respectively, k_s and m_s respectively represent the spring stiffness and mass of the local oscillator, $w_s = w^{JK} = -w^{JI}$ denotes the vertical displacement of the local oscillator and the beam at the node J .

Substituting **Eqs 9, 10** and **19** into **Eqs 16, 17** obtains the scattering relationship of the beam-oscillators coupling system at node J as follows:

$$A^J a^J + D^J d^J = 0 \quad (21)$$

where $a^J = \{(a^{JI})^T (a^{JK})^T\}^T$ and $d^J = \{(d^{JI})^T (d^{JK})^T\}^T$ are the amplitude vectors of the arriving wave and the leaving wave,

respectively, A^J and D^J respectively stand for the corresponding coefficient matrixes of a^J and d^J at the node J , respectively, which are expressed as

$$\begin{aligned} A^J &= \begin{bmatrix} A_d^{IJ} & -T_d^J A_d^{JK} \\ A_f^{IJ} & -(T_f^J A_f^{JK} + K^J A_d^{JK}) \end{bmatrix} \\ D^J &= \begin{bmatrix} D_d^{IJ} & -T_d^J D_d^{JK} \\ D_f^{IJ} & -(T_f^J D_f^{JK} + K^J D_d^{JK}) \end{bmatrix} \end{aligned} \quad (22)$$

According to the Bloch theorem of periodic structure, the following equations must be satisfied for the generalized displacement vector and generalized force vector in the unit cell of the proposed infinite long homogeneous beam coupled with periodic oscillators, which are listed as follows:

$$e^{iqa} W_d^{IJ} = T_d^J W_d^{KJ} \quad (23)$$

$$e^{iqa} W_f^{IJ} = T_f^J W_f^{KJ} \quad (24)$$

As the same, substituting Eqs 10, 11 into Eqs 22, 23 obtains

$$A^{*J} a^{*J} + D^{*J} d^{*J} = 0 \quad (25)$$

where $a^{*J} = \{(a^{IJ})^T (a^{KJ})^T\}^T$ and $d^{*J} = \{(d^{IJ})^T (d^{KJ})^T\}^T$ are the amplitude vectors of the arriving wave and the leaving wave, respectively, A^{*J} and D^{*J} respectively stand for the corresponding coefficient matrixes of a^{*J} and d^{*J} at the node J , which are expressed as

$$A^{*J} = \begin{bmatrix} e^{iqa} A_d^{IJ} & -T_d^J A_d^{KJ} \\ e^{iqa} A_f^{IJ} & -T_f^J A_f^{KJ} \end{bmatrix} \quad D^{*J} = \begin{bmatrix} e^{iqa} D_d^{IJ} & -T_d^J D_d^{KJ} \\ e^{iqa} D_f^{IJ} & -T_f^J D_f^{KJ} \end{bmatrix} \quad (26)$$

By combining Eqs 20, 24, the global scattering relationship in a unit cell of the infinite long homogeneous beam coupled with periodic oscillators can be obtained as follows:

$$Aa + Dd = 0 \quad (27)$$

where $a = \{(a^{IJ})^T (a^{IK})^T (a^{KJ})^T\}^T$ and $d = \{(d^{IJ})^T (d^{IK})^T (d^{KJ})^T\}^T$ respectively stand for the global amplitude vectors of the arriving wave and the leaving wave of the proposed unit cell, A and D respectively denoted the corresponding coefficient matrixes of a and d at the node J , which the expressions are expressed as follows:

$$\begin{aligned} A &= \begin{bmatrix} e^{iqa} A_d^{IJ} & 0 & 0 & -T_d^J A_d^{KJ} \\ 0 & A_d^{IJ} & -T_d^J A_d^{JK} & 0 \\ 0 & A_f^{IJ} & -(T_f^J A_f^{JK} + K^J A_d^{JK}) & 0 \\ e^{iqa} A_f^{IJ} & 0 & 0 & -T_f^J A_f^{KJ} \end{bmatrix} \\ D &= \begin{bmatrix} e^{iqa} D_d^{IJ} & 0 & 0 & -T_d^J D_d^{KJ} \\ 0 & D_d^{IJ} & -T_d^J D_d^{JK} & 0 \\ 0 & D_f^{IJ} & -(T_f^J D_f^{JK} + K^J D_d^{JK}) & 0 \\ e^{iqa} D_f^{IJ} & 0 & 0 & -T_f^J D_f^{KJ} \end{bmatrix} \end{aligned} \quad (28)$$

For the flexural wave in any section of the beam, the leaving wave of the left end is exactly the arriving wave of the right node, and vice versa. For any section (e.g., section J) of the beam, the phase relationships can be expressed as follows:

$$a^{JK} = P^{JK} d^{KJ} \quad (29)$$

$$a^{KJ} = P^{JK} d^{JK} \quad (30)$$

where $P^{JK} = -P_h(L^{JK})$ is the phase matrix of the beam section J .

Thus, according to the phase relationships of each section of the beam, the global phase relationship is obtained as

$$a = P d^* \quad (31)$$

where $d^* = \{(d^{IJ})^T (d^{IJ})^T (d^{KJ})^T (d^{KJ})^T\}^T$ is the rearranged global amplitude vector of the leaving wave in the unit cell of the infinite long homogeneous beam coupled with periodic oscillators, $P = \text{diag}\{P^{IJ} P^{IJ} P^{JK} P^{JK}\}$ is the global phase matrix.

Comparing the global leaving wave amplitude vectors d^* and d of the infinite long homogeneous beam coupled with periodic oscillators unit cell, the two vectors have the same elements with different arrangement orders. Thus, the relationship between the amplitude vectors d^* and d is obtained as follows:

$$d^* = U d \quad (32)$$

$$U = \begin{bmatrix} 0 & I_2 & 0 & 0 \\ I_2 & 0 & 0 & 0 \\ 0 & 0 & 0 & I_2 \\ 0 & 0 & I_2 & 0 \end{bmatrix} \quad (33)$$

where U is the permutation matrix between d^* and d , in which I_2 stands for the two-order unit matrix.

After substituting Eqs 30, 31 into Eq. 26, the flexural wave dispersion relation in the unit cell of the infinite long homogeneous beam coupled with periodic oscillators can be yielded as follows:

$$(APU + D)d = 0 \quad (34)$$

where $R = APU + D$ denotes the reverberation-ray matrix of the periodic beam-oscillators coupling system.

In order to obtain the non-zero solution of the global leaving wave amplitude vector d , namely, the determinant of the reverberation-ray matrix R must be zero, which is

$$\det(R) = 0 \quad (35)$$

Thus, the relationship of the flexural wave number q and frequency f in the unit cell of the proposed infinite long homogeneous beam coupled with periodic oscillators can be solved by Eq. 34, which is the flexural wave dispersion relations and vibration band gaps of the proposed periodic beam-oscillators coupling system.

3 RESULTS AND DISCUSSIONS

3.1 Bad Gaps Characteristics in Homogeneous Beam Coupled With Periodic Oscillators

This section calculates and analyses the flexural wave band gaps and vibration attenuation characteristics in the proposed homogeneous beam coupled with periodic oscillators. In order to facilitate the band gaps characteristics study and the effects analysis of the parameters on band gaps characteristics, as a

TABLE 1 | The parameters of homogeneous beam and periodic oscillators in the calculation example study, in which the subscript 0 is defined to distinguish the calculation example study and parametric study.

Parameter	k_{s0} (N/m)	m_{s0} (kg)	a_0 (m)	c_s (N-s/M)	I_0 (m ⁴)	A_0 (m ²)
Value	5.0×10^7	8	1.0	0	2.0×10^{-5}	3.0×10^{-3}

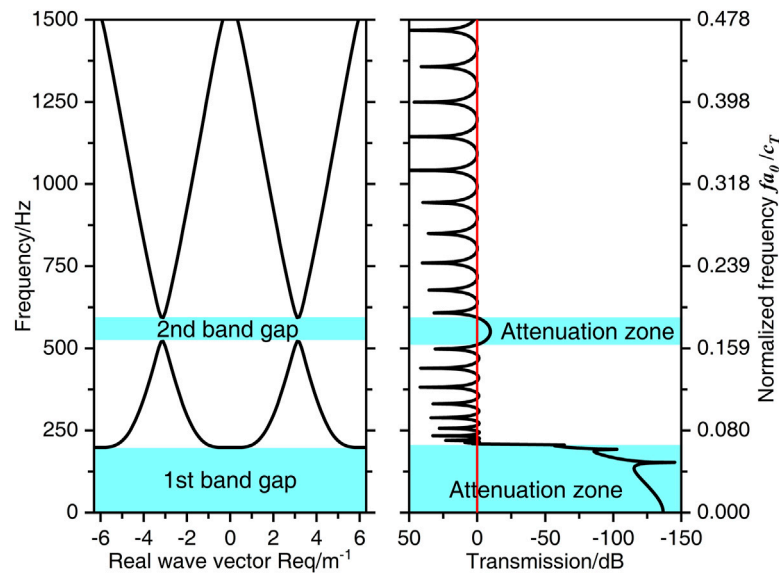


FIGURE 2 | (A) The flexural wave band gaps characteristics of the infinite long homogeneous beam coupled with periodic oscillators. (B) The flexural wave vibration transmission spectrum of the finite long homogeneous beam coupled with periodic oscillators with 12 unit cells.

calculation example study, the material parameters of the homogeneous beam are considered as: the Young's modulus $E = 2.1 \times 10^{11}$ Pa, mass density $\rho = 7850$ kg/m³ and Poisson's ratio $\nu = 0.28$. And geometrical parameters of the homogeneous beam and periodic oscillators are presented in **Table 1**.

According to the flexural wave band gaps calculation method obtained in the previous section, **Figure 2A** shows the band gaps characteristics calculation results of the proposed infinite long homogeneous beam coupled with periodic oscillators in the calculation example study, in which the left vertical axis and the right vertical axis are the frequency and normalized frequency of the flexural wave. The normalized frequency is defined as $f a_0 / c_T$ to obtain more general results, in which the c_T is the transversal wave speed in steel which the value is 3140 m/s. It is clear that in the frequency range of 0–1500 Hz, there are two band gaps of 0–198.3 Hz and 522.8–592.3 Hz in the proposed periodic beam-oscillators coupling system, and which the bandwidths are 198.3 Hz and 69.5 Hz, respectively.

3.2 Numerical Calculation Validation Based on Finite Element Method

To verify the effectiveness of the flexural wave band gaps characteristics calculation method obtained in this paper and demonstrate the existences of the flexural wave band gaps and

vibration attenuation characteristics in the proposed periodic beam-oscillators coupling system, a structural dynamic characteristic analysis of a finite long homogeneous beam coupled with periodic oscillators with 12 unit cells based on finite element method is conducted in this section. The flexural wave band gaps and vibration attenuation characteristics of various periodic structures had been analyzed by the numerical calculation of the finite array periodic structures, the numerical calculation method is an effective and efficient calculation method of band gaps and vibration attenuation characteristics and has been widely used to demonstrate the effectiveness of the band gaps calculation methods (Waki et al., 2009; Zhou et al., 2015; Nobrega et al., 2016; Xiang et al., 2020). As shown in **Figure 3A**, the finite array finite element model with 12 unit cells of the proposed periodic beam-oscillators coupling system is established in Abaqus CAE at the beginning of the numerical calculation, the finite element model is constituted of a homogeneous beam with a rectangular section and coupled with 12 periodic oscillators in parallel connection, which the separation distance is 1.0 m and each unit cell contains 400 beam elements, the vibration direction of the periodic oscillators is vertical direction and the length direction of the homogeneous beam is along X-axis with 12.0 m dimensions. The structural and material parameters of the finite element model are the same with those in the calculation example

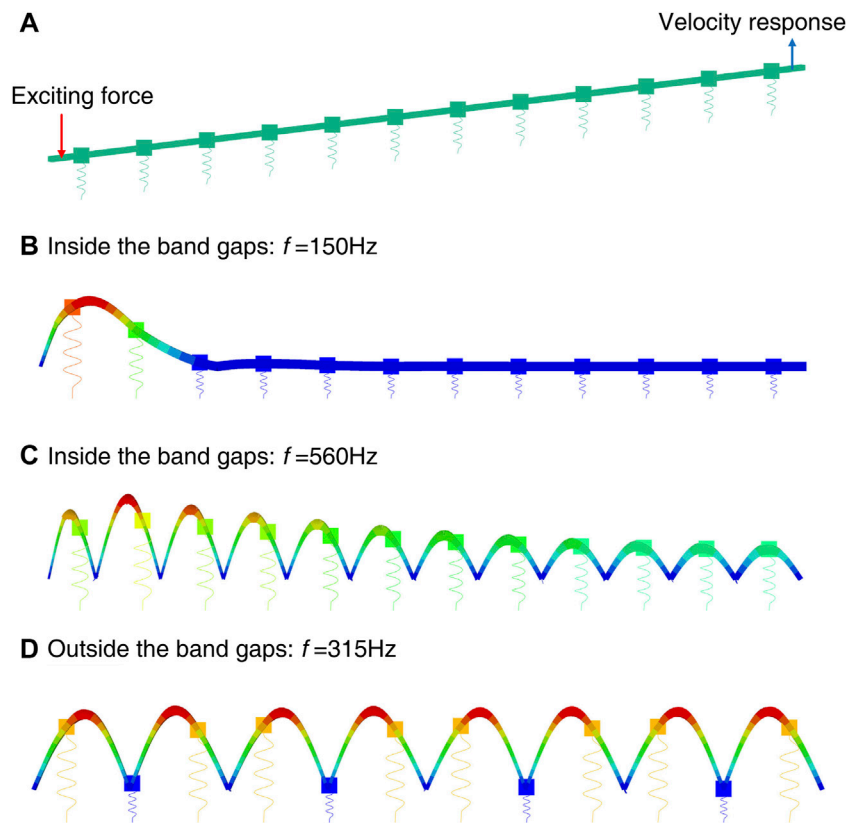


FIGURE 3 | (A) Finite element model of the finite long homogeneous beam coupled with periodic oscillators with 12 unit cells; **(B–D)** The flexural wave vibration attenuation characteristics at particular frequencies.

study in the previous section. The left end of the finite element model is vertically excited by the unit sweep excitation force of 0–1500 Hz with 1 Hz frequency interval during the numerical calculation, the vertical vibration velocity responses of the nodes near the excitation point was used to detect the incident vibration wave signal while those of the nodes near the right end was used to probe the transmitted vibration wave signal, thus the vertical vibration velocity responses of the nodes at both ends of the beam are extracted to detect the vibration transmission spectrum of the flexural wave in the homogeneous beam coupled with periodic oscillators. The sketch map of the excitation force and velocity response are illustrated in **Figure 3A**. At last, the flexural wave vibration attenuation characteristics at particular frequencies are captured and presented in **Figures 3B–D**. After the vibration signal processing and spectral analysis, the band gaps and vibration attenuation characteristics of the flexural wave in the periodic beam-oscillators coupling system are represented by the vibration transmission spectrum drawn in **Figure 2B**.

Calculation results show the existences of two significant vibration attenuation bands in the frequency bands from 0 to 209 Hz and from 511 to 594 Hz respectively in light blue regions as illustrated in **Figure 2B**, which the bandwidths and locations of the vibration attenuation bands are well consistent with the corresponding flexural wave band gaps, thus the calculation

method of flexural wave band gaps characteristics obtained in this paper is validated. The vertical vibration velocity responses at the right part of the beam at 150 and 560 Hz in **Figures 3B,C** show obvious vibration attenuations, it can be concluded that the propagation of flexural wave in particular frequencies is prohibited, which the effectiveness of the numerical verification method is also further proved. Furthermore, compared the calculation results in **Figures 3B–D**, the significant reduction of structural vibration in **Figures 3B,C** indicate that band gaps and vibration attenuations of the flexural wave can appear in the homogeneous beam coupled with periodic oscillators. Different from the vibration attenuations caused by the damping of traditional materials, the vibration attenuation in band gaps frequency ranges of the flexural wave in periodic structures have relatively larger attenuation. The vibration attenuations in band gaps are caused by Bragg reflection and local resonance, which are mainly determined by the periodicity of the periodic structures and the local resonance of the microstructure, respectively. Whereas, as absorbing and consuming the energy of structural vibration is the properties of material damping, the vibration attenuations caused by material damping are appear in all frequency range while the main effective region is medium/high frequency with smaller attenuation amplitudes than those attenuation amplitudes in band gaps frequency ranges.

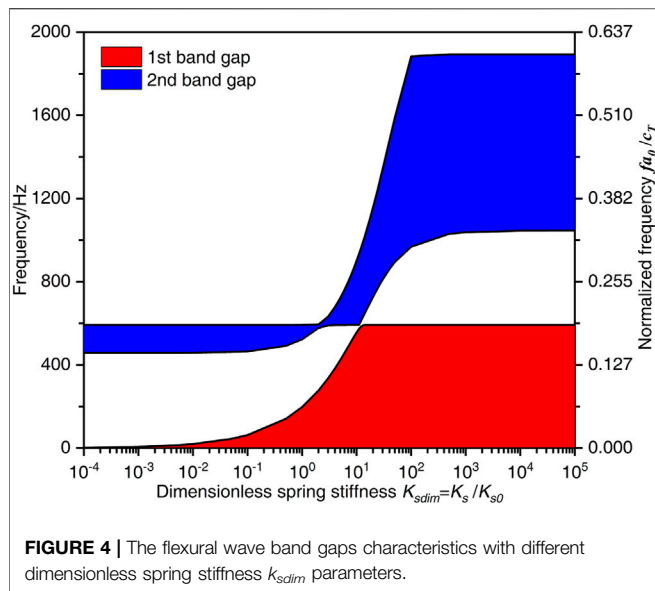


FIGURE 4 | The flexural wave band gaps characteristics with different dimensionless spring stiffness k_{sdim} parameters.

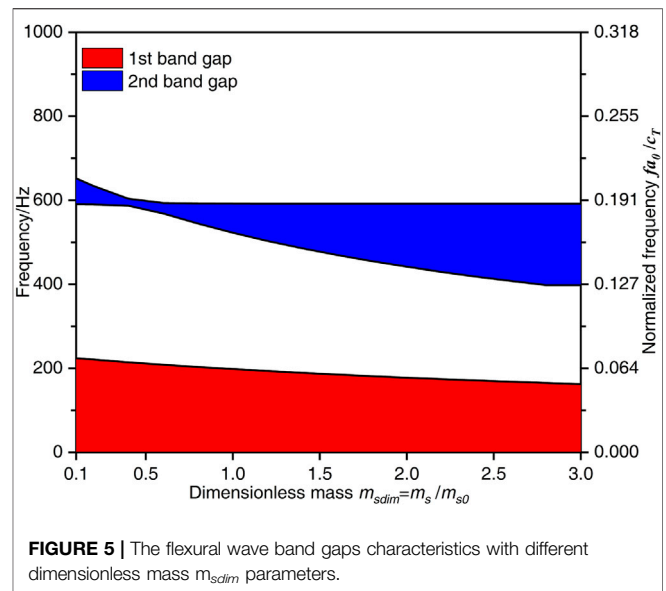


FIGURE 5 | The flexural wave band gaps characteristics with different dimensionless mass m_{sdim} parameters.

3.3 Parametric Study

During the parametric studies, the control variable method is used to calculate the flexural wave dispersion relations of the homogeneous beam coupled with periodic oscillators with different parameters values, and then the effects of the parameters on the flexural wave band gaps and vibration attenuation characteristics are studied in this section.

3.3.1 Effect of Spring Stiffness on the Band Gaps Characteristics

In order to study the effects of periodic oscillators spring stiffness k_s on the band gaps characteristics of the flexural wave, the ratio of $k_{sdim} = k_s/k_{s0}$ is defined as dimensionless spring stiffness to realize the dimensionless parameters study, where $k_{s0} = 5.0 \times 10^7$ N/m is the spring stiffness in the calculation example study. During the calculation, the k_{sdim} gradually increases from 10^{-4} to 10^4 while the material parameters and geometrical parameters of the periodic beam-oscillators coupling system keep constant. The effects of periodic oscillators spring stiffness k_s on the flexural wave band gaps with different k_{sdim} are illustrated in **Figure 4**.

It can be observed from **Figure 4** that the spring stiffness k_s has significant influences on the band gaps characteristics of the flexural wave. Which the band gaps increase to a high-frequency region in a multistep manner when the dimensionless spring stiffness k_{sdim} increases. For the first band gap of the flexural wave in the periodic beam-oscillators coupling system, when the k_{sdim} increases in the range from 10^{-4} to 10^5 , the lower limit frequency remains constant at 0 Hz, while the upper limit frequency accelerated increases to about 592 Hz when the $k_{sdim} = 15$, and then keeps constant with the k_{sdim} in the range from 15 to 10^5 . As the lower limit frequency maintains invariable at 0 Hz, the bandwidth of the first band gap accelerated increases to about 592 Hz and then keeps constant at about 592 Hz when the k_{sdim} in the range from 15 to 10^5 . This

change phenomenon is because the formation mechanism of the first band gap, which is determined by the local resonance of the periodic oscillators, therefore the increase of k_{sdim} causes the eigenfrequency of the periodic oscillators to increase and resulting in the band gap shifts to a high-frequency region, and there is a critical frequency value $f = 590$ Hz which is caused by the coupling effects of the periodic oscillators and the homogeneous beam.

The second band gap increase to a high-frequency region in a multistep manner with the dimensionless spring stiffness k_{sdim} increases from 10^{-4} to 10^5 . At the beginning, the lower limit frequency keeps at about 460 Hz unchanged when the k_{sdim} in the range of $10^{-4} \sim 10^{-1}$ and gradually increases to 519 Hz when the k_{sdim} is 3, and then keeps constant when the k_{sdim} in the range of 3–11, subsequently, the lower limit frequency gradually increases to about 1040 Hz when the k_{sdim} is 10^3 and keeps invariant at last when the k_{sdim} is in the range from 10^3 to 10^5 . The upper limit frequency gradually increases to 1894 Hz from 591 Hz when the k_{sdim} is in the range of $2 \sim 10^2$, while keeps constant at 591 Hz and about 1894 Hz when the k_{sdim} are $10^{-4} \sim 2$ and $10^2 \sim 10^5$, respectively. Therefore, the bandwidth of the second band gap maintains invariable at 134 Hz at the beginning, and after that decreases to the minimum value at 42 Hz when the $k_{sdim} = 3$, subsequently, the bandwidth gradually increases to 916 Hz when the k_{sdim} is 100 and then keeps constant at about 850 Hz when the k_{sdim} in the range of $500 \sim 10^5$. This phenomenon can be explained that the second band gap is determined by the coupling effects between the Bragg scattering of periodic oscillators and the propagation of the flexural wave in homogeneous beam. The reaction forces of the periodic oscillators acting on the homogeneous beam increases when the spring stiffness k_s increases, resulting in the increase of the bending stiffness of the homogeneous beam, which leads to an increase in the eigenfrequency of the proposed homogeneous beam coupled with periodic oscillators.

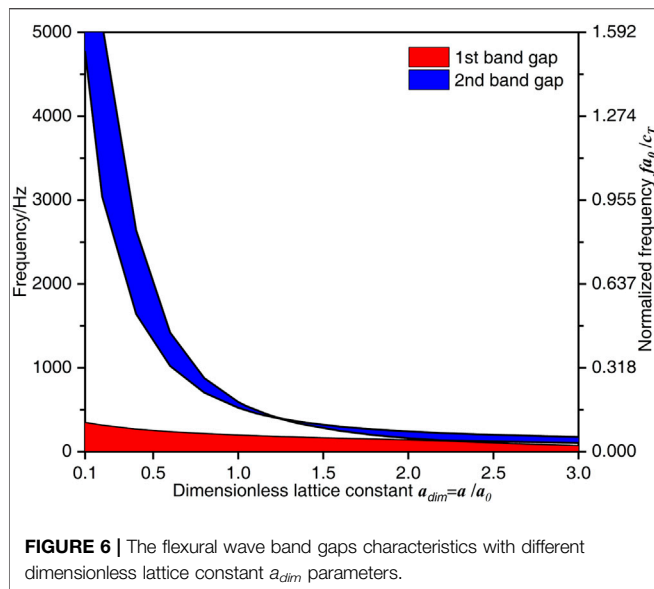


FIGURE 6 | The flexural wave band gaps characteristics with different dimensionless lattice constant a_{dim} parameters.

3.3.2 Effect of Periodic Oscillators Mass on the Band Gaps Characteristics

The effects of the periodic oscillators mass m_s on the flexural wave band gaps characteristics in the proposed periodic beam-oscillators coupling system are obtained in **Figure 5**, in which the dimensionless mass $m_{sdim} = m_s/m_{s0}$ is the ratio of the mass of the periodic oscillators to the one m_{s0} defined in the calculation example study and takes the value from 0.1 to 3.0.

It can be seen that, the two band gaps of the flexural wave in the proposed homogeneous beam coupled with periodic oscillators move to the low frequency region in different forms when the dimensionless mass m_{sdim} increases from 0.1 to 3.0. For the first flexural wave band gap, as the lower limit frequency keeps constant at 0 Hz, and the upper limit frequency gradually decreases from 224 to 162 Hz when the dimensionless mass m_{sdim} in the range of 0.1–3.0, thus, the bandwidth also gradually decreases from 224 to 162 Hz. This change gradually phenomenon is because the formation mechanism of the first band gap, which is determined by the local resonance of the periodic oscillators, therefore the increase of m_{sdim} causes the eigenfrequencies of the periodic oscillators to decrease and resulting in the band gap moves to a low-frequency region.

For the second flexural wave band gap, the lower limit frequency keeps constant at 590 and 398 Hz when the dimensionless mass m_{sdim} increase from 0.1 to 0.4 and 2.8 to 3.0, respectively, while gradually decreases when the m_{sdim} increases from 0.4 to 2.8. The upper limit frequency gradually decreases from 652 to 592 Hz when the m_{sdim} increases from 0.1 to 0.8 and then remains unchanged at last. Therefore, the bandwidth of the second flexural wave band gap decreases to the minimum value of 16.9 Hz when the $m_{sdim} = 0.4$, and then slowly increases to about 193 Hz when the $m_{sdim} = 2.8$ and no longer changes at last. This phenomenon can be explained that the second band gap is determined by the coupling effects between the Bragg scattering of periodic oscillators and the

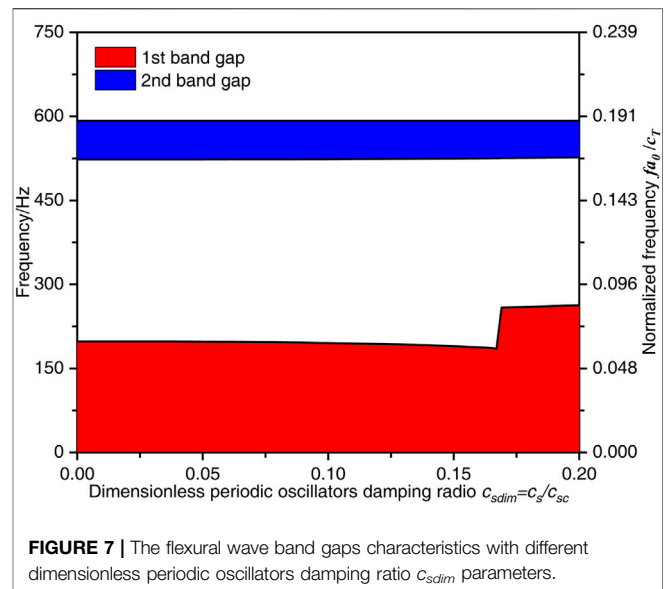


FIGURE 7 | The flexural wave band gaps characteristics with different dimensionless periodic oscillators damping ratio c_{sdim} parameters.

propagation of the flexural wave in homogeneous beam. The reaction forces of the periodic oscillators acting on the homogeneous beam decreases when the mass m_s increases, resulting in the decrease of the bending stiffness of the homogeneous beam, which leads to an reduce in the eigenfrequency of the proposed homogeneous beam coupled with periodic oscillators, and there also has a critical frequency value $f = 590$ Hz.

3.3.3 Effect of Lattice Constant on the Band Gaps Characteristics

Figure 6 demonstrates the effects of the lattice constant a on the flexural wave band gaps characteristics in the infinite long homogeneous beam coupled with periodic oscillators, in which the dimensionless lattice constant $a_{dim} = a/a_0$ is the ratio of the lattice constant of the periodic beam-oscillators coupling system to the one a_0 defined in the calculation example study and takes the value from 0.1 to 3.0.

It can be found from **Figure 6** that the increase of the dimensionless lattice constant a_{dim} moves both the two band gaps of the flexural wave to the low-frequency region by different ways. For the first band gap of the flexural wave in the proposed periodic beam-oscillators coupling system, as the lower limit frequency keeps constant at 0 Hz, the upper limit frequency or the bandwidth reduces from 350 to 73 Hz when the a_{dim} decreases from 0.1 to 3.0. For the second band gap of the flexural wave, both the lower limit frequency and upper limit frequency rapidly decrease when the a_{dim} in the range of 0.1–1.25, and then gradually decreases when the a_{dim} in the range of 1.25–3.0, the bandwidth decreases in the beginning and then gets the local minimum value of 6.5 Hz when the $a_{dim} = 1.25$, and then increases to about 80 Hz at last. This phenomenon can be explained that the second band gap is determined by the coupling effects between the Bragg scattering of periodic oscillators and the propagation of the flexural wave in homogeneous beam, since the wavelength corresponding to

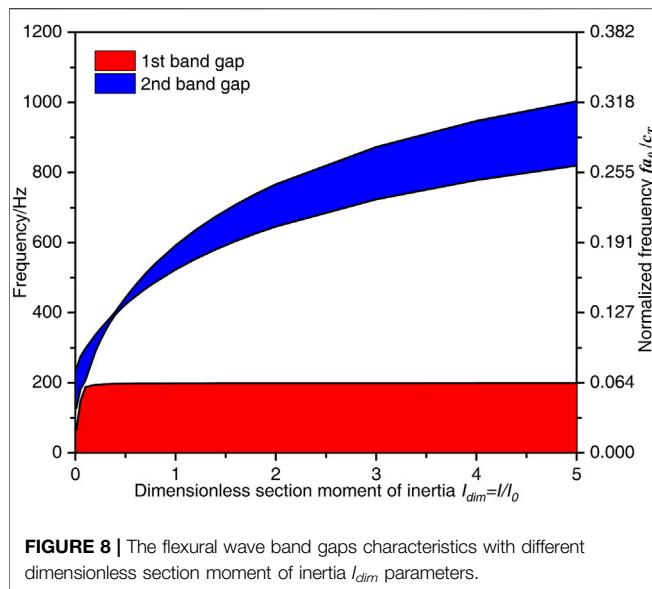


FIGURE 8 | The flexural wave band gaps characteristics with different dimensionless section moment of inertia I_{dim} parameters.

the intermediate frequency of the band gap of the flexural wave in the periodic structure is about twice the lattice constant according to the Bragg scattering theory, the increase of a_{dim} causes the band gap of the flexural wave to move to a low-frequency region.

3.3.4 Effect of Periodic Oscillators Damping on the Band Gaps Characteristics

Figure 7 shows the effects of periodic oscillators damping c_s on the band gaps characteristics of the flexural wave, in which the dimensionless periodic oscillators damping ratio $c_{sdim} = c_s/c_{sc}$ is the ratios of the periodic oscillators damping of the periodic beam-oscillators coupling system to the critical damping c_{sc} which is defined as $c_{sc} = 2\sqrt{k_s m_s} = 40000N \cdot s/m$ and takes the value from 0 to 0.2.

It can be observed from Figure 7 that, the increase of the dimensionless periodic oscillators damping ratio c_{sdim} has little effect on the second band gap of the flexural wave, whereas the upper limit frequency (the bandwidth) of the first band gap of the flexural wave slowly decreases from 199 to 185 Hz when the dimensionless periodic oscillators damping ratio c_{sdim} in the range of 0–0.168, after that it has a big jump growth to 259 Hz when the $c_{sdim} = 0.17$ and then increases to 262 Hz at last. The increase of the c_{sdim} causes the upper limit frequency of the first band gap to decrease in the beginning is because the formation mechanism of the first band gap, which the increase of c_{sdim} causes the translational stiffness coefficient of the periodic oscillators acting on the beam to decrease. While the jump growth when the c_{sdim} in the range of 0.17–0.20 is because the larger periodic oscillators damping absorbs and consumes the energy of the flexural wave in specific frequency range.

3.3.5 Effect of Section Moment of Inertia on the Band Gaps Characteristics

The effects of the section moment of inertia I on the flexural wave band gaps characteristics in the proposed periodic beam-oscillators coupling system are illustrated in Figure 8 in which

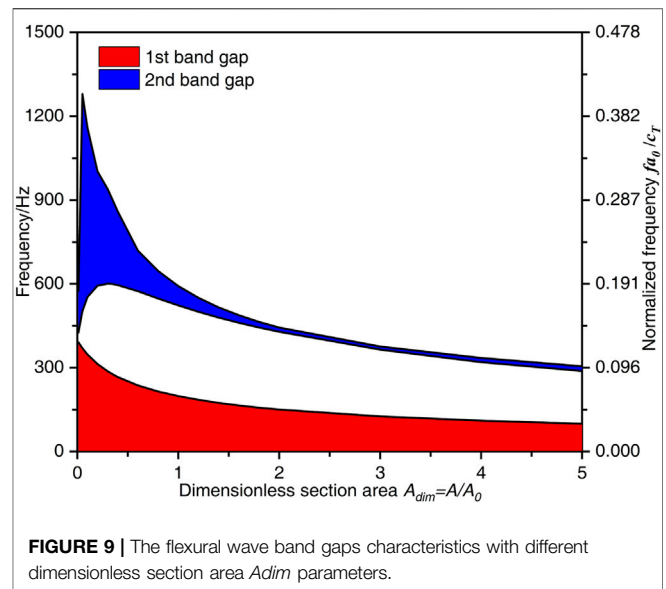


FIGURE 9 | The flexural wave band gaps characteristics with different dimensionless section area A_{dim} parameters.

the dimensionless section moment of inertia $I_{dim} = I/I_0$ is the ratio of the section moment of inertia of the homogeneous beam to the one I_0 defined in the calculation example study and takes the value from 0.01 to 5.0.

It can be found from Figure 8 that the lower limit frequency and upper limit frequency of the first flexural wave band gap almost keep constant, while the second flexural wave band gap has a significant increase and moves up to the high-frequency region. The lower limit frequency or the bandwidth of the first flexural wave band gap rapidly increases from 66 to 198 Hz when the I_{dim} increases from 0.01 to 0.4 and then keeps invariant. The lower limit frequency and upper limit frequency of the second flexural wave band gap significantly increase from 128 to 819 Hz and 240–1003 Hz when the I_{dim} in the range 0.01–5.0, respectively, which the bandwidth of the second band gap gradually decreases to the minimum value of 9.3 Hz when the $I_{dim} = 0.4$ and then gradually increases to about 184 Hz. This change phenomenon is because the formation mechanism of the first band gap, which is determined by the local resonance of the periodic oscillators, while the second band gap is determined by the coupling effects between the Bragg scattering of periodic oscillators and the propagation of the flexural wave in homogeneous beam. The increase of the I_{dim} causes bending stiffness of the homogeneous beam to enhance and leads to an increase in the eigenfrequency of the homogeneous beam while can not change the eigenfrequency of the periodic oscillators.

3.3.6 Effect of Section Area on the Band Gaps Characteristics

Figure 9 demonstrates the effects of the section area A on the band gaps characteristics of the flexural wave in the homogeneous beam of the periodic beam-oscillators coupling system, in which the dimensionless section area $A_{dim} = A/A_0$ is the ratio of the section area of the homogeneous beam to the one A_0 defined in the calculation example study and takes the value from 0.01 to 5.0.

TABLE 2 | The material parameters of the homogeneous beam.

	Steel	Copper	Aluminum
Young's modulus E (Pa)	2.1×10^{11}	1.1×10^{11}	7.0×10^{10}
Mass density ρ ($\text{kg}\cdot\text{m}^{-3}$)	7850	8900	2600
Poisson's ratio ν	0.28	0.34	0.33

Other geometrical parameters were listed in **Table 1**.

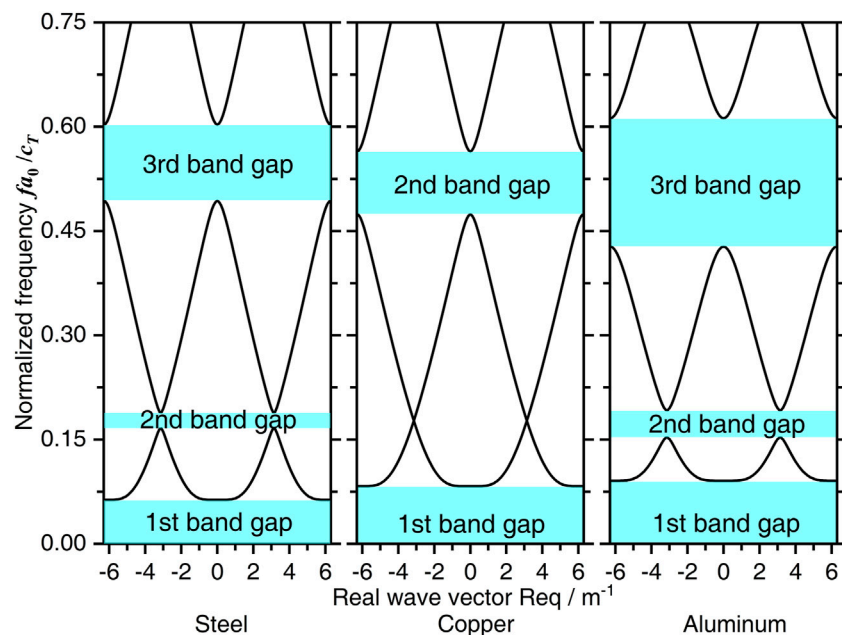
The **Figure 9** shows that the lower limit frequency (the bandwidth) of the first band gap of the flexural wave shift to a low-frequency region, whereas the lower limit frequency and the upper limit frequency of the second band gap of the flexural wave increase first and then move to a low-frequency region. To be specific, the lower limit frequency or the bandwidth of the first band gap decreases from 392 to about 100 Hz when the A_{dim} decreases from 0.01 to 5.0. The lower limit frequency of the second band gap gradually increases from 426 Hz to the maximum value of 600.8 Hz when the A_{dim} increases from 0.01 to 0.3, and then gradually decreases to 288 Hz at last, as the same, the upper limit frequency rapidly increases from 575 Hz to the maximum value of 1280.3 Hz when the A_{dim} increases from 0.01 to 0.05 and then gradually decreases to 305 Hz in the end. Therefore, the bandwidth of the second flexural wave band gap increases to the maximum value of 778.3 Hz, and then rapidly decreases to about 12 Hz at last. This change phenomenon is because the formation mechanism of the first band gap, which is determined by the local resonance of the periodic oscillators, while the second band gap is determined by the coupling effects between the Bragg scattering of periodic oscillators and the propagation of the flexural wave in homogeneous beam. The increase of the A_{dim} causes both the mass of the periodic

oscillators and the bending stiffness of the homogeneous beam to reduce, which leads to the decrease in the eigenfrequencies of the periodic oscillators and the homogeneous beam, respectively.

3.3.7 Effect of Material Parameters on the Band Gaps Characteristics

To investigate the effect of material parameters of the homogeneous beam on the band gaps characteristics of the flexural wave in the periodic beam-oscillators coupling system, change the material of the homogeneous beam as steel, copper as well as aluminum, which the material parameters of the homogeneous beam are shown in **Table 2**, and the other geometrical parameters are the same as those defined in the calculation example study and listed in **Table 1**. **Figure 10** respectively obtained the effects of different material parameters on the band gaps characteristics of the flexural wave, in which the normalized frequency fa_0/c_T is the ratio of the fa_0 to the transversal wave speed in steel, copper or aluminum, and the values are 3140, 2260, and 3080 m/s, respectively.

It can be observed from **Figure 10** that, when the normalized frequency fa_0/c_T in the range of 0–0.75, there are three flexural wave band gaps in the infinite long homogeneous beam coupled

**FIGURE 10** | The flexural wave band gaps characteristics with different homogeneous beam material properties.

with periodic oscillators when the material of the homogeneous beam is steel or aluminum, while it only has two flexural wave band gaps when the homogeneous beam material is copper. The lower limit frequencies or the bandwidths are similar when the material is copper and aluminum, which are higher than that when the material is steel. The locations and bandwidths of the second flexural wave band gap are similar when the material is steel and aluminum, which the normalized band gaps are 0.166–0.189 and 0.153–0.192, respectively. The third flexural wave band gap locations of the steel and aluminum are almost similar to those of the second band gap when the material is copper, which the normalized lower limit frequencies are 0.493, 0.474, 0.428 and the normalized upper limit frequencies are 0.603, 0.565, 0.612 respectively when the material is steel, copper and aluminum.

4 CONCLUSION

In this paper, we propose a periodic beam-oscillators coupling system as the simple physical model for analyzing the dynamic characteristics of periodic support beams and low-frequency flexural wave vibration of slender stiffened plate structures in ship and offshore structures, the calculation method for the flexural wave band gaps in the proposed infinite long homogeneous beam coupled with periodic oscillators is established by the method of reverberation-ray matrix combined with Bloch theorem. The effectiveness of the flexural wave band gaps theoretical calculation method has been verified by the numerical results expressed by the flexural wave vibration transmission spectrum. Parametric studies show that the flexural wave band gaps can be adjusted and optimized manually by adjusting structural and material parameters. The studies are of great guiding significance for the vibration and noise control design of periodic support beams and slender stiffened plate structures, such as the 1D periodic structures in high-speed railway, building foundations, bridge structures, ships and offshore structures, and the 2D periodic stiffened plates in bridge structures, ships and offshore structures. The main conclusions are as follows:

- 1) The formation mechanism of the first band gap, which is determined by the local resonance of the periodic oscillators, while the second band gap is determined by the coupling effects between the Bragg scattering of periodic oscillators and the propagation of the flexural wave in homogeneous beam. As the lower limit frequency of the first flexural wave band gap keeps constant at 0 Hz, it is conducive to the application of the

flexural wave band gap characteristics to the low-frequency vibration and noise control of the periodic structure.

- 2) As can be seen from the studies of the effects of spring stiffness and mass of the periodic oscillators on the flexural wave band gap characteristics, there is a critical frequency value $f = 590$ Hz, the lower limit frequency and upper limit frequency of the second band gap remains constant at about 590 Hz when the k_{sdim} in the range of 10^{-4} –2 and 3–11, respectively. Similar to this, the initial frequency and the terminal frequency of the second band gap keep constant at about 590 Hz when the m_{sdim} in the range of 0.1–0.4 and 0.8–3.0, respectively. This phenomenon can be explained that the second band gap is determined by the coupling effects between the Bragg scattering of periodic oscillators and the propagation of the flexural wave in homogeneous beam.
- 3) The effects of periodic oscillators damping on the first flexural wave band gap is due to the increase of c_{sdim} causes the translational stiffness coefficient of the periodic oscillators acting on the beam to decrease.
- 4) With the dimensionless section moment of inertia I_{dim} increase, the frequencies of the second band gap have significant gradually increase while those of the first band gap almost keep constant. It is conducive to artificially modulating and optimizing the second band gap characteristic by tuning the section moment of inertia I .

DATA AVAILABILITY STATEMENT

The original contributions presented in the study are included in the article/Supplementary Materials, further inquiries can be directed to the corresponding author.

AUTHOR CONTRIBUTIONS

XY conceived the idea of the manuscript. LT and GW developed the theoretical formulations and the numerical simulation. LT and CW wrote and edited the manuscript. All authors conducted subsequent improvements to the article and approved the submitted version.

FUNDING

This research was supported by the National Natural Science Foundation of China (Nos 51979054 and 51809054).

REFERENCES

- An, S., Shu, H., Liang, S., Shi, X., and Zhao, L. (2018). Band gap Characteristics of Radial Wave in a Two-Dimensional Cylindrical Shell with Radial and Circumferential Periodicities. *Aip Adv.* 8 (3), 035110. doi:10.1063/1.5023734
- Chen, T., and Chen, B. (1991). *Ship Structural Mechanics*. Shanghai Jiaotong University Press.
- Dupont, G., Movchan, A., Enoch, S., and Guenneau, S. (2019). Analysis of Low Frequency Acoustic Stop Bands in Cubic Arrays of Thick Spherical Shells with Holes. *Front. Mater.* 6 (50). doi:10.3389/fmats.2019.00050
- Enferadi, M. H., Ghasemi, M. R., and Shabakhty, N. (2019). Wave-induced Vibration Control of Offshore Jacket Platforms through SMA Dampers. *Appl. Ocean Res.* 90, 101848. doi:10.1016/j.apor.2019.06.005

- Faiz, M. S., Addouche, M., Zain, A. R. M., Siow, K. S., Chaalane, A., and Khelif, A. (2020). Experimental Demonstration of a Multichannel Elastic Wave Filter in a Phononic Crystal Slab. *Appl. Sci.* 10 (13), 4594. doi:10.3390/app10134594
- Gripp, J. A. B., and Rade, D. A. (2018). Vibration and Noise Control Using Shunted Piezoelectric Transducers: A Review. *Mech. Syst. Signal Process.* 112, 359–383. doi:10.1016/j.ymssp.2018.04.041
- Guo, Y. Q., and Fang, D. N. (2014). Analysis and Interpretation of Longitudinal Waves in Periodic Multiphase Rods Using the Method of Reverberation-Ray Matrix Combined with the Floquet-Bloch Theorem. *J. Vibration Acoustics-Transactions Asme* 136 (1). doi:10.1115/1.4025438
- Guo, Y. Q., and Fang, D. N. (2011). Formation of Longitudinal Wave Band Structures in One-Dimensional Phononic Crystals. *J. Appl. Phys.* 109 (7), 073515. doi:10.1063/1.3567911
- Han, J., Kitazawa, D., Kinoshita, T., Maeda, T., and Itakura, H. (2019). Experimental Investigation on a Cabin-Suspended Catamaran in Terms of Motion Reduction and Wave Energy Harvesting by Means of a Semi-active Motion Control System. *Appl. Ocean Res.* 83, 88–102. doi:10.1016/j.apor.2018.12.003
- He, Z. C., Xiao, X., and Li, E. (2017). Design for Structural Vibration Suppression in Laminate Acoustic Metamaterials. *Composites B: Eng.* 131, 237–252. doi:10.1016/j.compositesb.2017.07.076
- Hirdaris, S. E., Bai, W., Dessi, D., Ergin, A., Gu, X., Hermundstad, O. A., et al. (2014). Loads for Use in the Design of Ships and Offshore Structures. *Ocean Eng.* 78 (1), 131–174. doi:10.1016/j.oceaneng.2013.09.012
- Ibrahim, R. A. (2008). Recent Advances in Nonlinear Passive Vibration Isolators. *J. Sound Vibration* 314 (3), 371–452. doi:10.1016/j.jsv.2008.01.014
- Kandasamy, R., Cui, F., Townsend, N., Foo, C. C., Guo, J., Shenoi, A., et al. (2016). A Review of Vibration Control Methods for marine Offshore Structures. *Ocean Eng.* 127 (nov15), 279–297. doi:10.1016/j.oceaneng.2016.10.001
- Keir, J., Kessissoglou, N. J., and Norwood, C. J. (2005). Active Control of Connected Plates Using Single and Multiple Actuators and Error Sensors. *J. Sound Vibration* 281 (1–2), 73–97. doi:10.1016/j.jsv.2004.01.007
- Kim, H.-G., Nerse, C., and Wang, S. (2019). Topography Optimization of an Enclosure Panel for Low-Frequency Noise and Vibration Reduction Using the Equivalent Radiated Power Approach. *Mater. Des.* 183, 108125. doi:10.1016/j.matdes.2019.108125
- Kushwaha, M. S., Halevi, P., Dobrzynski, L., and Djafari-Rouhani, B. (1993). Acoustic Band Structure of Periodic Elastic Composites. *Phys. Rev. Lett.* 71 (13), 2022–2025. doi:10.1103/physrevlett.71.2022
- Lan, C.-C., Yang, S.-A., and Wu, Y.-S. (2014). Design and experiment of a Compact Quasi-Zero-Stiffness Isolator Capable of a Wide Range of Loads. *J. Sound Vibration* 333 (20), 4843–4858. doi:10.1016/j.jsv.2014.05.009
- Lee, S., Ahn, C. H., and Lee, J. W. (2018). Vibro-acoustic Metamaterial for Longitudinal Vibration Suppression in a Low Frequency Range. *Int. J. Mech. Sci.* 144, 223–234. doi:10.1016/j.ijmecsci.2018.05.010
- Li, B., and Yang, H. (2020). Design of Active Vibration Reduction System for Intelligent Ship Mechanical Equipment. *J. Coastal Res.* 115, 235–237. doi:10.2112/jcr-si115-074.1
- Li, L., and Guo, Y. (2016). Analysis of Longitudinal Waves in Rod-type Piezoelectric Phononic Crystals. *Crystals* 6 (4), 45. doi:10.3390/cryst6040045
- Li, X. Y., Zhao, X., and Li, Y. H. (2014). Green's Functions of the Forced Vibration of Timoshenko Beams with Damping Effect. *J. Sound Vibration* 333 (6), 1781–1795. doi:10.1016/j.jsv.2013.11.007
- Liu, B., and Yang, L. (2017). Transmission of Low-Frequency Acoustic Waves in Seawater Piping Systems with Periodical and Adjustable Helmholtz Resonator. *Jmse* 5 (4), 56. doi:10.3390/jmse5040056
- Liu, C., Jing, X., and Li, F. (2015). Vibration Isolation Using a Hybrid Lever-type Isolation System with an X-Shape Supporting Structure. *Int. J. Mech. Sci.* 98, 169–177. doi:10.1016/j.ijmecsci.2015.04.012
- Liu, G., Lu, K., Zou, D., Xie, Z., Rao, Z., and Ta, N. (2017). Development of a Semi-active Dynamic Vibration Absorber for Longitudinal Vibration of Propulsion Shaft System Based on Magnetorheological Elastomer. *Smart Mater. Struct.* 26 (7), 075009. doi:10.1088/1361-665X/aa73f3
- Liu, Z., Zhang, X., Mao, Y., Zhu, Y. Y., Yang, Z., Chan, C. T., et al. (2000). Locally Resonant Sonic Materials. *Science* 289 (5485), 1734–1736. doi:10.1126/science.289.5485.1734.%J.Science
- Mead, D. J. (1970). Free Wave Propagation in Periodically Supported, Infinite Beams. *J. Sound Vibration* 11 (2), 181–197. doi:10.1016/S0022-460X(70)80062-1
- Mead, D. M. (1996). Wave Propagation in Continuous Periodic Structures: Research Contributions from Southampton, 1964–1995. *J. Sound Vibration* 190 (3), 495–524. doi:10.1006/j.jsvi.1996.0076
- Muhammadand Lim, C. W. (2019). Elastic Waves Propagation in Thin Plate Metamaterials and Evidence of Low Frequency Pseudo and Local Resonance Bandgaps. *Phys. Lett. A* 383 (23), 2789–2796. doi:10.1016/j.physleta.2019.05.039
- Murawski, L., and Charchalis, A. (2014). Simplified Method of Torsional Vibration Calculation of marine Power Transmission System. *Mar. Structures* 39, 335–349. doi:10.1016/j.marstruc.2014.10.004
- Nateghi, A., Sangiuliano, L., Claeys, C., Deckers, E., Pluymers, B., and Desmet, W. (2019). Design and Experimental Validation of a Metamaterial Solution for Improved Noise and Vibration Behavior of Pipes. *J. Sound Vibration* 455, 96–117. doi:10.1016/j.jsv.2019.05.009
- Nobrega, E. D., Gautier, F., Pelat, A., and Dos Santos, J. M. C. (2016). Vibration Band Gaps for Elastic Metamaterial Rods Using Wave Finite Element Method. *Mech. Syst. Signal Process.* 79, 192–202. doi:10.1016/j.ymssp.2016.02.059
- Ou, J., Long, X., Li, Q. S., and Xiao, Y. Q. (2007). Vibration Control of Steel Jacket Offshore Platform Structures with Damping Isolation Systems. *Eng. Structures* 29 (7), 1525–1538. doi:10.1016/j.engstruct.2006.08.026
- Richards, D., and Pines, D. J. (2003). Passive Reduction of Gear Mesh Vibration Using a Periodic Drive Shaft. *J. Sound Vibration* 264 (2), 317–342. doi:10.1016/S0022-460X(02)01213-0
- Sharma, B., and Sun, C. T. (2016). Local Resonance and Bragg Bandgaps in sandwich Beams Containing Periodically Inserted Resonators. *J. Sound Vibration* 364, 133–146. doi:10.1016/j.jsv.2015.11.019
- Shen, H., Wen, J., Paidoussis, M. P., Yu, D., Asgari, M., and Wen, X. (2012). Control of Sound and Vibration for Cylindrical Shells by Utilizing a Periodic Structure of Functionally Graded Material. *Phys. Lett. A* 376 (45), 3351–3358. doi:10.1016/j.physleta.2012.08.048
- Shi, W., Tan, X., Gao, Z., and Moan, T. (2016). Numerical Study of Ice-Induced Loads and Responses of a Monopile-type Offshore Wind Turbine in Parked and Operating Conditions. *Cold Regions Sci. Tech.* 123, 121–139. doi:10.1016/j.coldregions.2015.12.007
- Som, A., and Das, D. (2018). Seismic Vibration Control of Offshore Jacket Platforms Using Decentralized Sliding Mode Algorithm. *Ocean Eng.* 152, 377–390. doi:10.1016/j.oceaneng.2018.01.013
- Toky, A., Singh, R. P., and Das, S. (2020). Localization Schemes for Underwater Acoustic Sensor Networks - A Review. *Comp. Sci. Rev.* 37, 100241. doi:10.1016/j.cosrev.2020.100241
- Waki, Y., Mace, B. R., and Brennan, M. J. (2009). Numerical Issues Concerning the Wave and Finite Element Method for Free and Forced Vibrations of Waveguides. *J. Sound Vibration* 327 (1–2), 92–108. doi:10.1016/j.jsv.2009.06.005
- Wang, T., Sheng, M. P., and Guo, H. B. (2016). Multi-large Low-Frequency Band Gaps in a Periodic Hybrid Structure. *Mod. Phys. Lett. B* 30, 1650116. doi:10.1142/S0217984916501116
- Wang, W., Chen, L. Y., and Zhang, Y. F. (2013). Study on Vibration Reduction Design of Steel-Composite Material Hybrid Mounting for Ship Based on Material Selection Optimization. *Amr* 694–697, 415–424. doi:10.4028/www.scientific.net/amr.694-697.415
- Waye, K. P. (2011). “Effects of Low Frequency Noise and Vibrations: Environmental and Occupational Perspectives,” in *Encyclopedia of Environmental Health*. Editor J. Nriagu. Second Edition (Oxford: Elsevier), 264–277. doi:10.1016/b978-0-444-63951-6.00245-x
- Wu, W., Chen, X., and Shan, Y. (2014). Analysis and experiment of a Vibration Isolator Using a Novel Magnetic spring with Negative Stiffness. *J. Sound Vibration* 333 (13), 2958–2970. doi:10.1016/j.jsv.2014.02.009
- Xiang, H., Ma, X., and Xiang, J. (2020). Band Gaps and Transmission Characteristics Analysis on a Two-Dimensional Multiple-Scatter Phononic Crystal Structure. *Materials* 13 (9), 2106. doi:10.3390/ma13092106
- Xu, S.-F., Xu, Z.-L., and Chuang, K.-C. (2021). Hybrid Bandgaps in Mass-Coupled Bragg Atomic Chains: Generation and Switching. *Front. Mater.* 8 (430). doi:10.3389/fmats.2021.774612
- Yaman, O., Tuncer, T., and Tasar, B. (2021). DES-pat: A Novel DES Pattern-Based Propeller Recognition Method Using Underwater Acoustical Sounds. *Appl. Acoust.* 175, 107859. doi:10.1016/j.apacoust.2020.107859

- Zhou, C. W., Lainé, J. P., Ichchou, M. N., and Zine, A. M. (2015). Wave Finite Element Method Based on Reduced Model for One-Dimensional Periodic Structures. *Int. J. Appl. Mech.* 07 (2), 1550018. doi:10.1142/s1758825115500180
- Zhou, X. Q., Yu, D. Y., Shao, X., Wang, S., and Tian, Y. H. (2014). Band gap Characteristics of Periodically Stiffened-Thin-Plate Based on center-finite-difference-method. *Thin-Walled Structures* 82, 115–123. doi:10.1016/j.tws.2014.04.010
- Zuo, S., Huang, H., Wu, X., Zhang, M., and Ni, T. (2018). Low-frequency Band gap of Locally Resonant Phononic Crystals with a Dual-Base Plate. *The J. Acoust. Soc. America* 143 (3), 1326–1332. doi:10.1121/1.5025041

Conflict of Interest: The authors declare that the research was conducted in the absence of any commercial or financial relationships that could be construed as a potential conflict of interest.

Publisher's Note: All claims expressed in this article are solely those of the authors and do not necessarily represent those of their affiliated organizations, or those of the publisher, the editors and the reviewers. Any product that may be evaluated in this article, or claim that may be made by its manufacturer, is not guaranteed or endorsed by the publisher.

Copyright © 2022 Tang, Yao, Wu and Wang. This is an open-access article distributed under the terms of the Creative Commons Attribution License (CC BY). The use, distribution or reproduction in other forums is permitted, provided the original author(s) and the copyright owner(s) are credited and that the original publication in this journal is cited, in accordance with accepted academic practice. No use, distribution or reproduction is permitted which does not comply with these terms.



Radial Seismic Metamaterials Based on Layering Theory: Broadband Shielding of Ultra-Low Frequency Seismic Surface Waves

Haixia Liu¹, Lixia Li^{1,2*}, Qi Jia¹, Sanhe Jiang¹, Pengguo Li¹ and Xicheng Zhang³

¹School of Mechanical and Electrical Engineering, Institute of Mechanical Power, Xi'an University of Architecture and Technology, Xi'an, China, ²Institute of Mechanics, Xi'an University of Architecture and Technology, Xi'an, China, ³School of Civil Engineering, Institute of Engineering Structure and Earthquake Resistance, Xi'an University of Architecture and Technology, Xi'an, China

OPEN ACCESS

Edited by:

Fuyin Ma,
Xi'an Jiaotong University, China

Reviewed by:

Xianchen Xu,
University of Missouri, United States
Nansha Gao,
Northwestern Polytechnical
University, China

*Correspondence:

Lixia Li
jlili_18@163.com

Specialty section:

This article was submitted to
Metamaterials,
a section of the journal
Frontiers in Materials

Received: 30 March 2022

Accepted: 12 April 2022

Published: 10 May 2022

Citation:

Liu H, Li L, Jia Q, Jiang S, Li P and
Zhang X (2022) Radial Seismic
Metamaterials Based on Layering
Theory: Broadband Shielding of Ultra-
Low Frequency Seismic
Surface Waves.
Front. Mater. 9:908058.
doi: 10.3389/fmats.2022.908058

In this paper, a novel radial seismic metamaterial (LRSM) based on layering theory is proposed. Compared with traditional seismic metamaterials, the structure of LRSM is a periodic array of multi-layer rings distributed along the radial direction. By using the finite element method, the dispersion relationship and displacement vector field of LRSM with different layers are studied, and the influence of structural geometric parameters and circumferential continuity on the band gap characteristics of LRSM is discussed. The frequency domain analysis of finite periodic structure and the three-dimensional transient wave propagation analysis are carried out. The results show that the LRSM has ultra-low frequency broadband characteristics, which is produced by the coupling between the local resonance of the LRSM and the surface wave mode. Comparing three LRSMs with different layers, the initial frequency and bandwidth do not change monotonically with the increase of the number of layers. There is an optimal bandgap characteristic in two layers, and the relative bandwidth can reach 83.9%. The increase of the number causes the change of the structural stiffness, which is caused by the change of the local resonance strength. The position and width of the band gap in the LRSM are very sensitive to the height of the structure. The increase of the height of the LRSM can move the first band gap to the low frequency, and the total bandwidth increases, which is mainly caused by the increase of the equivalent mass of the system with the increase of the height of the structure. Further, it is verified that LRSM can effectively attenuate seismic surface waves of 0.1–20 Hz, and its maximum amplitude attenuation can exceed 85%. The novel periodic structure proposed in this paper can provide new options for the fields of earthquake and low-frequency vibration reduction.

Keywords: elastic metamaterial, local resonance, band gap, finite element method, axisymmetric model

INTRODUCTION

Earthquakes are violent events caused by the movement of the earth's medium. According to statistics, millions of earthquakes occur every year on the earth, among which there are thousands of earthquakes with magnitudes above five (Reitherman, 2012; Wilson et al., 2014). Earthquakes propagate in the form of elastic waves radiating from the epicenter to the surrounding area. When

they meet the earth's surface, they will generate surface waves that only propagate along the earth's surface (Dobrin and Savit, 1960; Telford et al., 1990). Its vibration can cause the resonance of urban buildings, especially high-rise buildings, and cause strong damage to the buildings (Lim and Reddy, 2019; Liu et al., 2020; Zeng et al., 2020). Recently developed metamaterials offer new ways to control seismic surface waves.

Metamaterials are periodic composite materials composed of subwavelength units, which have physical properties not found in natural materials, such as negative mass density (Wang et al., 2015; Wang et al., 2021) double negative modulus (Li and Chan, 2004), etc., which is an important research topic. The bandgap characteristics of metamaterials with wave regulation, the acoustic/elastic waves within the bandgap range are effectively attenuated and reflected, providing new ideas for shock absorption technology. Designing seismic metamaterials based on metamaterial theory has become an active research field (Chen and Wang, 2014; Krödel et al., 2015; Achaoui et al., 2016). S. Brûlé et al. (2014) periodically distributed holes in homogeneous soil to form a seismic metamaterial with soil as matrix and vertical holes as scatterers. Through numerical simulation and experimental verification, it was proved that its structure has a high effect on the center frequency. The 50 Hz seismic wave has obvious blocking effect; Miniaci et al. (2016) proposed a super-large two-dimensional seismic metamaterial, which can realize the isolation and shielding of 4.1–5.5 Hz seismic surface waves by burying periodic square steel piles in the soil.; Palermo et al. (2016) designed a seismic metamaterial with periodic arrangement of special resonators. Since each resonator in the array is designed to present a different eigenfrequency, it can effectively block seismic surface waves with a frequency of 4.9–7.5 Hz. Zeng et al. (Du et al., 2018) designed seismic metamaterials to expand the wide band gap based on the “fraction theory” (Norris et al., 2008); Sang-Hong Kim et al. (Kim and Das, 2012) designed a seismic wave with a cylindrical shell waveguide composed of multiple Holmhertz resonators Attenuator, which can block the transmission of seismic wave energy in a wide frequency range. Bogdan Ungureanu et al. (Ungureanu et al., 2015) designed a negative modulus metamaterial unit cell, which can effectively protect target buildings in a wide frequency range. Achaoui et al. (2017) proposed that the columnar seismic metamaterial is fixed on the bedrock, which can isolate seismic waves below 20 Hz. Although researchers at home and abroad have achieved a lot of research results on the low-frequency broadband characteristics of surface waves, the research work on ultra-low frequency (0.1–5 Hz) seismic surface waves is still very limited, and the current space of seismic metamaterials Periodicity is defined by lattice vectors in Cartesian coordinates.

Torrent et al. (Torrent and Sánchez-Dehesa, 2009; Torrent and Sánchez-Dehesa, 2010a; Torrent and Sánchez-Dehesa, 2010b) first proposed radial metamaterials whose structures are periodically distributed in the radial direction. The existence of the acoustic band gap was verified through numerical and experimental studies. Li et al. (2014) combined elastic wave equation and finite element theory, proposed radial elastic metamaterials, studied the band gap characteristics of

elastic waves in radial metamaterials, and proved that radial elastic metamaterials can effectively block elastic waves in the band gap. Researchers have found that radial metamaterials exhibit special omnidirectional wave shielding properties (Carbonell et al., 2011; Xu et al., 2012; Gao et al., 2016b; Shi et al., 2016), and have ultra-low frequency broadband characteristics (Ma et al., 2014; Shu et al., 2015; Gao et al., 2017; Jiang and He, 2017; An et al., 2018). Therefore, radial periodic structures are introduced into seismic metamaterials to study the propagation characteristics of seismic surface waves.

Furthermore, layered theory (Pennec et al., 2010; Elford et al., 2011; Neto et al., 2015) has been used to generate multi-order resonances to widen the acoustic/elastic wave band gap in metamaterials. In this paper, a layered radial seismic metamaterial (LRSM) is proposed, and its band gap characteristics are calculated by the finite element method. The effects of geometric parameters and the internal circumferential continuity of the structure on the shielding properties of radial seismic metamaterials are studied. Finally, the frequency response analysis and full-scale 3D transient wave propagation simulation are used to verify. In this paper, a high-performance, low-cost seismic metamaterial for engineering applications is realized by applying the periodic composite of steel and rigid foam, a common material in construction.

LAYERED RADIAL SEISMIC METAMATERIAL

Radial Seismic Metamaterial Model

As shown in **Figure 1**, the proposed model in this paper is a radial periodic array with layered structural features on the surface of a semi-infinite base, as shown in **Figure 1A**. The protection building is located in the center of the LRSM, and the schematic diagram of its array distribution cross-section is shown in **Figure 1B**.

In this paper, three radial seismic metamaterials (LRSMs) with different layers are studied, as shown in **Figure 1C–E**, respectively, and their structural radius parameter r remains unchanged. According to the survey data of different earthquakes, it is the most difficult to formulate protective measures for the long waves with the frequency distribution of seismic surface waves in the range of 0.1–20 Hz, and the corresponding wavelengths vary from several hundred meters to several meters (Zeng et al., 2019). Therefore, the lattice constant $a = 2.5$ m, which is much smaller than the wavelength of seismic waves (Du et al., 2018). The height of the LRSM is $h = 4a$. The depth of the basement is $H = 20a$ to ensure that it is sufficient to separate body and surface waves in seismic waves. **Figure 1C** shows a radial seismic metamaterial unit cell composed of a single-layer steel ring, which is defined as LRSM-1, where the distance $e = 0.1a$ between the outer diameter of the steel ring and the cell boundary, and the steel ring thickness $t_s = 0.2a$. **Figure 1D** shows the second radial seismic metamaterial unit cell, which is defined as LRSM-2, which is based on the single-layer steel ring structure, which is a foam ring with a thickness of $t_f = 0.1a$ and a steel ring with a thickness of t_s in turn

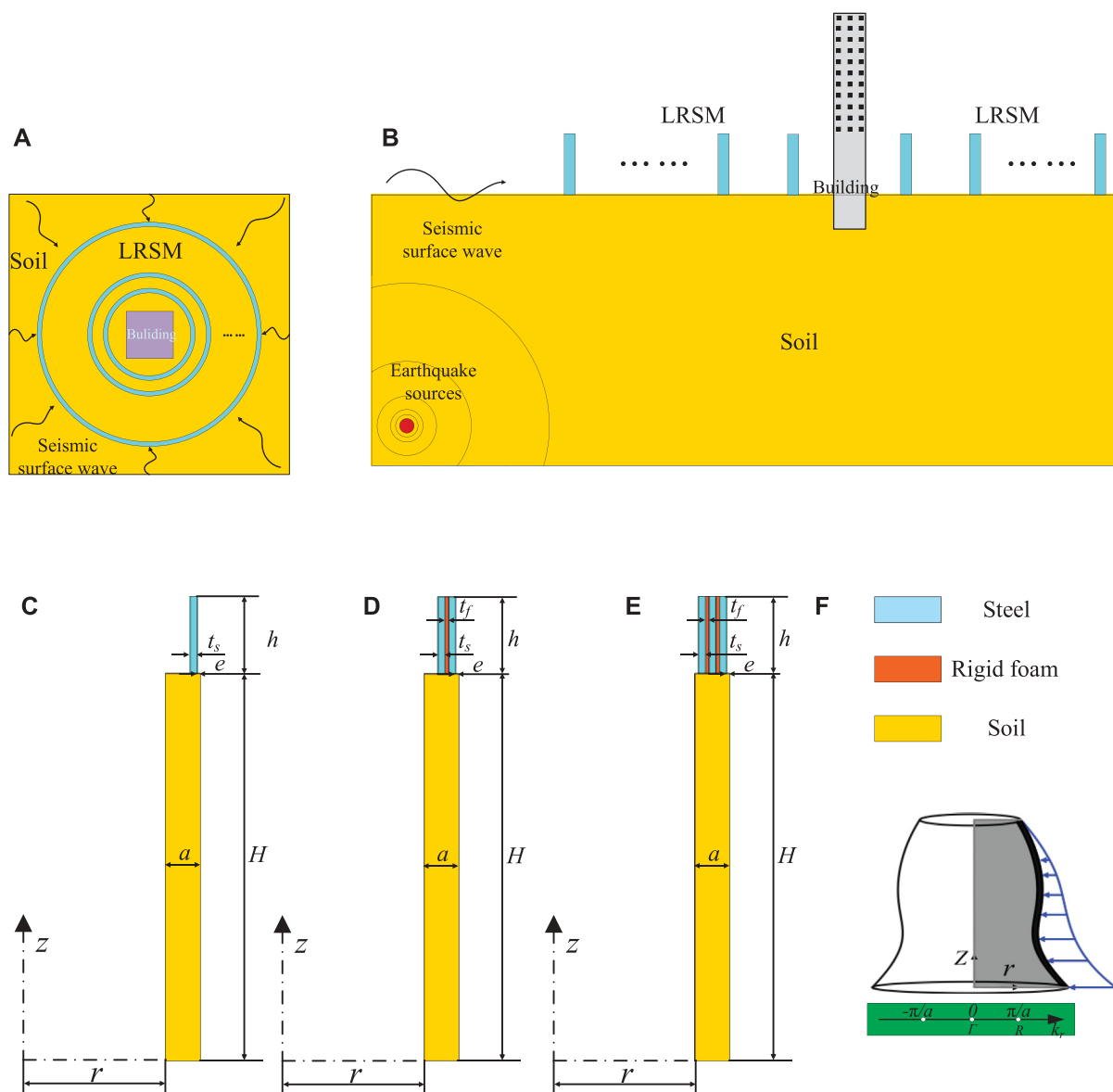


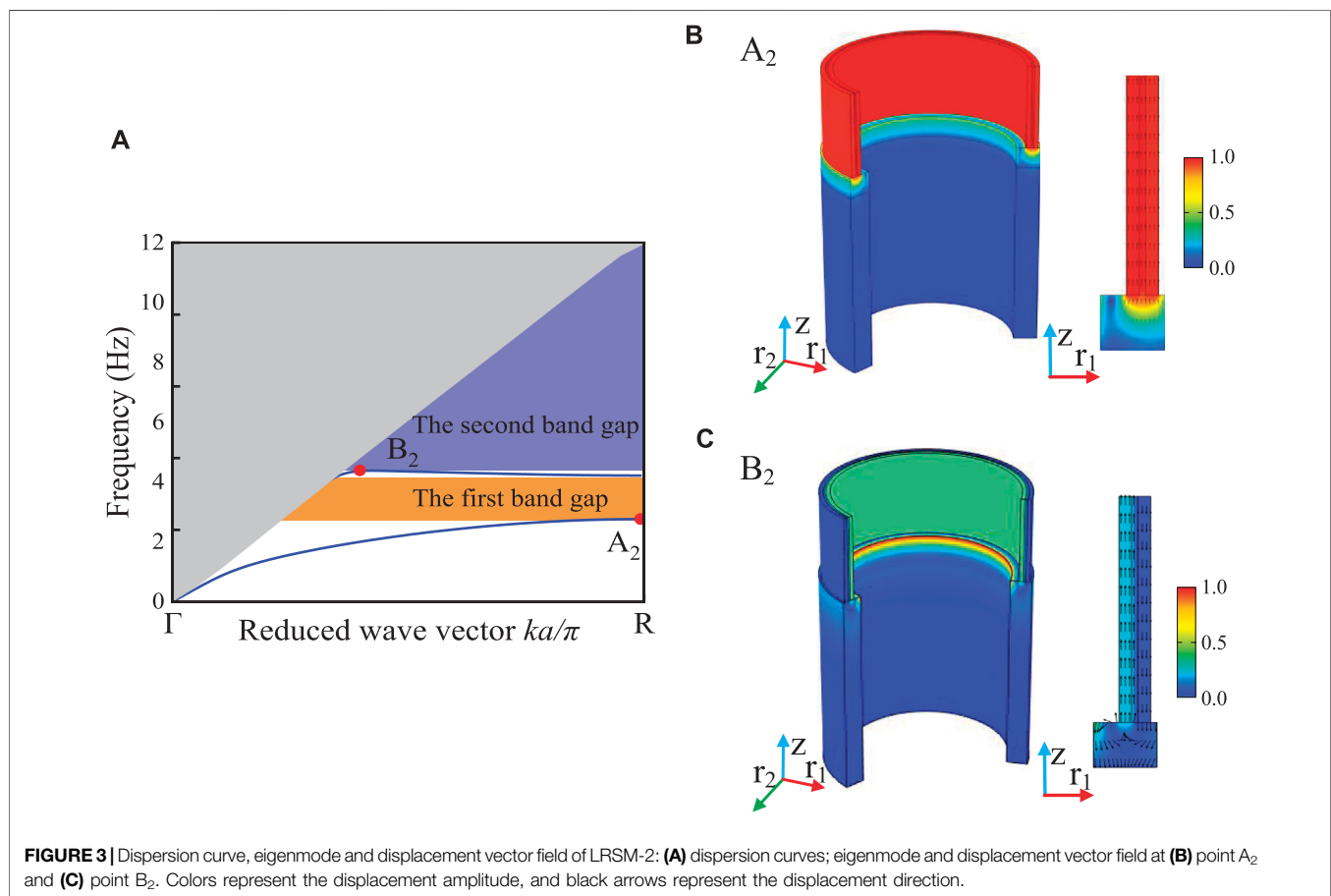
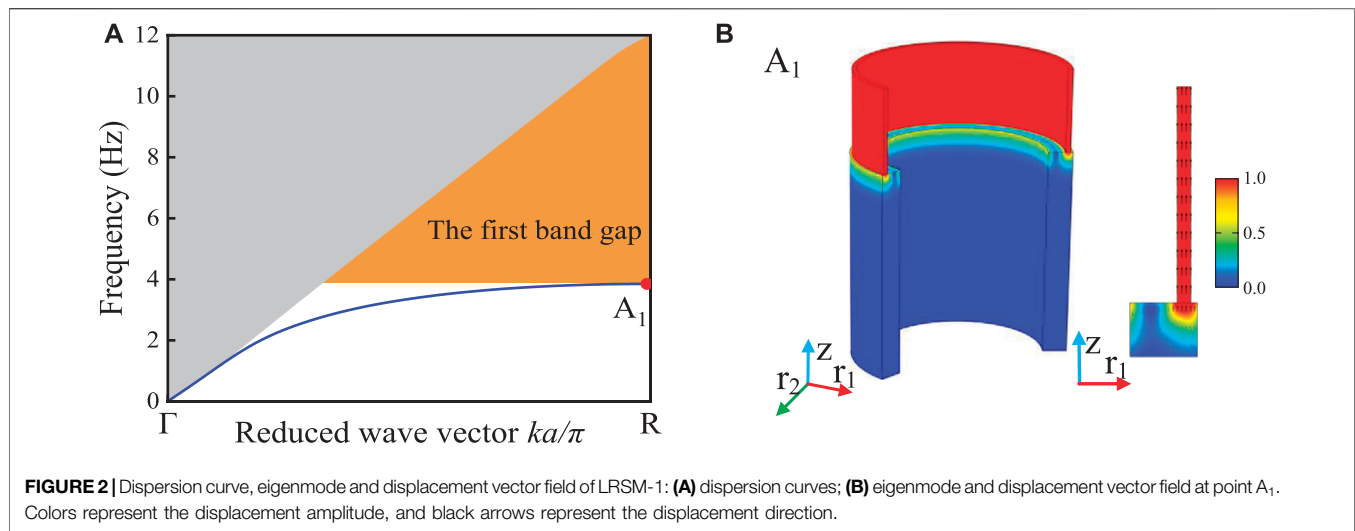
FIGURE 1 | Radial seismic metamaterials: **(A)** and **(B)** radial seismic metamaterials surrounding important buildings; **(C)** LRSM-1; **(D)** LRSM-2; **(E)** LRSM-3; **(F)** the formation mode of the radial seismic metamaterials and diagram of BZ wave vector (Γ -R) in reciprocal space. The blue, orange and yellow represent steel, hard foam and soil, respectively.

in the radial direction. **Figure 1E** shows the third radial seismic metamaterial unit cell. On the basis of LRSM-2, a foam ring of thickness t_f and a steel ring of thickness t_s are successively nested in the radial direction, which is defined as LRSM-3. By periodically repeating the LRSM unit cell along the r -direction and rotating around the Z -axis, an infinite system of LRSMs is formed, as shown in **Figure 1F**. In order to consider the engineering application of the structure, conventional building materials are chosen as the raw material of LRSM, such as steel and rigid foam, and the material of the base is soil (Zeng et al., 2018). In this paper, the material is assumed to be linear elastic, homogeneous and isotropic (Du et al., 2017). The material

TABLE 1 | Material properties of LRSM cell and substrate.

Material	Density	Young's modulus	Poisson's ratio
	$\rho/\text{kg}\cdot\text{m}^{-3}$	E/Pa	μ
Steel	7,784	2.07×10^{11}	0.3
Rigid foam	1,053	1.65×10^5	0.39
Soil	1800	2×10^7	0.3

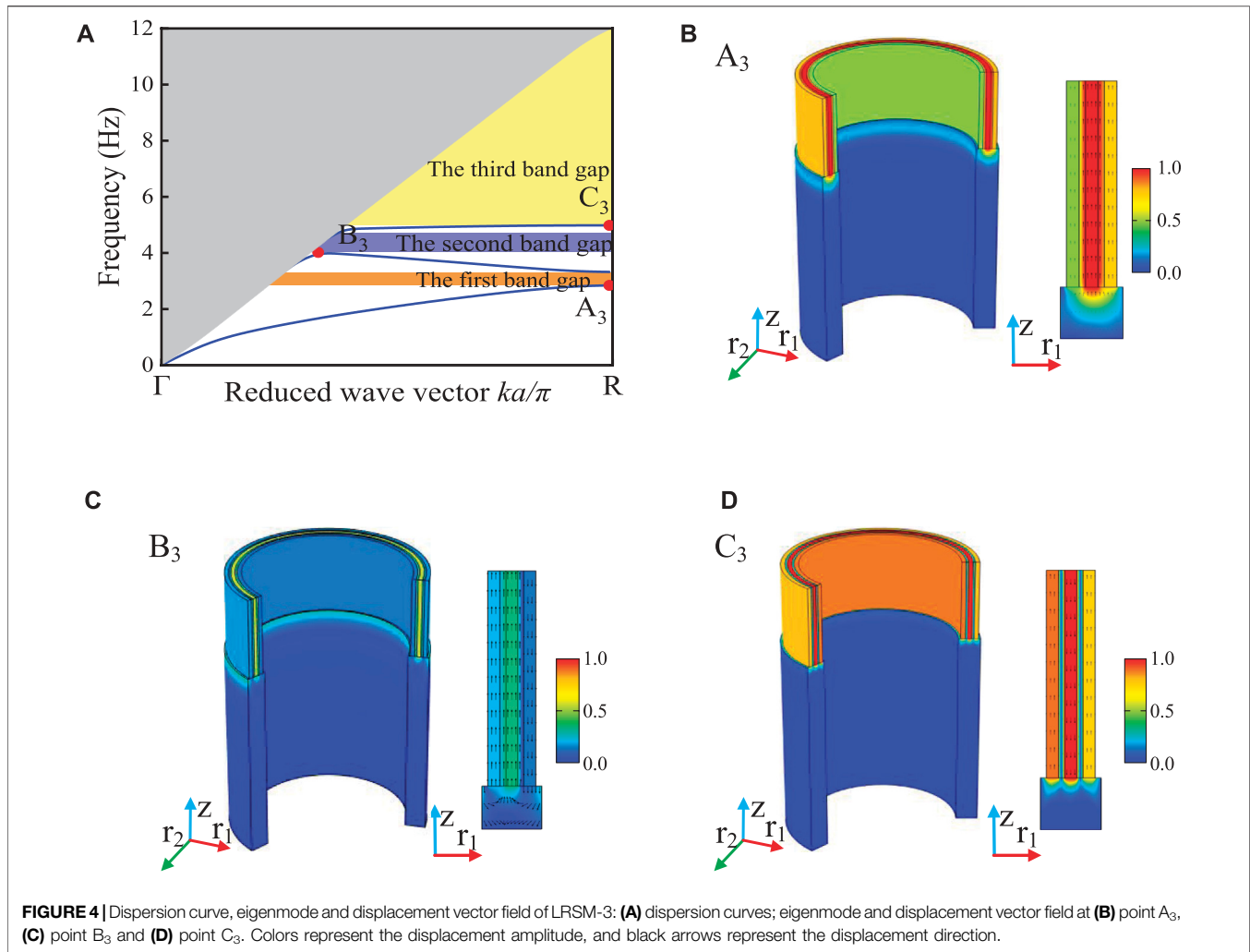
properties of the unit cell and substrate are shown in **Table 1**. The following material parameters are common parameters in engineering applications.



Theoretical Method

Due to the particularity of the structure, the two-dimensional axisymmetric finite element method based on cylindrical coordinate system is used to study the band gap characteristics of the metamaterial structure. The elastic wave equation in cylindrical

coordinate system is established to calculate the dispersion relation curve in infinite system. Where u , v , w are the displacement components of the cylindrical coordinate system, ρ is the density, t is the time, λ and μ are the elastic wave constants of the material, r , θ , z are the coordinate components of the cylindrical coordinate system.



$$\begin{aligned}\rho \frac{\partial^2 u}{\partial t^2} &= (\lambda + 2\mu) \frac{\partial \theta_t}{\partial r} - \frac{2\mu}{r} \frac{\partial w'_z}{\partial \theta} + 2\mu \frac{\partial w'_\theta}{\partial z}, \\ \rho \frac{\partial^2 v}{\partial t^2} &= (\lambda + 2\mu) \frac{\partial \theta_t}{r \partial \theta} - 2\mu \frac{\partial w'_z}{\partial z} + 2\mu \frac{\partial w'_r}{\partial r}, \\ \rho \frac{\partial^2 w}{\partial t^2} &= (\lambda + 2\mu) \frac{\partial \theta_t}{\partial z} - \frac{2\mu}{r} \frac{\partial}{\partial r} (r w'_\theta) + \frac{2\mu}{r} \frac{\partial w'_r}{\partial \theta},\end{aligned}\quad (1)$$

The volume strain θ_t and rotational components (w'_r , w'_θ , w'_z) are defined as:

$$\begin{aligned}\theta_t &= \frac{1}{r} \frac{\partial(ru)}{\partial r} + \frac{1}{r} \frac{\partial v}{\partial \theta} \frac{\partial w}{\partial z}, \quad w'_r = \frac{1}{2} \left(\frac{1}{r} \frac{\partial w}{\partial \theta} + \frac{1}{r} \frac{\partial v}{\partial z} \right), \\ w'_\theta &= \frac{1}{2} \left(\frac{1}{r} \frac{\partial u}{\partial \theta} + \frac{\partial w}{\partial r} \right), \quad w'_z = \frac{1}{2} \left(\frac{1}{r} \frac{\partial(rv)}{\partial \theta} + \frac{\partial u}{\partial \theta} \right),\end{aligned}\quad (2)$$

Since the periodic structure of the lattice unit is infinite along the radial direction, according to Bloch's theorem, only a single lattice unit is considered. Its lattice boundary condition equation is:

$$u(r + ra, z) = u(r, z) e^{ik_r r a}, \quad (3)$$

where r is the radial position, a is the lattice constant, and k_r is the component of the Bloch wave vector K_r in the radial direction.

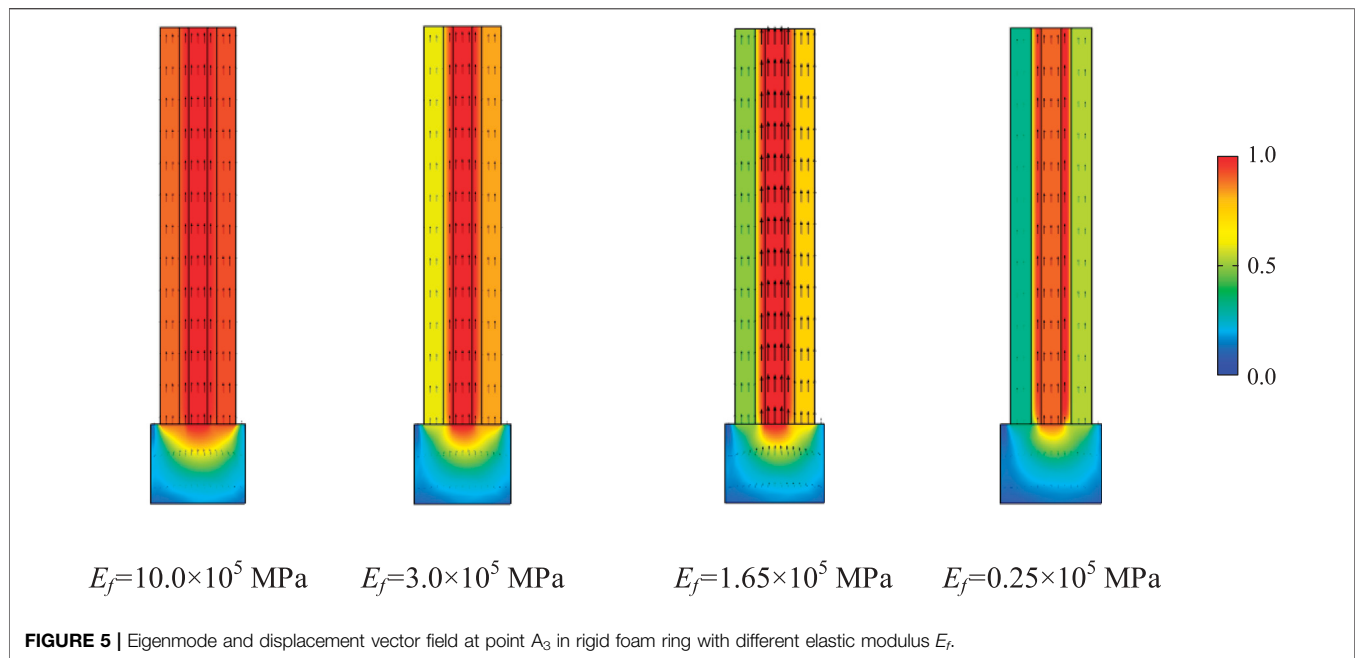
By Eq. 3, applying a periodic boundary condition on r , the dispersion relation curve of the radial metamaterial structure can be obtained by sweeping the Bloch wave vector K_r across the boundary of the first irreducible Brillouin zone.

According to finite element theory (Li et al., 2014), Eq. 1a can be transformed into a generalized eigenvalue equation with discrete form:

$$(K - \omega^2 M)u = 0 \quad (4)$$

where K is the stiffness matrix of the metamaterial structure, M is the mass matrix of the metamaterial structure, and u is the eigenvector.

After obtaining the finite element generalized eigenequation Eq. 4, by giving a set of Bloch wave vectors K_r , the eigenfrequency ω of each order of a single lattice unit is calculated under the condition of the wave vector, and substituted into the finite



element equation, namely Eigenvectors of all orders ($u = [u^1, u^2, \dots, u^n]^T$) can be obtained. Then, according to the eigenvectors, the displacement value of each point in the lattice unit is established, and the eigenmode displacement vector field of a single lattice unit can be obtained through the differentiated color display (Gao et al., 2016a). In this paper, this efficient finite element method (Achaoui et al., 2017; Gao et al., 2017) will be used to study the band gap properties of seismic radial metamaterial structures.

LAYERED RADIAL SEISMIC METAMATERIAL ULTRA-LOW FREQUENCY BROADBAND CHARACTERISTICS

Ultra-Low Frequency Broadband Characteristics and Its Mechanism Analysis

The dispersion curves of three different LRSMs are shown in **Figures 2A, 3A, 4A**. In the dispersion graph, the sound cone surrounded by the gray area is important for separating surface and bulk waves, all bulk modes are located outside the sound cone, and surface wave modes are inside the sound cone (Colombi et al., 2016). In this paper, the relative band gap bandwidth (NRBW), which is the ratio of the total band gap width to the acoustic cone height (Zeng et al., 2018), is introduced to evaluate the LRSM surface wave band gap characteristics. For LRSM-1, it can be seen from **Figure 2A** that below 12 Hz, LRSM-1 has only one energy band curve, the complete band gap of surface wave is 3.12–11.96 Hz, and its NRBW is 73.9%, which is much higher than that of Miniaci (Miniaci et al., 2016), Palermo (Palermo et al., 2016) and Colombi (Colombi et al., 2016), etc. (NRBW is less than 20%).

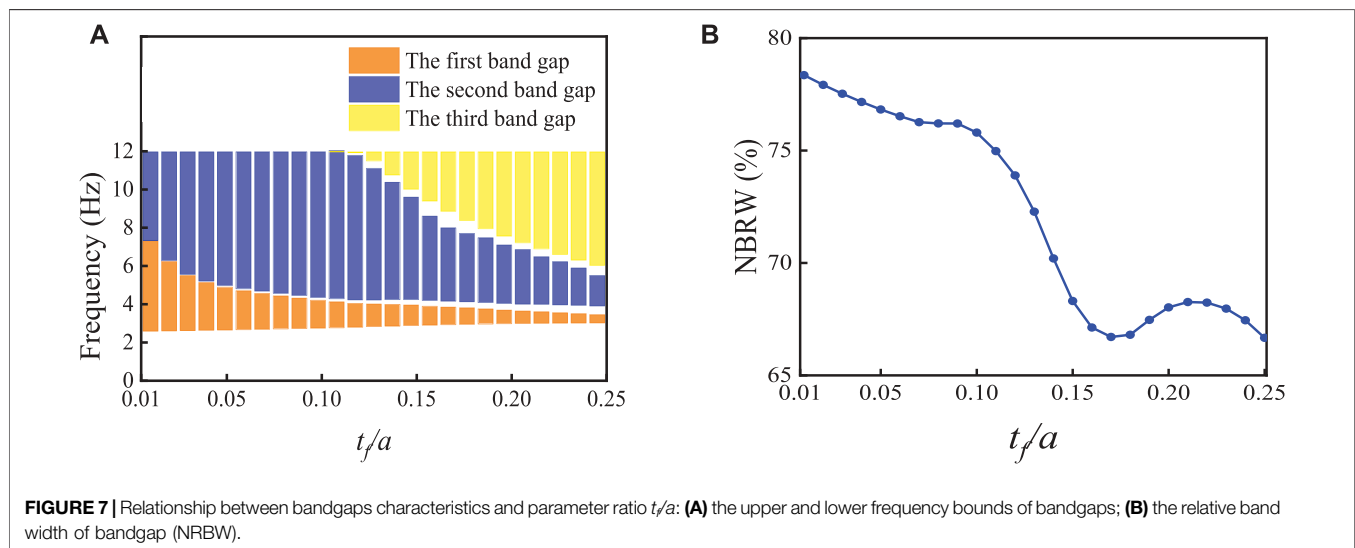
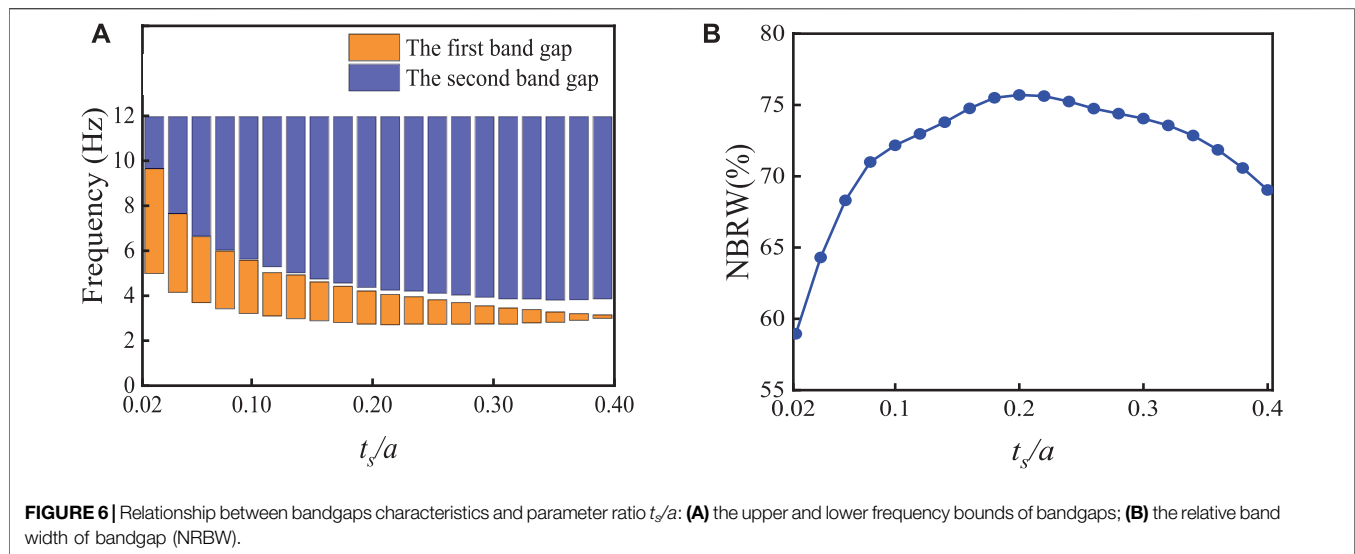
In order to study the generation mechanism of LRSM-1 ultra-low frequency broadband, the eigenmodes and displacement vector fields at point A_1 in the single dispersion curve of **Figure 2A** are calculated, as shown in **Figure 2B**. The black arrows represent the direction of the vibrational displacement, and the color represents the magnitude of the vibrational displacement. At point A_1 , it appears as the coupling mode of the in-phase vibration of the steel ring along the axial direction and the Rayleigh wave mode. The elastic stiffness of the structure is provided by the soil base, and its local vibration mode can be equivalent to a typical “mass-spring” system. The frequency of the resonance bandgap can be determined by the natural frequency of the local resonance and can be evaluated in terms of the equivalent mass that provides the mass part (LRSM) and the equivalent stiffness that provides the elastic part (soil base) for this vibration mode:

$$f = \frac{1}{2\pi} \sqrt{\frac{Ke}{Me}} \quad (5)$$

where Ke is the equivalent stiffness of the system and Me is the equivalent mass of the system.

It can be seen from **Eq. 5** that due to the circumferential continuity of LRSM-1, its equivalent mass Me is much higher than its equivalent stiffness Ke , so the initial frequency of the structural resonance band gap is in the ultra-low frequency range, and due to the structural sound The cone height is fixed (Zeng et al., 2018), so that the LRSM-1 exhibits very low frequency broadband characteristics.

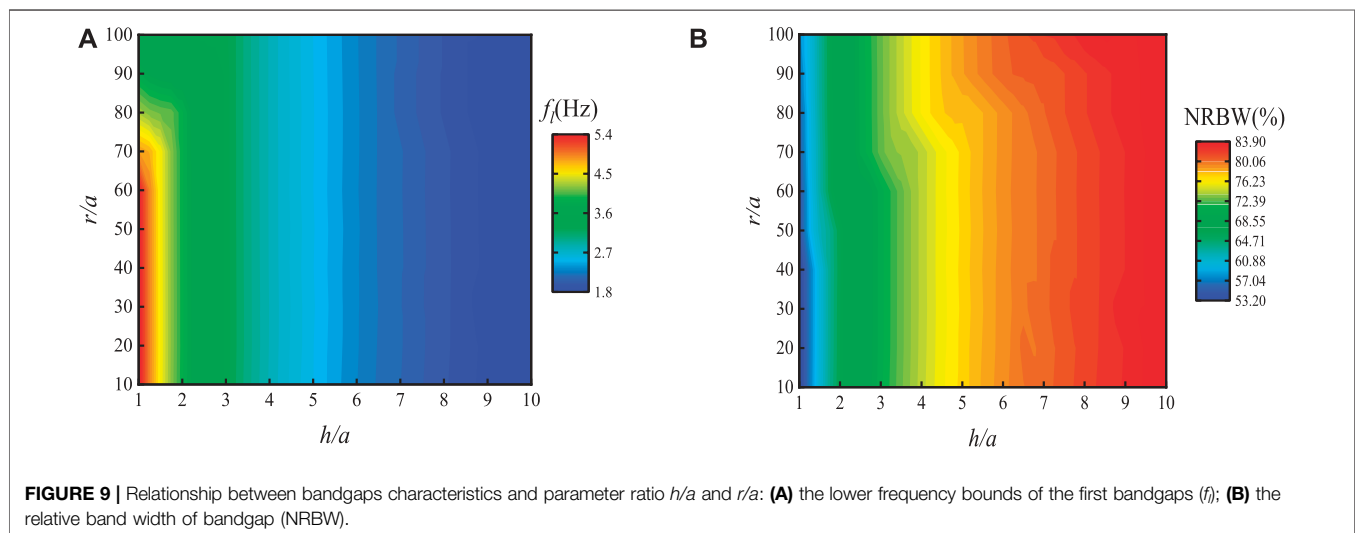
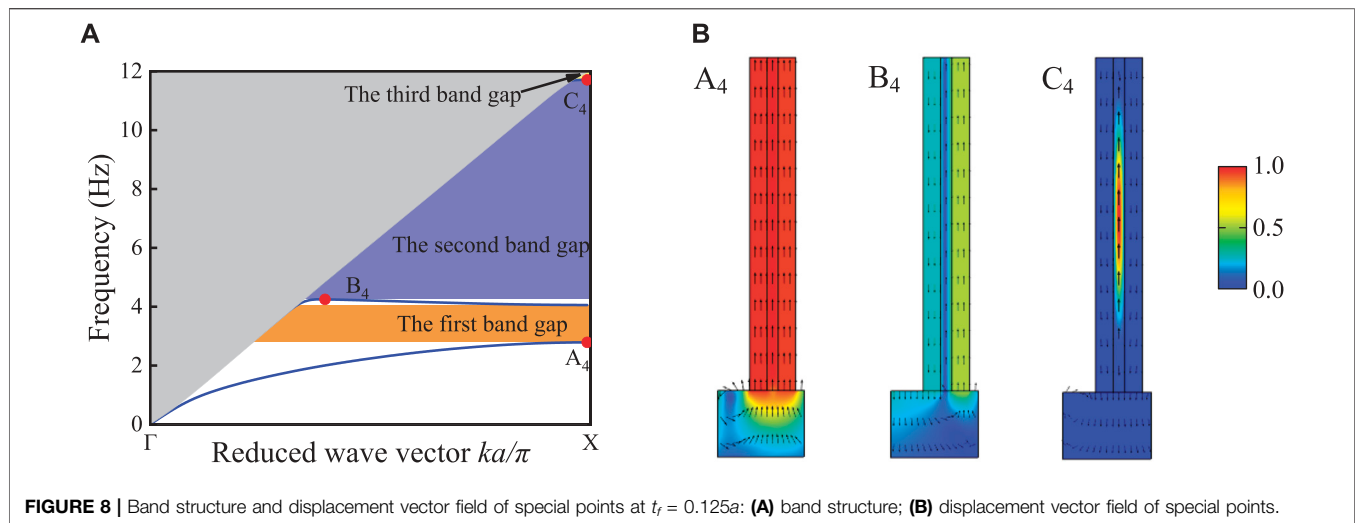
The dispersion curve of LRSM-2 is shown in **Figure 2B**, it has two energy band curves below 12 Hz, and produces two complete band gaps, namely 2.72–4.21 Hz and 4.38–11.96 Hz, and its NRBW is 75.5%. Compared with LRSM-1, the onset frequency of the first band gap is shifted down and a new resonance band



appears at 4.38 Hz. Further, by calculating the eigenmodes and displacement vector fields of the special points A_2 and B_2 on the two energy band curves, as shown in **Figures 3B,C**, respectively, to study the physical mechanism of the change of the band gap structure. The vibration mode of point A_2 , similar to point A_1 , is the overall axial in-phase vibration of the multilayer structure, but the initial frequency of the first band gap is lower than that of point A_1 due to the increase of the equivalent mass of the structure. The vibration mode at point B_2 is shown as the axial anti-phase resonance of the two-layer steel ring, and the energy is concentrated in the inner steel ring layer.

The dispersion curve of LRSM-3 is shown in **Figure 4A**. It can be seen from the figure that there are three energy bands below 12 Hz, forming three complete band gaps, which are 2.84–3.32 Hz, 4.02–4.85 Hz, and 4.98–11.96 Hz respectively., its NRBW is 69.3%. Compared with LRSM-2, the starting

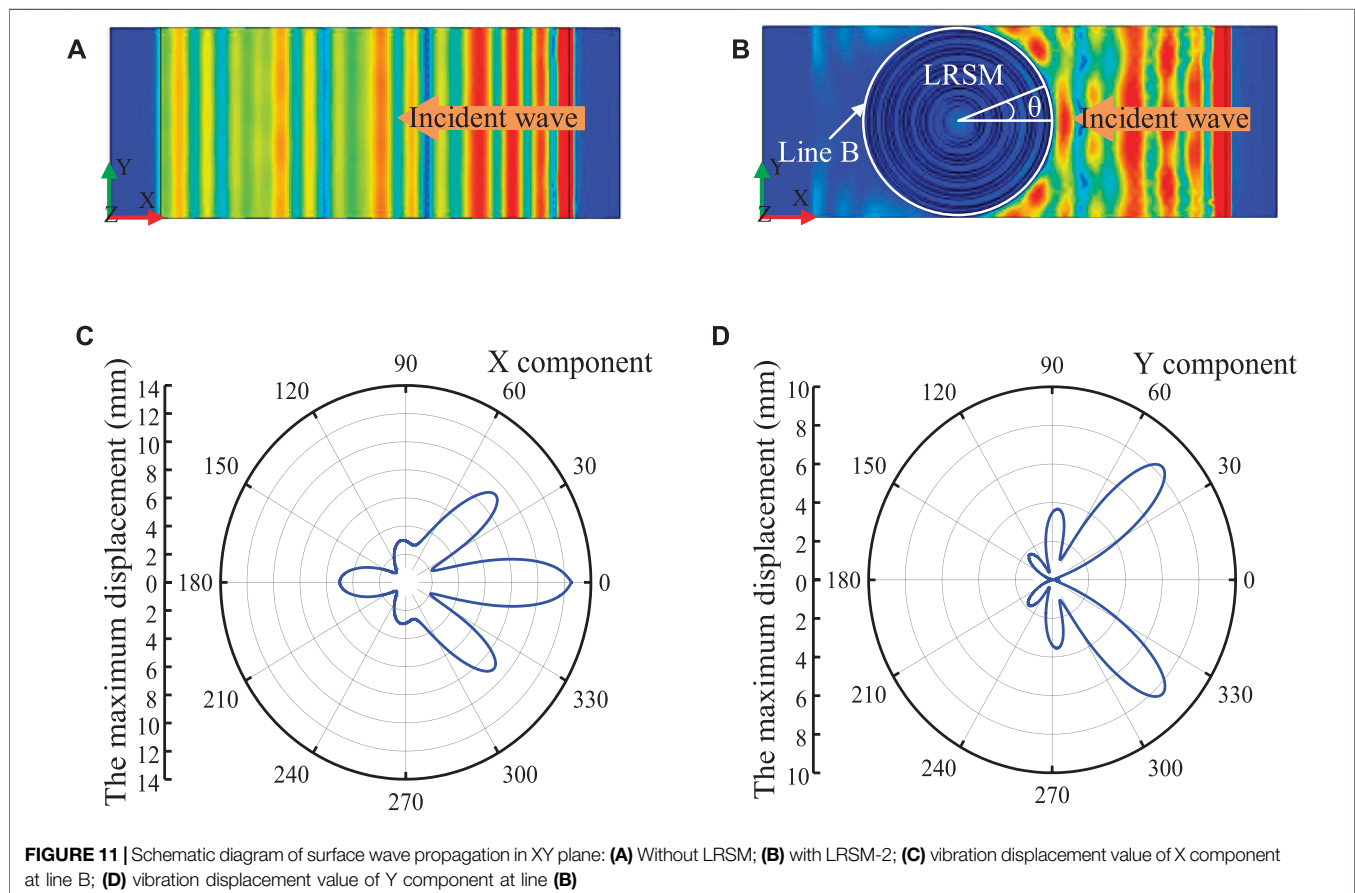
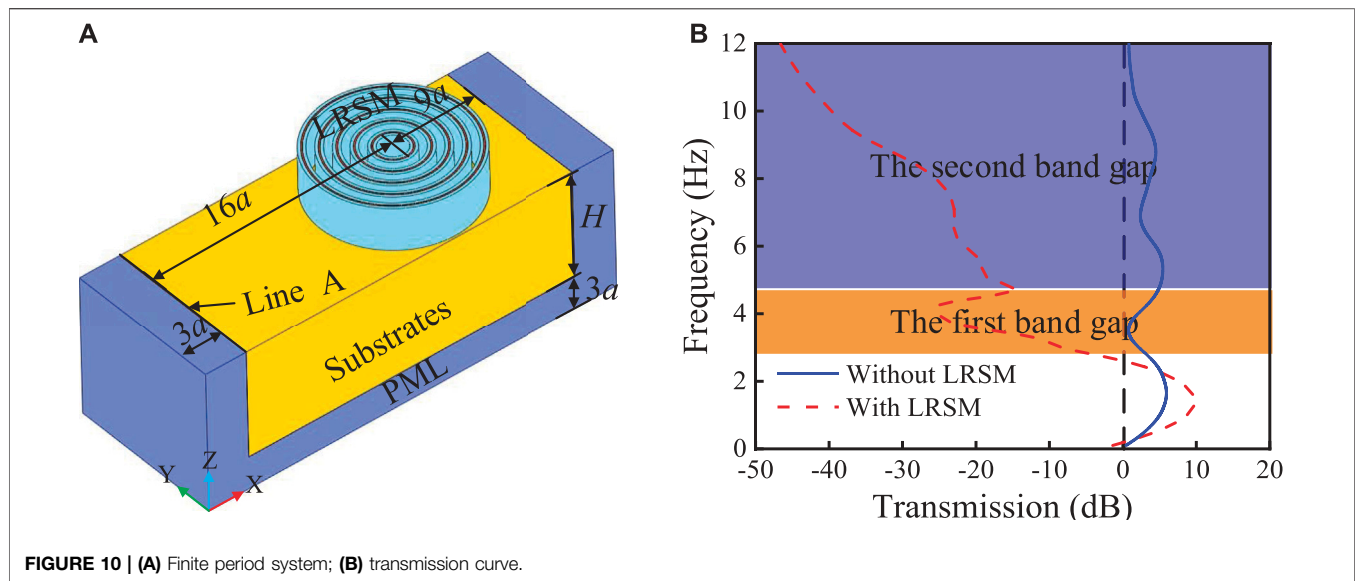
frequency of the first band gap is increased, while the starting frequency of the second band gap is decreased, and a new resonance band appears around 5 Hz. **Figure 4B,C,D** are the eigenmodes and displacement vector fields of the special points A_3 , B_3 and C_3 of the dispersion curve, respectively. At point A_3 , although the multi-layer structure exhibits axial in-phase vibration as a whole, its amplitudes are different, which is manifested as different amplitude resonance in the same phase of the structure's axial direction. The vibration energy is concentrated in the foam ring and steel ring in the middle, and the vibrational energy of the inner steel ring is the smallest, which is manifested as a decrease in the onset frequency of the first bandgap of LRSM-3. This is caused by the coupling resonance of the three-layer steel rings with different amplitudes due to the small stiffness of the foam rings on both sides of the middle steel ring. In order to further study the



effect of the foam ring on the initial frequency of the first band gap of LRSM-3, the vibration modes of point A_3 under different elastic modulus E_f states of the foam ring were calculated, as shown in **Figure 5**. As the elastic modulus E_f of the rigid foam ring decreases, the stiffness provided by the foam ring in the middle decreases, and the structure gradually changes from the overall axial resonance with the same amplitude to the coupled resonance with different amplitudes for each layer. The eigenmodes and displacement vector field of point B_3 are shown in **Figure 4C**, which is similar to the eigenmodes of point B_2 , showing the anti-phase resonance of the inner two-layer steel ring and the outer steel ring. **Figure 4D** shows the eigenmode and displacement vector field at point C_3 . At point C_3 , a more complex axial in-phase coupling resonance is presented, and the vibration energy is mainly concentrated in the middle steel ring. Therefore, as the number of layers in the system increases, more and more complex surface wave vibration modes will appear, resulting in new energy bands. As the

number of layers of steel rings increases, the initial frequency of LRSM does not decrease monotonically, and the total bandwidth does not increase monotonically. The intensity of the resonance changes, so that the structure exhibits a complex axial resonance mode. When LRSM-2, it presents the lowest onset frequency and the largest bandwidth of the band gap, which is different from the traditional layered seismic metamaterial (MSM) (Zeng et al., 2020).

In conclusion, all three LRSM structures exhibit ultra-low frequency broadband characteristics, and the vibration mode in the low frequency band is only the axial vibration mode, which is caused by the unique large-mass annular structure of LRSM. The LRSM barrier is fixed on the soil surface, and the unit cell is a large-mass annular structure, not only the resonance frequency is ultra-low frequency, but also the annular structure fixed on the soil surface has special stability in the circumferential direction (Budiansky and Hutchinson, 1966): so the LRSM band structure is simple, and only presents as an axial vibration mode, showing ultra-low frequency broadband characteristics.



Influence of Geometric Parameters on Band Gap Characteristics

The ultra-low frequency broadband characteristics of LRSM are caused by the local resonance coupling between Rayleigh mode and the LRSM structure. The structural parameters of LRSM have

an important influence on the ultra-low frequency broadband characteristics. In this section, the influence of geometric parameters on the complete band gap is analyzed while keeping other parameters unchanged. This study was conducted on LRSM-2.

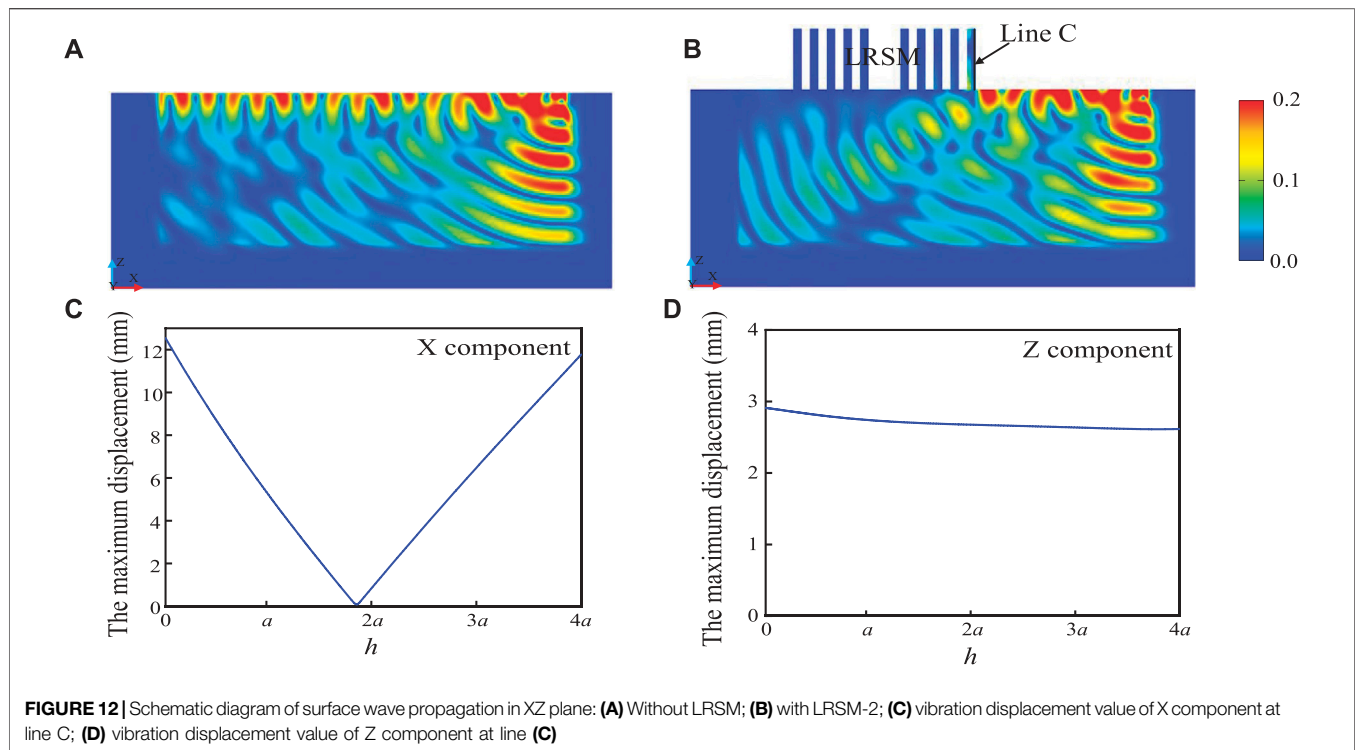


FIGURE 12 | Schematic diagram of surface wave propagation in XZ plane: (A) Without LRSM; (B) with LRSM-2; (C) vibration displacement value of X component at line C; (D) vibration displacement value of Z component at line C

Figure 6 shows the effect of the steel ring thickness t_s on the change of the band gap characteristics. In **Figure 6A**, as t_s/a increases, the first full bandgap bandwidth gradually decreases, and the second bandgap bandwidth increases and moves to low frequencies. The first band gap of LRSM-2 is caused by the overall axial in-phase resonance of the structure, and the change of the thickness t_s of the steel ring has a great influence on the equivalent mass and equivalent stiffness of the structure. When $t_s/a < 0.2$, the increase of the resonance mass in the structure will be dominant, with the increase of the parameter t_s/a , the equivalent mass increases, and the initial frequency of the first band gap moves rapidly to the low frequency; when $t_s/a = 0.2$, the change of the steel ring thickness t_s makes the equivalent mass of the structure and the equivalent stiffness increase close to each other. Therefore, the initial frequency of the first band gap remains basically unchanged, and the cut-off frequency moves to the low frequency. The band gap is then narrowed. For the second band gap, with the increase of t_s/a , the axial resonance coupling between the structure and the soil base gradually increases, and the initial frequency gradually shifts to the low frequency. Since the height of the sound cone of the structure is fixed, its bandwidth increases and shifts to low frequencies. With the increase of t_s/a , the NRBW shows a trend of first increasing and then decreasing. When $t_s/a = 0.2a$, the NRBW is the largest, reaching to 75.8% (as shown in **Figure 6B**).

Figure 7 shows the effect of the rigid foam ring thickness t_f of LRSM-2 on the band gap characteristics (the position parameter e remains unchanged). It can be seen from **Figure 7A** that with the

increase of t_f , the center frequencies of the first and second band gaps are both moved down, and the bandwidth is gradually narrowed. When $t_f = 0.125a$, the third band gap begins to appear. **Figure 7B** shows the effect of rigid foam ring thickness t_f on the NRBW. It can be seen from the figure that with the increase of rigid foam ring thickness t_f , the NRBW shows an overall decreasing trend. When $t_f/a = 0.01a$, the NRBW achieves the optimal value of 78.3%.

Figures 8A,B show the eigenmode and displacement vector field of band structure and special points when $t_f = 0.125a$, respectively. By comparing **Figure 3B**, it can be found that the vibration mode of point A_2 in **Figure 3** is consistent with that of point A_4 in **Figure 8**, both of which are axial in-phase local resonances, and the resonance intensity is similar, indicating that the increase in the thickness of hard foam ring t_f has little effect on the axial in-phase resonance mode of the system, so the initial frequency of the first band gap remains basically unchanged. The mode shape of point B_4 in **Figure 8** is stronger than that of point B_2 in **Figure 3**, which indicates that with the increase of the thickness t_f of the rigid foam ring, the local resonance effect is enhanced, resulting in the onset of the second band gap. The initial frequency is shifted to lower frequencies. In addition, with the further increase of the thickness t_f of the rigid foam ring, the system stiffness of the resonant structure decreases, which makes the structure appear a new local resonance mode, that is, the anti-phase resonance between the inner and outer steel rings and the central foam ring, as shown at point C_4 in **Figure 8B**, so the third band gap is opened.

Figure 9 shows the effect of height h and center radius r on the complete bandgap characteristic, where the height h and center radius r are generally considered to vary in the range of $1a$ - $10a$ and

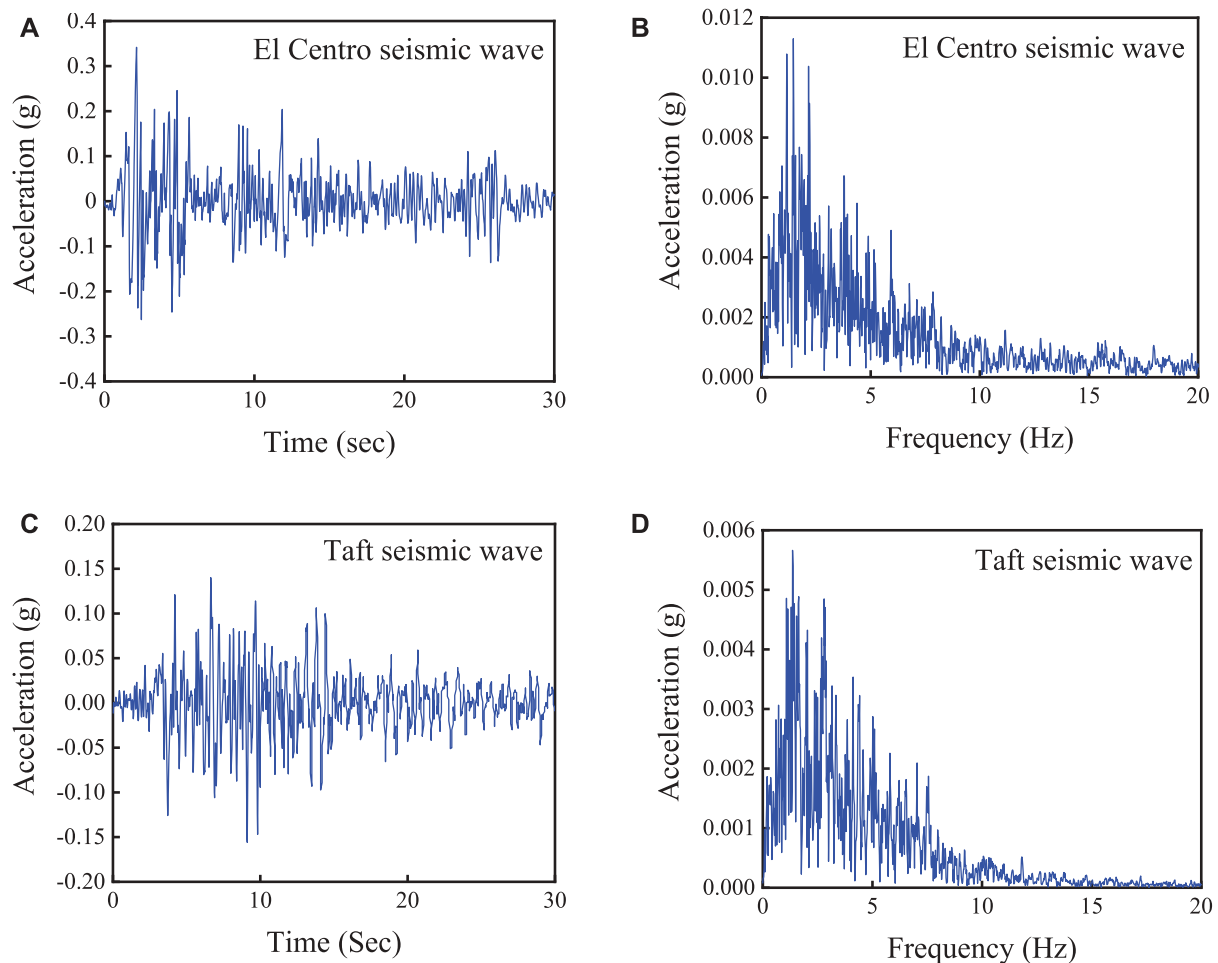


FIGURE 13 | Seismic excitation signal: **(A)** time evolution of El Centro seismic signal; **(B)** frequency content of El Centro seismic wave signal; **(C)** time evolution of Taft seismic wave signal; **(D)** frequency content of Taft seismic wave signal.

10a–100a, respectively. **Figure 9A** shows the relationship between the initial frequency (f_1) of the first band gap and the height h and the center radius r . As the height h increases, f_1 shifts to low frequencies, which is caused by the constant increase in the equivalent mass of the LRSM-2. In addition, it is worth noting that when the LRSM-2 center radius is greater than $75a$, for the lower height steel ring ($h < 1.5a$), f_1 does not shift to high frequencies with decreasing height h , but remains at 3.6 Hz nearby, this is due to the fact that the LRSM-2 gradually equalizes the increment of the equivalent mass and the equivalent stiffness of the system with the increase of the center radius r , therefore, f_1 remains almost unchanged. In addition, with the increase of the height h , the NRBW showed a trend of rapid increase; the increase of the center radius r also caused the increase of the NRBW. It can be observed that the structure height h has a more significant effect on NRBW. When the parameter $h/a = 10$, the NRBW can reach 83.9% (as shown in **Figure 9B**). The above results will better guide the design of LRSMs to obtain the desired bandgap properties in different geophysical environments.

RESEARCH ON THE SEISMIC SHIELDING PERFORMANCE OF LAYERED RADIAL SEISMIC METAMATERIAL

Frequency Domain Response Analysis

In order to verify the shielding performance of LRSM-2, five periodic systems are designed in the transmission calculation as shown in **Figure 10A**. The base is soil, and the height of $20a$ is enough to ensure the separation of the body wave and the surface wave in the seismic wave, so that only the surface wave can reach the LRSM (Zeng et al., 2018). To prevent unwanted reflections caused by boundary wave scattering from the substrate region and bring the results closer to realistic conditions, a perfectly matched layer (PML) with a thickness of $3a$ was placed on the bottom and sides of the substrate. At line A, a line source is set up to simulate an incident wave as a generator of surface waves, where the line source vibrates at a monochromatic frequency with sagittal polarization characteristics that excite seismic waves on a uniform surface. The transmission quantities of seismic surface

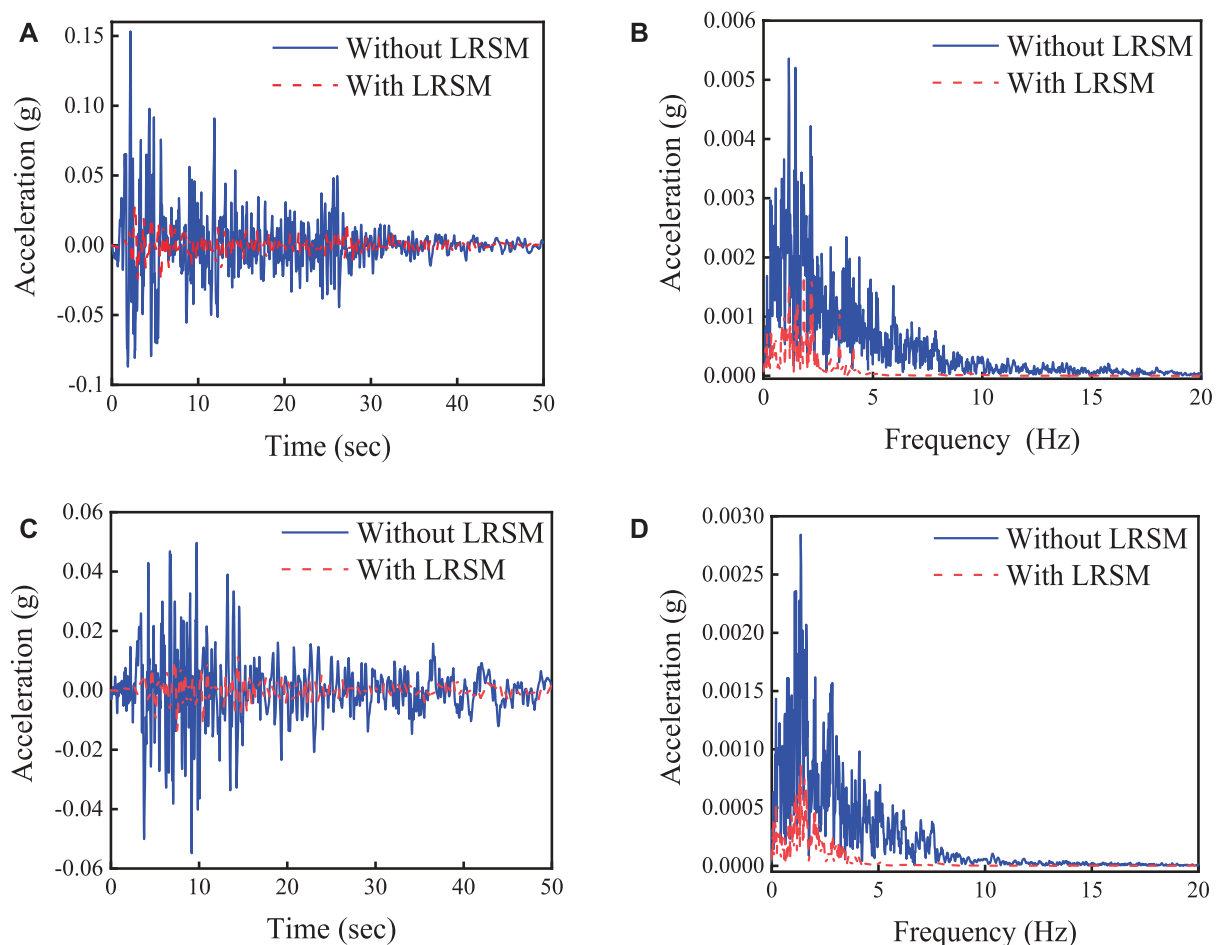


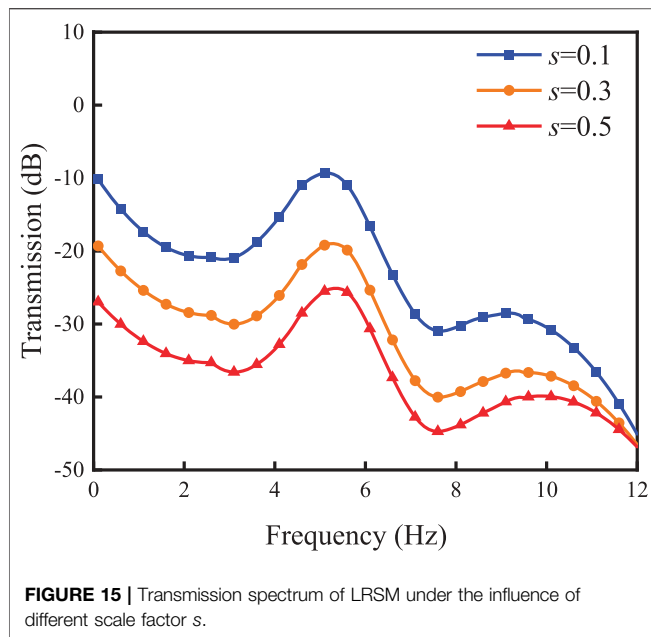
FIGURE 14 | Excitation signal response: **(A)** excitation signal response of El Centro seismic wave; **(B)** fourier spectrum of El Centro seismic excitation signal response; **(C)** excitation signal response of Taft seismic wave; **(D)** fourier spectrum of Taft seismic excitation signal response.

waves without LRSM and with LRSM in the range of 0.1–12 Hz are shown in **Figure 10B**, and complete attenuation areas are found in the ranges of 2.72–4.21 Hz and 4.38–11.96 Hz, which is consistent with **Figure 3**. The band gaps in (a) are consistent, and it can be found that within the band gap range, the amount of transmission with LRSM is significantly lower than that without LRSM.

Figures 11A,B show the propagation states of surface waves along the X direction in the soil without LRSM and with LRSM at 8 Hz, respectively. It can be seen from the figure that when there is no LRSM, the incident surface wave covers the soil matrix with almost no energy loss; while for the homogeneous soil with LRSM, the incident surface wave is effectively shielded. The X and Y components of the vibration displacement at the boundary line B are shown in **Figures 11C,D**, respectively. It can be observed from **Figure 11C** that the overall vibration displacement amplitude presents a maple leaf-shaped distribution, and the X component of the vibration displacement at the edge line B has a large difference in the circumferential distribution. The maximum vibration displacement value is 12.5 mm, located at 0°. The vibration displacement value is only 0.9 mm at the 135° position, so the

LRSM dissipates energy differently around the circumference in resisting seismic waves. In **Figure 11D**, the vibration displacement of the Y component presents a butterfly-shaped symmetrical distribution as a whole in polar coordinates, and the displacement values are the largest at the positions of 45° and 315°. In actual construction, the position with large displacement can be reinforced, which can effectively improve its ability to resist seismic waves.

Figures 12A,B show the XZ plane propagation states of surface waves in soils without and with LRSM, respectively. In **Figure 12A**, when the surface wave propagates in a half-space homogeneous medium, the energy is hardly attenuated, and it can carry energy for a long distance; in **Figure 12B**, the LRSM-2 band gap Surface waves are converted into body waves, and their vibrational energy is effectively dissipated, which is consistent with the “rainbow trap” effect (Colombi et al., 2016). The X and Z components of the vibrational displacement at line C are shown in **Figures 11C,D**, respectively. As shown in **Figure 12C**, the minimum value of the vibration displacement of line C on the X component appears at the inflection point of 2.9a, and its value is only 0.01 mm, the maximum displacement at the bottom is



12.5 mm, and the maximum displacement at the top is 11.7 mm. This shows that the line C presents a concave shape, and if its bottom is reinforced, such as burying the LRSM in the soil, its stability will be improved. In **Figure 12D**, due to the stable characteristics of the radial structure (Budiansky and Hutchinson, 1966), the vibration displacement of the Z component of line C is almost kept at around 2.7 mm, which is much smaller than that of the seismic metamaterial arranged based on Cartesian coordinates (Zeng et al., 2020), which is only 19.2% of its value, which indicates that the LRSM has better stability than the seismic metamaterial based on Cartesian coordinate arrangement (Miniaci et al., 2016).

Seismic Time History Analysis

To investigate the effect of the LRSM system on the surface wave amplitude variation, a transient harmonic analysis was performed on a finite LRSM system with five periods. In this paper, the classical EI seismic wave signal (1940, El Centro Site, Vertical, Peak = 0.2468 g, Duration = 53.78 sec) and Taft seismic wave signal (Kishida et al., 2021) (1952, Taft Lincoln School, Peak = -0.1793 g, Duration = 54.40 s) are used respectively, as shown in **Figures 13A,C**, the acceleration spectrum of the seismic wave signal intercepts its first 30 s data, this range already contains the most intense part and main energy of the seismic record. Among them, the main frequency range of the seismic wave are concentrated in the frequency range of 0.1–10 Hz, as shown in **Figures 13B,D**. At line A, the Taft seismic wave excitation signal is input, and a transient explicit response with a duration of 35 s is performed to ensure that the seismic wave excitation signal emitted by line A can reach and pass through the LRSM. Apply low-reflection boundary conditions on the sides and bottom of the soil to simulate half-space and reduce reflections caused by the bottom and surrounding boundaries of the model.

Under the seismic wave excitation signal, the acceleration amplitude of the response signal at the axisymmetric center point with or without LRSM was recorded respectively (as shown in **Figure 14A**), in order to analyze the amplitude change of the surface wave in the region with or without LRSM. It can be observed from **Figure 14** that due to the existence of LRSM, the vibration of the surface wave is effectively suppressed, and its maximum amplitude can be attenuated by more than 85% (wherein, the blue solid line represents the seismic wave amplitude signal without LRSM, and the red dotted line represents the seismic wave amplitude signal with LRSM. seismic wave amplitude signal). Subsequently, the acquired signal is Fourier transformed and the frequency content is compared to evaluate the damping performance of the LRSM, as shown in **Figure 14B**. The results show that the LRSM effectively attenuates seismic waves in the 0.1–20 Hz range, providing a virtually undisturbed region.

Influence of Layered Radial Seismic Metamaterial Circumference Continuity

The LRSM-2 designed in this paper is a circular ring with a larger diameter, but it is still inconvenient to arrange in engineering. Therefore, this section studies the effect of the internal circular continuity of the LRSM on the attenuation of surface waves. In the LRSM structure shown in **Figure 11B**, a thin PML layer is added every 60° (angle $\theta = 1^\circ$), and by changing the scale factor s of the PML, the energy propagation in the LRSM is controlled, which can be equivalent to Change the LRSM inner circumference continuity. As shown in **Figure 15**, when the internal circumferential continuity of the structure is changed, the local resonance effect of the LRSM is strengthened, and with the continuous increase of the scale factor s , the ability of the LRSM to attenuate surface waves is gradually enhanced. This is because the single period of LRSM is transformed from a single local oscillator resonance to a coupling resonance of multiple local oscillators. This means that in the construction of LRSM, the implementation scheme of block splicing can be adopted, which reduces the engineering difficulty and cost, and has better shielding characteristics.

CONCLUSION

In this paper, a novel layered radial seismic metamaterial is proposed to block the effects of seismic surface waves on protected building areas. Using the finite element method, the dispersion curves of LRSMs with different layers in half space as seismic barriers are studied. Through the calculation of the displacement vector field, the ultra-low frequency broadband mechanism of the LRSM is discussed, and the influence of the geometric parameters and the circumferential continuity of the LRSM on the bandgap characteristics is discussed. Finally, dispersion analysis and full-scale 3D transient wave propagation simulations are performed in a finite-period system to evaluate its damping performance.

The results show that the LRSM has ultra-low frequency broadband characteristics and can effectively attenuate seismic surface waves in the range of 0.1–20 Hz, and the maximum amplitude attenuation exceeds 85%. For LRSM, the increase of the number of layers will generate new band gaps, but the initial frequency and total bandwidth do not show monotonic changes like traditional seismic metamaterials, but show optimal band gap characteristics when the structure is LRSM-2 (The band gap relative bandwidth NRBW can exceed 80%). Compared with traditional seismic metamaterials, LRSMs have only a single axial resonance, which is caused by the circumferential stability of LRSMs. Further, by observing the dispersion curve of the LRSM, when the number of layers of the steel ring increases, new flat bands will appear. The stiffness will affect the local resonance strength. By analyzing the vibration displacement of LRSM in the circumferential and axial directions, it is shown that the energy dissipation of RSM is mainly concentrated in the circumferential direction, and the distribution is different; the vibration displacement value along the axial direction is only 2.7 mm, which is much lower than that of traditional seismic metamaterials. It is shown that LRSM has better stability in resisting seismic waves. The position and width of the band gap in the LRSM are very sensitive to the structure height, and the increase of the LRSM height can move the first band gap to the low frequency, and the total bandwidth increases, mainly due to the increase of the system equivalent mass M_e with the increase of the height h . With the decrease of the circumferential continuity of the LRSM, the LRSM gradually transforms from the overall ring oscillator resonance to the coupling of multiple sector

oscillator resonances, and the ability to attenuate surface waves is continuously enhanced. This paper demonstrates the feasibility of radial periodic structures as seismic wave shielding. The proposed radial metamaterials provide new design guidelines for solving engineering problems such as vibration and noise in half space.

DATA AVAILABILITY STATEMENT

The datasets presented in this study can be found in online repositories. The names of the repository/repositories and accession number(s) can be found in the article/Supplementary Material.

AUTHOR CONTRIBUTIONS

The contribution of HL is analysing the model. The contribution of LL, QJ, PL, and XZ is data processing.

FUNDING

The Natural Science Foundation of China Shaanxi Province under Grant No. 15JK1405, National Natural Science Foundation of China under Grant No. 51405368 and Natural Science Foundation of China Shaanxi Province under Grant No. 2017JM5024 have supported this research.

REFERENCES

- Achaoui, Y., Antonakakis, T., Brûlé, S., Craster, R. V., Enoch, S., and Guenneau, S. (2017). Clamped Seismic Metamaterials: Ultra-low Frequency Stop Bands. *New J. Phys.* 19 (6), 063022. doi:10.1088/1367-2630/aa6e21
- Achaoui, Y., Ungureanu, B., Enoch, S., Brûlé, S., and Guenneau, S. (2016). Seismic Waves Damping with Arrays of Inertial Resonators. *Extreme Mech. Lett.* 8, 30–37. doi:10.1016/j.eml.2016.02.004
- An, S., Shu, H., Liang, S., Shi, X., and Zhao, L. (2018). Band gap Characteristics of Radial Wave in a Two-Dimensional Cylindrical Shell with Radial and Circumferential Periodicities. *AIP Adv.* 8 (3), 035110. doi:10.1063/1.5023734
- Brûlé, S., Javelaud, E. H., Enoch, S., and Guenneau, S. (2014). Experiments on Seismic Metamaterials: Molding Surface Waves. *Phys. Rev. Lett.* 112 (13), 133901. doi:10.1103/PhysRevLett.112.133901
- Budiansky, B., and Hutchinson, J. W. (1966). A Survey of Some Buckling Problems. *AIAA J.* 4 (9), 1505–1510. doi:10.2514/3.3727
- Carbonell, J., Torrent, D., Díaz-Rubio, A., and Sánchez-Dehesa, J. (2011). Multidisciplinary Approach to Cylindrical Anisotropic Metamaterials. *New J. Phys.* 13 (10), 103034. doi:10.1088/1367-2630/13/10/103034
- Chen, Y., and Wang, L. (2014). Isolation of Surface Wave-Induced Vibration Using Periodically Modulated Piles. *Int. J. Appl. Mech.* 06 (04), 1450042. doi:10.1142/s1758825114500422
- Colombi, A., Roux, P., Guenneau, S., Gueguen, P., and Craster, R. V. (2016). Forests as a Natural Seismic Metamaterial: Rayleigh Wave Bandgaps Induced by Local Resonances. *Sci. Rep.* 6 (1), 19238. doi:10.1038/srep19238
- Dobrin, M. B., and Savit, C. H. (1960). *Introduction to Geophysical Prospecting*. New York: McGraw-Hill.
- Du, Q., Zeng, Y., Huang, G., and Yang, H. (2017). Elastic Metamaterial-Based Seismic Shield for Both Lamb and Surface Waves. *AIP Adv.* 7 (7), 075015. doi:10.1063/1.4996716
- Du, Q., Zeng, Y., Xu, Y., Yang, H., and Zeng, Z. (2018). H-fractal Seismic Metamaterial with Broadband Low-Frequency Bandgaps. *J. Phys. D: Appl. Phys.* 51 (10), 105104. doi:10.1088/1361-6463/aaaac0
- Elford, D. P., Chalmers, L., Kusmartsev, F. V., and Swallowe, G. M. (2011). Matryoshka Locally Resonant Sonic crystal. *The J. Acoust. Soc. America* 130 (5), 2746–2755. doi:10.1121/1.3643818
- Gao, N., Hou, H., Wu, J. H., and Cheng, B. (2016a). Low Frequency Band Gaps below 10 Hz in Radial Flexible Elastic Metamaterial Plate. *J. Phys. D: Appl. Phys.* 49 (43), 435501. doi:10.1088/0022-3727/49/43/435501
- Gao, N., Hou, H., and Xin, H. (2017). A Single and Double Slotting Radial Acoustic Metamaterial Plate. *Mod. Phys. Lett. B* 31 (12), 1750128. doi:10.1142/s0217984917501287
- Gao, N., Wu, J. H., Yu, L., and Xin, H. (2016b). Design of Radial Phononic crystal Using Annular Soft Material with Low-Frequency Resonant Elastic Structures. *Phys. Lett. A* 380 (41), 3326–3332. doi:10.1016/j.physleta.2016.08.010
- Jiang, T., and He, Q. (2017). Dual-directionally Tunable Metamaterial for Low-Frequency Vibration Isolation. *Appl. Phys. Lett.* 110 (2), 021907. doi:10.1063/1.4974034
- Kim, S.-H., and Das, M. P. (2012). Seismic Waveguide of Metamaterials. *Mod. Phys. Lett. B* 26 (17), 1250105. doi:10.1142/s0217984912501059
- Kishida, T., Contreras, V., Bozorgnia, Y., Abrahamson, N. A., Ahdi, S. K., Ancheta, T. D., et al. (2021). *NGA-sub Ground Motion Database*. Abu Dhabi, United Arab Emirates: UCLA. Retrieved from <https://escholarship.org/uc/item/3bn528xc>.
- Krödel, S., Thomé, N., and Daraio, C. (2015). Wide Band-gap Seismic Metastructures. *Extreme Mech. Lett.* 4, 111–117. doi:10.1016/j.eml.2015.05.004
- Li, J., and Chan, C. T. (2004). Double-negative Acoustic Metamaterial. *Phys. Rev. E Stat. Nonlin Soft Matter Phys.* 70 (5), 055602. doi:10.1103/PhysRevE.70.055602

- Li, Y., Chen, T., Wang, X., Yu, K., and Chen, W. (2014). Propagation of Lamb Waves in One-Dimensional Radial Phononic crystal Plates with Periodic Corrugations. *J. Appl. Phys.* 115 (5), 054907. doi:10.1063/1.4864425
- Lim, C., and Reddy, J. (2019). Built-up Structural Steel Sections as Seismic Metamaterials for Surface Wave Attenuation with Low Frequency Wide Bandgap in Layered Soil Medium. *Eng. Structures* 188, 440–451. doi:10.1016/j.engstruct.2019.03.046
- Liu, Z., Qin, K.-Q., and Yu, G.-L. (2020). Partially Embedded Gradient Metabarrier: Broadband Shielding from Seismic Rayleigh Waves at Ultralow Frequencies. *J. Eng. Mech.* 146 (5), 04020032. doi:10.1061/(asce)em.1943-7889.0001752
- Ma, T., Chen, T., Wang, X., Li, Y., and Wang, P. (2014). Band Structures of Bilayer Radial Phononic crystal Plate with crystal Gliding. *J. Appl. Phys.* 116 (10), 104505. doi:10.1063/1.4895138
- Miniaci, M., Krushynska, A., Bosia, F., and Pugno, N. M. (2016). Large Scale Mechanical Metamaterials as Seismic Shields. *New J. Phys.* 18 (8), 083041. doi:10.1088/1367-2630/18/8/083041
- Neto, A. G., e Silva, J. C., de Carvalho, J. N., do Nascimento Cruz, J., and Ferreira, H. P. A. (2015). “Analysis of the Resonant Behavior of FSS Using Matryoshka Geometry,” in 2015 SBMO/IEEE MTT-S International Microwave and Optoelectronics Conference (IMOC) (João Pessoa, Brazil: IEEE), 1–5.
- Norris, R. C., Hamel, J. S., and Nadeau, P. (2008). Phononic Band gap Crystals with Periodic Fractal Inclusions: Theoretical Study Using Numerical Analysis. *J. Appl. Phys.* 103 (10), 104908. doi:10.1063/1.2931955
- Palermo, A., Krödel, S., Marzani, A., and Daraio, C. (2016). Engineered Metabarrier as Shield from Seismic Surface Waves. *Sci. Rep.* 6 (1), 39356. doi:10.1038/srep39356
- Pennec, Y., Vasseur, J. O., Djafari-Rouhani, B., Dobrzyński, L., and Deymier, P. A. (2010). Two-dimensional Phononic Crystals: Examples and Applications. *Surf. Sci. Rep.* 65 (8), 229–291. doi:10.1016/j.surfrep.2010.08.002
- Reitherman, R. K. (2012). *Earthquakes and Engineers: An International History*. Reston, VA: American Society of Civil Engineers.
- Shi, X., Shu, H., Zhu, J., Wang, X., Dong, L., Zhao, L., et al. (2016). Research on Wave Bandgaps in a Circular Plate of Radial Phononic crystal. *Int. J. Mod. Phys. B* 30 (23), 1650162. doi:10.1142/s0217979216501629
- Shu, H.-S., Wang, X.-G., Liu, R., Li, X.-G., Shi, X.-N., Liang, S.-J., et al. (2015). Bandgap Analysis of Cylindrical Shells of Generalized Phononic Crystals by Transfer Matrix Method. *Int. J. Mod. Phys. B* 29 (24), 1550176. doi:10.1142/s0217979215501763
- Telford, W. M., Telford, W., Geldart, L., Sheriff, R. E., and Sheriff, R. E. (1990). *Applied Geophysics*. Cambridge, United Kingdom: Cambridge University Press.
- Torrent, D., and Sánchez-Dehesa, J. (2009). Radial Wave Crystals: Radially Periodic Structures from Anisotropic Metamaterials for Engineering Acoustic or Electromagnetic Waves. *Phys. Rev. Lett.* 103 (6), 064301. doi:10.1103/PhysRevLett.103.064301
- Torrent, D., and Sánchez-Dehesa, J. (2010a). Acoustic Resonances in Two-Dimensional Radial Sonic crystal Shells. *New J. Phys.* 12 (7), 073034. doi:10.1088/1367-2630/12/7/073034
- Torrent, D., and Sánchez-Dehesa, J. (2010b). Anisotropic Mass Density by Radially Periodic Fluid Structures. *Phys. Rev. Lett.* 105 (17), 174301. doi:10.1103/physrevlett.105.174301
- Ungureanu, B., Achaoui, Y., Enoch, S., Brûlé, S., and Guenneau, S. (2015). Auxetic-like Metamaterials as Novel Earthquake Protections. *arXiv* 2, 17–30. preprint arXiv:1510.08785. doi:10.1051/epjam/2016001
- Wang, L., Xia, D., Fu, Q., Ding, X., and Wang, Y. (2021). A Switchable Ultra-wideband Metamaterial Absorber with Polarization-Insensitivity and Wide-Incident Angle at THz Band. *Front. Mater.* 8, 296. doi:10.3389/fmats.2021.729495
- Wang, Y.-F., Wang, Y.-S., and Laude, V. (2015). Wave Propagation in Two-Dimensional Viscoelastic Metamaterials. *Phys. Rev. B* 92 (10), 104110. doi:10.1103/physrevb.92.104110
- Wilson, G., Wilson, T. M., Deligne, N. I., and Cole, J. W. (2014). Volcanic hazard Impacts to Critical Infrastructure: A Review. *J. Volcanology Geothermal Res.* 286, 148–182. doi:10.1016/j.jvolgeores.2014.08.030
- Xu, Z., Wu, F., and Guo, Z. (2012). Low Frequency Phononic Band Structures in Two-Dimensional Arc-Shaped Phononic Crystals. *Phys. Lett. A* 376 (33), 2256–2263. doi:10.1016/j.physleta.2012.05.037
- Zeng, Y., Xu, Y., Deng, K., Peng, P., Yang, H., Muzamil, M., et al. (2019). A Broadband Seismic Metamaterial Plate with Simple Structure and Easy Realization. *J. Appl. Phys.* 125 (22), 224901. doi:10.1063/1.5080693
- Zeng, Y., Xu, Y., Deng, K., Zeng, Z., Yang, H., Muzamil, M., et al. (2018). Low-frequency Broadband Seismic Metamaterial Using I-Shaped Pillars in a Half-Space. *J. Appl. Phys.* 123 (21), 214901. doi:10.1063/1.5021299
- Zeng, Y., Xu, Y., Yang, H., Muzamil, M., Xu, R., Deng, K., et al. (2020). A Matryoshka-like Seismic Metamaterial with Wide Band-gap Characteristics. *Int. J. Sol. Structures* 185–186, 334–341. doi:10.1016/j.ijsolstr.2019.08.032

Conflict of Interest: The authors declare that the research was conducted in the absence of any commercial or financial relationships that could be construed as a potential conflict of interest.

Publisher's Note: All claims expressed in this article are solely those of the authors and do not necessarily represent those of their affiliated organizations, or those of the publisher, the editors and the reviewers. Any product that may be evaluated in this article, or claim that may be made by its manufacturer, is not guaranteed or endorsed by the publisher.

Copyright © 2022 Liu, Li, Jia, Jiang, Li and Zhang. This is an open-access article distributed under the terms of the Creative Commons Attribution License (CC BY). The use, distribution or reproduction in other forums is permitted, provided the original author(s) and the copyright owner(s) are credited and that the original publication in this journal is cited, in accordance with accepted academic practice. No use, distribution or reproduction is permitted which does not comply with these terms.



Acoustic Hologram Reconstruction With Unsupervised Neural Network

Boyi Li^{1†}, Mengyang Lu^{2†}, Chengcheng Liu¹, Xin Liu^{1,3*} and Dean Ta^{1,4}

¹Academy for Engineering and Technology, Fudan University, Shanghai, China, ²School of Communication and Information Engineering, Shanghai University, Shanghai, China, ³State Key Laboratory of Medical Neurobiology, Fudan University, Shanghai, China, ⁴Center for Biomedical Engineering, Fudan University, Shanghai, China

OPEN ACCESS

Edited by:

Han Jia,
Institute of Acoustics (CAS), China

Reviewed by:

Yifan Zhu,
Southeast University, China
Xuecong Sun,
Key Laboratory of Noise and Vibration
Research, Institute of Acoustics,
Chinese Academy of Sciences, Beijing

*Correspondence:

Xin Liu
xinliu.c@gmail.com

[†]These authors have contributed
equally to this paper

Specialty section:

This article was submitted to
Metamaterials,
a section of the journal
Frontiers in Materials

Received: 09 April 2022

Accepted: 28 April 2022

Published: 02 June 2022

Citation:

Li B, Lu M, Liu C, Liu X and Ta D (2022)
Acoustic Hologram Reconstruction
With Unsupervised Neural Network.
Front. Mater. 9:916527.
doi: 10.3389/fmats.2022.916527

An acoustic hologram is crucial in various acoustics applications. The reconstruction accuracy of the acoustic field from the hologram is important for determining the performance of the acoustic hologram system. However, challenges remain in acoustic hologram reconstruction where the conventional reconstruction methods generally lack accuracy, complexity, and flexibility. Although the deep learning (DL)-based method has been used to overcome these limitations, it needs the labeled training data to optimize the network with a supervised strategy. To address the problem, we put forward a new unsupervised DL-based reconstruction method in this work, termed PhysNet-AH, which is implemented by integrating a convolutional neural network with a physical model representing the process of acoustics hologram formation. The results demonstrate that we only need to provide PhysNet-AH with a single acoustic field recorded from the hologram, the network parameters can be optimized automatically without the labeled training data, and finally implement the acoustic hologram reconstruction with high accuracy, in terms of SSIM and mean squared error indicators. Furthermore, with the trained model, the robustness and generalization capability of PhysNet-AH have also been well-demonstrated by reconstructing the acoustic fields from different diffraction distances or different datasets. As a result, PhysNet-AH opens the door for fast, accurate, and flexible acoustic hologram-based applications.

Keywords: acoustic hologram, acoustic field reconstruction, unsupervised learning, physical model network, wave propagation

1 INTRODUCTION

Recently, the acoustic hologram has gained extensive attention in acoustics applications, for example, biomedicine (Sapozhnikov et al., 2015; Jiménez-Gambín et al., 2019; Baudoin et al., 2020; Ma et al., 2020), particle manipulation (Melde et al., 2016; Baudoin et al., 2019; Baresch and Garbin 2020), 3-D display (Kruizinga et al., 2017; Fushimi et al., 2019), acoustic metasurface/metamaterial (Fan et al., 2020; Zhu et al., 2021), etc. Briefly, the acoustic hologram is a technique that allows recording and reconstructing information of the desired acoustic field. The accurate reconstruction of the hologram is important for an acoustic hologram system. Currently, various methods have been proposed for acoustic hologram reconstruction. However, these methods generally have some limitations in computation complexity, reconstruction accuracy, flexibility of implementation (Marzo et al., 2015; Sapozhnikov et al., 2015; Melde et al., 2016; Marjan et al., 2018; Michael 2019; Fushimi et al., 2021), etc.

Currently, deep learning (DL) has been successfully used to solve inverse problems in imaging fields, for example, scattered image recovery (Sinha et al., 2017; Li et al., 2018; Yang et al., 2019), phase imaging

(Rivenson et al., 2018), and digital hologram reconstruction (Wang et al., 2018; Wu et al., 2018; Ren et al., 2019; Francesc et al., 2020; Yin et al., 2020). Especially, a DL method based on U-Net has been introduced to generate a hologram for the desired acoustic field, as demonstrated by Lin et al., (2021). Nevertheless, it is noteworthy that the DL method requires large paired data (the raw data and the labeled data) for training a good network. However, in many conditions, it is hard or impossible to acquire enough labeled data. In addition, the computational cost for the network training is generally high because of the amount of the used training data. These factors limit the practicability and flexibility of the DL-based method in acoustic holograms.

To overcome the limitations, here, we put forward a new DL-based method to reconstruct acoustic holograms with an unsupervised strategy, termed PhysNet-AH, which is achieved by combining a convolutional neural network (CNN) with a physical model representing the process of acoustic hologram formation. The main superiority of the PhysNet-AH method is that it can be achieved without the need for a training label. That is, we only need to input a single acoustic field intensity from the hologram into the PhysNet-AH model, and the network parameters will be automatically optimized and eventually implement acoustic hologram reconstructions with high accuracy. As a result, we can eliminate the need for a great quantity of the labeled data in the training stage of the network. To our knowledge, similar methods have not yet been reported previously in the acoustic hologram field.

Briefly, this method uses an end-to-end network combining the CNN and Transformer (Khan et al., 2021; Liu et al., 2021) to learn the local and the global features of the acoustic hologram. Together, referring to the study by Wang F et al., (2020), a physical model is constructed and used during network training. Here, the physical model enables the calculation of the diffracted acoustic field from the network output by the angular spectrum approach, which is sequentially utilized to calculate loss with input data for optimizing the network parameters. In this work, PhysNet-AH is evaluated with a series of acoustic structures, such as digits, letters, and some symbols, acquired from different public datasets (MNIST and Chars74K). The results confirm that even though only a single unlabeled data source is utilized to train the model, PhysNet-AH makes the possibility of reconstructing the diffracted fields from the holographic structure with high accuracy, robustness, and generalization.

The organization of the rest of this study is as follows. In **Section 2**, the unsupervised DL method containing network framework, loss function, optimization strategy and angular spectral approach is introduced. **Section 3** verifies the effectiveness of the method for acoustic holographic reconstruction in different conditions and analyzes the results. Finally, in **Section 4**, the relevant results are discussed and summarized.

2 METHODS

The framework of the proposed unsupervised PhysNet-AH method is shown in **Figure 1**. Briefly, when using the proposed method, we only need to provide PhysNet-AH a single acoustic field intensity $\varphi(x, y; z = d)$ from the hologram, which is a

diffracted pattern of a target object $\mathfrak{N}(x, y; z = 0)$, with a holographic recording distance $z = d$. The network parameters can be automatically optimized, and finally the acoustic hologram reconstruction can be implemented. Especially, when training the network, the proposed PhysNet-AH method does not require the ground truth $\mathfrak{N}(x, y; z = 0)$. Instead, a physical model H is constructed and then used to calculate the acoustic field intensity $\tilde{\varphi}(x, y; z = d)$ from $\tilde{\mathfrak{N}}(x, y; z = 0)$ by the angular spectrum approach. Sequentially, the error between the calculated $\tilde{\varphi}(x, y; z = d)$ and the measured $\varphi(x, y; z = d)$ is calculated to update the network parameters. Comparably, in the conventional DL-based methods, the ground truth $\mathfrak{N}(x, y; z = 0)$ must be known and the network is optimized by calculating the error between $\mathfrak{N}(x, y; z = 0)$ and $\tilde{\mathfrak{N}}(x, y; z = 0)$. The angular spectral approach used for data generation and physical model is detailed in **Section 2.1**. The proposed unsupervised neural network method integrated with the physical mode is described in **Section 2.2**.

2.1 Data Generation Based on the Angular Spectral Approach

In this work, we adopt the angular spectral approach (ASA) to synthesize the training and testing dataset. The ASA is an effective method to calculate the diffraction propagation of waves, which can calculate the acoustics fields parallel to the initial plane from a holographic recording by spreading each spatial frequency component of the diffraction wave (Zeng and McGough 2008; Zeng and McGough 2009). In detail, the acoustics field in an initial plane is defined as the input of the angular spectrum approach, and the output from the angular spectrum approach is the acoustics fields at the hologram recording distance of d . The spatial frequency domain propagation of acoustic waves in a linear homogeneous medium is described as follows:

$$P(k_x, k_y, z) = P_0(k_x, k_y, 0)e^{jz\sqrt{k^2 - k_x^2 - k_y^2}}, \quad (1)$$

where k_x and k_y represent the discretized transverse wavenumbers and $k_x^2 + k_y^2 + k_z^2 = k^2$. Here, $k = \omega/c$, ω denotes the angular frequency, and c denotes the sound speed in the medium. z is the diffraction distance, that is, the hologram recording distance from the initial plane. $P_0(k_x, k_y, 0)$ represents the angular spectrum of the input acoustics field $p_0(x, y, 0)$ at the initial plane, which is the 2-D Fourier transform of the field with regard to x and y . $P(k_x, k_y, z)$ is the angular spectrum of the acoustics field in z plane parallel to the initial plane.

The acoustics field in each subsequent plane is then obtained by applying a 2-D inverse Fourier transform to $P(k_x, k_y, z)$, with respect to k_x and k_y , as follows:

$$p(x, y, z) = \frac{1}{4\pi^2} \iint P(k_x, k_y, z) dk_x dk_y. \quad (2)$$

The resulting intensity map $\varphi = \|p(x, y, z)\|^2$ is utilized as the diffraction data to train the network.

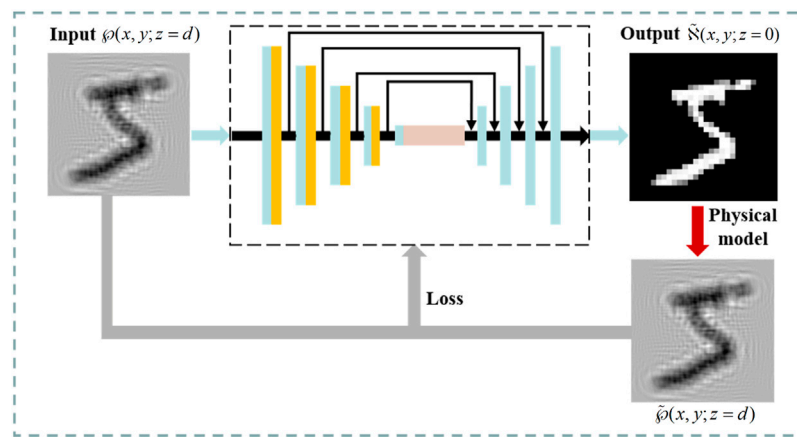


FIGURE 1 | Flowchart of the PhysNet-AH method for acoustic hologram reconstruction. Measured acoustic field intensity $\varphi(x, y; z = d)$ from the hologram at the distance of d is the input of the network. The output of the network is the estimated target object $\hat{\mathbf{N}}(x, y; z = 0)$, which is then numerically propagated by physical model H to synthesize the acoustic field intensity $\hat{\varphi}(x, y; z = d)$. The mean square error, l_1 loss, and structure similar loss between $\varphi(x, y; z = d)$ and $\hat{\varphi}(x, y; z = d)$ are calculated as the loss to optimize the model.

2.2 Network Architecture

To implement the unsupervised learning strategy, in this work, PhysNet-AH is constructed by integrating a neural network with a physical model. Considering that U-Net is an effective end-to-end convolutional neural network used for solving various image tasks, here, U-Net is used as the main structure of the network, as shown in the black dotted rectangle of **Figure 1**. In detail, the network consists of four downsampling blocks, three multiple sequence alignment (MSA) Transformers (Rao et al., 2021), and four upsampling blocks. Also, the skipped connections are applied between every two blocks between downsampling and upsampling layers to achieve residual learning. The input to the network is a measured diffracted acoustic field intensity from the holographic recording at the distance of d , and the corresponding output is the estimate of the acoustics target object at the initial plane. Sequentially, the output is numerically propagated by the physical model to synthesize the acoustic field intensity at the distance of d , which is further used to calculate the loss for optimizing the network parameters during training. Details about the network are described as follows:

First, two 3×3 convolution layers, each followed by batch normalization (BN) and a ReLU, are adopted to extract the shallow feature maps of the input. In each downsampling block, a 2×2 maximum pooling with a stride of 2, two 3×3 convolution layers followed by BN and ReLU, and a Channel Attention (CA) layer are stacked sequentially to encode the shallow features into the more abstract and meaningful features. Then, three MSA Transformers are used as the bottleneck to enrich the extracted features and achieve the global information feature extraction. After encoding, four upsampling blocks, where each block contains a transposed convolution and two convolution layers with BN and ReLU, are utilized to enlarge the feature size and decode the abstract feature to the output. Furthermore, skip connections are adopted between the features of the same size (see the black arrows in

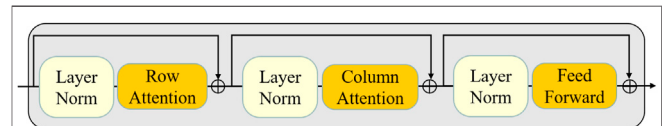


FIGURE 2 | Architecture of the MSA Transformer block. Here, the residual connection is used between the adjacent sub-modules. The first sub-module is used to achieve a single attention map of all rows by using an axial attention layer. The second sub-module is used to extract the feature for columns of input feature maps by using a multihead self-attention layer. The last sub-module is implemented by using a multilayer perceptron layer.

Figure 1). Here, the feature of the downsampling blocks and the corresponding upsampling feature are concatenated by these skip connections to achieve feature reuse.

A transformer based on the self-attention mechanism is recently proposed, which is capable of learning and extracting information among any position of data. Inspired by the global information extraction of the transformer, researchers gradually apply it to computer vision tasks and have achieved remarkable performance (Ho et al., 2019; Wang H et al., 2020; Khan et al., 2021; Liu et al., 2021; Rao et al., 2021). So, in this work, the MSA Transformer block is utilized at the bottleneck of the network. The MSA Transformer block considers the features obtained by downsampling blocks as aligned sequences, where rows of features correspond to sequences and columns are positioned in the aligned sequences. For the core of this block, the axial attention and multi-head self-attention are adopted for row attention implementation and column attention implementation, respectively, which have high computational efficiency and enable the model to capture the full feature map context (Ho et al., 2019; Wang H et al., 2020; Rao et al., 2021). The structure of this block is demonstrated in **Figure 2**.

The design of the loss function is extremely important in the unsupervised method. To more effectively update network parameters (weights and bias), here, the loss function is

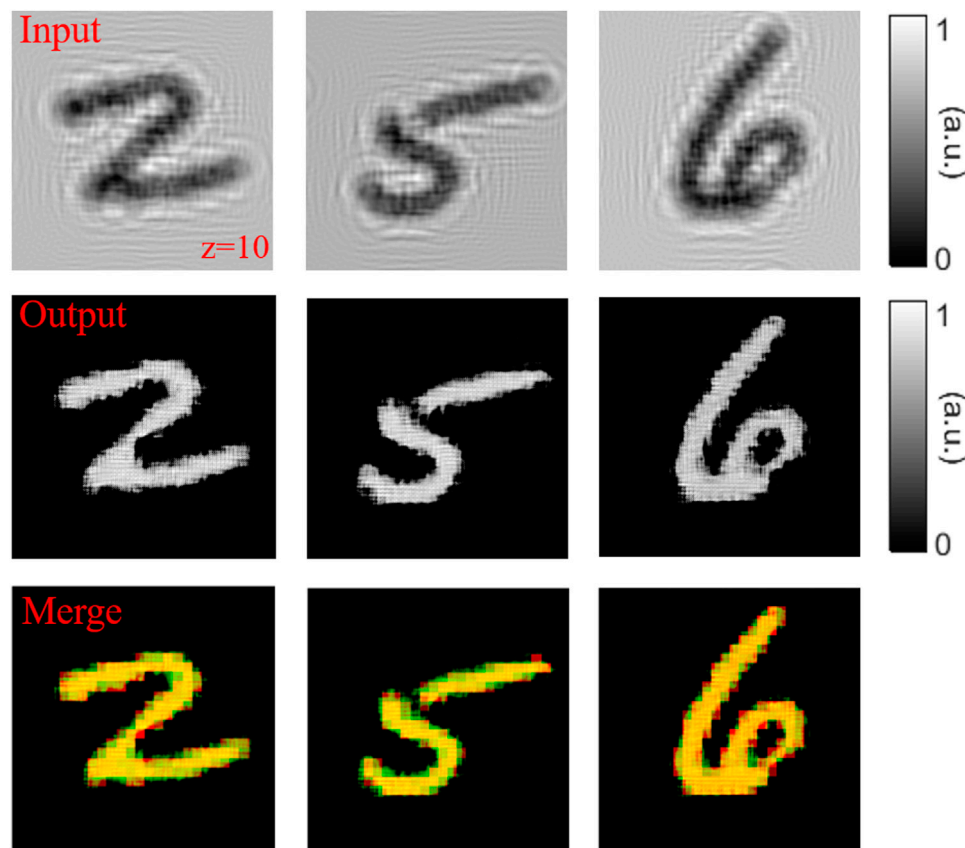


FIGURE 3 | Acoustic hologram reconstruction results of different acoustic targets are utilized to evaluate the feasibility of the PhysNet-AH. The first row shows the diffraction-limited acoustic field intensity from the holograms for digits 2, 5, and 6 at $z = 10$ mm, which are used as the input of the network. The second row shows the holographic reconstruction of the abovementioned acoustics fields, which are obtained by PhysNet-AH. The last row shows the merged images of the target digits (ground truth) and the corresponding reconstructed images. Red displays the ground truth, green corresponds to the reconstructed results of PhysNet-AH, and yellow represents their overlaps.

calculated by combining mean squared error loss, l_1 loss, and structural similarity (SSIM) loss (Wang et al., 2004). The formula is described as follows:

$$\ell(\varphi, \tilde{\varphi}) = \|\varphi - \tilde{\varphi}\|_2^2 + \lambda_1 \|\tilde{\varphi}\|_1 + \lambda_2 (1 - \text{SSIM}(\varphi, \tilde{\varphi})), \quad (3)$$

where φ is the input of the network, $\tilde{\varphi}$ denotes the diffracted acoustic field calculated by propagating the network output with physical model H , and λ_1 and λ_2 denote the weight coefficients. Here, referring to the study by Zhao et al., (2017), $\lambda_1 = 0.2$ and $\lambda_2 = 0.8$.

During the training process, Adam optimization is adopted, and the maximum training epoch is 500. The decay strategy is used for the learning rate in order to ensure that the training quickly and stably converges. In detail, the attenuation is set to 0.5 for every 200 epochs, with the initial learning of 0.001. The proposed unsupervised PhysNet-AH method is implemented by Pytorch, and the training process is executed on equipment with a 16-GB NVidia Tesla V100 GPU, 2 Intel Xeon Gold 6130, and 192 G DDR4 REG ECC. In this work, the computational time for the training procedure is about 10 min.

3 EXPERIMENTS AND RESULTS

In this work, the numerical simulation of the acoustic hologram is realized by the angular spectrum approach. In detail, the target image with the size of 256×256 pixels is placed in the x - y plane at $z = 0$ mm (the initial plane) and is then illuminated by a plane wave. Here, the excitation frequency is set as 2 MHz, the sound speed is set as 1,500 m/s, and the wavelength is $750 \mu\text{m}$. The diffracted pattern is recorded at $z = 10$ mm (13.33λ), 20 mm (26.67λ) and 30 mm (39.99λ) from the initial plane. The size of the recorded acoustics field from the hologram is set as $38.4 \times 38.4 \text{ mm}^2$ ($51.2\lambda \times 51.2\lambda$), with a resolution of 256×256 pixels. Here, the acoustics target images are acquired from the Modified National Institute of Standards and Technology (MNIST) database including the handwritten digits and the letters (Deng 2012) and the Chars74K database containing the symbols used in both English and Kannada (Campos et al., 2009). These data are sequentially used to generate the training and testing data by the ASA method.

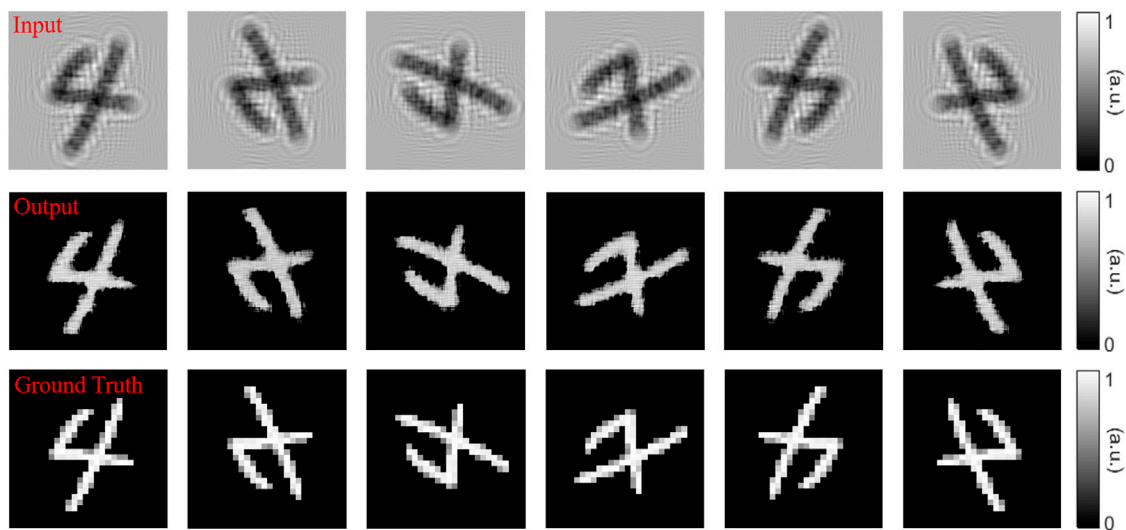


FIGURE 4 | Acoustic hologram reconstructed results for the rotated target images of digit 4 which are used to evaluate the robustness of PhysNet-AH. The first row shows the diffracted acoustic field intensity from the hologram of the rotated images of 4 at $z = 10$ mm. The second row shows the corresponding reconstruction results. The last row shows the target images (ground truth).

3.1 Evaluating the Feasibility of PhysNet-AH in Acoustic Hologram Reconstruction

First, we verify the feasibility of PhysNet-AH in implementing acoustic hologram reconstruction, which is demonstrated by using unseen target images randomly selected from the test dataset. **Figure 3** shows the corresponding reconstruction results. The 1st row of **Figure 3** shows the diffraction-limited acoustic field intensity from the holograms for different target digits (2, 5, and 6) at the distance ($z = 10$ mm), which are utilized as the input of the network. The 2nd row of **Figure 3** shows the holographic reconstruction of the abovementioned acoustics fields, which are acquired by the proposed PhysNet-AH method. The last row of **Figure 3** describes the merged images of the target digits (ground truth) and the reconstructed images. Here, the true digits are represented in red, and the reconstructed images are shown in green. Correspondingly, the overlapping parts of the two images are shown in yellow.

The results demonstrate that there is a high overlap (see the yellow color in the last row of **Figure 3**) between the ground truth and the result reconstructed by PhysNet-AH, indicating that high reconstruction accuracy can be acquired by the proposed method. Furthermore, to quantitatively evaluate the acoustics field reconstruction quality of PhysNet-AH, two quantitative indicators, that is, mean squared error (MSE) and structural similarity index (SSIM) are calculated. In this case, the normalized MSEs between the reconstruction images and the true target images (ground truth) of the digits 2, 5, and 6 are 0.013, 0.013, and 0.019, respectively. The corresponding SSIMs of digits 2, 5, and 6 are all above 0.8. These quantitative results further confirm that the proposed unsupervised PhysNet-AH method enables effectively implementing holographic

reconstruction by the network model trained only with a single unlabeled sample.

3.2 Evaluating the Robustness of PhysNet-AH in Acoustic Hologram Reconstruction

To evaluate the robustness of the PhysNet-AH in acoustic hologram reconstruction, the rotated acoustic fields are incorporated into the trained model and the corresponding results are shown in **Figure 4**. The 1st row of **Figure 4** depicts the diffracted acoustic field from the hologram of the rotated digit 4 at $z = 10$ mm. The 2nd row of **Figure 4** depicts the corresponding reconstruction results from the abovementioned diffracted acoustic fields. The true target images are described in the 3rd row of **Figure 4**.

The results show that as expected, PhysNet-AH can effectively reconstruct the diffracted acoustic field from the holographic structure, even if the test image is the transformation of the original target image. Furthermore, to quantitatively evaluate the robustness of the model, SSIM and MSE indicators are calculated for each case. Here, a high average SSIM of 0.83 with a standard deviation of 0.005 and a low average MSE of 0.015 with a standard deviation of 0.0007 are obtained, indicating that good stability and anti-disturbance capability can be obtained by PhysNet-AH.

Moreover, we also demonstrate the reconstruction capability of PhysNet-AH at different diffraction distances, which is used to further evaluate the robustness of PhysNet-AH. **Figure 5** depicts the corresponding reconstruction results. The 1st row of **Figure 5** depicts the diffracted acoustic fields from the holograms of digits 3 at different distances ($z = 10, 20$, and 30 mm). We can observe that the diffracted images have more self-interference-related

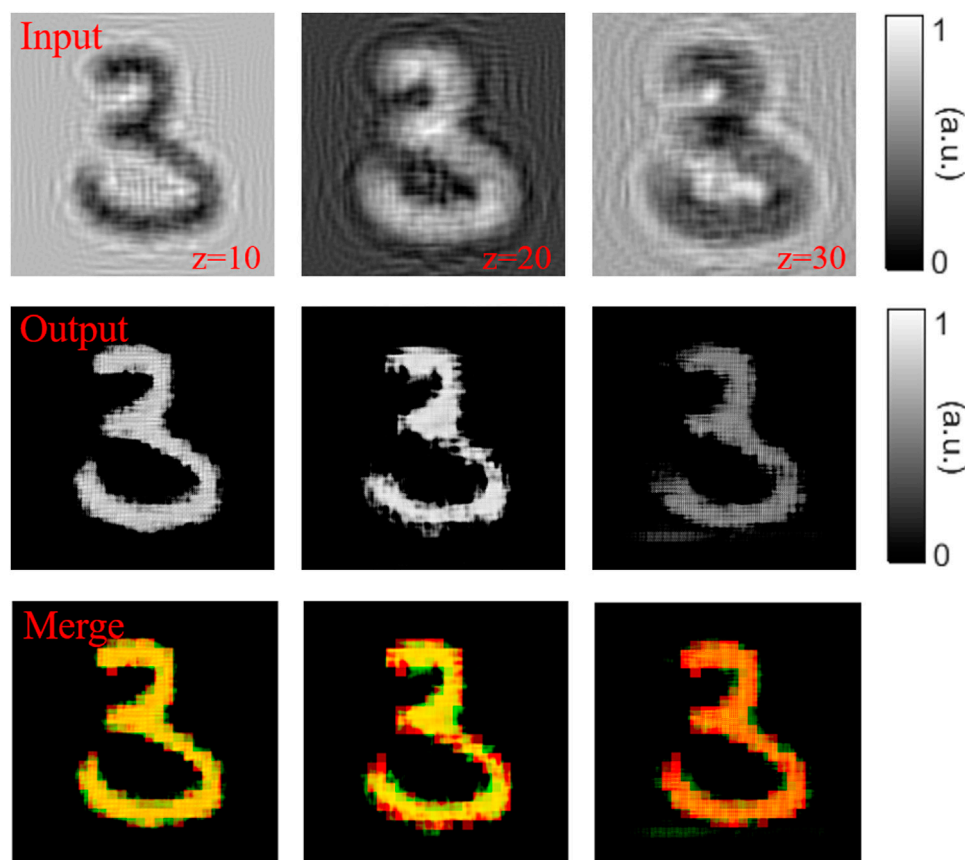


FIGURE 5 | Acoustic hologram reconstruction results of digit 3 at different holographic recording distances ($z = 10, 20$, and 30 mm) are used to evaluate the robustness of PhysNet-AH. The first row shows the diffracted acoustic field intensity from the holograms of digit 3 at $z = 10, 20$, and 30 mm. The second row shows the corresponding reconstruction results from the abovementioned acoustics fields. The last row shows the merged images of the target digits (ground truth) and the reconstructed images. Red represents the ground truth, green represents the reconstructed results of PhysNet-AH, and yellow represents their overlaps.

TABLE 1 | Quantitative results of acoustic hologram reconstruction at different diffraction distances ($z = 10$ mm, $z = 20$ mm, and $z = 30$ mm). For each distance, 100 independent trials are used and calculated.

Distance	SSIM	MSE
$Z = 10$ mm	0.84 ± 0.03	0.016 ± 0.006
$Z = 20$ mm	0.79 ± 0.02	0.031 ± 0.010
$Z = 30$ mm	0.76 ± 0.03	0.047 ± 0.018

spatial patterns with the increase in distance, which results in a blur and is hard to distinguish the true structure. The 2nd row of **Figure 5** depicts the reconstruction images obtained by PhysNet-AH. Comparably, the last row of **Figure 5** depicts the merged images with the true target digit and the reconstructed image, where red corresponds to the ground truth, green corresponds to the reconstructed results, and yellow represents their convergence.

The results show that even though only single unlabeled data is utilized to train the network model, and the proposed PhysNet-AH method can also effectively reconstruct the acoustic field at different diffraction distances. In addition, we also quantitatively

evaluate the reconstruction quality of PhysNet-AH at $z = 10$, $z = 20$, and $z = 30$ mm, in terms of SSIM and MSE indicators. **Table 1** summarizes the corresponding quantitative results calculated from 100 independent trials at each distance. These quantitative results further confirm the reconstruction robustness of PhysNet-AH. In addition, we can also observe that although PhysNet-AH can effectively implement acoustic hologram reconstruction for different diffraction distances, the reconstruction performance decreases slightly with the increase in the distance.

3.3 Evaluating the Generalization of PhysNet-AH in Acoustic Hologram Reconstruction

To further validate the generalization of PhysNet-AH, we test the trained model with the MNIST and the Chars74K datasets, which are different from the training data. The 1st row of **Figure 6** depicts the diffracted acoustic field intensities of different letters and symbols from different datasets. The 2nd row of **Figure 6** depicts the reconstructed acoustic field. Comparably, the last row of **Figure 6** depicts the ground truth in different datasets.

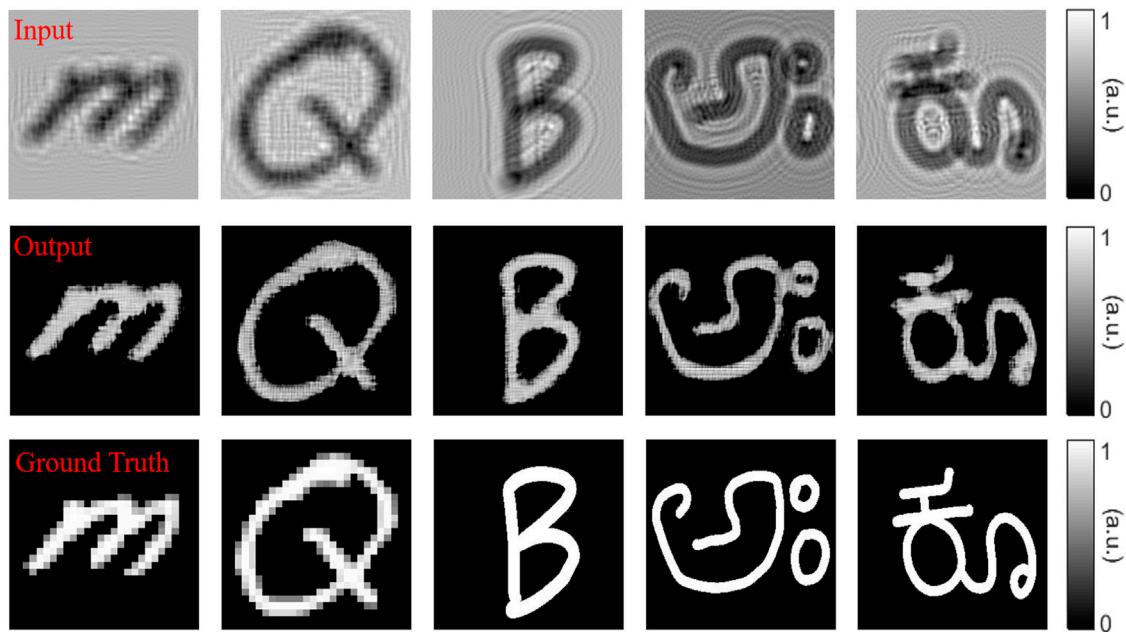


FIGURE 6 | Generalization evaluation of the proposed unsupervised PhysNet-AH method with different datasets. The first row shows the diffracted acoustic field intensities from different datasets at $z = 10$ mm. The second row shows the corresponding reconstruction results from the abovementioned acoustic fields. The last row shows the target images (ground truth) of the two English letters “m” and “Q” in the MNIST dataset, one English letter B, and two symbols of Kannada in the Chars74K dataset.

The results show that although the model is trained only with a single digit from the MNIST dataset, PhysNet-AH can also effectively reconstruct the acoustic fields from a different database, for example, the MNIST letters and the symbols used in both English and Kannada with an overall satisfactory reconstruction quality. However, there are still some divergences between the reconstruction results and ground truth, especially for the complex structure (see the 4th and 5th columns in **Figure 6**). The main reason maybe the lack of enough information for unseen data because the network model of PhysNet-AH is trained only by single unlabeled data without the training label.

4 DISCUSSION

Challenges remain in acoustic hologram reconstruction. The conventional reconstruction methods generally lack computation complexity, reconstruction accuracy, and flexibility of implementation. Although the DL-based method has been used to overcome these limitations, it needs large labeled data to optimize the network with a supervised strategy. This work puts forward a new unsupervised DL-based reconstruction method (PhysNet-AH), which is realized by integrating a convolutional neural network with a physical model. Different from the conventional DL-based methods, the proposed unsupervised method is trained to learn the underlying relations between the acoustic field domain and target domain only from a single unlabeled sample. Then, the trained model can be used to effectively reconstruct the acoustic field from the hologram without human intervention.

The results demonstrate that PhysNet-AH can effectively reconstruct the diffracted acoustics fields from a holographic recording, even though only single unlabeled data is adopted to train the network (see **Figures 3–6**). Furthermore, the diffracted acoustic field generated from different transformations/distances (see **Figure 4** and **Figure 5**) or the diffracted acoustic field generated from different datasets (see **Figure 6**) can also be effectively reconstructed by the trained model, indicating good robustness and generalization capability of PhysNet-AH in practical applications. Moreover, the quantitative results from SSIM and MSE indicators further confirm the reconstruction capability of PhysNet-AH, where a high SSIM and low MSE are obtained, respectively. Based on the previous results, we believe that the proposed PhysNet-AH method can effectively implement acoustic field reconstruction only using one sample without the need for the labeled data and make it possible to implement acoustic hologram reconstruction in an unsupervised way, without reducing the reconstruction performance, which greatly extends the practicability of PhysNet-AH in applications.

However, it should be noted that in this work, the reconstruction capability of PhysNet-AH is validated based on the simulated data. As a data-driven method, the performance of PhysNet-AH might have limitations in practical applications. In addition, in this work, U-Net is selected and used as the main framework of the network. Considering that the network architecture may affect the hologram reconstruction quality, the reconstruction accuracy may be further improved by using more effective networks. Furthermore, as a proof of concept, here, the angular spectral approach is used to construct the acoustic hologram physical model. For simplification, the

reconstruction results from the more complex physical model (e.g., including scattering, attenuation, etc.) are not demonstrated. Moreover, our current work mainly focuses on implementing single acoustics field reconstruction, and the reconstruction of multiple acoustics fields from one hologram has not been investigated. The systemic study will be performed in future work.

In conclusion, PhysNet-AH as an unsupervised learning method paves the way for implementing acoustic hologram reconstruction with high accuracy, robustness, and generalization, which extends the flexibility in various acoustic hologram-based applications.

DATA AVAILABILITY STATEMENT

The raw data supporting the conclusions of this article will be made available by the authors, without undue reservation.

REFERENCES

- Baresch, D., and Garbin, V. (2020). Acoustic Trapping of Microbubbles in Complex Environments and Controlled Payload Release. *Proc. Natl. Acad. Sci. U.S.A.* 117 (27), 15490–15496. doi:10.1073/pnas.2003569117
- Baudoin, M., Gerbedoen, J. C., Riaud, A., Matar, O. B., Smagin, N., and Thomas, J. L. (2019). Folding a Focalized Acoustical Vortex on a Flat Holographic Transducer: Miniaturized Selective Acoustical Tweezers. *Sci. Adv.* 5 (4), eaav1967–7. doi:10.1126/sciadv.aav1967
- Baudoin, M., Thomas, J. L., Sahely, R. A., Gerbedoen, J. C., Gong, Z., Sivory, A., et al. (2020). Spatially Selective Manipulation of Cells with Single-Beam Acoustical Tweezers. *Nat. Commun.* 11 (4244), 4244–4310. doi:10.1038/s41467-020-18000-y
- Campos, T., Babu, B. R., and Varma, M. (2009). “Character Recognition in Natural Images,” in Proceedings of the International Conference on Computer Vision Theory and Applications.
- Deng, L. (2012). The MNIST Database of Handwritten Digit Images for Machine Learning Research [Best of the Web]. *IEEE Signal Process. Mag.* 29 (6), 141–142. doi:10.1109/msp.2012.2211477
- Fan, S.-W., Zhu, Y., Cao, L., Wang, Y.-F., Li Chen, A., Merkel, A., et al. (2020). Broadband Tunable Lossy Metasurface with Independent Amplitude and Phase Modulations for Acoustic Holography. *Smart Mat. Struct.* 29 (10), 105038. doi:10.1088/1361-665x/abaa98
- Francesc, L., Pablo, M., Martin, B., and Sven, E. (2020). Sound Field Reconstruction in Rooms: Inpainting Meets Super-resolution. *J. Acoust. Soc. Am.* 148, 649–659. doi:10.1121/10.0001687
- Fushimi, T., Marzo, A., Drinkwater, B. W., and Hill, T. L. (2019). Acoustophoretic Volumetric Displays Using a Fast-Moving Levitated Particle. *Appl. Phys. Lett.* 115, 064101. doi:10.1063/1.5113467
- Fushimi, T., Yamamoto, K., and Ochiai, Y. (2021). Acoustic Hologram Optimisation Using Automatic Differentiation. *Sci. Rep.* 11, 12678. doi:10.1038/s41598-021-91880-2
- Ho, J., Kalchbrenner, N., Weissenborn, D., and Salimans, T. (2019). Axial Attention in Multidimensional Transformers. arXiv 1912.12180. doi:10.48550/arXiv.1912.12180
- Jiménez-Gambín, S., Jiménez, N., Benlloch, J. M., and Camarena, F. (2019). Holograms to Focus Arbitrary Ultrasonic Fields through the Skull. *Phys. Rev. Appl.* 12 (1), 014016. doi:10.1103/PhysRevApplied.12.014016
- Khan, S., Naseer, M., Hayat, M., Zamir, S. W., Khan, F. S., and Shah, M. (2021). Transformers in Vision: a Survey. arXiv 2101.01169v4. doi:10.48550/arXiv.2101.01169
- Kruizinga, P., van der Meulen, P., Fedjajevs, A., Mastik, F., Springeling, G., de Jong, N., et al. (2017). Compressive 3D Ultrasound Imaging Using a Single Sensor. *Sci. Adv.* 3 (12), e1701423. doi:10.1126/sciadv.1701423
- Li, Y., Xue, Y., and Tian, L. (2018). Deep Speckle Correlation: a Deep Learning Approach toward Scalable Imaging through Scattering Media. *Optica* 5 (10), 1181–1190. doi:10.1364/optica.5.001181

AUTHOR CONTRIBUTIONS

BL and ML performed the analysis and drafted the manuscript. CL and XL supported the analysis design and made constructive discussions. XL and DT supervised the project, made critical revisions, and approved the final version.

FUNDING

This work was supported in part by the National Natural Science Foundation of China (61871263, 12034005, 11827808), in part by the Explorer Program of Shanghai (21TS1400200), in part by the Natural Science Foundation of Shanghai (21ZR1405200, 20S31901300), and in part by the China Postdoctoral Science Foundation (2021M690709).

- Lin, Q., Wang, J., Cai, F., Zhang, R., Zhao, D., Xia, X., et al. (2021). A Deep Learning Approach for the Fast Generation of Acoustic Holograms. *J. Acoust. Soc. Am.* 149, 2312–2322. doi:10.1121/10.0003959
- Liu, Z., Lin, Y., Cao, Y., Hu, H., Zhang, Z., Lin, S., et al. (2021). Swin Transformer: Hierarchical Vision Transformer Using Shifted Windows. arXiv: 2103.14030v1. doi:10.48550/arXiv.2103.14030
- Ma, Z., Holle, A. W., Melde, K., Qiu, T., Poeppel, K., Kadiri, V. M., et al. (2020). Acoustic Holographic Cell Patterning in a Biocompatible Hydrogel. *Adv. Mat.* 32 (4), 1904181. doi:10.1002/adma.201904181
- Marjan, B., Ahmed, E., Muhammad, R., and Shima, S. (2018). Acoustic Holograms in Contactless Ultrasonic Power Transfer Systems: Modeling and Experiment. *J. Appl. Phys.* 124, 244901. doi:10.1063/1.5048601
- Marzo, A., Seah, S. A., Drinkwater, B. W., Sahoo, D. R., Long, B., and Subramanian, S. (2015). Holographic Acoustic Elements for Manipulation of Levitated Objects. *Nat. Commun.* 6, 8661. doi:10.1038/ncomms9661
- Melde, K., Mark, A. G., Qiu, T., and Fischer, P. (2016). Holograms for Acoustics. *Nature* 537, 518–522. doi:10.1038/nature19755
- Michael, D. (2019). Phase and Amplitude Modulation with Acoustic Holograms. *Appl. Phys. Lett.* 115, 053701. doi:10.1063/1.5110673
- Rao, R., Liu, J., Verkuil, R., Meier, J., Canny, J. F., Abbeel, P., et al. (2021). MSA Transformer. bioRxiv 2021.02.12.430858. doi:10.1101/2021.02.12.430858
- Ren, Z., Xu, Z., and Lam, E. Y. (2019). End-to-end Deep Learning Framework for Digital Holographic Reconstruction. *Adv. Phot.* 1 (1), 016004. doi:10.1117/1.ap.1.1.016004
- Rivenson, Y., Zhang, Y., Günaydin, H., Teng, D., and Ozcan, A. (2018). Phase Recovery and Holographic Image Reconstruction Using Deep Learning in Neural Networks. *Light Sci. Appl.* 7, 17141. doi:10.1038/lsa.2017.141
- Sapozhnikov, O. A., Tsysar, S. A., Khokhlova, V. A., and Kreider, W. (2015). Acoustic Holography as a Metrological Tool for Characterizing Medical Ultrasound Sources and Fields. *J. Acoust. Soc. Am.* 138 (3), 1515–1532. doi:10.1121/1.4928396
- Sinha, A., Lee, J., Li, S., and Barbastathis, G. (2017). Lensless Computational Imaging through Deep Learning. *Optica* 4 (9), 1117–1125. doi:10.1364/optica.4.001117
- Wang, F., Bian, Y., Wang, H., Lyu, M., Pedrini, G., Osten, W., et al. (2020). Phase Imaging with an Untrained Neural Network. *Light Sci. Appl.* 9, 77. doi:10.1038/s41377-020-0302-3
- Wang, H., Zhu, Y., Green, B., Adam, H., Yuille, A., and Chen, L. C. (2020). Axial-deeplab: Stand-Alone Axial-Attention for Panoptic Segmentation. arXiv 2003.07853. doi:10.48550/arXiv.2003.07853
- Wang, H., Lyu, M., and Situ, G. (2018). eHoloNet: A Learning-Based End-To-End Approach for In-Line Digital Holographic Reconstruction. *Opt. Express* 26 (18), 22603–22614. doi:10.1364/oe.26.022603
- Wang, Z., Bovik, A. C., Sheikh, H. R., and Simoncelli, E. P. (2004). Image Quality Assessment: from Error Visibility to Structural Similarity. *IEEE Trans. Image Process.* 13 (4), 600–612. doi:10.1109/tip.2003.819861
- Wu, Y., Rivenson, Y., Zhang, Y., Wei, Z., Günaydin, H., Lin, X., et al. (2018). Extended Depth-Of-Field in Holographic Imaging Using Deep-Learning-Based Autofocusing and Phase Recovery. *Optica* 5 (6), 704–710. doi:10.1364/optica.5.000704

- Yang, M., Liu, Z.-H., Cheng, Z.-D., Xu, J.-S., Li, C.-F., and Guo, G.-C. (2019). Deep Hybrid Scattering Image Learning. *J. Phys. D. Appl. Phys.* 52 (11), 115105. doi:10.1088/1361-6463/aafa3c
- Yin, D., Gu, Z., Zhang, Y., Gu, F., Nie, S., Ma, J., et al. (2020). Digital Holographic Reconstruction Based on Deep Learning Framework with Unpaired Data. *IEEE Photonics J.* 12 (2), 1–12. doi:10.1109/jphot.2019.2961137
- Zeng, X., and McGough, R. J. (2008). Evaluation of the Angular Spectrum Approach for Simulations of Near-Field Pressures. *J. Acoust. Soc. Am.* 123 (1), 68–76. doi:10.1121/1.2812579
- Zeng, X., and McGough, R. J. (2009). Optimal Simulations of Ultrasonic Fields Produced by Large Thermal Therapy Arrays Using the Angular Spectrum Approach. *J. Acoust. Soc. Am.* 125, 2967–2977. doi:10.1121/1.3097499
- Zhao, H., Gallo, O., Frosio, I., and Kautz, J. (2017). Loss Functions for Image Restoration with Neural Networks. *IEEE Trans. Comput. Imaging* 3 (1), 47–57. doi:10.1109/tci.2016.2644865
- Zhu, Y., Gerard, N. J., Xia, X., Stevenson, G. C., Cao, L., Fan, S., et al. (2021). Systematic Design and Experimental Demonstration of Transmission-Type Multiplexed Acoustic Metaholograms. *Adv. Funct. Mat.* 31 (27), 2101947. doi:10.1002/adfm.202101947
- Conflict of Interest:** The authors declare that the research was conducted in the absence of any commercial or financial relationships that could be construed as a potential conflict of interest.
- Publisher's Note:** All claims expressed in this article are solely those of the authors and do not necessarily represent those of their affiliated organizations, or those of the publisher, the editors, and the reviewers. Any product that may be evaluated in this article, or claim that may be made by its manufacturer, is not guaranteed or endorsed by the publisher.

Copyright © 2022 Li, Lu, Liu, Liu and Ta. This is an open-access article distributed under the terms of the Creative Commons Attribution License (CC BY). The use, distribution or reproduction in other forums is permitted, provided the original author(s) and the copyright owner(s) are credited and that the original publication in this journal is cited, in accordance with accepted academic practice. No use, distribution or reproduction is permitted which does not comply with these terms.



Ultra-Broadband Sound Absorbing Materials Based on Periodic Gradient Impedance Matching

Fei Wu¹, Xiao Zhang¹, Zegang Ju², Jiang Zhao², Man Hu^{2*}, Mingyuan Gao², Jun Luo¹ and Huayan Pu¹

¹College of Mechanical and Vehicle Engineering, Chongqing University, Chongqing, China, ²College of Engineering and Technology, Southwest University, Chongqing, China

OPEN ACCESS

Edited by:

Fuyin Ma,
Xi'an Jiaotong University, China

Reviewed by:

Jie Zhou,
Northwestern Polytechnical
University, China
Yawen Wang,
University of Texas at Arlington,
United States

*Correspondence:

Man Hu
humanyyyes@126.com

Specialty section:

This article was submitted to
Metamaterials,
a section of the journal
Frontiers in Materials

Received: 31 March 2022

Accepted: 26 April 2022

Published: 03 June 2022

Citation:

Wu F, Zhang X, Ju Z, Zhao J, Hu M,
Gao M, Luo J and Pu H (2022) Ultra-
Broadband Sound Absorbing
Materials Based on Periodic Gradient
Impedance Matching.
Front. Mater. 9:909666.
doi: 10.3389/fmats.2022.909666

Ultra-broadband sound absorption with periodic gradient impedance matching is of great concern in the research of acoustic materials. This study investigates the impedance matching of composite acoustic metamaterials comprising micro-perforated plates (MPPs) and subsequent Fabry–Pérot (FP) channels. Based on the impedance matching theory, ultra-broadband sound absorption has been realized through a design with 36 channels whose thickness is only 50 mm. Also, the average sound absorption coefficient of 88% and an absorption frequency bandwidth (490–4000 Hz) can be achieved by preserving the matching impedance. Furthermore, by changing the thickness of the perfect absorber being 100 mm, the average sound absorption coefficient can reach greater than 90% in the frequency range of 250–4500 Hz. The proposed structure is validated analytically and experimentally. This work can help with designing and improving the method of acoustic metasurfaces and especially have the potential in ultra-broadband sound absorber designs.

Keywords: metamaterials, sound absorption, broadband, periodic gradient, impedance matching

INTRODUCTION

Broadband noise widely exists in mechanical engineering and aerospace engineering. In recent years, acoustic metamaterials have developed rapidly due to their excellent broadband sound absorption performance and flexible spatial arrangement and occupation. The total thickness of a micro-perforated plate (García-Chocano et al., 2012; Wang et al., 2014; Jiménez et al., 2016; Tang et al., 2017; Ryoo and Jeon, 2018), decorated membrane resonators (DMRs) (Yang et al., 2008, 2015; Ma et al., 2013, 2014; Yang and Sheng, 2017; Wang et al., 2018), and coiled-up channel (Cai et al., 2014; Li and Assouar, 2016; Liu et al., 2017; Shen et al., 2019) is much less than the wavelength at the working frequency. The appearance of acoustic metamaterials makes up for the defect that the structure of traditional porous materials (Biot, 1962) and porous plate absorbers (Sakagami et al., 2009) is too large in size for low-frequency sound absorption. Owing to the characteristics of deep sub-wavelength thickness and adjustable bandwidth of acoustic metamaterials, the design of ultra-broadband sound absorbers turns into one of the most notable subjects in this field. Usually, the optimization method for broadening the bandwidth is to skillfully combine different units of metamaterials in series or in parallel. Based on this method, a series of broadband sound absorbers are obtained (Qian et al., 2017; Bucciarelli et al., 2019; Mosa et al., 2019). A double-layered DMR structure with an interval of 28 mm was proposed. It had four discrete absorption peaks in the range of 100–1000 Hz, and the sound absorption performance in the frequency band between the absorption peaks was unsatisfactory (Mei

et al., 2012). Some scholars arranged a micro-perforated plate above 25 coplanar imperfect Helmholtz resonators to achieve efficient sound absorption in the 870–3224 Hz frequency band, and the thickness of the structure was 3.9 cm (Huang et al., 2020). A new type of sound absorber comprising six rectangular labyrinth sound-absorbing units was proposed, in which the rectangular labyrinth was arranged in a hexagonal shape. The research results showed its strong sound-absorbing performance in the range of 400–1400 Hz (Kumar and Lee, 2020). Y. Han et al. improved the sound absorption bandwidth and reduced the working frequency by using the coiled channel with variable cross-sections (Han et al., 2020). Some scholars proposed a sound absorber suitable for high-temperature environments, which is a double-layered structure comprising two perforated plates and a honeycomb structure. At 100°C, its broadband sound absorption capacity is more than three times higher than that of the traditional structure (Li et al., 2021). M. Duan et al. introduced an embedded neck and rubber coating based on the Helmholtz resonator. The design realized quasi-perfect absorption from 306 to 921 Hz, which achieved a low-frequency broadband perfect absorption at the 100-Hz level of underwater acoustics (Duan et al., 2021). The size of the sound absorber structure tends to increase while broadening the frequency band, which limits its application in engineering. According to its structural characteristics, the spiral channel has two characteristics: low frequency and sub-wavelength. Scholars proposed a metamaterial sound absorber with a thickness of 115.8 mm comprising multiple parallel spatial crimped FP channels, which can achieve quasi-perfect absorption from 400 to 3,000 Hz (Yang et al., 2017). In another work, 10 coiled FP channels with sound absorption peak gradient were connected in parallel with the cotton filled, and the average sound absorption coefficient in the frequency band of 500–2,000 Hz was greater than 0.9 (Chang et al., 2018). Recently, a 72-mm-thick sound absorber comprising one micro-perforated plate and 12 back cavity units showed excellent broadband sound absorption and achieves quasi-perfect sound absorption in the frequency band of 380–3,600 Hz (Rui Liu et al., 2020). In the aforementioned research, for achieving both low-frequency and broadband sound absorption, the size of the sound absorber tends to be larger than single functional designs, and meanwhile, the working space in special applications is very limited. To promote the application of metamaterials in engineering, it is necessary to balance low-frequency, broadband, and structural size in the design. With its unique structural characteristics, the FP channel has good performance in low frequency and small size.

In this study, we design an ultra-broadband sound absorber comprising 36 units, each of which comprises a micro-perforated plate and a coiled-up channel or a straight channel. Through the observation of the relative impedance of the structure, it can be found that the gradient parallel has a good impedance matching. The average sound absorption coefficient of the proposed absorber is 0.89 in the frequency range of 490–4,000 Hz, and the thickness of the structure is only 1/13 wavelength (50 mm). In addition, by increasing the channel length to 100 mm, the broadband of the design is further broadened, and the average sound absorption coefficient reaches 0.886 at 250–4,500 Hz with a thickness wavelength ratio of only 1/14.

GRADIENT DESIGN FOR IMPEDANCE MATCHING

Structural Design

As shown in **Figure 1A**, for the ultra-broadband sound absorber, each basic unit comprises a coiled-up channel (yellow part) or a straight channel (green part), and a micro-perforated plate is placed above the channels. With respect to the flatness and space utilization of the structure, we limit the thickness of the structure to 50 mm. The appropriate channel equivalent length is obtained by increasing the number of channel folding. The micro-perforated plate is introduced to use its large acoustic impedance to absorb low-frequency noise with a shorter equivalent sound absorption length. The coiled-up channels are introduced to double the equivalent sound absorption length through the folding of the channels to further decrease the working resonance frequency and the occupied space of the structure. The thickness of the structure is 50 mm (the thickness of the micro-perforated plate is 0.5 mm), and the cross-sectional area of all channels is 8.5 mm × 8.5 mm. The diameter of the micropores is 0.3 mm, and the perforation rate is 7%. The depth of the cavity behind the plate is 50 mm, and the side length is 58 mm (considering the thickness of the sidewall). It is worth noting that the units are separated by baffles to form an independent sound absorption channel. By gradually changing the height of the baffle relative to the micro-perforated plate, the coiled-up channel and sub-channel (straight channel) with equivalent sound absorption length gradient are obtained. In fact, when the length gradient of the coiled-up channel drops below the thickness of the structure, it becomes a straight channel. We place it in the remaining space after the channel is folded to maximize the use of space and make the structure more compact. **Figure 1B** shows the three-dimensional structure of the coiled-up channel, and the main structural parameters are indicated. The sound wave propagation direction is parallel to the z-axis, and the red dotted line represents the equivalent propagation path of the sound wave in the channel.

Theoretical Calculation

Generally, the overall performance of a sound absorber is characterized by the sound absorption coefficient of **Eq. 1**.

$$\alpha = 1 - \left| \left(\frac{Z_s}{Z_0} - 1 \right) / \left(\frac{Z_s}{Z_0} + 1 \right) \right|^2 \quad (1)$$

Here, Z_s is the acoustic impedance of the sound absorber; $Z_0 = \rho_0 C_0$ is the characteristic impedance of the air. In this work, the air density is $\rho_0 = 1.205 \text{ kg/m}^3$ and the sound velocity is $C_0 = 343 \text{ m/s}$. It can be seen from **Eq. 1** that the relative acoustic impedance (Z_s/Z_0) is related to the sound absorption coefficient. When the impedance of the structure matches well with the characteristic impedance of the air, the perfect sound absorption effect can be achieved. The acoustic impedance of the sound absorber is usually expressed in a complex form, which comprises the real part representing the viscous effect of air and the imaginary part representing the inertial effect of air. The acoustic impedance of the absorber can be calculated from **Eq. 2** (Wu et al., 2019).

$$Z_s = Z_M + \phi Z_{C1}^L \quad (2)$$

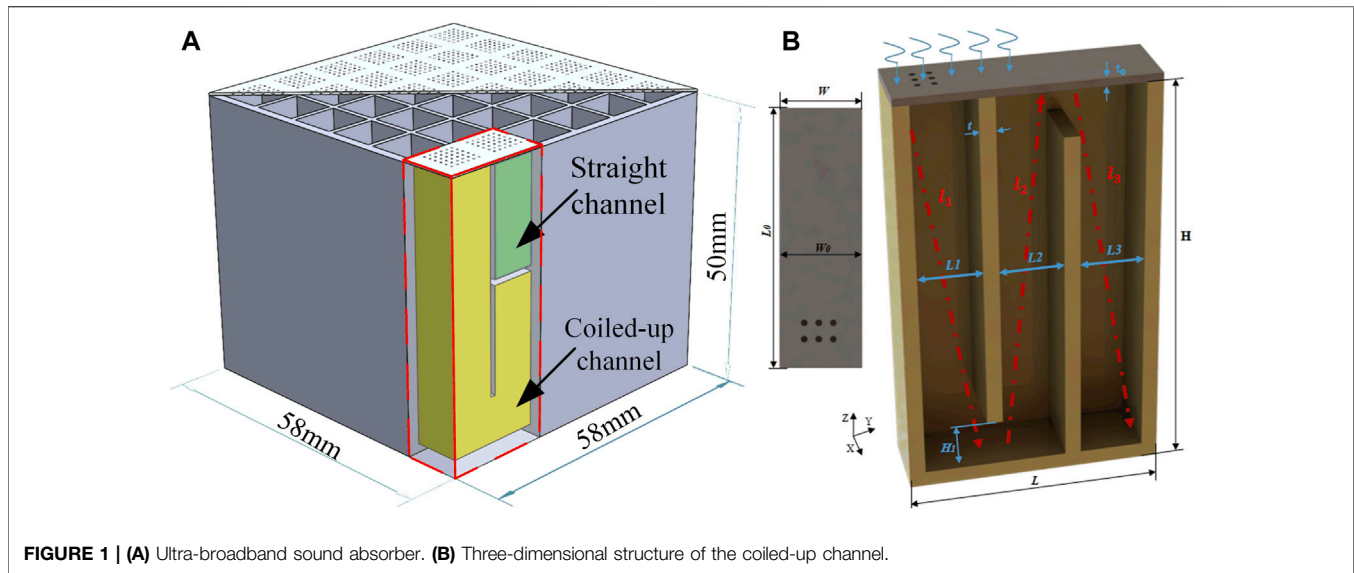


FIGURE 1 | (A) Ultra-broadband sound absorber. **(B)** Three-dimensional structure of the coiled-up channel.

Z_M and Z_{C1}^L represent the surface impedance of the micro-perforated plate and the surface impedance of the first channel at the entrance, respectively. $\phi = S_0/S_i$ is the area correction coefficient, where S_0 and S_i refer to the cross-sectional areas of the cells and channels, respectively. The Z_M can be calculated by Eq. 3.

$$Z_M = \frac{32\rho_0\mu t}{p d^2} \left(\sqrt{1 + \frac{k^2}{32}} + \frac{\sqrt{2}k}{8} \right) + \frac{j\omega\rho_0 t}{p} \left(1 + \frac{1}{\sqrt{9 + \frac{k^2}{2}}} + 0.85 \frac{d}{t} \right), \quad (3)$$

where μ is the kinematic viscosity of air; p , t , and d are the perforation rate, thickness, and diameter of the micro-perforated plate, respectively; ω refers to the angular frequency of the sound wave; and k refers to the perforation constant. The coiled-up channels can be simplified as a series of straight coaxial sub-channels in theoretical analysis. The effective propagation length in this sub-channel is expressed as l_i ($i = 1, 2, 3, \dots$). The surface impedance Z_1^L of the inlet at the top of the channel can be obtained by Eq. 4.

$$Z_i^L = m_i \frac{-jZ_{i+1}^L \cot(k_i l_i) + m_i}{Z_{i+1}^L - j m_i \cot(k_i l_i)} \quad (i = 1, 2, 3, \dots, N-1). \quad (4)$$

For $i = N$, $Z_N^L = -jm_N \cot(k_N l_N)$. $Z_{i+1}^L = Z_{i+1}^L / \phi_i$ and $\phi_i = S_{i+1}/S_i$. S_i and l_i represent the cross-sectional area and equivalent length of each channel, respectively. ρ_i^{eq} and C_i^{eq} refer to equivalent density and compressibility coefficient, respectively, which can be obtained by Eq. 5.

$$\left\{ \begin{array}{l} E = \sum_{k=0}^{\infty} \sum_{n=0}^{\infty} \left[\alpha_k^2 \beta_n^2 \left(\alpha_k^2 + \beta_n^2 + \frac{j\omega}{v} \right) \right]^{-1} \\ \rho_i^{\text{eq}} = \rho_0 \frac{v L_i^2 W_0^2}{4i\omega} E^{-1} \\ C_i^{\text{eq}} = \frac{1}{P_0} \left(1 - \frac{4i\omega(\gamma-1)}{v L_i^2 W_0^2} E \right) \end{array} \right. \quad (5)$$

where the kinematic viscosity $v = \mu/\rho_0$ and its derivative $v' = k/\rho_0 C_v$, with μ , k , and C_v represent air viscosity, thermal conductivity, and constant volume-specific heat, respectively. $\alpha_k = (k+0.5)\pi/W_0$, $\beta_n = (k+0.5)\pi/L_i$. P_0 and γ refer to the air pressure and the ratio of specific heat, respectively.

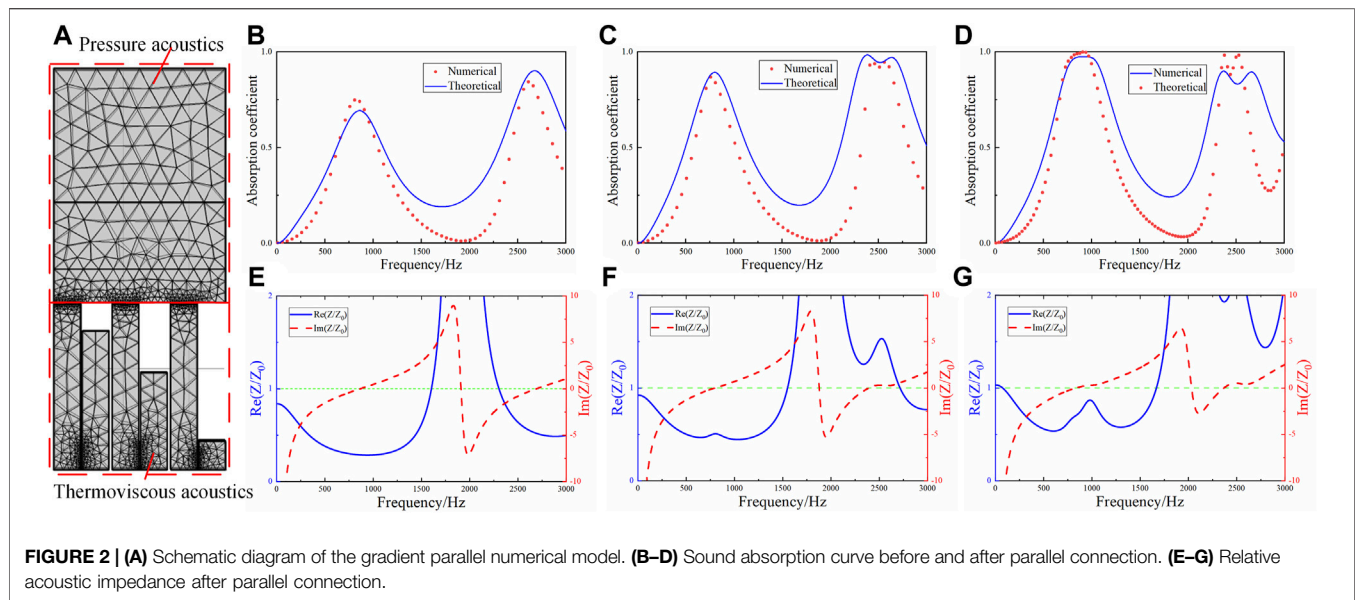
By assembling multiple acoustic units with different resonance characteristics in parallel, the broadband noise can be absorbed perfectly without adding other sound-absorbing materials (such as sound-absorbing cotton, etc.). The acoustic impedance of a sound absorber comprising multiple sound absorption units is calculated by Eq. 6 (Huang et al., 2020).

$$Z = \frac{n}{\sum_{i=1}^n (Z_{si}^{-1})}, \quad (6)$$

where Z_{si} represents the acoustic impedance of each sound absorption unit, and the number of units given in this study is $i = 36$.

Performance Analysis

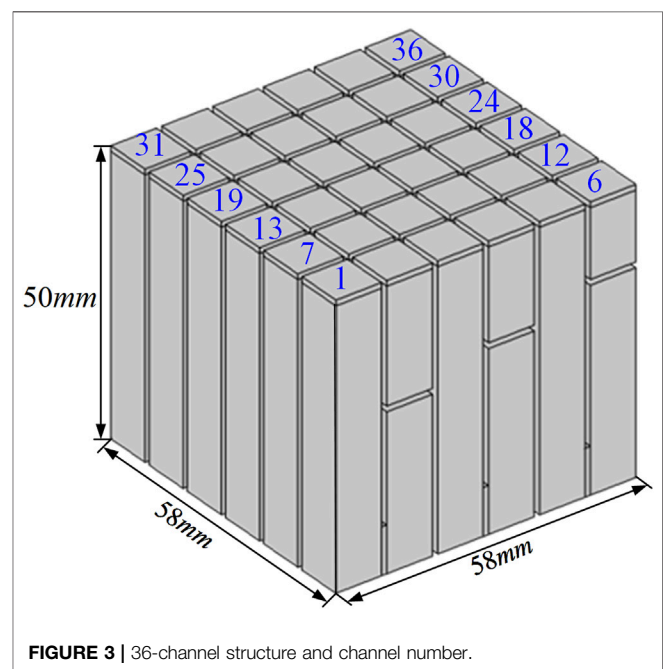
In this section, we analyze the performance of the sound absorption unit from the perspective of relative impedance. The micro-perforated plate and its upper area are defined as the pressure acoustic domain when establishing the numerical model. The micro-perforated plate and folded channels are defined as the thermal viscous acoustic domain as shown in Figure 2A. Figure 2B shows the sound absorption performance of the basic unit with a channel length of 79 mm, and the theoretical results (blue line) and numerical results (red dots) are both calculated. It can be seen from the figure that the coiled-up channel can have multiple absorption peaks in a wide frequency range, which represents the multiorder resonance frequency of the sound absorption structure, making broadband sound absorption easier. Figure 2E shows the relative impedance diagram of the device. When the impedance matches well, perfect sound absorption can be achieved. Moreover, the imaginary part of the relative impedance is equal to 0, and the real part is equal to 1. In



particular, the imaginary part curve of the relative impedance intersects the zero line three times, two of which correspond to the absorption peak in **Figure 2B**. The remaining one corresponds to the absorption valley of the curve, which is caused by the large deviation of the real part from the ideal value. Then, we assembled another unit with a channel length of 91.5 mm in parallel, and its relative impedance curve is shown in **Figure 2F**. It can be seen that the imaginary part curve is easier to converge to the best straight line. In the frequency band near 2,500 Hz, the real part and imaginary part are very close to the ideal state, and the sound absorption curve in **Figure 2C** shows that the average sound absorption coefficient in this part of the frequency band is more than 0.9. In order to further broaden the frequency band, we assembled another unit with a channel length of 58.5 mm in parallel to form a three-channel structure, and its sound absorption curve and relative impedance curve are shown in **Figures 2D,G**. It can be seen that the impedance matching has been further improved. Although the sound absorption coefficient of the high-frequency part has decreased, the low-frequency part of more interest has been significantly widened.

Based on the results of the 3-channel parallel arrangement, we speculate that adding parallel elements (according to the gradient) will help the relative impedance curve of the overall structure converge to the optimal value locally or globally in a wide frequency range, which will also be reflected in the final design. The channel number and channel length of the sound absorber designed in this article are shown in **Figure 3** and **Table 1**, respectively.

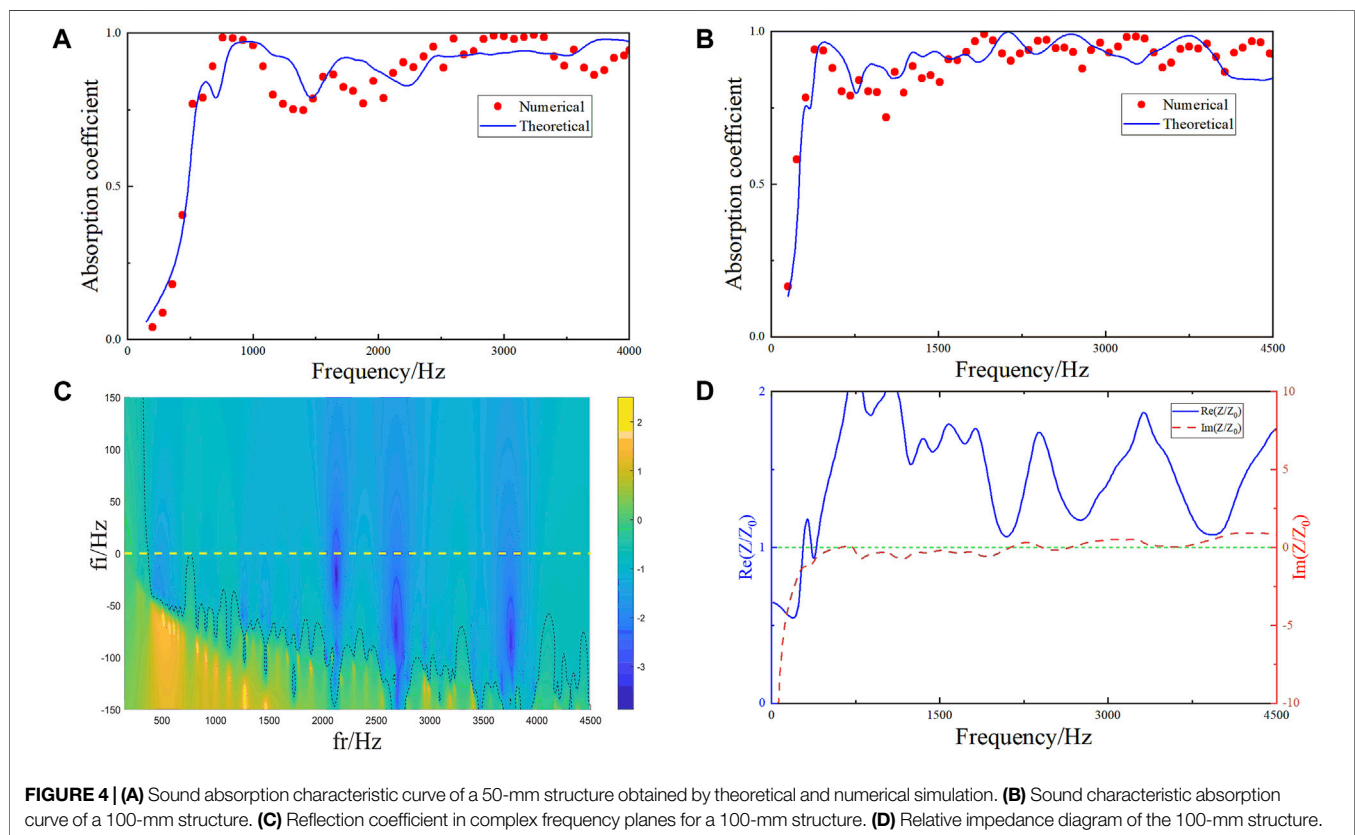
The sound absorption performance of the absorber is calculated by theoretical calculation and numerical simulation. In **Figure 4A**, the theoretical and numerical solutions prove the effectiveness of the results by mutual verification. The average sound absorption coefficient of the sound absorption structure in the frequency range of 490–4,000 Hz reaches 0.893. Moreover, perfect sound absorption is achieved at multiple frequency positions ($\alpha > 0.95$).



The absorption coefficient reaches 0.8 at 550 Hz with the thickness of the sound absorption structure only 1/13 of wavelength at this frequency, while the ratio of the thickness to wavelength is 1/1.7 at 4,000 Hz, indicating that the sound absorption structure meets the sub-wavelength design requirements in the whole frequency band. Furthermore, we double the channel length of each sound-absorbing unit and keep the other parameters unchanged; then, the second broadband sound-absorbing structure with a thickness of 100 mm is obtained. As shown in **Figure 4B**, the frequency range of sound absorption of the structure is broadened, and the average sound absorption coefficient of the sound absorption structure in the frequency range of 250–4,500 Hz is 0.886. The thickness ratio to

TABLE 1 | Channel length of each sound absorption unit.

S/N	D/mm	S/N	D/mm	S/N	D/mm	S/N	D/mm	S/N	D/mm	S/N	D/mm
1	79	7	91.5	13	58.5	19	71	25	142	31	125
2	21	8	8.5	14	41.5	20	29	26	4	32	12.5
3	83	9	95.8	15	62.5	21	75	27	4	33	12.5
4	17	10	4.2	16	37.5	22	25	28	134	34	117
5	87.5	11	54.5	17	67	23	96	29	8	35	16.5
6	12.5	12	45.5	18	33	24	4	30	8	36	16.5



the wavelength at 250 Hz is 1/14, which meets the design requirements of the sub-wavelength. **Figure 4C** shows the complex frequency plane of the 100-mm structure, in which the contour line (dotted line) represents the contour line with the sound absorption coefficient of 0.8, which only intersects the real axis at about 770 Hz, that is, the sound absorption coefficient of other frequency bands, except 770 Hz, greater than 0.8 between 400 and 4,500 Hz. The zero point at 2,130 Hz is almost on the real axis, where perfect sound absorption is achieved. The sound absorption characteristic curve is more complicated than a structure with a thickness of 50 mm. The sound absorption unit with a larger equivalent sound absorption length can often form multiple absorption peaks in a wider frequency band, which shows that the curve fluctuates more dramatically. However, compared with the performance of the three-channel sound absorption structure, the fluctuation of the relative impedance in **Figure 4D** has been greatly improved.

TEST VERIFICATION

In this study, the theoretical calculations, numerical simulations, and experiments are compared to ensure the accuracy of the conclusion. The experimental equipment is shown in **Figure 5A**. The cross section of the waveguide is square (60×60 mm) and made of an acrylic plate to simulate sound-hard boundary conditions. One side of the waveguide is the loudspeaker, which is used as the input of the test, and the other side is the place where the sample is installed. The microplate of the experimental sample is made of a metal material, and the micropores on the microplate are cut by laser. The channel under the plate is made of resin 3D printing and connected with the plate by gluing. The sound transfer function is obtained by calculating the sound pressure signals collected by two sensors arranged above the waveguide. The sound transfer functions of the two signals are obtained by measuring the sound pressure at the two sensors. The incident sound pressure and reflected sound

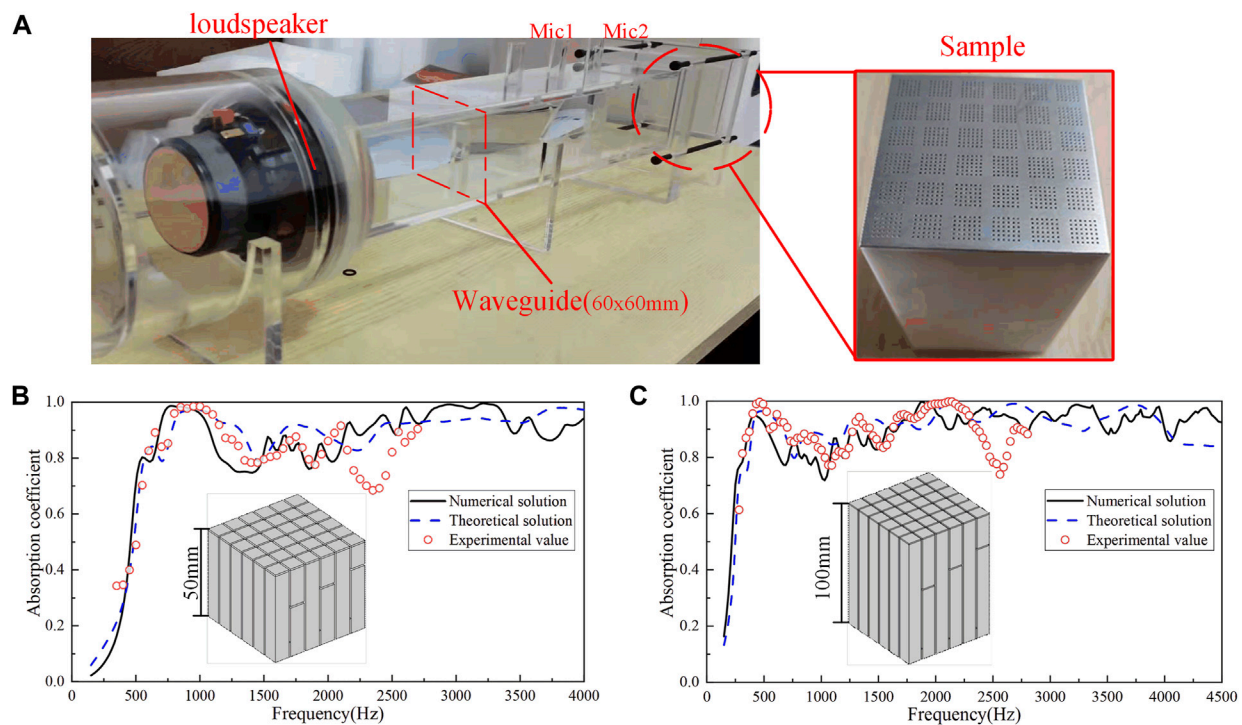


FIGURE 5 | (A) Experimental setup. **(B)** Absorption coefficients of 50-mm samples **(C)** Absorption coefficients of 100-mm samples.

pressure and the sound absorption coefficient of the sample are calculated on this basis.

The cutoff frequency of the test system is 2,700 Hz, and the comparison of experimental and simulation results is shown in **Figures 5B,C**. There is a slight deviation between the experimental results and the simulation within the test range, among which most prominence is found near 2,500 Hz, which is mainly due to the manufacturing error of the sample and the gap between the components of the test system. Generally speaking, the experimental results are in good agreement with the simulation results. It can be proven that the two designed structures perform well in low frequency and broadband sound absorption.

CONCLUSION

In this study, a 36-channel ultra-broadband sound absorber based on gradient parallel connection is designed, in which each channel comprises a crimped channel and micro-perforated plate. Theoretical, simulation, and experimental results show that the broadband sound absorption structure achieves high-efficiency sound absorption with an average sound absorption coefficient of 0.893 in the frequency range of 490–4,000 Hz with a structural thickness of 50 mm, and the sound absorption coefficient reaches 0.8 at 550 Hz with the thickness-wavelength ratio of the sound absorption structure being only 1/13. In addition, the structure achieves an average sound absorption coefficient of 0.886 in the 250–4,500 Hz frequency band with a thickness of 100mm, and the sound absorption coefficient reaches 0.8 at 250 Hz. Moreover, the thickness-to-wavelength ratio is 1/14. Both

designs meet the sub-wavelength requirements, and the sound absorption bandwidth is greatly improved compared with the traditional sound absorption structure. The proposed structures are easy to manufacture and have great potential applications in noise control engineering. Through the research of impedance matching, the gradient parallel design of the structure can effectively broaden the sound absorption band, which provides an effective design method for broadband sound absorption structures.

DATA AVAILABILITY STATEMENT

The original contributions presented in the study are included in the article/Supplementary Material; further inquiries can be directed to the corresponding author.

AUTHOR CONTRIBUTIONS

FW: conceptualization and writing—review and editing. XZ: methodology and writing—original draft. ZJ: investigation and software. JZ: data curation. MH: resources and writing—review and editing. HP: project administration. JL: supervision. MG: resources.

FUNDING

This work was supported by the Key Laboratory of aeroacoustics and the AVIC Aerodynamics Research Institute.

REFERENCES

- Biot, M. A. (1962). Generalized Theory of Acoustic Propagation in Porous Dissipative Media. *J. Acoust. Soc. Am.* 34, 1254–1264. doi:10.1121/1.1918315
- Bucciarelli, F., Malfense Fierro, G. P., and Meo, M. (2019). A Multilayer Microperforated Panel Prototype for Broadband Sound Absorption at Low Frequencies. *Appl. Acoust.* 146, 134–144. doi:10.1016/j.apacoust.2018.11.014
- Cai, X., Guo, Q., Hu, G., and Yang, J. (2014). Ultrathin Low-Frequency Sound Absorbing Panels Based on Coplanar Spiral Tubes or Coplanar Helmholtz Resonators. *Appl. Phys. Lett.* 105, 121901. doi:10.1063/1.4895617
- Chang, H., Liu, L., Zhang, C., and Hu, X. (2018). Broadband High Sound Absorption from Labyrinthine Metasurfaces. *AIP Adv.* 8, 045115. doi:10.1063/1.5024303
- Duan, M., Yu, C., Xin, F., and Lu, T. J. (2021). Tunable Underwater Acoustic Metamaterials via Quasi-Helmholtz Resonance: From Low-Frequency to Ultra-broadband. *Appl. Phys. Lett.* 118, 071904. doi:10.1063/5.0028135
- García-Chocano, V. M., Cabrera, S., and Sánchez-Dehesa, J. (2012). Broadband Sound Absorption by Lattices of Microperforated Cylindrical Shells. *Appl. Phys. Lett.* 101, 184101. doi:10.1063/1.4764560
- Han, Y., Wang, X., Xie, G., Tang, X., and Chen, T. (2020). Low-frequency Sound-Absorbing Metasurface with a Channel of Nonuniform Cross Section. *J. Appl. Phys.* 127, 064902. doi:10.1063/1.5119408
- Huang, S., Zhou, Z., Li, D., Liu, T., Wang, X., Zhu, J., et al. (2020). Compact Broadband Acoustic Sink with Coherently Coupled Weak Resonances. *Sci. Bull.* 65, 373–379. doi:10.1016/j.scib.2019.11.008
- Jiménez, N., Huang, W., Romero-García, V., Pagneux, V., and Groby, J.-P. (2016). Ultra-thin Metamaterial for Perfect and Quasi-Omnidirectional Sound Absorption. *Appl. Phys. Lett.* 109, 121902. doi:10.1063/1.4962328
- Kumar, S., and Lee, H. P. (2020). Labyrinthine Acoustic Metastructures Enabling Broadband Sound Absorption and Ventilation. *Appl. Phys. Lett.* 116, 134103. doi:10.1063/5.0004520
- Li, Y., and Assouar, B. M. (2016). Acoustic Metasurface-Based Perfect Absorber with Deep Subwavelength Thickness. *Appl. Phys. Lett.* 108, 063502. doi:10.1063/1.4941338
- Li, Z., Wang, Z., Guo, Z., Wang, X., and Liang, X. (2021). Ultra-broadband Sound Absorption of a Hierarchical Acoustic Metamaterial at High Temperatures. *Appl. Phys. Lett.* 118, 161903. doi:10.1063/5.0044656
- Liu, L., Chang, H., Zhang, C., and Hu, X. (2017). Single-channel Labyrinthine Metasurfaces as Perfect Sound Absorbers with Tunable Bandwidth. *Appl. Phys. Lett.* 111, 083503. doi:10.1063/1.4986142
- Ma, G., Yang, M., Xiao, S., Yang, Z., and Sheng, P. (2014). Acoustic Metasurface with Hybrid Resonances. *Nat. Mater.* 13, 873–878. doi:10.1038/nmat3994
- Ma, G., Yang, M., Yang, Z., and Sheng, P. (2013). Low-frequency Narrow-Band Acoustic Filter with Large Orifice. *Appl. Phys. Lett.* 103, 011903. doi:10.1063/1.4812974
- Mei, J., Ma, G., Yang, M., Yang, Z., Wen, W., and Sheng, P. (2012). Dark Acoustic Metamaterials as Super Absorbers for Low-Frequency Sound. *Nat. Commun.* 3, 756. doi:10.1038/ncomms1758
- Mosa, A. I., Putra, A., Ramlan, R., Prasetyo, I., and Esraa, A.-A. (2019). Theoretical Model of Absorption Coefficient of an Inhomogeneous MPP Absorber with Multi-Cavity Depths. *Appl. Acoust.* 146, 409–419. doi:10.1016/j.apacoust.2018.11.002
- Qian, Y. J., Zhang, J., Sun, N., Kong, D. Y., and Zhang, X. X. (2017). Pilot Study on Wideband Sound Absorber Obtained by Adopting a Serial-Parallel Coupling Manner. *Appl. Acoust.* 124, 48–51. doi:10.1016/j.apacoust.2017.03.021
- Rui Liu, C., Hui Wu, J., Yang, Z., and Ma, F. (2020). Ultra-broadband Acoustic Absorption of a Thin Microperforated Panel Metamaterial with Multi-Order Resonance. *Compos. Struct.* 246, 112366. doi:10.1016/j.compstruct.2020.112366
- Ryoo, H., and Jeon, W. (2018). Dual-frequency Sound-Absorbing Metasurface Based on Visco-Thermal Effects with Frequency Dependence. *J. Appl. Phys.* 123, 115110. doi:10.1063/1.5017540
- Sakagami, K., Nakamori, T., Morimoto, M., and Yairi, M. (2009). Double-leaf Microperforated Panel Space Absorbers: A Revised Theory and Detailed Analysis. *Appl. Acoust.* 70, 703–709. doi:10.1016/j.apacoust.2008.09.004
- Shen, Y., Yang, Y., Guo, X., Shen, Y., and Zhang, D. (2019). Low-frequency Anechoic Metasurface Based on Coiled Channel of Gradient Cross-Section. *Appl. Phys. Lett.* 114, 083501. doi:10.1063/1.5081926
- Tang, Y., Ren, S., Meng, H., Xin, F., Huang, L., Chen, T., et al. (2017). Hybrid Acoustic Metamaterial as Super Absorber for Broadband Low-Frequency Sound. *Sci. Rep.* 7, 43340. doi:10.1038/srep43340
- Wang, C., Huang, L., and Zhang, Y. (2014). Oblique Incidence Sound Absorption of Parallel Arrangement of Multiple Micro-perforated Panel Absorbers in a Periodic Pattern. *J. Sound Vib.* 333, 6828–6842. doi:10.1016/j.jsv.2014.08.009
- Wang, X., Luo, X., Zhao, H., and Huang, Z. (2018). Acoustic Perfect Absorption and Broadband Insulation Achieved by Double-Zero Metamaterials. *Appl. Phys. Lett.* 112, 021901. doi:10.1063/1.5018180
- Wu, F., Xiao, Y., Yu, D., Zhao, H., Wang, Y., and Wen, J. (2019). Low-frequency Sound Absorption of Hybrid Absorber Based on Micro-perforated Panel and Coiled-Up Channels. *Appl. Phys. Lett.* 114, 151901. doi:10.1063/1.5090355
- Yang, M., Chen, S., Fu, C., and Sheng, P. (2017). Optimal Sound-Absorbing Structures. *Mat. Horiz.* 4, 673–680. doi:10.1039/C7MH00129K
- Yang, M., Meng, C., Fu, C., Li, Y., Yang, Z., and Sheng, P. (2015). Subwavelength Total Acoustic Absorption with Degenerate Resonators. *Appl. Phys. Lett.* 107, 104104. doi:10.1063/1.4930944
- Yang, M., and Sheng, P. (2017). Sound Absorption Structures: From Porous Media to Acoustic Metamaterials. *Annu. Rev. Mat. Res.* 47, 83–114. doi:10.1146/annurev-matsci-070616-124032
- Yang, Z., Mei, J., Yang, M., Chan, N. H., and Sheng, P. (2008). Membrane-Type Acoustic Metamaterial with Negative Dynamic Mass. *Phys. Rev. Lett.* 101, 204301. doi:10.1103/PhysRevLett.101.204301

Conflict of Interest: The authors declare that the research was conducted in the absence of any commercial or financial relationships that could be construed as a potential conflict of interest.

Publisher's Note: All claims expressed in this article are solely those of the authors and do not necessarily represent those of their affiliated organizations, or those of the publisher, the editors, and the reviewers. Any product that may be evaluated in this article, or claim that may be made by its manufacturer, is not guaranteed or endorsed by the publisher.

Copyright © 2022 Wu, Zhang, Ju, Zhao, Hu, Gao, Luo and Pu. This is an open-access article distributed under the terms of the Creative Commons Attribution License (CC BY). The use, distribution or reproduction in other forums is permitted, provided the original author(s) and the copyright owner(s) are credited and that the original publication in this journal is cited, in accordance with accepted academic practice. No use, distribution or reproduction is permitted which does not comply with these terms.

Advantages of publishing in Frontiers



OPEN ACCESS

Articles are free to read for greatest visibility and readership



FAST PUBLICATION

Around 90 days from submission to decision



HIGH QUALITY PEER-REVIEW

Rigorous, collaborative, and constructive peer-review



TRANSPARENT PEER-REVIEW

Editors and reviewers acknowledged by name on published articles

Frontiers

Avenue du Tribunal-Fédéral 34
1005 Lausanne | Switzerland

Visit us: www.frontiersin.org

Contact us: frontiersin.org/about/contact



REPRODUCIBILITY OF RESEARCH

Support open data and methods to enhance research reproducibility



DIGITAL PUBLISHING

Articles designed for optimal readership across devices



FOLLOW US

@frontiersin



IMPACT METRICS

Advanced article metrics track visibility across digital media



EXTENSIVE PROMOTION

Marketing and promotion of impactful research



LOOP RESEARCH NETWORK

Our network increases your article's readership